Quantifying and perturbing the movement of extracellular proteins in zebrafish embryos

Dissertation

der Mathematisch-Naturwissenschaftlichen Fakultät

der Eberhard Karls Universität Tübingen

zur Erlangung des Grades eines

Doktors der Naturwissenschaften

(Dr. rer. nat.)

vorgelegt von

M.Sc. David Mörsdorf

aus Saarbrücken

Tübingen

2019

Gedruckt mit Genehmigung der Mathematisch-Naturwissenschaftlichen Fakultät der Eberhard Karls Universität Tübingen.

Tag der mündlichen Qualifikation:	04.12.2019
Dekan:	Prof. Dr. Wolfgang Rosenstiel
1. Berichterstatter:	Prof. Dr. Patrick Müller
2. Berichterstatter:	Prof. Dr. Ana J. García-Sáez

Declaration about this Work and Affidavit

The work I describe here was performed as part of my PhD studies under the supervision of Prof. Dr. Patrick Müller at the Friedrich Miescher Laboratory of the Max Planck Society in Tübingen. It was funded in part by the International Max Planck Research School “From Molecules to Organisms”.

I hereby declare, that this thesis is the result of my own work and that I have credited all other sources and resources accordingly. I followed good scientific practice rules to perform experiments and analyze data.

Table of Contents

Acknowledgments

I thank Prof. Dr. Patrick Müller for supervising my PhD project and for all the support I got since I joined his lab. I am thankful for his mentorship and guidance on experimental design, data analysis and result presentation. I thank him for supporting my career by sponsoring the attendance of meetings and workshops.

I also want to express my gratitude to Prof. Dr. Ana J. García-Sáez and Prof. Dr. Boris Maček, who have guided my project over the years as members of my Thesis Advisory Committee and were always available for discussions and collaborations.

I thank the International Max Planck Research School "From Molecules to Organisms" for funding me and for organizing workshops and symposia. Thanks to the coordinators of the PhD programs, Dr. Sarah Danes and Dr. Dagmar Sigurdardottir, for their help and support.

I want to thank the following colleagues and friends for scientific discussions and/or providing materials: Dr. Katherine W. Rogers for help with staining protocols, the *squint-RFP* and *lefty1/2-RFP* constructs, countless scientific discussions and her thorough feedback on the thesis manuscript. Dr. María Almuedo-Castillo for teaching me fluorescence *in situ* hybridization and for her close collaboration in the scaling project. Autumn Penecilla Pomreinke for help with staining protocols and feedback on the thesis manuscript. Dr. Olga Matsarskaia for feedback on the thesis manuscript. Dr. Daniel Čapek for discussions about Wnt signaling and feedback on the thesis manuscript. Gary H. Soh for help with staining protocols, providing the *squint-mCherry* construct and for generating *MZsqt*$^{-/-}$*;cyc*$^{-/-}$ germ line mutants. Hannes Preiß for help with staining protocols, his advice on Morpholino use and feedback on the thesis manuscript. Dr. Alexander Bläße for help with PyFRAP and FRAP analysis. Amit Landge for discussing mathematical models.

I thank all members of the Müller lab for the great and inspirational working environment. I am particularly thankful to the present and former technical personnel of the lab for providing technical help and organizing the lab: Maria Langegger, Christine Henzler, Catrin Weiler and Sarah Keim. I am deeply grateful to our animal caretaker Dieter Labusch for taking great care of the fish and maintaining aquaria.

I thank all personnel of the Light Microscopy Facility at the Max Planck Institute for Developmental Biology. I am especially thankful for the great support I got from Dr. Christian Feldhaus and Aurora Panzera. I thank Dr. Mirita Franz-Wachtel at the Proteome Center of the University of Tübingen for the mass spectrometry analysis, her help with data interpretation and for helpful discussions.

I cannot thank enough my parents who have supported me tremendously during my studies in Tübingen. I am grateful that they have always encouraged me to pursue my interests and have provided advice as well as practical help wherever I needed it. I also thank all other family members and friends for support, especially my sisters and my childhood friend Thomas Kunz who I can always rely on. Special thanks go to Dr. Annamaria Sgromo for her personal and scientific support. She has provided feedback on the thesis manuscript and is always there to help me. I am lucky to be able to count on her and have her as my constant source of motivation.

I am very happy that I joined Patrick's group for my PhD. Over the years I have not only learned a lot, but I also had the freedom to pursue my own research ideas. I am especially happy for the many great scientists I met and friends I made during my PhD – I hope to see them all again in the future!

Abbreviations

ActRIIB	Activin receptor type II B
ALK4	Activin receptor-like kinase
APEX	Engineered ascorbic acid peroxidase
BioID	Proximity-dependent biotin identification
cDNA	Coding deoxyribonucleic acid
CoIP	Co-immunoprecipitation
CRISPR/Cas9	Clustered regularly interspaced short palindromic repeats/CRISPR-associated 9
cx43.4/Cx43.4	*connexin43.4*/Connexin43.4
cyc/Cyc	*cyclops*/Cyclops
DAPI	4′,6-diamidino-2-phenylindole
D. melanogaster	*Drosophila melanogaster*
dpf	Day(s) post fertilization
Dpp	Decapentaplegic
dvr1/Dvr1	*decapentaplegic and vg-related 1*/Decapentaplegic and Vg-related 1
ECM	Extracellular matrix
EGF	Epidermal growth factor
EGF-CFC	Containing an EGF-like and a CFC (Cripto, FRL-1, Cryptic) motif
EGL-20-YPET	Egg laying defective-20-Yellow fluorescent protein for energy transfer (fusion)
ER	Endoplasmic reticulum
EVL	Enveloping layer
FA	Formaldehyde
epcam/Epcam	*epithelial cell adhesion molecule*/Epithelial cell adhesion molecule
FCS	Fluorescence correlation spectroscopy
FISH	Fluorescence *in situ* hybridization
FGF	Fibroblast growth factor
FRAP	Fluorescence recovery after photobleaching
Gdf3	Growth and differentiation factor 3
GFP	Green fluorescent protein
gsc	*goosecoid*
HEPES	4-(2-hydroxyethyl)-1-piperazineethanesulfonic acid
hpf	Hour(s) post fertilization
hsp90b1/Hsp90b1	*heat shock protein 90 b1*/Heat shock protein 90 b1
HSPG	Heparan sulfate proteoglycans
IF	Immunofluorescence
jupb/Jupb	*junction plakoglobin b*/Junction plakoglobin b

LP	Laser power
lft1/Lft1	*lefty1*/Lefty1
lft2/Lft2	*lefty2*/Lefty2
MIP	Maximum intensity projection
MO	Morpholino
mRNA	Messenger ribonucleic acid
MS	Mass spectrometry
MS4A	Membrane-spanning 4-domain family, subfamily A
MZsqt$^{-/-}$;cyc$^{-/-}$	Maternal-zygotic *sqt$^{-/-}$;cyc$^{-/-}$*
oep/Oep	*one-eyed pinhead*/One-eyed pinhead
RFP	Red fluorescent protein
RT	Room temperature
PBS	Phosphate-buffered saline
PCR	Polymerase chain reaction
PEP	Posterior error probability
PM	Plasma membrane
pSmad2/3	Phosphorylated Smad2/3
SSC	Saline sodium citrate
SDS-PAGE	Sodium dodecyl sulfate polyacrylamide gel electrophoresis
secGFP	Secreted GFP
Smad	Sma- and Mad-related protein
sqt/Sqt	*squint*/Squint
SUEL	Sea urchin egg lectin
TBS	Tris-buffered saline
tdgf1/Tdgf1	*teratocarcinoma-derived growth factor 1*/Teratocarcinoma-derived growth factor 1
tpte/Tpte	*transmembrane phosphatase with tensin homology*/ Transmembrane phosphatase with tensin homology
Tris	Tris(hydroxymethyl)aminomethane
TGF-β	Transforming growth factor-β
VLDL	Very low density lipoprotein
vldlr/Vldlr	*very low density lipoprotein receptor*/ Very low density lipoprotein receptor
WT	Wildtype
Xnr1	*Xenopus* nodal-related 1
YSL	Yolk syncytial layer

Summary

Cell-cell communication mediated by secreted signaling molecules is crucial to coordinate early embryonic development. In the classical morphogen model secreted signaling molecules control embryogenesis as follows: After secretion from a source they disperse in the tissue and instruct target cells at a distance to adopt different cell fates that are defined by signaling levels. Thus, the signal's distribution controls the cellular patterning of the tissue. However, the mechanisms underlying signal distribution *in vivo* and the requirement for signals acting at a distance remain controversial.

Nodals are extracellular signaling molecules of the Transforming growth factor-β (TGF-β) superfamily and are required for mesoderm and endoderm formation in vertebrates. In the zebrafish *Danio rerio*, Nodals were proposed to function as classical morphogens that disperse from localized Nodal-secreting cells to act on distant cells. However, recent findings suggest that Nodals signal only to neighboring cells and that their signaling is propagated to distant cells by a combination of auto-induction and cell-to-cell signal relay, thus challenging the classical morphogen model. To directly test the two models of Nodal signaling I performed *in vivo* experiments to observe the endogenous Nodal signaling range. My results suggest that zebrafish Nodals can signal directly – *i.e.* without relay – to cells at a distance from their source. However, the importance of Nodal dispersal for its function during embryonic patterning remains to be determined.

The morphogen model predicts that an altered signal dispersal leads to an altered signaling range and aberrant tissue patterning. To examine whether extracellular signal movement is required for the signal's biological function, tools that restrict extracellular signal mobility are needed. Recently developed synthetic signal binders can be used to reversibly tether extracellular signals to the cell membrane and perturb signal spreading. I investigated how the transient membrane-tethering can be harnessed to experimentally reduce the effective diffusivity of extracellular proteins and thus regulate their mobility in a tuned manner. This approach allowed me to hinder the diffusion of the long-range Nodal inhibitor Lefty1 and investigate its long-range function in live zebrafish embryos.

In zebrafish, Nodals have lower effective diffusion coefficients and a shorter range than their antagonists, the long-range Leftys. To explain the contrasting mobilities of these two TGF-β-related factors that are similar in molecular weight, binding partners in the extracellular matrix were proposed to act as diffusion regulators. My aim was to reveal these hypothetical diffusion regulators. I established a co-immunoprecipitation approach for zebrafish Nodals and Leftys and identified putative interaction partners by mass spectrometry. Surprisingly, known Nodal interaction partners were not identified as diffusion regulators with this approach, raising the possibility that other factors regulate the Nodal/Lefty system.

In my work I investigated extracellular signal movement and focused on its modulation by diffusion regulators. My findings highlight that synthetic membrane tethers can be used as experimental diffusion regulators and that they serve as valuable tools to challenge models of long-range morphogen function.

Zusammenfassung

Sezernierte Signalproteine sind unabdingbar für die Zell-Zell-Kommunikation in der frühen Embryogenese. Im klassischen Morphogenmodell koordinieren diese die zelluläre Musterbildung folgendermaßen: Ausgehend von einem Quellgewebe verteilen sie sich im Embryo und induzieren in entfernt gelegenen Zellen konzentrationsabhängig spezifische Zelltypen. Demnach ist die Verteilung des Morphogens im Gewebe entscheidend für die Embryogenese. Obwohl viele Signalmoleküle als Morphogene bezeichnet werden, sind die Mechanismen der embryonalen Musterbildung oft unklar. Besonders strittig ist, wie wichtig die direkte Signalübermittlung an entfernt gelegene Zellen ist.

Die sezernierten Nodal Signalproteine, welche in Wirbeltieren für die Bildung von Mesoderm und Endoderm benötigt werden, gelten im Zebrafisch seit Langem als Musterbeispiel für Morphogene. Im klassischen Modell verteilen sich Nodals im Gewebe um auf entfernt gelegene Zellen zu wirken. Allerdings deuten Erkenntnisse der letzten Jahre darauf hin, dass Nodals nur auf benachbarte Zellen wirken und die Nodal Signalaktivität sich durch eine Kombination von Zell-Zell-Signalübertragung und positiver Autoregulation im Embryo ausbreitet. Um die beiden Modelle der Nodal Funktionsweise zu vergleichen habe ich die endogene Nodal Signalreichweite in Zebrafischembryos untersucht. Meine Ergebnisse deuten darauf hin, dass Nodals direkt auf entfernt gelegene Zellen wirken können. Die Relevanz dieses Sachverhalts für die embryonale Musterbildung bedarf noch weiterer Untersuchung.

Laut Morphogenmodell führt eine reduzierte Signalreichweite zu Musterbildungsdefekten. Um diese Vorhersage zu testen ist es nötig die Signalmobilität zu manipulieren. Kürzlich entwickelte Methoden erlauben es extrazelluläre Signalproteine reversibel an die Zellmembran zu binden. Ich habe untersucht wie diese transiente Immobilisierung genutzt werden kann um die effektive Diffusivität sezernierter Proteine zu reduzieren und damit ihre Mobilität *in vivo* zu modulieren. Basierend auf diesem Ansatz experimenteller Diffusionsregulation, habe ich die Mobilität des Nodal Antagonisten Lefty1 reduziert um die biologische Relevanz dessen langer Reichweite im Zebrafischembryo zu testen.

Im Zebrafischembryo haben Nodals eine kürzere Reichweite und geringere effektive Diffusivität als Leftys. Um zu erklären warum Nodals und Leftys – die beide zur Transforming growth factor-β Superfamilie gehören und ein vergleichbares Molekulargewicht haben – verschiedene Mobilitäten aufweisen, wurde postuliert, dass Bindepartner in der Extrazellulären Matrix als Diffusionsregulatoren fungieren. Um potenzielle Nodal/Lefty Interaktionspartner zu extrahieren, habe ich Zebrafisch Nodals und Leftys immunpräzipitiert und mögliche Bindepartner dann über Massenspektrometrie identifiziert. Überraschenderweise konnte ich bekannte Nodal Interaktionspartner nicht als Diffusionsregulatoren identifizieren, was Fragen über die endogene Regulation von Nodals und Leftys aufwirft.

In meiner Arbeit habe ich untersucht wie die extrazelluläre Mobilität von Signalproteinen moduliert werden kann. Meine Ergebnisse zeigen, dass die effektive Diffusion eines extrazellulären Proteins durch dessen transiente Immobilisierung an der Zellmembran reguliert werden kann. Diese Methode ist nützlich um das Morphogenmodell bezüglich Signalreichweiten zu testen.

1. Publications of this Thesis and Author Contributions

1.) **Mörsdorf D.** and Müller P. (2019). "Tuning protein diffusivity with membrane tethers." *Biochemistry* **58**(3): 177-181.

I initiated and together with Patrick Müller outlined the project. I wrote a first draft of the manuscript and performed all experiments. The manuscript was revised with the help of Patrick Müller. I analyzed the results together with Patrick Müller.

2.) Almuedo-Castillo M., Bläßle A., **Mörsdorf D.**, Marcon L., Soh G. H., Rogers K. W., Schier A. F. and Müller P. (2018). "Scale-invariant patterning by size-dependent inhibition of Nodal signalling." *Nature Cell Biology* **20**(9): 1032-1042.

The study was conceived by Patrick Müller, Alexander Schier and María Almuedo-Castillo. The experiments were performed by María Almuedo-Castillo, Gary Soh, Katherine Rogers and myself. The results were analyzed with the help of Alexander Bläßle and Patrick Müller. Patrick Müller, Alexander Bläßle and Luciano Marcon performed mathematical modeling. María Almuedo-Castillo and Patrick Müller wrote the manuscript.

Specifically, I performed parts of the yolk syncytial layer injections and time-lapse microscopy to image the dispersal of Lefty1-GFP *in vivo*. I performed the fluorescence recovery after photobleaching (FRAP) experiments to quantify the effect of the morphotrap on Lefty1-GFP mobility and evaluated the effects of the morphotrap on Lefty1-GFP activity. Additionally, I performed anti-Lefty1 and anti-Histone3 western blots of experimentally-shortened (provided by María Almuedo-Castillo) and untreated embryos to estimate the endogenous Lefty1 levels. I also helped revise the manuscript.

3.) Bläßle A., Soh G., Braun T., **Mörsdorf D.**, Preiss H., Jordan B. M. and Müller P. (2018). "Quantitative diffusion measurements using the open-source software PyFRAP." *Nature Communications* **9**(1): 1582.

Patrick Müller, Ben Jordan and Alexander Bläßle conceived the study. Alexander Bläßle implemented the software. The experiments were performed by Gary Soh, Alexander Bläßle, Theresa Braun, Hannes Preiß and myself. Data analysis was performed by Patrick Müller and Alexander Bläßle.

I provided FRAP datasets for the study and tested the PyFRAP software before publication. Additionally, I provided feedback on the manuscript.

2. Introduction

2.1 Morphogen distribution and movement in embryology

A longstanding question in developmental biology is how the stereotypical body plan of a species is generated reproducibly from morphologically simple tissues during embryogenesis. Early embryological studies have shown that certain "organizer" tissues in the early embryo can determine the development of surrounding cells (Spemann and Mangold 1924). It was subsequently proposed that organizing activity may be due to diffusible "evocator" substances from the organizer (Waddington 1936), but the exact mechanisms underlying this inductive effect are still under debate today (Harland and Gerhart 1997, Schier and Talbot 2001, Stern 2001, Shih *et al.* 2010, Martinez Arias and Steventon 2018). Secreted signaling molecules and inhibitors are crucial for the organizing process as well as patterning the tissue into defined cell types (Thisse and Thisse 2015, Martyn *et al.* 2018). The fact that organizers control surrounding tissues implies that the secreted factors have to move from the organizer to act on distant cells.

To explain how biological patterns can arise during morphogenesis, Alan Turing proposed a theoretical model in which two chemical species can generate a pattern based on reactions between them and diffusion (Turing 1952). Turing used the term "morphogen" to describe a "form producer" substance that may pattern tissues through such a reaction-diffusion system. Another theory to explain cellular patterning and how cells identify their position in a tissue during differentiation is Wolpert's theory of positional information (Wolpert 1968, Wolpert 1969). It proposes that a field of cells can be patterned in response to different concentrations of a substance in the tissue. This principle of threshold-based responses to a concentration gradient was soon combined with the idea that diffusion from a localized source in a tissue could cause the graded distribution of a substance (Crick 1970). Both aspects are reflected in the modern morphogen concept, the definition of which has changed over time (Wolpert 1989, Wolpert 2011) and is still a matter of perspective today: A classical morphogen is a (secreted signaling) molecule that acts at a distance from its source and induces differential responses at different concentrations (Figure 1; Tabata and Takei 2004, Nahmad and Lander 2011, Rogers and Schier 2011, Sagner and Briscoe 2017). The *Drosophila melanogaster* Bicoid was the first morphogen to be identified (Driever and Nüsslein-Volhard 1988). Bicoid and the *D. melanogaster* Dorsal (Moussian and Roth 2005) are transcription factors and thus special cases of morphogens (Rogers and Schier 2011). Today, many signaling molecules are considered to be morphogens, among them are the signaling proteins Fibroblast growth factor (FGF), Hedgehog, Wnt, the Transforming growth factor-β (TGF-β) superfamily members Activin, Nodal and Bone morphogenetic protein (Decapentaplegic (Dpp) in *D. melanogaster*) as well as the small molecule retinoic acid (Nellen *et al.* 1996, Zecca *et al.* 1996, Strigini and Cohen 1997, Gurdon *et al.* 1999, Chen and Schier 2001, Jiang and Hui 2008, Schilling *et al.* 2012, Bökel and Brand 2013, Bier and De Robertis 2015, van Boxtel *et al.* 2015, Routledge and Scholpp 2019).

Loss of morphogen signaling typically leads to devastating developmental defects (Driever and Nüsslein-Volhard 1988, Mullins *et al.* 1996, Zecca *et al.* 1996, Feldman *et al.* 1998). In the classical morphogen model, morphogen mobility and the resulting morphogen distribution are critical for proper patterning (Figure 1). Studies have shown that an altered morphogen distribution or mobility can result in aberrant embryonic patterning (Driever and Nüsslein-Volhard 1988, Strigini and Cohen 1997, Harmansa *et al.* 2015). Intriguingly, there are cases where patterning is maintained despite an altered morphogen distribution (Alexandre *et al.* 2014) or where aberrant embryonic patterning does not preclude the development into normally patterned adults (Driever and Nüsslein-Volhard 1988, Dougan *et al.* 2003, Mizutani *et al.* 2005). These findings emphasize the importance of testing whether the classical morphogen model applies to the proposed morphogens by perturbing their mobility.

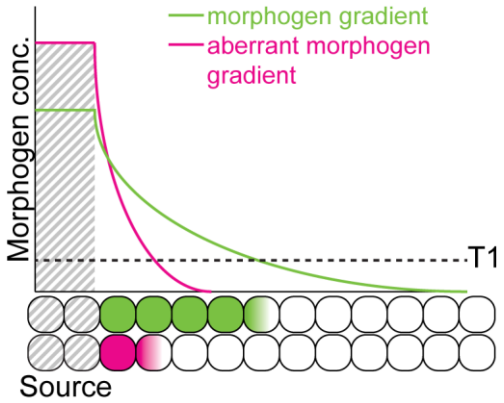

Figure 1: The morphogen model. The morphogen is produced at a localized source (gray stripes, left) to pattern cells (illustrated below x-axis) at a distance. Cells that experience a morphogen concentration above the threshold T1 respond to the signal and adopt a defined cell type (colored cells). In the morphogen model, the distribution of the morphogen (green/magenta lines) is crucial to properly pattern the tissue because cells differentially respond to distinct morphogen threshold concentrations in order to pattern complex tissues with more than two different cell types (not shown).

2.2 Transport of extracellular signaling molecules

Cell-cell communication is crucial in multicellular organisms and communities of single-celled organisms to coordinate developmental programs as well as responses to environmental cues (Hill and Treisman 1995, Downward 2001, Brivanlou and Darnell 2002, Loomis 2014). Extracellular signaling molecules represent a useful means to transmit information between cells because they can act over large distances and in complex tissues (Tata 2005, Benham 2012). How signals are transported from the signal-producing source cells to the target cells depends on the biological context. Hormones, for example, can be transported rapidly through an animal via the bloodstream (Tata 2005). On a smaller scale, bacteria can communicate through quorum sensing of diffusible molecules (West *et al.* 2012, Whiteley *et al.* 2017). In tissues that lack specialized transport systems like blood vessels, passive as well as active transport is possible (Müller and Schier 2011, Müller *et al.* 2013). Passive transport by extracellular diffusion is a mechanistically simple way to achieve signal dispersal in a tissue upon secretion. Although diffusion is slow over long distances, biomolecules can in theory diffuse over

embryo-scale distances within biologically relevant time scales (Crick 1970, Lander 2007, Müller and Schier 2011). Alternative means of signal transport include active transport by cell protrusions (González-Méndez *et al.* 2019, Kornberg 2019), extracellular vesicles (McGough and Vincent 2016), transcytosis (Kicheva *et al.* 2007, Wartlick *et al.* 2009) or cilia-generated flow (Müller and Schier 2011, Olstad *et al.* 2019).

It is important to realize that long-range transport of secreted signaling molecules is not necessary to propagate signaling through a tissue. Short-range signaling molecules can propagate their signaling through relay mechanisms (van Boxtel *et al.* 2015, Wilcockson *et al.* 2017, Rogers and Müller 2019). In this case the signaling molecules transmit information only to neighboring cells, where auto-induction generates more signal to reach adjacent cells (that are at a distance from the initial source cell; Figure 2). Since signal propagation by relay depends on many sequential steps (signal transduction, production and secretion), it is unclear how fast signaling can be propagated in this way (Ohi and Wright 2007).

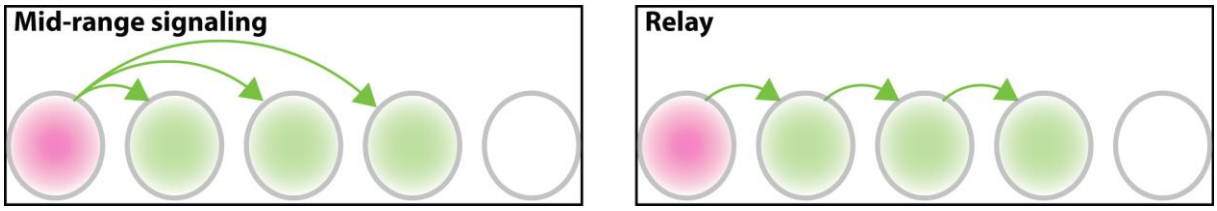

Figure 2: Long-range signaling can be mediated by a secreted signal acting directly at a distance or by signal-mediated relay. The left panel shows a source cell (magenta) that secretes a signal which directly acts on distant cells (green). The relay model in the right panel is based on positive feedback-mediated cell-to-cell signaling.

To understand signaling molecule function and how it is regulated in order to ensure correct patterning, it is important to characterize not only the spatial pattern of signaling activity and signal expression, but also to know the distribution as well as the transport and turnover kinetics of signaling molecules (Lander 2007, Pomreinke *et al.* 2017). The mechanisms of signal transport and the characteristics of signal dispersal are critical in the morphogen context. Although the term morphogen is used frequently for signaling molecules (Section 2.1), the precise mechanisms underlying the downstream specification of cells and tissue types often remain unclear. While there is a debate about the concentration-dependent interpretation of morphogen signaling (Chen and Schier 2001, van Boxtel *et al.* 2015, Sagner and Briscoe 2017, van Boxtel *et al.* 2018), another central controversy concerns morphogen transport: It is controversial whether diffusion can efficiently transport signaling molecules and faithfully generate concentration gradients over a long range (Crick 1970, Kerszberg and Wolpert 1998, Lander *et al.* 2002, Wolpert 2011, Wolpert 2016, Kornberg 2019), or whether other mechanisms such as relay are used (Jones *et al.* 1996, Reilly and Melton 1996). A big challenge in the field is that signaling molecules can only rarely be visualized directly (Harmansa *et al.* 2015, Pani and Goldstein 2018) and often their localization is only inferred from target gene induction (*in situ* hybridization) or reporters (Chen and Schier 2001, van Boxtel *et al.* 2015). With modern technologies, details about morphogen function including morphogen transport and signaling kinetics can be assessed (Dubrulle *et al.* 2015, Pomreinke

et al. 2017). For example, recently developed approaches have been used to hinder signal dispersal (Harmansa *et al.* 2015, Harmansa *et al.* 2017) and are an important tool to test predictions of the morphogen model. Harmansa *et al.* (2015) have shown that Dpp dispersal is crucial for patterning the developing *D. melanogaster* wing. Experiments that hinder the dispersal of secreted signals in other systems are necessary to reveal the mechanisms underlying morphogen function.

2.3 Measuring diffusive movement

Since the discovery of morphogen gradients (Driever and Nüsslein-Volhard 1988), many studies have focused on characterizing gradient establishment and morphogen transport by diffusion (Gregor *et al.* 2005, Müller *et al.* 2012, Zhou *et al.* 2012, Pomreinke *et al.* 2017, Almuedo-Castillo *et al.* 2018). Diffusion is based on Brownian motion and can be described by a random walk on the molecular level (Crick 1970, Gregor *et al.* 2005, Lander 2007, Müller *et al.* 2013). Diffusion constants describing free diffusion can be measured *in vitro* for example by nuclear magnetic resonance (Stejskal and Tanner 1965) or fluorescence correlation spectroscopy (FCS) for fluorescent species (Elson and Magde 1974, Magde *et al.* 1974, Schwille *et al.* 1997). In model systems where appropriate live imaging of fluorescent molecules such as fluorescent proteins (Rodriguez *et al.* 2017) is possible, FCS allows diffusion measurements *in vivo*, and has been used with fluorescently-labeled secreted signaling molecules (Yu *et al.* 2009, Zhou *et al.* 2012, Müller *et al.* 2013, Wang *et al.* 2016, Pomreinke *et al.* 2017). The sub-micrometer FCS measurements report local diffusion; however, diffusion-driven transport over micrometer distances in complex tissue architectures is usually much slower and characterized by effective or global diffusion constants (Müller *et al.* 2013). Fluorescence recovery after photobleaching (FRAP) is commonly used to measure effective transport in living cells and tissues (Poo and Cone 1973, Liebman and Entine 1974, Bläßle *et al.* 2018, Soh and Müller 2018). The effective mobility results from additional processes that reduce transport rates with respect to free diffusion. These include tortuous movement around cells and reversible binding events (Müller *et al.* 2013, Bläßle *et al.* 2018). The free diffusion coefficient (D_{free}) of Green fluorescent protein (GFP), for example, is ~90 µm^2/s in water/buffer (Terry *et al.* 1995, Swaminathan *et al.* 1997, Guiot *et al.* 2000, Petrášek and Schwille 2008, Bläßle *et al.* 2018) and ~89 µm^2/s in the extracellular space of zebrafish embryos (Yu *et al.* 2009, Wang *et al.* 2016). In contrast, the effective GFP diffusivity in the extracellular space of zebrafish embryos is ~40 µm^2/s, reflecting tortuosity effects (Müller *et al.* 2012, Bläßle *et al.* 2018). FRAP measurements can also yield information about binding interactions underlying effective diffusivity (Carrero *et al.* 2003, Sprague *et al.* 2004). If the binding reaction rates are fast compared to diffusion, the effective diffusion coefficient (D_{eff}) resulting from the reversible interaction with an immobilized binder is (Crank 1975, Sprague *et al.* 2004, Miura *et al.* 2009, Müller *et al.* 2013):

$$D_{eff} = \frac{D_{free}}{\frac{[Binder]}{K_d} + 1}$$

Thus, immobile structures that bind signaling molecules can act as diffusion regulators and reduce signal mobility. Since the ratio of diffusivity and decay rate directly influences the length of gradients formed by diffusion (Eldar *et al.* 2003, Gregor *et al.* 2005, Reeves *et al.* 2006, Kicheva *et al.* 2007, Lander 2007, Müller *et al.* 2013, Wang *et al.* 2016), diffusion regulators can directly impact signal range.

2.4 Nodal signaling in zebrafish embryogenesis

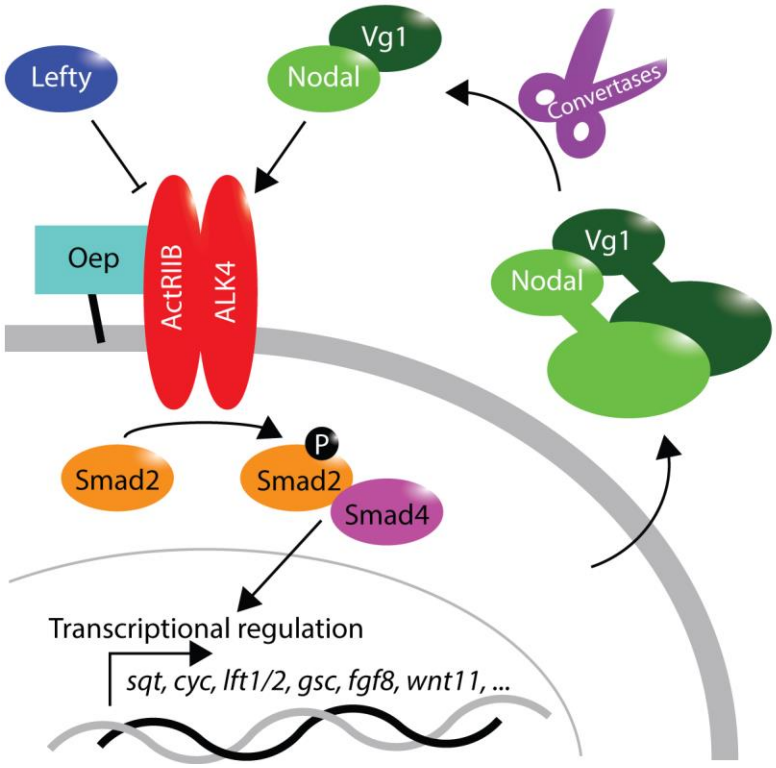

Figure 3: Illustration of the Nodal signaling pathway. Zebrafish Nodals form heterodimers with Vg1/Dvr1/Gdf3 and signal through dimeric Activin receptors (*e.g.* ActRIIB and ALK4). Nodals are secreted as pro-proteins and proteolytically processed by convertases. Oep is an essential co-receptor of Nodal signaling and is membrane-anchored via a glycosylphosphatidylinositol. Leftys are TGF-β superfamily members that antagonize Nodal signaling. Nodal signaling regulates transcription through Smad effector proteins.

Nodals are conserved secreted signaling molecules of the TGF-β superfamily and required for the formation of mesoderm and endoderm (mesendoderm) in vertebrates (Schier 2009, Hill 2018, Zinski *et al.* 2018). In zebrafish, two Nodals, Squint and Cyclops, are crucial for mesendoderm induction (Feldman *et al.* 1998, Rebagliati *et al.* 1998, Dougan *et al.* 2003). Nodal signaling in zebrafish requires the formation of heterodimers with the related TGF-β molecule Vg1/Dvr1/Gdf3 (Bisgrove *et al.* 2017, Montague and Schier 2017, Pelliccia *et al.* 2017) as well as proteolytic processing by convertases (Constam 2014, Tessadori *et al.* 2015). Nodals activate Activin receptors, conserved serine/threonine kinase receptors (Schier 2003, Shi and Massagué 2003, Weiss and Attisano 2013, Derynck and Budi 2019), which requires the EGF-CFC protein Tdgf1/Oep as additional co-receptor (Gritsman *et al.* 1999, Yan *et al.* 2002) and results in phosphorylation of the downstream effectors Smad2/3 (Dick *et al.* 2000, Brivanlou and Darnell 2002, Jia *et al.* 2008, Dubrulle *et al.* 2015). Phosphorylated Smad2/3 (pSmad2/3)

binds Smad4 to regulate target gene expression required for mesendodermal differentiation (Schier and Talbot 2005, Bennett *et al.* 2007a, Ross and Hill 2008, Derynck and Budi 2019) (Figure 3). Importantly, among the transcriptional targets of Nodal signaling are Nodals themselves as well as the secreted Nodal antagonists Lefty1 and Lefty2 that provide feedback regulation (Meno *et al.* 1999, Chen and Schier 2002, Feldman *et al.* 2002, Dougan *et al.* 2003, Bennett *et al.* 2007a, Rogers *et al.* 2017).

In the zebrafish embryo, Nodal transcripts are maternally deposited, detected at the dorsal margin around sphere stage (4 hpf; Kimmel 1995) and thereafter found in the extraembryonic yolk syncytial layer (YSL) as well as the embryonic margin (Feldman *et al.* 1998, Bennett *et al.* 2007b, Fan *et al.* 2007, van Boxtel *et al.* 2015). Nodal signaling becomes active around sphere stage and expands its signaling domain at the margin during gastrulation (Harvey and Smith 2009, Dubrulle *et al.* 2015, van Boxtel *et al.* 2015). The zebrafish Nodal Squint was proposed as a morphogen that can signal at a long range (Chen and Schier 2001). However, most indications of Nodals acting at a distance are based on overexpression studies in which the experimental readouts include the induction of Nodal targets at a distance from Nodal-overexpressing cells (Chen and Schier 2001) and the diffusive dispersal of Squint-GFP from source cells (Müller *et al.* 2012). It has recently become clear that Nodal-mediated mesoderm induction at a distance from Nodal-producing cells is at least in part due to relay by FGF signals (Rodaway *et al.* 1999, van Boxtel *et al.* 2015, van Boxtel *et al.* 2018). Therefore, it is currently unclear whether endogenous Nodal signaling can act directly – *i.e.* without relay – at a distance. According to the "mid-range morphogen" model, endogenous Nodals disperse by diffusion and activate mesendodermal target genes at a distance (Chen and Schier 2001, Müller *et al.* 2012). In contrast, the "relay" model states that endogenous Nodals signal on a cell-to-cell basis to directly induce endoderm locally but induce mesoderm only indirectly through FGF relay (Figure 4; van Boxtel *et al.* 2015, van Boxtel *et al.* 2018).

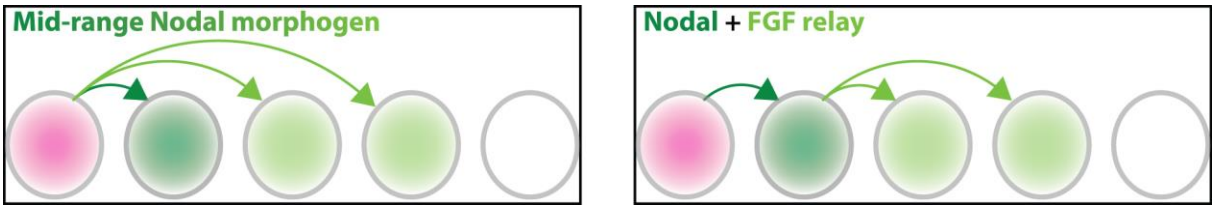

Figure 4: Models of Nodal signaling in mesendodermal patterning. In the "mid-range morphogen" model (left), Nodal induces endoderm at a short range (dark green) from the source (magenta) but can directly signal at a distance to induce mesoderm (light green). In contrast, in the "relay" model, Nodal acts exclusively at a short range to induce endoderm (dark green) and the long-range mesoderm inducer FGF (light green) (van Boxtel *et al.* 2015).

Whereas Nodal positive feedback is well established (Meno *et al.* 1999, Chen and Schier 2002, Feldman *et al.* 2002, Dougan *et al.* 2003, Bennett *et al.* 2007a, Rogers *et al.* 2017) and supports the relay model, it is generally unclear whether the relay kinetics (Nodal signaling kinetics, transcription rates, Nodal translation, secretion and processing) are fast enough to efficiently propagate signaling (Ohi and Wright 2007, Rogers and Müller 2019).

Leftys are TGF-β superfamily members and secreted, long-range Nodal antagonists (Chen and Schier 2002, Rogers *et al.* 2017, Almuedo-Castillo *et al.* 2018). Leftys have a longer range than the Nodal signals and because they are linked through feedback regulation, Nodals and Leftys have been suggested to form a self-regulated reaction-diffusion system (Chen and Schier 2002, Marjoram and Wright 2011, Müller *et al.* 2012, Müller *et al.* 2013, Sekine *et al.* 2018). In zebrafish embryos, the longer range of the Leftys (Lefty1 and Lefty2) compared to Nodals is due to an approximately five-fold higher effective diffusivity (Müller *et al.* 2012). This difference in mobilities is surprising, considering that Nodals and Leftys are both TGF-β-related molecules and comparable in molecular weight. It is therefore possible that interactions with the extracellular matrix (ECM) modulate the dispersal of Nodals and Leftys. Specifically, it has been suggested that Nodals have a lower effective diffusivity due to interactions with extracellular diffusion regulators (Müller *et al.* 2012, Müller *et al.* 2013). Based on affinities obtained from FCS measurements, binding to Nodal receptors has been suggested to reduce Nodal mobility (Wang *et al.* 2016). Interestingly, overexpression of the Nodal co-receptor Oep reduces the diffusivity of Squint-GFP (Rogers 2015). Moreover, Cyclops-GFP is known to form membrane-associated clusters and it is possible that these clusters represent sites of Cyclops-GFP interaction that are responsible for its low mobility (Müller *et al.* 2012). Previous research in zebrafish has shown that Cyclops-GFP clusters can associate with the membrane-localized glycoprotein Knypek (Rogers 2015). Glycoproteins, particularly heparan sulfate proteoglycans (HSPGs), are known to regulate the dispersal and function of several signaling molecules during development (Baeg and Perrimon 2000, Häcker *et al.* 2005). Interactions with proteoglycans are known for the *Xenopus laevis* Nodal Xnr1 (Marjoram and Wright 2011) and acidic amino acids in the N-terminus of the mature Squint protein were suggested to reduce the binding to glycoproteins and explain the longer signaling range of Squint (mid-range) compared to Cyclops (short-range; Jing *et al.* 2006). Other examples of glycoprotein function in TGF-β superfamily signaling are Dally, which promotes Dpp signaling and dispersal, in *D. melanogaster* (Fujise *et al.* 2003, Belenkaya *et al.* 2004) and Betaglycan, a co-receptor for TGF-β (Andres *et al.* 1991, López-Casillas *et al.* 1991, Wang *et al.* 1991, Bilandzic and Stenvers 2011). Additionally, TGF-β is known to associate with the ECM in a latent complex, and release of active TGF-β requires the interaction with Integrin (Annes *et al.* 2004, Shi *et al.* 2011, Derynck and Budi 2019). Little is known about the ECM composition of early zebrafish embryos, but Fibronectin and Laminin were detected only after 65% epiboly (Latimer and Jessen 2010). However, transcripts of HSPGs such as Knypek, which is important for Wnt signaling, are detected also at blastula stages (Topczewski *et al.* 2001, Gupta and Brand 2013). Thus, a complete list of potential Nodal binders in the ECM is lacking. Identifying extracellular interaction partners of Nodals and Leftys may explain their different action ranges and shed light on the molecular mechanisms underlying mesendodermal patterning.

3. Aims of this Work

The central theme I address with my doctoral research is the movement of extracellular signaling molecules during zebrafish embryogenesis. Currently, the extracellular transport mechanisms during embryogenesis and the importance of the classical morphogen model remain controversial.

In my first project, I directly compared the "mid-range morphogen" and the "relay" models of Nodal signaling in zebrafish embryos. Previous experiments proposing Squint as "mid-range morphogen" were based on overexpression (Chen and Schier 2001), which may artificially increase signaling range. In contrast, I transplanted cells that endogenously secrete Nodals into tissues that do not normally receive Nodal signaling during zebrafish gastrulation. By comparing Nodal signaling in host tissues that either have or lack positive Nodal feedback, I was able to assess Nodal signaling range and the requirement for Nodal relay (Section 4.1).

Testing the classical morphogen model, where proper signal dispersal is thought to be crucial for morphogenesis, requires tools to perturb signal mobility and range. To understand how extracellular signal mobility can be modulated *in vivo*, I used synthetic binding interactions to experimentally introduce diffusion regulators. Based on the recently developed membrane-tethered GFP binders (Harmansa *et al.* 2015), I tested how binders of different affinities modulate the effective diffusion coefficient of extracellular GFP and Lefty1-GFP. The theoretical basis (Section 2.3) predicts that effective diffusivity can be tuned using binder concentration and affinity as experimentally amenable parameters. My aim was to establish experimental diffusion regulators as a tool to test models of morphogen transport (Section 4.2).

In my third project, I addressed the model of hindered Nodal diffusion in which diffusion regulators explain the different mobilities of zebrafish Nodals and Leftys (Müller *et al.* 2013). My aim was to identify zebrafish Nodal and/or Lefty binding partners that may act as diffusion regulators during embryogenesis. I used co-immunoprecipitation (CoIP) of FLAG-tagged Nodals and Leftys followed by mass spectrometry (MS) to identify proteins that interact with these bait proteins. In subsequent experiments I aimed to test whether they function as diffusion regulators *in vivo* (Section 4.3). Diffusion regulators are thought to underlie Nodal/Lefty dispersal and are thus expected to be crucial for mesendodermal patterning. Therefore, the identification of Nodal/Lefty interactors has the potential to reveal novel regulators of the conserved Nodal/Lefty system.

The overall aim of my studies on extracellular protein movement was to understand how the mobility of secreted signaling molecules is regulated during embryogenesis. I addressed different aspects of signal mobility, from assessing the endogenous Nodal signaling range to identifying putative *in vivo* Nodal diffusion regulators. Additionally, I explored the possibility of experimental diffusion regulation with membrane-tethered binders. These synthetic diffusion regulators will be a useful tool to test the importance of morphogen diffusion in future research.

4. Results and Discussion

4.1 Testing the endogenous Nodal signaling range

A. RESULTS

The work described in this section is not published yet. The experimental procedures are described in detail in Section 6.2.

Recent publications have proposed that during zebrafish gastrulation Nodal signaling does not act over a distance but is propagated through the tissue by a relay mechanism that is based on cell-to-cell signaling and positive feedback ("relay" model; van Boxtel *et al.* 2015, van Boxtel *et al.* 2018). This contrasts previous findings that transplanted cells overexpressing Squint can induce Nodal target genes at a distance ("mid-range morphogen" model; Chen and Schier 2001). However, it cannot be excluded that overexpression results in an increased Nodal signaling range beyond the typical endogenous range. To distinguish between these two models of Nodal signaling, I transplanted marginal cells from wildtype embryos that express Nodals at endogenous levels into the animal pole of host embryos, where there is no endogenous Nodal signaling. I then detected Nodal signaling in fixed embryos using pSmad2/3 immunofluorescence staining (Figure 5). This approach allowed me to directly observe the induction of Nodal signaling in the host embryos and, in contrast to previous experiments, is not based on overexpression. Using wildtype (WT) embryos or maternal-zygotic *squint*$^{-/-}$;*cyclops*$^{-/-}$ mutants (*MZsqt*$^{-/-}$;*cyc*$^{-/-}$) as hosts, I compared Nodal signaling in embryos with or devoid of Nodal feedback, respectively (Figure 5A). In the absence of Nodal feedback, Nodal signaling induction at a distance from the transplant would support the "mid-range morphogen" model, whereas an induction of Nodal signaling restricted to cells neighboring the transplant would corroborate the "relay" model (Figure 5B).

To label transplanted nuclei, I used zebrafish embryos expressing H2A.F/Z-GFP (referred to as H2A-GFP here; Pauls *et al.* 2001) as donors and 2 h after transplantation, pSmad2/3 was detected in the transplanted cells (Figure 6). pSmad 2/3 negative nuclei in the transplant presumably derive from non-margin tissue. Consistent with both the relay and the mid-range signaling model, margin transplants from H2A-GFP embryos induced Nodal signaling in animal pole tissues of WT hosts (Figure 6A). Strikingly, transplantations of these marginal tissues into *MZsqt*$^{-/-}$;*cyc*$^{-/-}$ embryos also induced Nodal signaling outside of the transplanted cells (Figure 6B). Interestingly, the pSmad2/3 signal inside and around the transplants was stronger in *MZsqt*$^{-/-}$;*cyc*$^{-/-}$ host embryos (Supplementary Figure 1). This may be due to the lack of endogenous Lefty expression, which depends on Nodal signaling (Meno *et al.* 1999, van Boxtel *et al.* 2015, Bisgrove *et al.* 2017, Montague and Schier 2017, Pelliccia *et al.* 2017). My results show that margin-derived H2A-GFP transplants can signal to cells at a distance in *MZsqt*$^{-/-}$;*cyc*$^{-/-}$ hosts (Figure 6B) and imply that positive Nodal feedback is not required to relay Nodal signaling (Figure 5B).

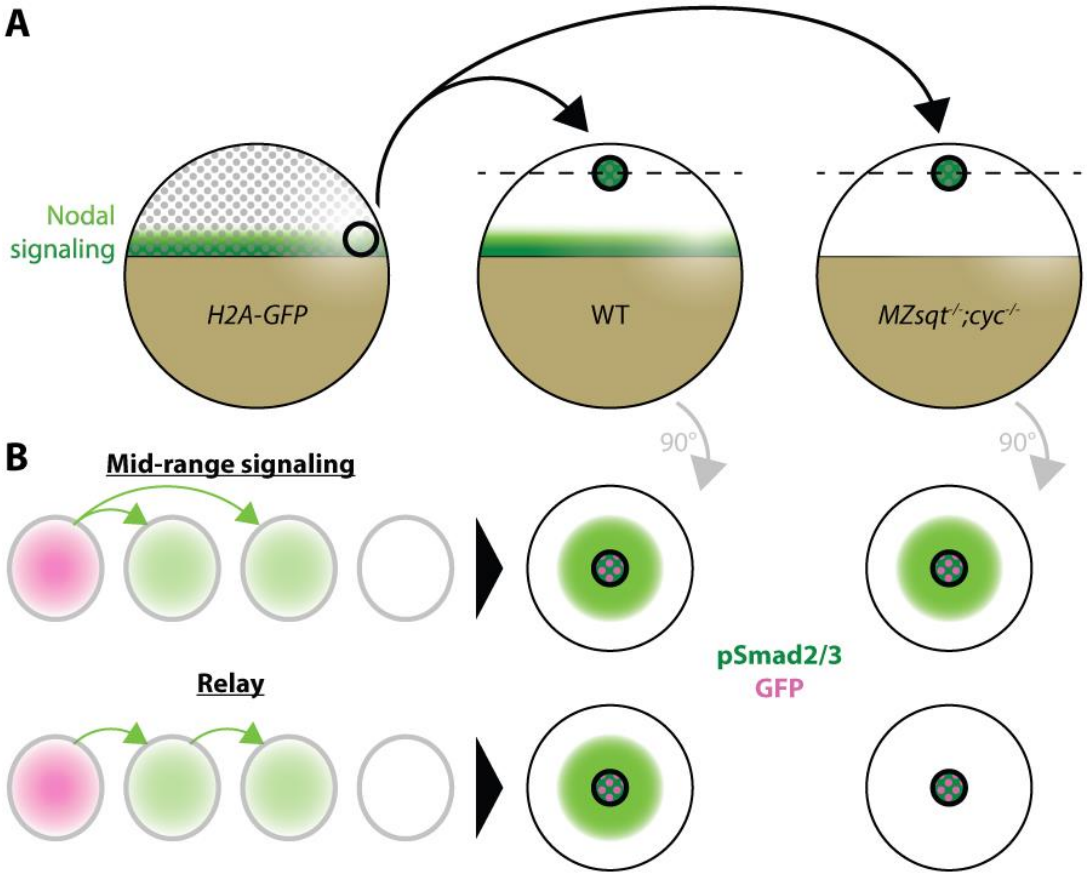

Figure 5: Margin transplantations to test the two prevailing models of Nodal signaling. A) Experimental outline of margin transplantations where embryos expressing a GFP-labeled histone variant (*H2A-GFP*; Pauls *et al*. 2001) are used to trace transplanted nuclei. **B)** The two models predict different outcomes for the margin transplantations into *MZsqt*$^{-/-}$*;cyc*$^{-/-}$. Nodal signaling at a distance from transplanted cells is not expected in the relay model because positive feedback is absent in the Nodal mutants.

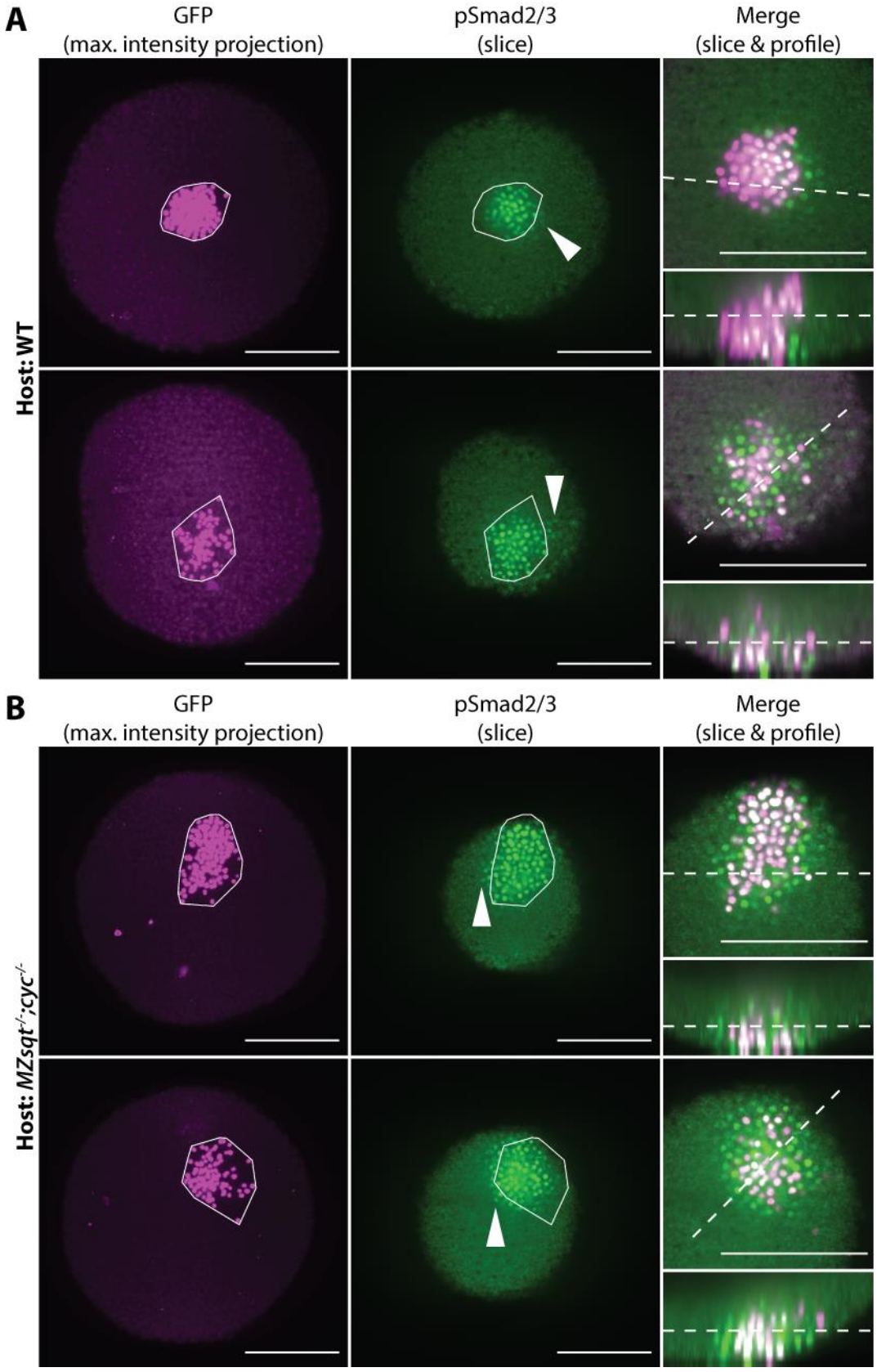

Figure 6: Margin transplantations from *H2A-GFP* embryos into the animal pole of host embryos. The embryos were fixed 2 h after transplantation. Left panels show maximum intensity projections of the GFP immunofluorescence signal. The outline of the transplant is shown as white line. The middle panels show pSmad2/3 immunofluorescence signal from a single slice (30 to 60 µm from the animal pole). White arrowheads point to pSmad2/3 positive nuclei outside of the transplant (white outline). A magnified view of the pSmad2/3

signal (green) from the middle panel merged with the GFP signal (magenta) of the same slice is shown in the right panels (top). The dashed line indicates the profile shown below. The white dashed line in the profiles (bottom right panels) indicates the slice depth. **A)** Two examples of wildtype (WT) host embryos with pSmad2/3 signal outside of the transplant. **B)** Two *MZsqt*$^{-/-}$;*cyc*$^{-/-}$ hosts with pSmad2/3 positive nuclei outside of the transplant. Scale bars: 200 µm.

B. DISCUSSION

Numerous reports in the literature support the idea that Nodals and Leftys function as a pair of a short/mid-range activator and a long-range inhibitor (Chen and Schier 2002, Marjoram and Wright 2011, Müller *et al.* 2012, Sekine *et al.* 2018). However, it has been controversial whether Nodals can signal directly at a distance (Chen and Schier 2001) or only by cell-to-cell relay in zebrafish embryos (van Boxtel *et al.* 2015, van Boxtel *et al.* 2018). In zebrafish, the endogenous Nodal signaling range has so far not been characterized in the absence of confounding feedback regulation. With respect to mesendodermal patterning, Nodal-induced FGF signaling has been shown to be required for long-range induction of mesodermal markers at the margin (Figure 4; van Boxtel *et al.* 2015).

In my proof-of-principle experiments I observed that transplanted cells expressing endogenous Nodal levels can induce Nodal signaling in distant nuclei even in tissues that lack Nodal feedback (Section 4.1, A). Although the range of Nodal signaling is limited to 2-3 nuclei from the transplant, this speaks against the relay model, where signaling is expected only in cells adjacent to transplanted cells. Since I fixed the embryos 2 h post-transplantation, the experimental time frame corresponds to the endogenous expansion of Nodal signaling at the margin over 2 h (Dubrulle *et al.* 2015, van Boxtel *et al.* 2015). Interestingly, I observed that marginal cells transplanted into *MZsqt*$^{-/-}$;*cyc*$^{-/-}$ embryos exhibited a stronger pSmad2/3 signal compared to those cells that were transplanted into wildtype tissues (Supplementary Figure 1). This possibly results from the loss of *lefty1/2* expression in the absence of Nodal signaling (Meno *et al.* 1999, van Boxtel *et al.* 2015, Bisgrove *et al.* 2017, Montague and Schier 2017, Pelliccia *et al.* 2017). While this finding seems to confirm the long range of Leftys observed with ectopic expression (Chen and Schier 2002, Almuedo-Castillo *et al.* 2018), future experiments will have to test this hypothesis by transplanting marginal cells into *lefty1*$^{-/-}$;*lefty2*$^{-/-}$ mutants (Rogers *et al.* 2017). Moreover, control experiments are needed to assess cell division and cell migration in transplanted embryos to rule out the possibility that Nodal signaling at a distance is the result of cell migration or division of pSmad2/3 positive host cells.

My experiments indicate that Nodal signaling in zebrafish can act at a distance without cell-to-cell relay at the animal pole of host embryos. Additional experiments should test whether Nodal signaling behaves similarly at the margin. This could be examined by transplanting marginal cells from H2A-GFP embryos into the margin of *MZsqt*$^{-/-}$;*cyc*$^{-/-}$ embryos. In the context of the FGF relay-based model for mesendodermal patterning (Figure 4), it will be important to address the relevance of Nodal signaling at a distance. If transgenic knock-in lines expressing GFP-tagged Nodals are available in the future, a GFP binder-based approach (Harmansa *et al.* 2015) could be used to abolish Nodal spreading and observe the effects on mesendodermal patterning and embryogenesis.

4.2 Experimental diffusion regulation using membrane-tethered nanobodies

A. RESULTS

i) Membrane-tethered nanobodies as diffusion regulators

Whether extracellular diffusion is sufficiently fast and precise to control the dispersal and the action range of signaling proteins in living tissues is a matter of debate (Kerszberg and Wolpert 1998, Lander *et al.* 2002, Gregor *et al.* 2005, Lander 2007, Wolpert 2011). In the context of the classical morphogen model, diffusion would have to establish the correct morphogen distribution for patterning to occur properly. To test such a diffusion-based model, tools that interfere with diffusion-driven transport are needed. The morphotrap, a membrane-tethered anti-GFP nanobody that traps GFP-tagged extracellular molecules on the cell surface, was developed to test the importance of extracellular Dpp-GFP mobility (Harmansa *et al.* 2015). Harmansa et al. have shown that "trapping" Dpp-GFP on the source cells in the developing fly wing results in patterning defects, implying an important role for Dpp movement in wing patterning.

In the light of diffusion regulation by reversible binding to immobile binders (Section 2.3), morphotrap-mediated "trapping" is the result of a very low effective diffusion coefficient due to high binding affinity (*in vitro* K_d approximately 0.32 nM; Saerens *et al.* 2005, Harmansa *et al.* 2015). From the equation that was introduced in Section 2.3, it is evident that lowering the binder dissociation constant and/or increasing binder concentration should reduce the effective diffusivity:

$$D_{eff} = \frac{D_{free}}{\frac{[Binder]}{K_d} + 1} \quad (1)$$

To test the importance of diffusion for the functional range of extracellular signals, a fine-tuned manipulation of effective diffusivities is needed. In the morphogen model, for example, an altered signal range is expected to change the morphogen gradient and signaling threshold-based tissue patterning. With the aim of generating a low-affinity diffusion regulator, I cloned alternative anti-GFP nanobodies of various *in vitro* affinities (Pellis *et al.* 2012, Fridy *et al.* 2014) into the morphotrap scaffold (Section 6.2).

ii) A weak membrane-tethered GFP binder can modulate the effective GFP diffusivity

In the following paragraphs, I summarize my results on the modulation of GFP diffusivity using a weak GFP binder that were published in Mörsdorf and Müller (2019). Details regarding the experiments can be found in the attached publication (Section 8).

To investigate the effects of membrane-tethering on extracellular mobility, I studied recombinant GFP, the mobility of which has previously been characterized in zebrafish embryos (Müller *et al.* 2012, Bläßle *et al.* 2018). In theory, the effective diffusivity of extracellular GFP can be modulated by changing binder affinity or binder concentration (Equation 1). My experiments focused on a weak GFP

binder that is based on the morphotrap scaffold (Harmansa *et al.* 2015, Almuedo-Castillo *et al.* 2018), but contains a low-affinity anti-GFP nanobody (*in vitro* K_d approximately 600 nM; Fridy *et al.* 2014) in contrast to the high-affinity morphotrap (nanobody *in vitro* K_d approximately 0.32 nM; Saerens *et al.* 2005, Harmansa *et al.* 2015).

I first wanted to test the effects of different binder affinities at comparable expression levels. To generate embryos with comparable expression levels of the morphotrap and the weak binder, I injected the same amount of morphotrap or weak binder mRNA. Since the morphotrap and the weak binder contain an intracellular mCherry tag (Harmansa *et al.* 2015), comparable expression levels were confirmed by mCherry fluorescence intensities (Supplementary Figure 2). Whereas morphotrap expression leads to strong membrane tethering of extracellular GFP, the weak binder only partially tethers GFP to the cell membrane (Figure 7A&B). The different affinities of the morphotrap and the weak binder are also reflected by FRAP measurements, where expression of the morphotrap results in a lower effective diffusion coefficient (5±2 µm^2/s) compared to expression of the weak binder (22±7 µm^2/s; 50 pg mRNA in Figure 8A&B), consistent with Equation 1.

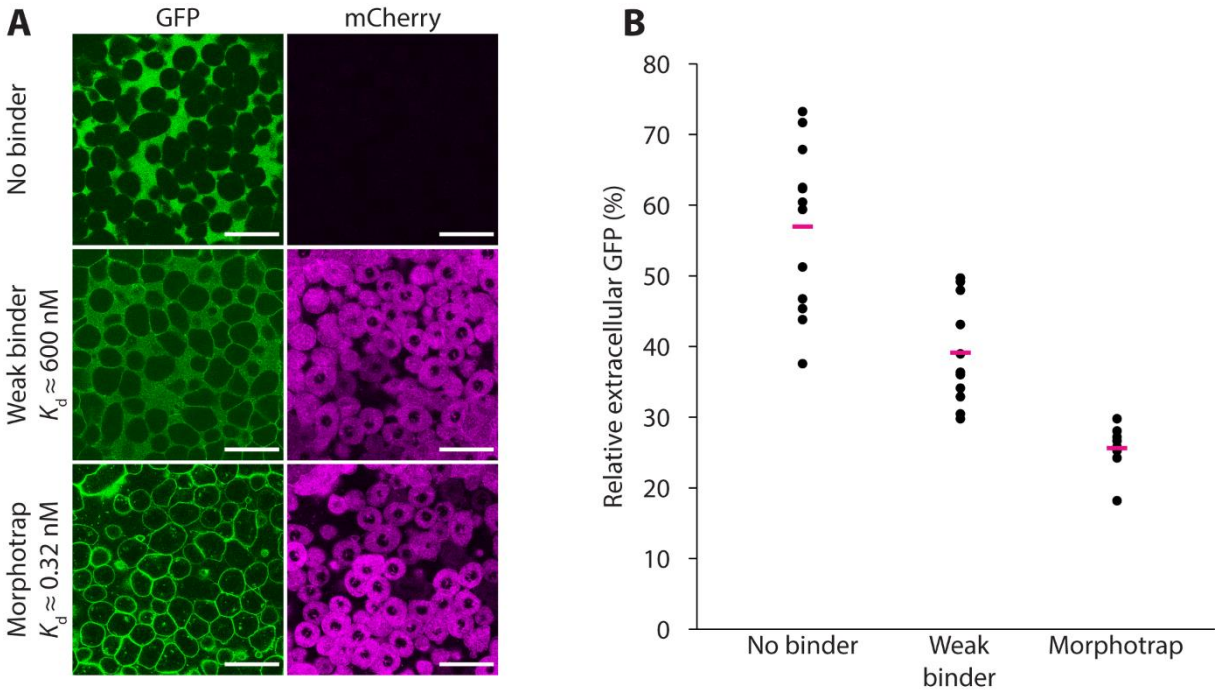

Figure 7: The weak GFP binder partially tethers GFP to the membrane. Figure was modified from Mörsdorf and Müller (2019). **A)** Zebrafish embryos expressing either no binder (top panel), the weak binder (middle panel), or the morphotrap (bottom panel) were injected extracellularly with GFP. The images on the left show GFP signal, the images on the right show the mCherry signal of the binders. The weak binder only partially tethers GFP to cell membranes, whereas the morphotrap results in strong membrane tethering. Scale bars: 50 µm. **B)** Quantification of extracellular GFP signal shows that the morphotrap strongly reduces free extracellular GFP levels. Magenta bars indicate mean values.

In a second approach, I sought to alter GFP mobility by changing the GFP binder expression level. I showed that titration of the weak binder allows the fine-tuning of the effective diffusivity of GFP, consistent with Equation 1 (Figure 8A). A mild reduction of effective GFP diffusivity is also possible with the morphotrap if low expression levels (25 pg mRNA) are used (Figure 8B; Equation 1). However,

modulating GFP mobility and detecting the mCherry signal to visualize the morphotrap may be difficult at lower expression levels.

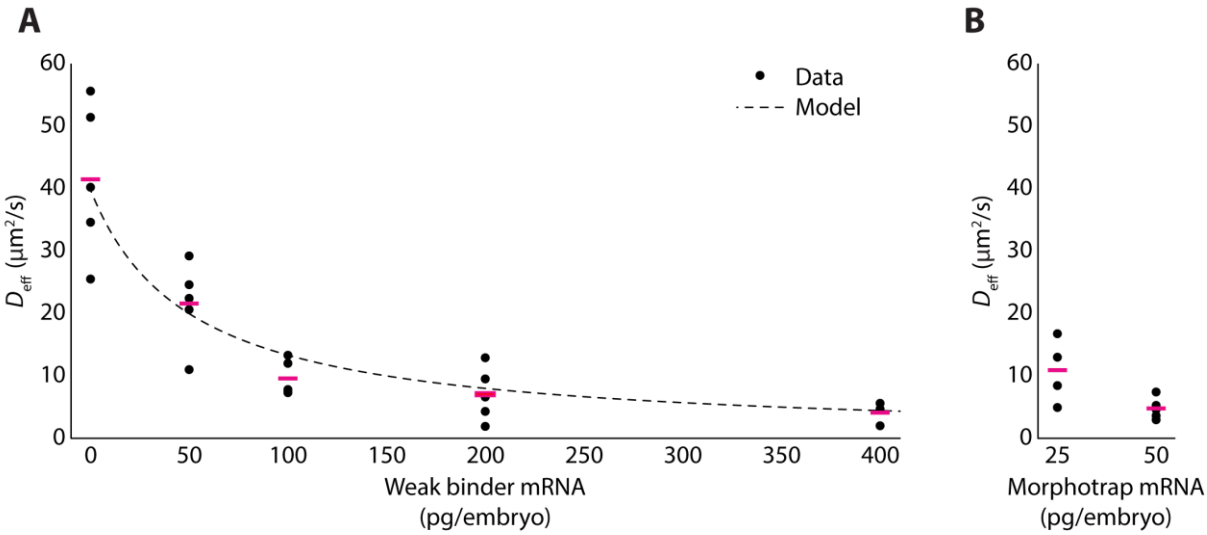

Figure 8: The weak GFP binder can act as diffusion regulator. Figure was modified from Mörsdorf and Müller (2019). **A)** Titration of the weak binder by mRNA microinjections leads to a stepwise reduction in D_{eff} measured by FRAP from 42±12 µm²/s (0 pg) to 22±7 (50 pg), 10±3 (100 pg), 7±4 (200 pg) and 4±2 µm²/s (400 pg). This trend is consistent with the model (Equation 1). Note that the in *vivo* K_d and binder concentrations are assumed here. **B)** Even at low expression levels, the morphotrap results in low effective GFP diffusivities (D_{eff} of 11±5 µm²/s for 25 pg and 5±2 µm²/s for 50 pg of mRNA). Magenta bars indicate mean effective diffusion constants.

iii) Lefty1-GFP diffusion regulation

Here I summarize my results on Lefty1-GFP membrane-tethering with the morphotrap and the weak GFP binders. Parts of this work were published in Almuedo-Castillo *et al.* (2018). Additional data from experiments with weak GFP binders is provided in Supplementary Figures 3-5. Details regarding the experiments can be found in the attached publication (Almuedo-Castillo *et al.* 2018; Section 8) and in Section 6.2.

Testing the importance of high mobility and long-range action for secreted molecule function *in vivo* requires the modulation of signal mobility and dispersal. The Nodal/Lefty system has been studied as a paramount example of a short-range activator and a long-range inhibitor pair (Meinhardt 2009, Schier 2009, Kondo and Miura 2010). In zebrafish, Leftys have higher *in vivo* diffusivities than Nodals (Müller *et al.* 2012), and Lefty-overexpressing transplants have been shown to repress Nodal target genes at a distance (Chen and Schier 2002). Additionally, such transplants can rescue *lefty1*$^{-/-}$;*lefty2*$^{-/-}$ mutants, where normally Nodal target gene expression is increased (Rogers *et al.* 2017). However, the importance of high mobility and long action range for Lefty's endogenous function in embryonic patterning had not been tested at the start of my project. Addressing whether long-range inhibition by Leftys is required for proper patterning requires the modulation of Lefty mobility *in vivo*.

In a collaboration with my colleague Dr. María Almuedo-Castillo I have explored diffusion regulation of Lefty1-GFP using the morphotrap (Harmansa *et al.* 2015) and the weak GFP binder (Section 4.2, A.ii) in zebrafish embryos. In initial experiments, I ubiquitously overexpressed Lefty1-

GFP and could show that its diffusivity can be hindered when the morphotrap is co-expressed. The reduction in the effective diffusion coefficient of Lefty1-GFP from 7.7±3.2 µm^2/s (Lefty1-GFP only) to 0.2±0.2 µm^2/s (Lefty1-GFP with morphotrap) is clearly evident from the recorded fluorescence recovery curves (Figure 9).

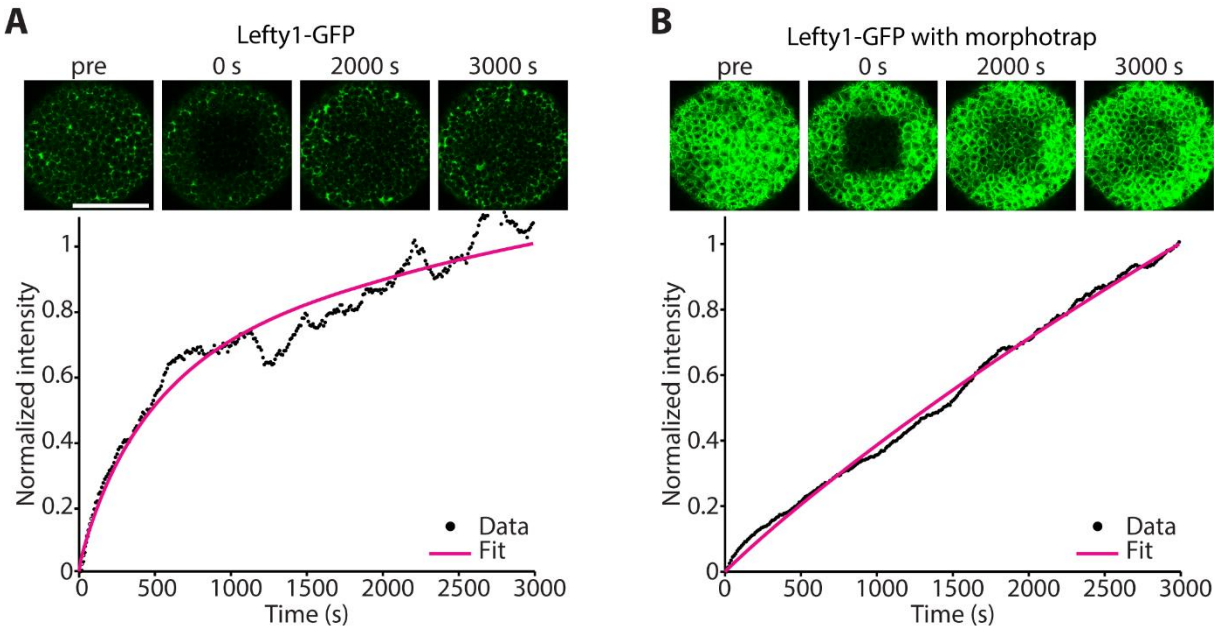

Figure 9: The morphotrap reduces Lefty1-GFP mobility. Figure adapted from Almuedo-Castillo *et al.* (2018). **A)** Representative FRAP experiment of an embryo expressing only Lefty1-GFP. **B)** Representative FRAP experiment of an embryo co-expressing Lefty1-GFP and the morphotrap. Note that the morphotrap increases GFP fluorescence (Kirchhofer *et al.* 2010). Scale bar: 200 µm.

Co-expressing the weak binder with Lefty1-GFP led to a weaker reduction in Lefty1-GFP mobility as expected, compared to the morphotrap (Supplementary Figure 3). However, when Lefty1-GFP was ubiquitously expressed, co-expression of the weak binder strongly reduced the potency of Lefty1-GFP to suppress mesendoderm formation. This is in contrast to morphotrap co-expression, which only has a mild effect on Lefty1-GFP activity (Supplementary Figure 4). Therefore, the weak GFP binder could not be used to test the effect that reduced diffusivity and range have on Lefty1-GFP function during patterning. I tested seven alternative anti-GFP nanobodies (Pellis *et al.* 2012, Fridy *et al.* 2014) in the morphotrap scaffold (Section 6.2) and found that they have variable effects on Lefty1-GFP activity (Supplementary Figure 5). Among those, the binder containing the GBP-5 nanobody (Pellis *et al.* 2012) appeared to be comparable to the morphotrap with respect to Lefty1-GFP activity. However, the effect this binder has on Lefty1-GFP diffusivity still has to be tested. These findings highlight that it is crucial to control for the biological activity of a GFP-tagged protein when anti-GFP nanobodies are used as *in vivo* diffusion regulators.

In Almuedo-Castillo *et al.* (2018), we investigated the robust tissue scaling that is observed during zebrafish development: Experimentally shortened embryos adjust ("scale") their early tissue patterning, including mesendodermal patterning, to their smaller body size and later develop into embryos with normal tissue proportions. My colleagues proposed a model in which the highly mobile Leftys adjust

Nodal signaling to the smaller embryo size by accumulating to higher levels (Figure 10). This model requires high Lefty diffusivity because Lefty has to reach the boundary of the patterning field. To test this requirement experimentally, we used an artificial, localized Lefty1-GFP source that mimics endogenous Lefty1 production. This system can not only rescue *lefty1*$^{-/-}$*;lefty2*$^{-/-}$ mutants, but also allows for the visualization and manipulation of Lefty1-GFP distribution. As expected, expression of the morphotrap in *lefty1*$^{-/-}$*;lefty2*$^{-/-}$ mutants hinders Lefty1-GFP dispersal from the localized source. Importantly, our experiments revealed that local Lefty1-GFP expression can efficiently rescue mesendoderm formation in experimentally shortened *lefty1*$^{-/-}$*;lefty2*$^{-/-}$ mutants when Lefty1-GFP mobility is high, but not when it is reduced by the morphotrap. This manipulation of Lefty mobility highlights the importance of Lefty long-range action to repress Nodal signaling and supports the proposed model (Figure 10).

In summary, together with Dr. María Almuedo-Castillo, I could show that membrane-tethered nanobodies can be used as diffusion regulators to modulate the range of secreted proteins in live zebrafish embryos, revealing a key role for high Lefty diffusivity in mediating scaling.

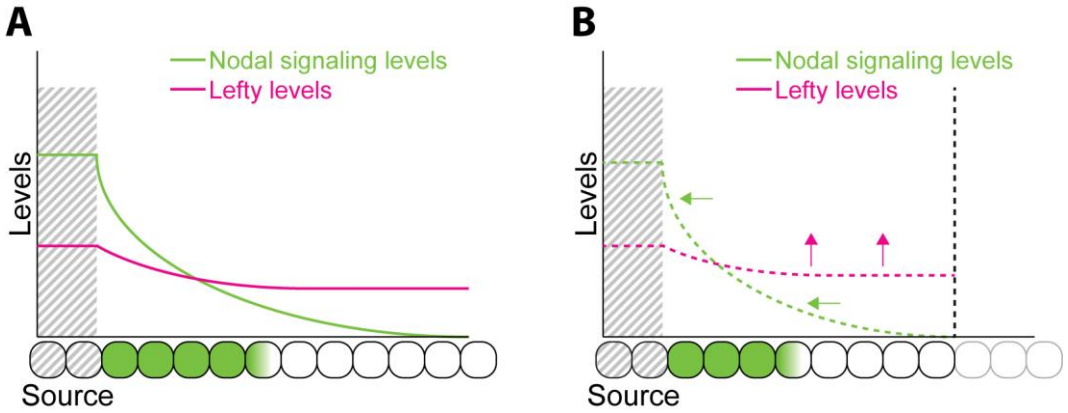

Figure 10: Highly diffusive Lefty is required to "sense" embryo size in the proposed model of mesendodermal scaling. A) Nodal and Lefty disperse from the source (gray stripes, left). Short-range Nodal forms a steep gradient and induces mesendoderm (green) close to the source. Lefty has a long range, forms a shallow gradient and represses mesendoderm induction by Nodal at a distance. **B)** The vertical dashed line illustrates the tissue boundary in experimentally shortened embryos. Here, the highly diffusive Lefty acts as a size sensor: It accumulates to higher levels, thus shortens the domain of active Nodal signaling and scales the mesendoderm to the embryo size. For details see Almuedo-Castillo *et al.* (2018).

B. Discussion

To study the roles of extracellular protein mobility in zebrafish embryos, I used recently developed membrane-tethered nanobodies (Harmansa *et al.* 2015) to generate low-affinity diffusion regulators. In agreement with the theory of reversible immobilization by binding (Section 2.3; Crank 1975), I found that strong binders, such as the morphotrap (Harmansa *et al.* 2015), drastically reduce the effective diffusivity of their diffusible binding partners. As predicted, lower expression levels of strong GFP binders lead to milder effects on GFP mobility. To achieve a fine-tuned diffusion regulation in zebrafish embryos, the weak GFP binder is, however, the better tool, because intermediate expression levels allow mild reduction in diffusivity while ensuring the robust detection of mCherry binder fluorescence as an

expression control. My proof-of-concept titration of the weak GFP binder shows the modulated diffusion regulation of extracellular GFP, the trend of which is in agreement with the mathematical model (Figure 8B; Section 4.2, A.i; Crank 1975). Fitting the mathematical model to the measured effective diffusivities is currently not possible, because the absolute concentrations of the weak binder in the experiments are not known. Future studies could infer the concentrations of GFP binders based on their mCherry fluorescence. Effective diffusion coefficients obtained by FRAP under the same conditions could then be fit to the model in order to obtain the *in vivo* affinities of the GFP binders. In future experiments the expression levels of GFP binders may have to be adjusted to the abundance of the GFP-tagged protein of interest in order to avoid binder saturation and allow optimal diffusion regulation.

In collaboration with Dr. María Almuedo-Castillo I used the morphotrap (Harmansa *et al.* 2015) to hinder the diffusion of Lefty1-GFP and address the importance of high Lefty diffusivity for its endogenous function. By ectopically expressing *lefty1-GFP* from the YSL, we closely mimicked endogenous *lefty1* expression (van Boxtel *et al.* 2015). In order to regulate the diffusion of endogenous Leftys using membrane-tethered nanobodies in the future, two approaches are plausible. Transgenic *lefty1-GFP* or *lefty2-GFP* knock-in lines expressing biologically active Lefty fusion proteins (Müller *et al.* 2012) would be compatible with the morphotrap or weak GFP binders as diffusion regulators. Alternatively, it may be possible to make nanobodies against zebrafish Leftys (Pellis *et al.* 2012, Fridy *et al.* 2014) and generate a membrane-tethered Lefty binder similar to the morphotrap (Harmansa *et al.* 2015). Regulating the diffusion of endogenous zebrafish Nodals and Leftys in future experiments will allow the requirement for their mobility *in vivo* to be directly tested, similar to the morphotrap experiments with Dpp-GFP in the *D. melanogaster* wing disc (Harmansa *et al.* 2015, Harmansa *et al.* 2017) or Wnt/EGL-20-YPET in *Caenorhabditis elegans* (Pani and Goldstein 2018). In the context of the threshold-based interpretation of morphogen gradients, reduced signal diffusivity can lead to counterintuitive changes in gene expression patterns (Lander 2007). It will therefore be crucial to observe the effects that, for example, reduced Nodal diffusivity has on mesendodermal gene expression patterns in zebrafish embryos.

4.3 A CoIP/MS approach to identify endogenous Nodal/Lefty diffusion regulators

A. RESULTS

The results in this section are not published yet. Detailed experimental procedures can be found in Section 6.2.

i) Identification of potential Nodal/Lefty binding partners by MS

Hindered Nodal diffusion was proposed to explain the short range and low effective diffusivities of Nodals compared to Leftys in zebrafish (Müller *et al.* 2013). Although Oep overexpression was shown to reduce Squint-GFP diffusivity, *oep* mRNA knockdown did not affect Nodal diffusivity (Rogers 2015). Thus, to date no interactions are known that act as endogenous Nodal or Lefty diffusion regulators.

To identify Nodal and Lefty interaction partners that could act as diffusion regulators during early zebrafish development I adopted a co-immunoprecipitation (CoIP) protocol. FLAG-tagged zebrafish Nodals (Squint-FLAG, Cyclops-FLAG) or Leftys (Lefty1-FLAG, Lefty2-FLAG; Müller *et al.* 2012) were expressed in zebrafish embryos and lysates were prepared around sphere stage (~4 hours post fertilization (hpf); Kimmel *et al.* 1995). Lysates from uninjected embryos and embryos expressing a secreted GFP (secGFP; Section 6.2) served as controls. In my initial experiments I found that this CoIP protocol can be used to specifically precipitate the EGF-CFC protein and Nodal co-receptor encoded by *tdgf1*/*oep* (Gritsman *et al.* 1999, Cheng *et al.* 2004) with Squint (Figure 11). The interaction of Nodals and EGF-CFC proteins is well established and serves as a positive control (Reissmann *et al.* 2001, Yan *et al.* 2002, Chen and Shen 2004, Cheng *et al.* 2004). I also tested formaldehyde crosslinking to stabilize potentially transient interactions. However, this did not lead to an obvious increase in the amount of Oep-GFP that co-immunoprecipitated with Squint-FLAG (Figure 11).

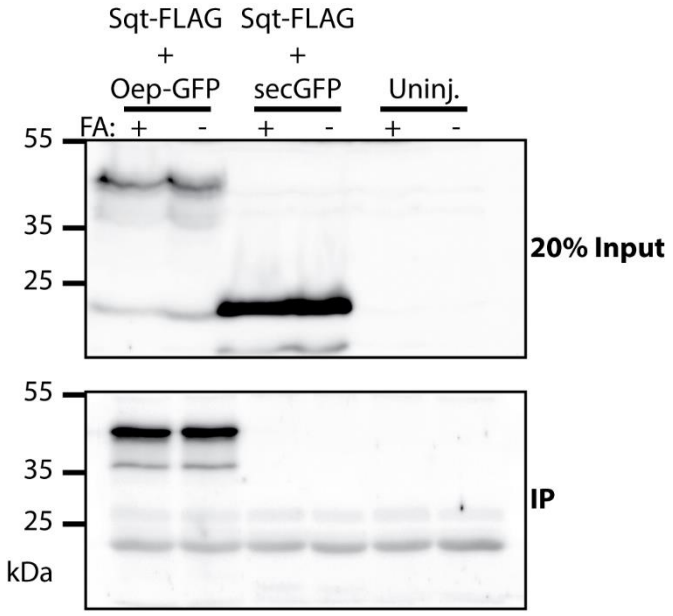

Figure 11: Anti-GFP western blot shows interaction between Oep-GFP and Squint-FLAG in an anti-FLAG CoIP. Western blots show 20% input controls (top panel) and CoIP fractions (bottom panel). Experiments with (+) and without (-) formaldehyde (FA) crosslinking are shown. "Uninj." is a control CoIP from uninjected embryos.

To increase the probability that low-affinity interactions are identified in the CoIP/MS experiments, the expression of FLAG-tagged proteins was strongly increased compared to previous studies (Müller *et al.* 2012). Supplementary Figure 6 shows that injection of increased levels of mRNA up to ~1 ng leads to increased Cyclops-FLAG expression. Importantly, it appears that the secretory machinery is not saturated under these conditions, as the signal of the corresponding GFP fusion proteins is mostly extracellular when they are expressed at similarly high levels (Supplementary Figure 7).

For the MS analysis of Nodal and Lefty binding partners I performed CoIPs from 82 embryos per sample. A western blot of the input fractions confirmed the presence of the bait proteins (Supplementary Figure 8). Silver stained protein gels (Supplementary Figure 9) were then submitted to the Proteome Center at the University of Tübingen for MS (Section 6.2). 72 proteins were identified in the Nodal/Lefty

samples that were not identified under control conditions (excluding bait proteins; Section 6.2 and Supplementary Table 1). To find proteins in this list that could potentially act as diffusion regulators for the extracellular Nodals and Leftys, I filtered the results based on the GO annotation for "Cellular Component" (Ashburner *et al.* 2000, The Gene Ontology Consortium 2019) or the presence of a signal peptide (Section 6.2). The resulting list of MS candidates is shown in Table 1.

Table 1: List of MS candidates that are absent from negative controls. X indicates the sample(s) in which peptides of the protein were identified: Squint-FLAG (Sqt), Cyclops-FLAG (Cyc), Lefty1-FLAG (Lft1) or Lefty2-FLAG (Lft2).

	Sample				
Gene name	**Sqt**	**Cyc**	**Lft1**	**Lft2**	**Comment**
cx43.4	X			X	Gap junction [1]
dvr1	X				Vg1/Gdf3 [2]
epcam		X		X	Cell adhesion [3]
hsp90b1	X		X	X	ER chaperone [4]
jupb	X				Junction plakoglobin b, γ-catenin [5]
si:ch211-226h8.14	X	X			Extracellular lectin [6]
si:dkey-7j14.6	X				MS4A homolog [7]
tpte	X				Transmembrane phosphatase [8]
vldlr	X			X	VLDL receptor [9]

[1] Essner *et al.* (1996), de Boer and van der Heyden (2005), Hatler *et al.* (2009); [2] Bisgrove *et al.* (2017), Montague and Schier (2017), Pelliccia *et al.* (2017); [3] Slanchev *et al.* (2009), Lu *et al.* (2013), Kuechlin *et al.* (2017); [4] Yang *et al.* (2007), Liu *et al.* (2013); [5] Miller and Moon (1997), Zhurinsky *et al.* (2000b); [6] Tateno (2010); [7] Eon Kuek *et al.* (2016); [8] Walker *et al.* (2001), Tapparel *et al.* (2003), Santos *et al.* (2007); [9] Imai *et al.* (2012), Di Donato *et al.* (2018)

The Dvr1/Vg1/Gdf3 protein, which is known to form (disulfide-linked) dimers with Nodals (Figure 3; Bisgrove et al. 2017, Montague and Schier 2017, Pelliccia et al. 2017), was identified in the Squint-FLAG sample (Table 1) and serves as a positive control.

In the following experiments I sought to test the function of the MS candidates with respect to Nodal signaling in zebrafish embryos. Because any kind of interaction may be identified with CoIP/MS, the candidate proteins are not necessarily diffusion regulators, but could have other functions, for example in Nodal secretion or signal transduction. A hypothetical diffusion regulator is expected to behave similarly to the membrane-tethered GFP binders from Section 4.2. However, I consider not only membrane-associated, but also secreted proteins as possible diffusion regulators in my approach.

ii) Validation of MS candidates by co-localization with tagged Nodals and Leftys

To visualize the MS candidates in the zebrafish embryo, I generated C-terminal GFP fusions of the proteins described in Table 1 (excluding Vg1, which is known to form heterodimers with Nodals and is required for Nodal signaling; Figure 3; Montague and Schier 2017). If the candidates bind Nodals/Leftys or localize to the same microscopic structures, co-localization with the Nodal/Lefty bait protein should be observed. The known localization of fluorescently-labeled zebrafish Nodals and Leftys (Müller *et al.* 2012, Rogers 2015) is illustrated in Figure 12.

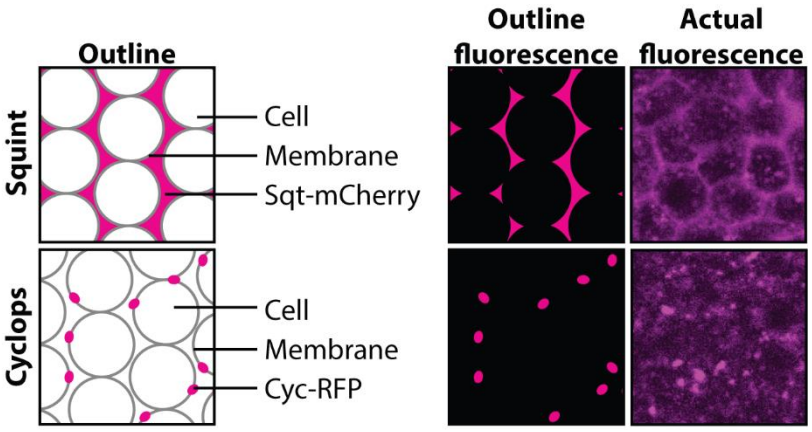

Figure 12: Illustration of the known distribution of fluorescently labeled zebrafish Nodals. Left panel: Whereas Squint fusion proteins are diffuse in the extracellular space, Cyclops forms membrane-associated clusters. Note that fluorescent Leftys are diffuse in the extracellular space, similar to Squint (Müller *et al.* 2012, Rogers 2015). Right panel: The Squint-mCherry and Cyclops-RFP fusion proteins also form cytoplasmic clusters.

I injected mRNAs encoding the fluorescent candidate fusions into zebrafish embryos at the one-cell stage in order to achieve uniform expression. I examined their subcellular localization and co-expressed fluorescent Nodals/Leftys to test whether this changes the localization of the MS candidate or the Nodal/Lefty. Confocal microscopy of embryos expressing GFP-tagged MS candidates revealed characteristic subcellular localizations (Table 2), some of which overlap with red-fluorescent Nodals (Figures 13-15). The results are summarized in Figures 13-15, where the MS candidates are separated by localization: Figure 13 shows intracellular candidates (Hsp90b1-GFP, Si:dkey7j14.6-GFP and Vldlr-GFP), Figure 14 summarizes the membrane-localized candidates (Epcam-GFP, Jupb-GFP and Tpte-GFP) and Figure 15 presents Cx43.4-GFP, which is expressed in a punctate pattern, as well as the extracellular candidate Si:ch211-226h8.14-GFP.

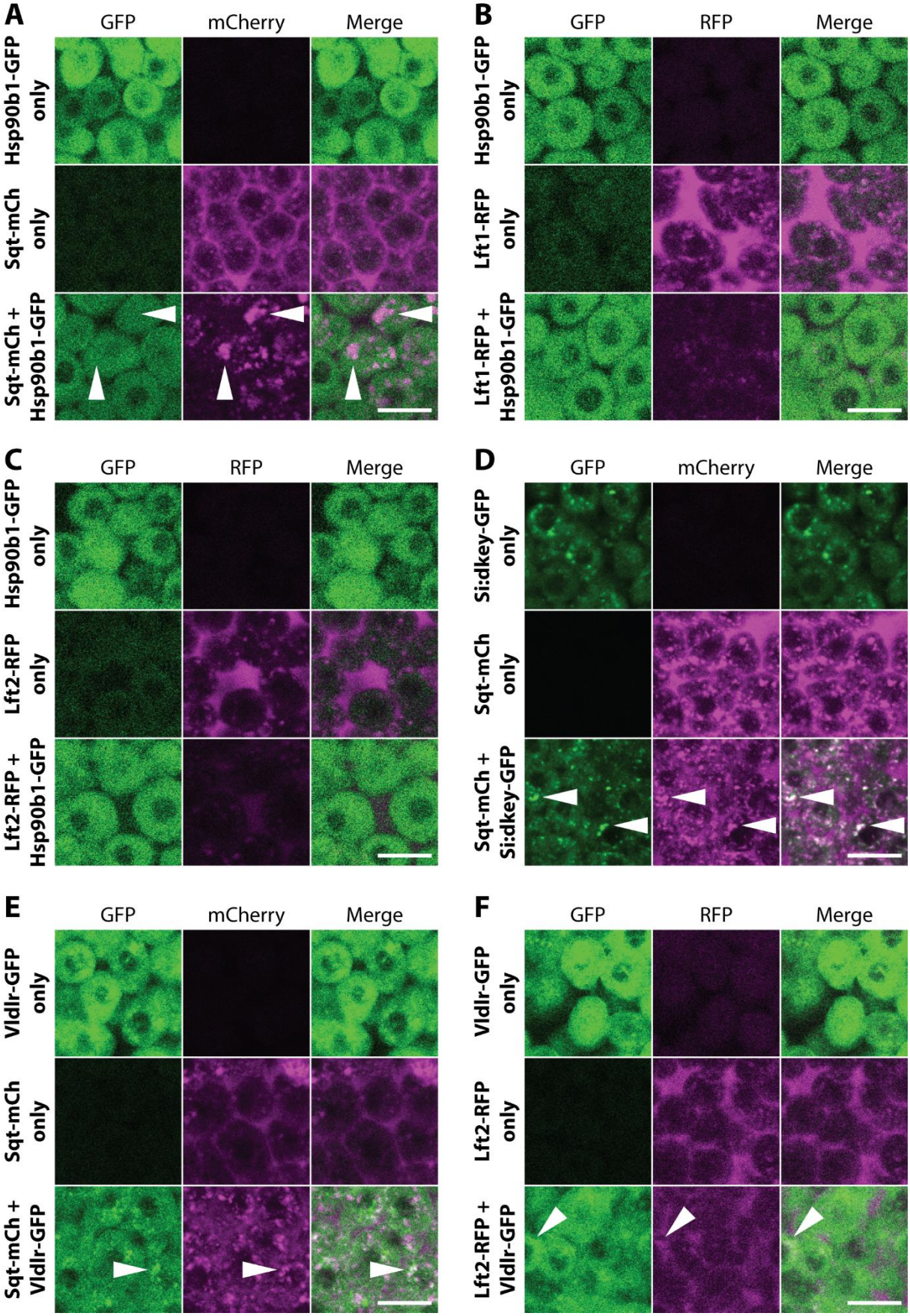

Figure 13: Intracellular MS candidates. A) Hsp90b1-GFP is mainly cytoplasmic and does not co-localize with Squint-mCherry. Co-expression of Hsp90b1-GFP increases cytoplasmic clusters with mCherry signal (arrowheads). **B-C)** Hsp90b1-GFP does not co-localize with RFP-tagged Leftys. Co-expression of Hsp90b1-GFP

and Lefty1-RFP **(B)** or Lefty2-RFP **(C)** appears to reduce overall Lefty-RFP levels. **D)** The Si:dkey7j14.6-GFP (Si:dkey-GFP) signal is intracellular and forms clusters that co-localize with cytoplasmic Sqt-mCherry signal (arrowheads). **E)** Vldlr-GFP localizes to the cytoplasm and partially overlaps with Sqt-mCherry in cytoplasmic clusters (arrowhead). **F)** Vldlr-GFP partially overlaps with Lft2-RFP only in a few cytoplasmic clusters (arrowhead). Scale bars: 25 µm.

Although the candidates Si:dkey7j14.6-GFP (Figure 13D), Vldlr-GFP (Figure 13E&F), Epcam-GFP (Figure 14A) and Si:ch211-226h8.14-GFP (Figure 15C&D) partially co-localize with the Squint-mCherry/Cyclops-RFP signal they do not markedly alter the extracellular localization of the Nodal signal. In contrast, co-expression of the chaperone Hsp90b1-GFP with tagged Squint, Lefty1 or Lefty2 appears to reduce their extracellular levels (Figure 13A-C). It is possible that Hsp90b1 overexpression interferes with Nodal/Lefty secretion. The signals of the candidate fusion proteins Jupb-GFP (Figure 14C), Tpte-GFP (Figure 14D) and Cx43.4-GFP (Figure 15A&B) do not obviously overlap with the fluorescent signals of their corresponding bait. The Connexin Cx43.4-GFP localizes to punctate structures, some of which are associated with the membrane (Figure 15A&B). The Squint-mCherry fusion protein also forms cytoplasmic clusters, which in rare cases overlap with the Cx43.4-GFP structures (Figure 15A). In order to test whether Cx43.4 has an effect on Squint localization, untagged Cx43.4 was co-expressed with Squint-GFP, which is mainly extracellular and forms few cytoplasmic clusters (Supplementary Figure 10). Although the overall GFP signal was reduced, the localization of Squint-GFP was unaltered compared to embryos expressing only Squint-GFP. Table 2 summarizes the MS candidate localization results.

Table 2: GFP fusion proteins of MS candidates mark different subcellular compartments. PM = plasma membrane.

Gene name	Localization	Co-localization
cx43.4	PM, cytoplasm	Partial
epcam	PM	Partial
hsp90b1	Cytoplasm	Partial
jupb	PM, cytoplasm, nucleus	No
si:ch211-226h8.14	Extracellular, PM	Partial
si:dkey-7j14.6	Cytoplasm	Yes
tpte	PM	No
vldlr	Cytoplasm	Partial

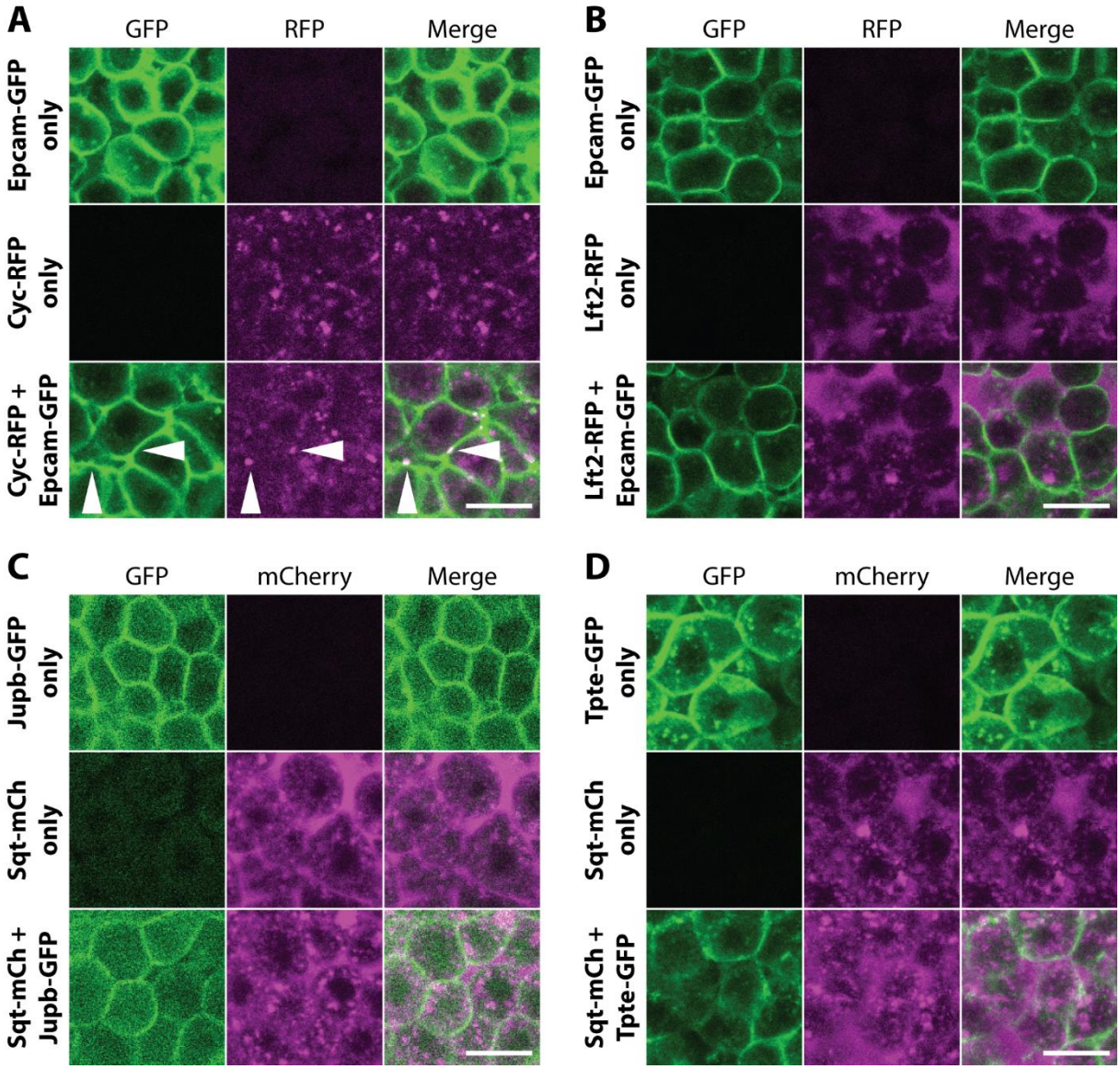

Figure 14: Membrane-localized MS candidates. A) Epcam-GFP localizes to the plasma membrane. Although the GFP signal overlaps with the membrane-associated Cyclops-RFP clusters (arrowheads), Epcam-GFP overexpression does not markedly change the appearance of the Cyclops-RFP signal. **B)** Epcam-GFP does not co-localize with Lefty2-RFP. **C)** Jupb-GFP localizes to the plasma membrane and appears to be present in the cytoplasm and nucleus. It does not co-localize with Squint-mCherry. **D)** Tpte-GFP localizes mainly to the cell membrane and does not co-localize with Squint-mCherry. Scale bars: 25 µm.

Among the MS candidates, the secreted lectin Si:ch211-226h8.14-GFP is the only with a mostly extracellular signal. Interestingly, it also forms membrane-associated clusters that co-localize with Cyclops-RFP clusters (Figure 15C). These clusters are present also in the absence of Cyclops-RFP overexpression, however, clusters are observed with variable frequency and cluster formation depends on high expression levels (Supplementary Figure 11).

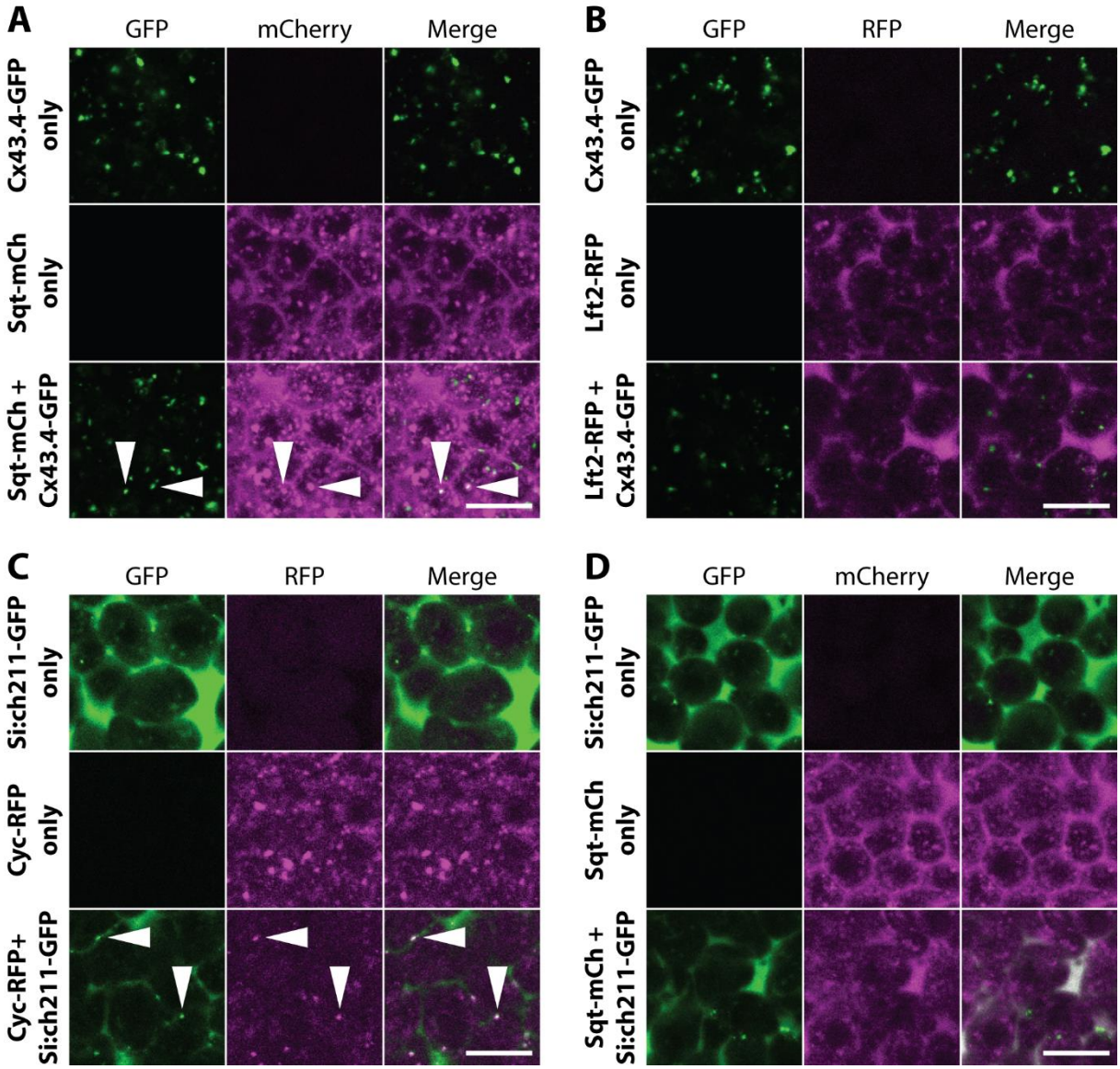

Figure 15: GFP fusion proteins of Cx43.4 and the secreted lectin encoded by *si:ch211-226h8.14* localize to punctate clusters and the extracellular space, respectively. A) The Squint-mCherry signal overlaps the Cx43.4-GFP signal only in a few cytoplasmic or membrane-associated clusters (arrowheads). **B)** Lefty2-GFP and Cx43.4-GFP do not co-localize. **C)** Si:ch211-226h8.14-GFP (Si:ch211-GFP) is mainly extracellular, but also co-localizes with Cyclops-RFP in membrane-associated clusters (arrowheads). The Si:ch211-GFP signal overlaps with the Sqt-mCherry signal in the extracellular space. Scale bars: 25 µm.

iii) Phenotypes resulting from MS candidate overexpression

The signals of several MS candidate GFP fusions overlap with those of fluorescently labeled Nodals or Leftys (Section 4.3, A.ii). However, such co-localization does not necessarily imply interaction (Dunn *et al.* 2011) and may be an artifact resulting from fluorescent tagging. To help identify any specific functions of the MS candidates in Nodal signaling, I overexpressed the untagged MS candidates in zebrafish embryos and evaluated the resulting phenotypes 1 day post fertilization (dpf). If the candidates have important functions in Nodal signaling, increasing their levels may cause Nodal-related phenotypes, such as defective mesendoderm formation (Toyama *et al.* 1995, Feldman *et al.* 1998, Rogers *et al.* 2017).

Upon microinjection of 250 pg mRNA, most MS candidates caused diverse, but mild phenotypes that were not clearly linked to Nodal signaling (Supplementary Figure 12). Only the overexpression of *si:ch211-226h8.14* or *jupb* led to distinct phenotypes (Figures 16&17). The phenotypes resulting from *si:ch211-226h8.14* overexpression were mostly tail defects, such as a shortened tail, and blood-related defects (blood accumulation). These phenotypes are not typical for defects in Nodal signaling, and only apparent with high amounts of *si:ch211-226h8.14* mRNA (Figure 16). In contrast, microinjection of 250 pg *jupb* mRNA results in early developmental defects without formation of a body axis (Figure 17A&B). The tissue "clumps" that were observed instead of well-formed embryos at 1 dpf are typical of excess Nodal activity (Rogers *et al.* 2017). At lower expression levels (microinjection of 50 pg *jupb* mRNA) the phenotypes were similar to mutations in repressors of Wnt/β-catenin signaling (Figure 17A&C) such as *headless* (Kim *et al.* 2000) or *masterblind* (Heisenberg *et al.* 2001), indicating increased Wnt/β-catenin signaling. Jupb/γ-catenin is homologous to β-catenin, supporting the idea that Jupb overexpression increases Wnt/β-catenin activity (Karnovsky and Klymkowsky 1995, Miller and Moon 1997, Zhurinsky *et al.* 2000b). Since Nodal genes are Wnt target genes (Shimizu *et al.* 2000, Agathon *et al.* 2003, Zinski *et al.* 2018), strong Jupb overexpression may also induce Nodal expression and explain the phenotypes observed with 250 pg *jupb* mRNA.

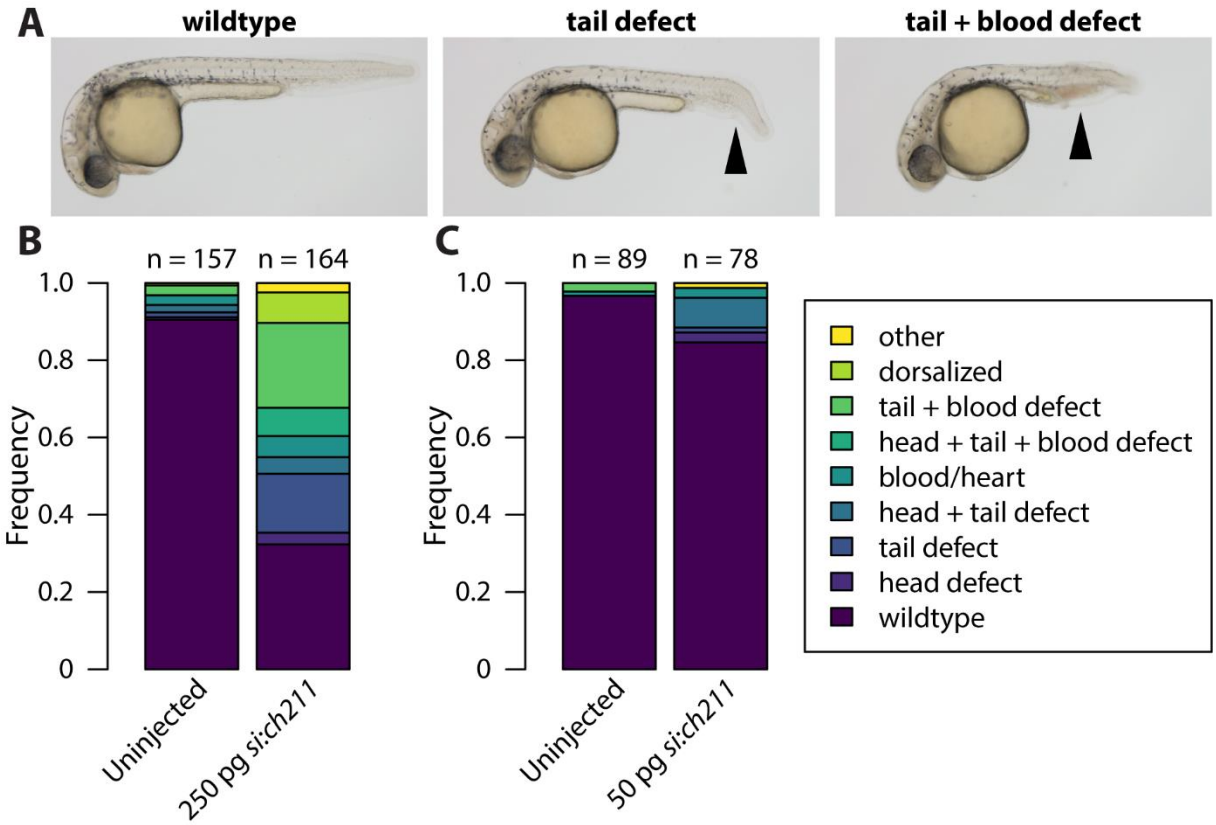

Figure 16: Expressing high amounts of secreted lectin mRNA results in tail and blood-related defects 1 dpf. A) Representative examples of phenotypes. **B)** Injection of 250 pg *si:ch211-226h8.14* mRNA (*si:ch211*) results in tail and blood-related defects. **C)** Injection of 50 pg *si:ch211-226h8.14* mRNA cause only mild defects. n is the number of embryos that were analyzed in the respective group.

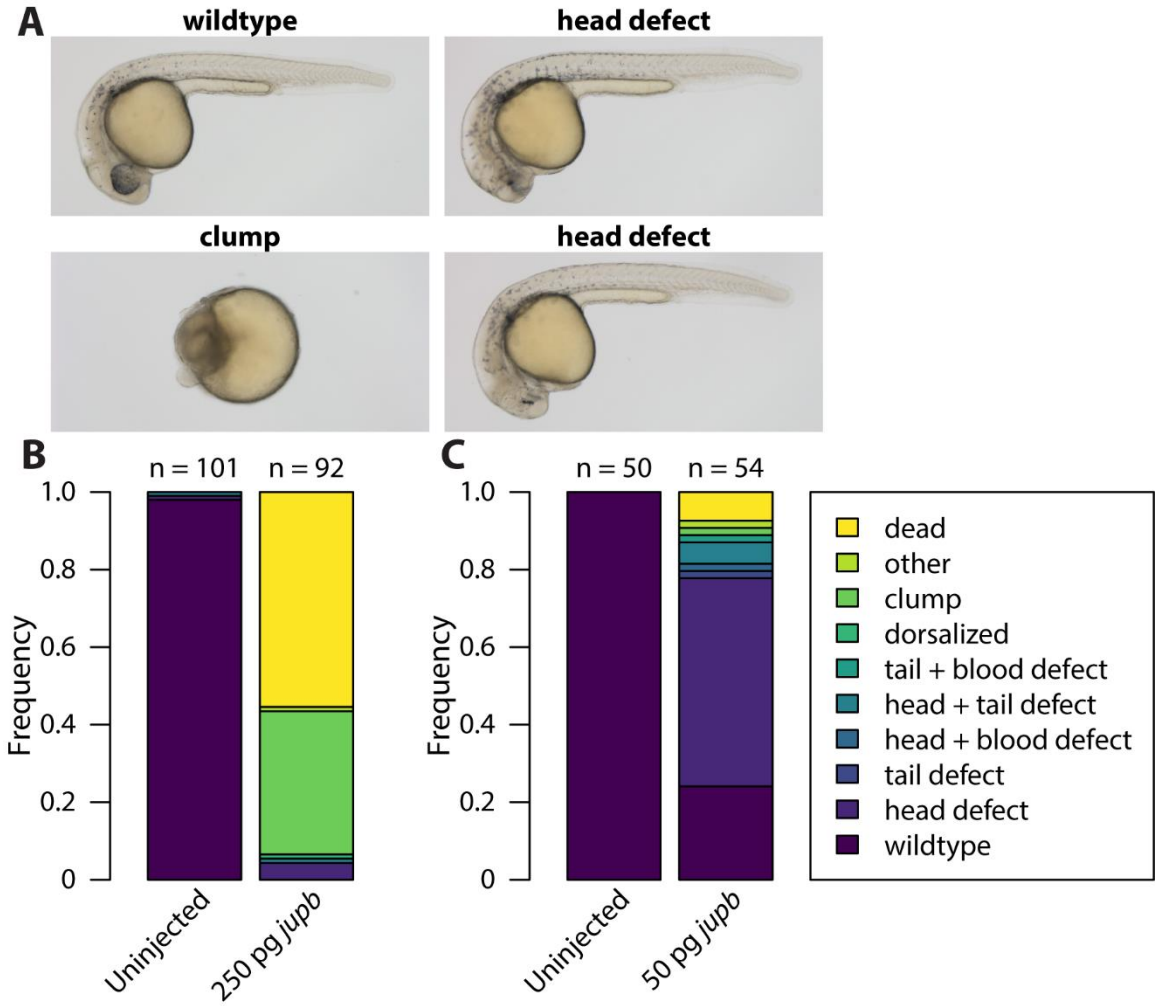

Figure 17: High levels of *jupb* mRNA cause phenotypes that indicate excess Nodal signaling. A) Representative examples of phenotypes. **B)** Microinjection of 250 pg *jupb* mRNA results in high lethality and severe phenotypes. **C)** Microinjection of 50 pg *jupb* mRNA results in head defects that are consistent with excess Wnt signaling (see text). n is the number of embryos that were analyzed in the respective group.

iv) Effects of MS candidate overexpression on Nodal signaling

The Jupb overexpression phenotypes were indicative of excess Nodal signaling and thus consistent with the proposed function of Jupb in Wnt/β-catenin signaling (Karnovsky and Klymkowsky 1995, Miller and Moon 1997, Williams *et al.* 2000, Zhurinsky *et al.* 2000b, Maeda *et al.* 2004). To test whether the phenotypes caused by *si:ch211-226h8.14* or *jupb* overexpression are associated with changes in Nodal signaling, I fixed zebrafish embryos overexpressing these MS candidates around shield stage (6 hpf; Kimmel *et al.* 1995) and detected pSmad2/3 by immunofluorescence staining. Using a double staining protocol (Section 6.2), I additionally stained the same embryos for expression of the Nodal target gene and dorsal marker *goosecoid* (*gsc*; Stachel *et al.* 1993, Thisse *et al.* 1994, Gritsman *et al.* 1999, Bennett *et al.* 2007a, Shih *et al.* 2010, Dubrulle *et al.* 2015) by fluorescence *in situ* hybridization (FISH; Figure 18). Maternal-zygotic *sqt*$^{-/-}$ mutant embryos (*MZsqt*$^{-/-}$), where *gsc* expression is reduced (Pei *et al.* 2007), and embryos overexpressing GFP or Squint-FLAG served as controls. Similar to uninjected controls, embryos overexpressing the secreted lectin exhibit pSmad2/3 signal around the margin and *gsc*

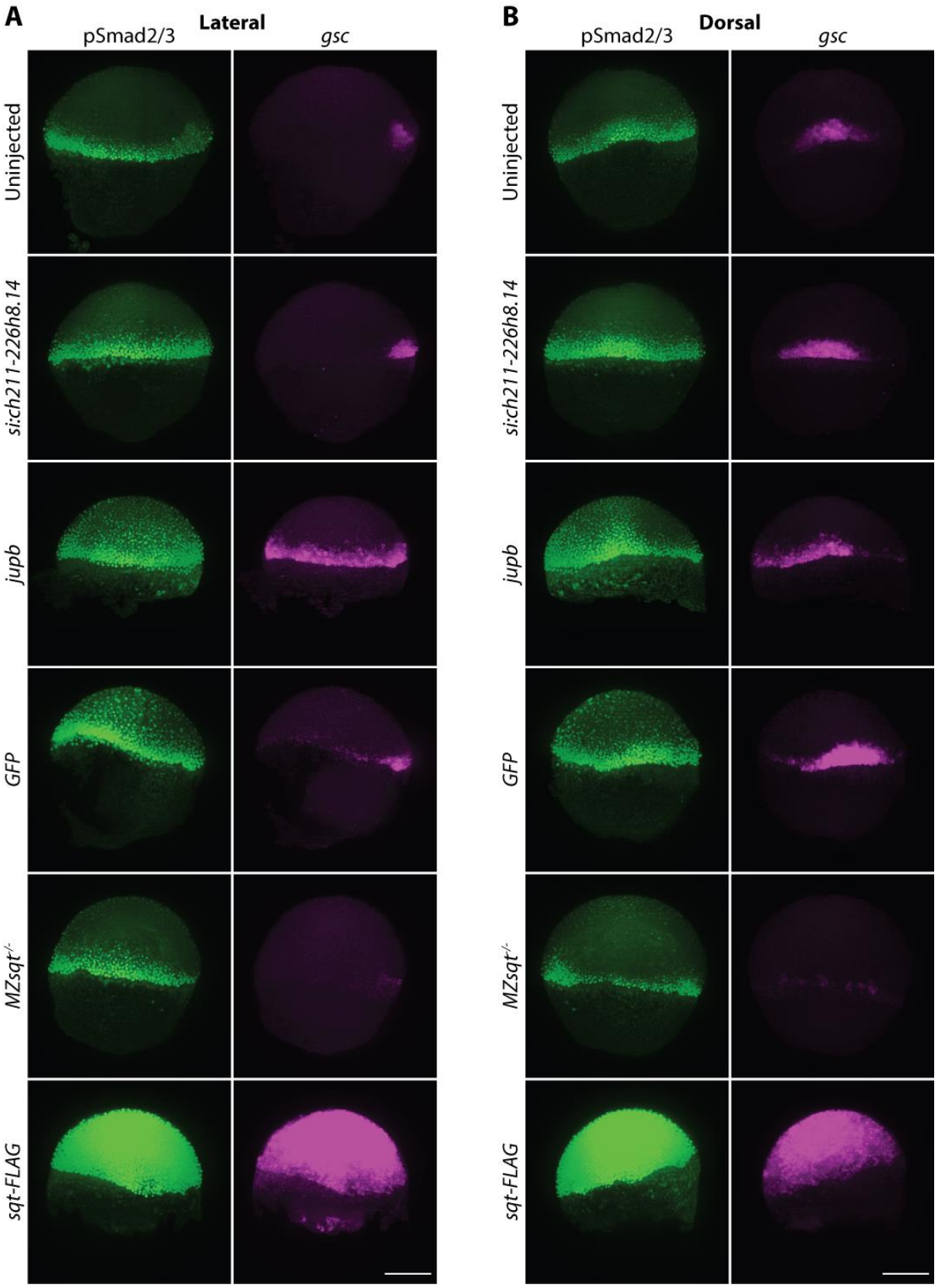

Figure 18: Nodal signaling appears largely unaltered in embryos overexpressing the secreted lectin Si:ch211-226h8.14. Embryos were injected with 250 pg of the indicated mRNAs (*si:ch211-226h8.14*, *jupb*, *GFP*). *MZsqt*$^{-/-}$ embryos and embryos injected with 30 pg *sqt-FLAG* mRNA serve as negative and positive controls, respectively. The embryos shown were fixed when uninjected control embryos had reached shield stage. Samples were stained for pSmad2/3 by immunofluorescence (green, left panels) and *gsc* expression by FISH (magenta, right panels). **A)** Lateral views, dorsal is to the right. **B)** Dorsal views of the same embryos. Scale bars: 200 µm.

expression on the dorsal margin. In contrast, embryos injected with *jupb* mRNA have a *gsc* signal that is distributed around the margin, without apparent radial asymmetry (Figure 18). This resembles previous findings that *gsc* expression is expanded in the margin when β-catenin is overexpressed in zebrafish embryos (Pelegri and Maischein 1998, Dougan *et al.* 2003) and again supports a function for Jupb in Wnt/β-catenin signaling. Additionally, in Figure 18 the pSmad2/3 signal of Jupb-overexpressing embryos appears to be extended towards the animal pole, compared to uninjected controls. An increase in Nodal signaling in these embryos is possibly due to increased Nodal expression downstream of Wnt/β-catenin (Shimizu *et al.* 2000, Agathon *et al.* 2003, Dougan *et al.* 2003). However, the pSmad2/3 signal appears also expanded in GFP-overexpressing embryos (Figure 18). This apparent expansion of pSmad2/3 in the maximum intensity projection (Figure 18) results, at least in part, from staining of enveloping layer (EVL) at the surface of the embryo (Supplementary Figure 13). It is unclear whether this signal is a staining artifact or represents active Nodal signaling in the EVL under these conditions. Consistent with the literature, *MZsqt*$^{-/-}$ embryos have reduced *gsc* expression (Pei *et al.* 2007) and also weaker dorsal pSmad2/3 staining (Figure 18). The remaining Nodal signaling in these embryos is explained by the action of Cyclops. Both *gsc* expression and pSmad2/3 signal are ubiquitous in positive control embryos injected with *squint-FLAG* mRNA (Figure 18), as expected for Nodal overexpression (Müller *et al.* 2012).

Together with the localization (Section 4.3, A.ii) and phenotype (Section 4.3, A.iii) assays these results suggest that Jupb is a regulator of Wnt signaling, whereas the evidence is less clear for the secreted lectin. Although Nodal signaling is not obviously altered in embryos overexpressing the secreted lectin, the secreted lectin can localize to Nodal-containing structures at the membrane (Section 4.3, A.ii).

v) Morpholino-mediated knockdown of secreted lectin transcripts

In the following experiments I focused on the secreted lectin to clarify its potential role in Nodal signaling. I chose it over the other MS candidates because the experiments described previously did not indicate functions for the others in Nodal signaling. To complement the results obtained with secreted lectin overexpression (Sections 4.3, A.iii and 4.3, A.iv), I wanted to deplete endogenous Si:ch211-226h8.14 levels using Morpholino-mediated knockdown, which is commonly used to block the processing or the translation of transcripts (Summerton and Weller 1997, Bill *et al.* 2009, Blum *et al.* 2015, Stainier *et al.* 2017). I tested three different Morpholinos (MOs): MO1 targets the start codon (designed to block translation) and MO2/3 target splice sites (designed to interfere with correct splicing, Supplementary Table 4). I titrated the amounts of MO that I injected and evaluated the resulting phenotypes 1 dpf (Figure 19, Supplementary Figures 14&15). Injecting MO1 caused minor phenotypes in a large fraction of embryos; however, the phenotypes were not obviously related to Nodal signaling (Supplementary Figure 14). MO3 gave rise to phenotypes only in a small fraction of embryos (Supplementary Figure 15). Of the three MOs, only MO2 caused strong phenotypes. Figure 19 shows

that amounts between 0.8 ng and 1.6 ng result in a large fraction of embryos with shortened tails, where the somites appear compressed. This is reminiscent of convergent extension phenotypes (Solnica-Krezel *et al.* 1996, Jessen *et al.* 2002, Williams and Solnica-Krezel 2019 pre-print). Importantly, amounts above 1.6 ng MO2 resulted in massive lethality.

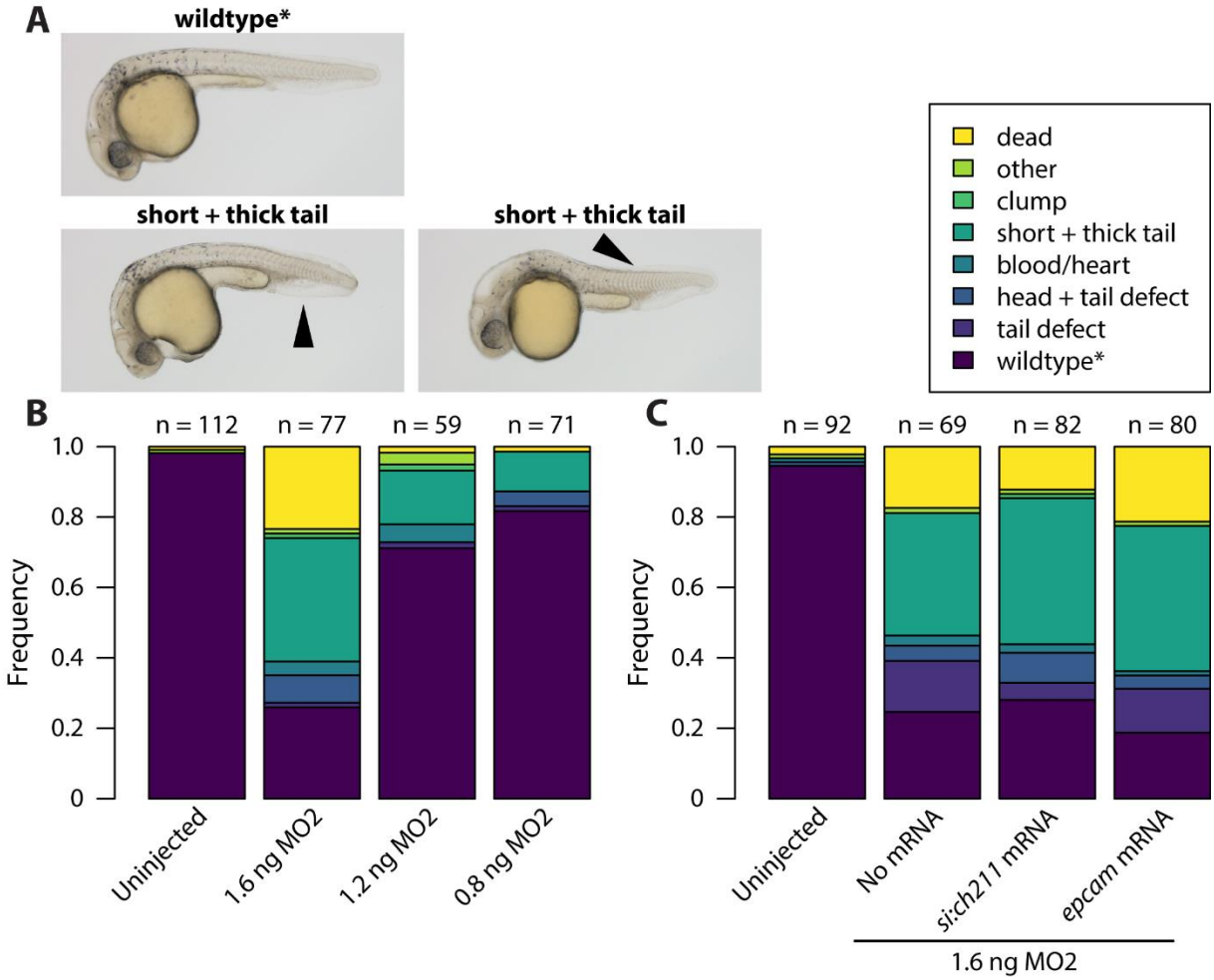

Figure 19: MO2-induced tail phenotypes are not rescued by injection of 50 pg *si:ch211-226h8.14* mRNA. A) Representative examples of phenotypes. **B)** Titration shows that 1.6 ng MO2 cause phenotypes in a large fraction of embryos. **C)** 50 pg *si:ch211-226h8.14* mRNA cannot rescue the phenotypes caused by 1.6 ng MO2. Equimolar amounts (83 pg) of *epcam* mRNA were co-injected with MO2 as rescue control. Note that embryos injected with 50 pg *si:ch211-226h8.14* mRNA alone mostly exhibit wildtype phenotypes (Figure 16) and that overexpression of *epcam* does not induce strong phenotypes (Supplementary Figure 12). Embryos with overall normal morphology, but necrotic tissue in the head are described as "wildtype*". n is the number of embryos that were analyzed in the respective group.

To determine whether MO-induced phenotypes are specific to the desired target transcript, rescue experiments are crucial (Eisen and Smith 2008, Bill *et al.* 2009, Blum *et al.* 2015, Stainier *et al.* 2017). In a control experiment, I tried to rescue phenotypes caused by the splice-inhibiting MO2 by co-injecting 50 pg *si:ch211-226h8.14* mRNA. 50 pg of secreted lectin mRNA alone caused very few phenotypes (Figure 16C). As shown in Figure 19C, co-injection of *si:ch211-226h8.14* mRNA does not rescue the phenotypes resulting from MO2 injection. This indicates that the phenotypes that are observed with 1.6 ng MO2 (Figure 19B) may be unspecific and not due to depletion of the secreted lectin. However, it

is also possible that 50 pg *si:ch211-226h8.14* mRNA are not sufficient to overcome the depletion of endogenous secreted lectin. Since high amounts of *si:ch211-226h8.14* mRNA also cause phenotypes (Figure 16), a careful titration of *si:ch211-226h8.14* mRNA could be performed in future experiments to test this possibility. An important consideration for MO-mediated *si:ch211-226h8.14* knockdown is the presence of secreted lectin transcripts in the zygote (White *et al.* 2017). This implies that corresponding mRNAs are maternally contributed, and therefore splice-inhibiting MOs should not effectively knock down expression (Draper *et al.* 2001, Eisen and Smith 2008, Bill *et al.* 2009). To overcome this, future experiments will require the generation of maternal-zygotic mutants.

vi) Nodal mobility is unaltered in embryos overexpressing secreted lectin

The phenotypes resulting from *si:ch211-226h8.14* overexpression (Section 4.3, A.iii) indicate that the secreted lectin may have important functions for early embryonic development. Moreover, the co-localization of Si:ch211-226h8.14-GFP with Cyclops-RFP implicates it as a potential Nodal binding partner (Section 4.3, A.ii). To test whether it can act as a diffusion regulator of the zebrafish Nodals Squint and Cyclops, I performed FRAP of Squint-GFP and Cyclops-GFP (Müller *et al.* 2012) with and without overexpression of *si:ch211-226h8.14* mRNA (Figure 20). The effective diffusion coefficients of Cyclops-GFP (0.8±0.4 µm^2/s) and Squint-GFP (4.4±1.9 µm^2/s) in control embryos were consistent with previous findings (Müller *et al.* 2012, Bläßle *et al.* 2018). When the secreted lectin is expressed in addition to the tagged Nodals, the effective diffusion coefficients are not obviously altered (1.1±0.5 µm^2/s for Cyc-GFP and 5.2±0.5 µm^2/s for Sqt-GFP; Figure 20).

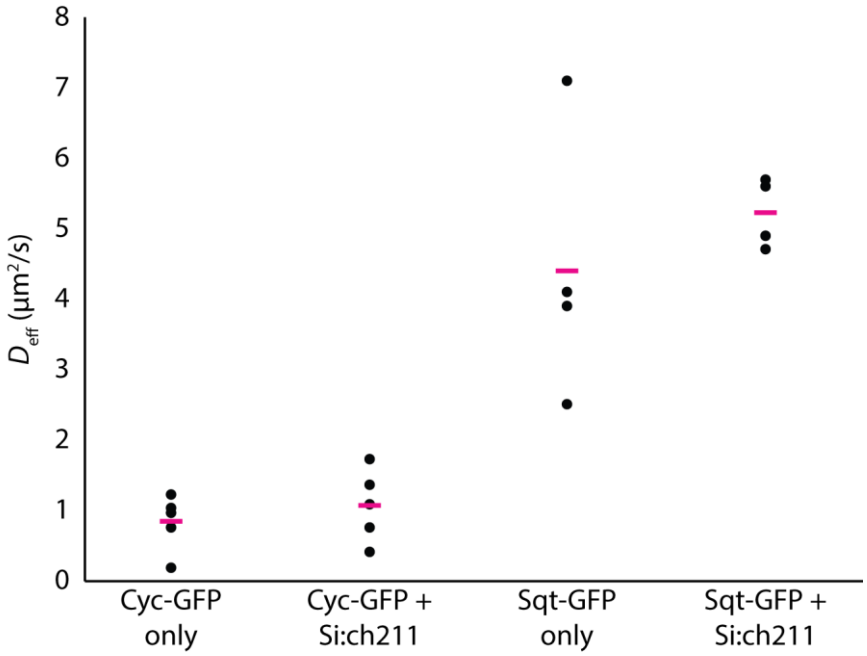

Figure 20: Overexpression of the secreted lectin Si:ch211-226h8.14 (Si:ch211) in zebrafish embryos does not change the effective diffusivity of Squint-GFP (Sqt-GFP) and Cyclops-GFP (Cyc-GFP). The mean effective diffusion coefficients (magenta bars) for Cyc-GFP are 0.8±0.4 µm^2/s in the absence and 1.1±0.5 µm^2/s in the presence of additional secreted lectin. For Sqt-GFP the mean effective diffusion coefficients are 4.4±1.9 µm^2/s without and 5.2±0.5 µm^2/s with secreted lectin overexpression.

B. DISCUSSION

My validation of the MS candidates revealed that *jupb* and *si:ch211-226h8.14* overexpression results in distinct phenotypes (Section 4.3, A.iii). Junction plakoglobin, also known as γ-catenin, is a β-catenin homolog (Zhurinsky *et al.* 2000b). There are two paralogs in zebrafish, *junction plakoglobin a* (*jupa*) and *junction plakoglobin b* (*jupb*). In zebrafish, Junction plakoglobin was proposed to have structural functions in cell junctions as well as negative functions in Wnt/β-catenin signaling (Martin *et al.* 2009). However, there are also several indications that Junction plakoglobin can activate transcription of Wnt targets either directly, or by stabilizing β-catenin (Karnovsky and Klymkowsky 1995, Miller and Moon 1997, Kolligs *et al.* 2000, Williams *et al.* 2000, Zhurinsky *et al.* 2000a, Maeda *et al.* 2004). The lack of head structures (Section 4.3, A.iii) as well as the expanded *gsc* expression (Section 4.3, A.iv) that are observed with *jupb* overexpression indicate increased Wnt/β-catenin signaling (Pelegri and Maischein 1998, Kim *et al.* 2000, Heisenberg *et al.* 2001, Dougan *et al.* 2003) and are therefore consistent with most literature. High *jupb* expression levels may induce "clump" phenotypes indicative of excess Nodal signaling (Rogers *et al.* 2017) possibly due to Nodal induction by Wnt signaling (Shimizu *et al.* 2000, Agathon *et al.* 2003, Dougan *et al.* 2003, Zinski *et al.* 2018). My validation experiments do not suggest a direct function for Jupb in Nodal signaling and it is unclear why Jupb was identified in my CoIP/MS screen as Squint-FLAG binding partner (Table 1). It is possible that *wnt11* upregulation by the Squint bait protein (Gritsman *et al.* 1999, Bennett *et al.* 2007a, Dubrulle *et al.* 2015) stabilized Jupb through β-catenin signaling, since Junction plakoglobin can stabilize the homologous β-catenin (Miller and Moon 1997). Upregulated Junction plakoglobin levels that would be present in the Squint-FLAG, but not in the secGFP-FLAG control may result in unspecific interactions with the bait or the antibody-conjugated beads used for CoIP. However, I cannot exclude that Squint has an unknown function in β-catenin/Junction plakoglobin signaling.

The *si:ch211-226h8.14* gene encodes a previously uncharacterized protein with a signal peptide and an SUEL (sea urchin egg lectin) domain. As the name suggests, SUELs are present in sea urchin eggs and their expression has been studied in early sea urchin embryogenesis (Sasaki and Aketa 1981, Ozeki *et al.* 1995). SUEL domains are found in proteins of many species including mammals and they may act in eggs as part of the innate immune system (Tateno 2010). In zebrafish, lectins homologous to Si:ch211-226h8.14 were found to be enriched in poor-quality eggs in a recent MS study (Yilmaz *et al.* 2017). Based on data from the zebrafish gene expression atlas (White *et al.* 2017), *si:ch211-226h8.14* transcripts are present in the egg at the earliest stages, implying maternal contribution. My results show that Si:ch211-226h8.14-GFP is efficiently secreted and its localization is mainly diffusely extracellular. Only at high expression levels does it additionally form membrane-associated clusters and the GFP signal of these clusters overlaps with Cyclops-RFP membrane-associated clusters. This suggests that the secreted lectin binds, possibly with low affinity, Cyclops or Cyclops-containing glycan structures of the ECM. The fact that both Squint and Cyclops carry consensus NXS/T glycosylation sites in their pro-domains may explain why the secreted lectin was identified in the Nodal CoIPs (Table 1).

Interestingly, the secreted lectin was not identified in the Lefty1/2 CoIP/MS, although Lefty1 is glycosylated (Westmoreland *et al.* 2007) and also Lefty2 carries consensus glycosylation sites. Thus, the secreted lectin may specifically bind Nodals. Although the secreted lectin does not appear to be a membrane-associated binder as the diffusion-regulating, membrane-tethered nanobodies (Section 4.2), it may be a mobile diffusion regulator: Theoretically, it could act as a positive diffusion regulator and increase Nodal diffusion by shuttling (Müller *et al.* 2013). Despite the evidence of Si:ch211-226h8.14 binding Nodals, overexpression of the secreted lectin did not unambiguously alter Nodal mobility based on FRAP (Section 4.3, A.vi). It is possible that endogenous Si:ch211-226h8.14 levels are high in order to assure maximum Nodal mobility, in which case a reduction of secreted lectin levels would be predicted to affect Nodal mobility. To test this hypothesis, future experiments could knock-out *si:ch211-226h8.14* using CRISPR/Cas9 (Gagnon *et al.* 2014, Wu *et al.* 2018). However, there are several homologous secreted lectins encoded in the zebrafish genome, which may function redundantly and additionally hinder a specific gene targeting.

In zebrafish, Nodals have lower diffusivities than Leftys (Müller *et al.* 2012). Among the Nodals, Cyclops-GFP forms membrane-associated clusters, possibly an indication for binders similar to the experimental diffusion regulators in Section 4.2. Intriguingly, Squint-GFP is also present in membrane-associated clusters at high expression levels (Supplementary Figure 7), raising the possibility that the two zebrafish Nodals have different affinities for membrane-associated binders. To date, the putative binders remain elusive; however, HSPGs are potential players for the regulation of Nodal mobility during embryogenesis since they are known to regulate the dispersal of Xnr1 (Marjoram and Wright 2011) and other TGF-β superfamily members (Baeg and Perrimon 2000, Häcker *et al.* 2005). Surprisingly, several known Nodal binders could not be identified in my CoIP/MS analysis. These include the type I and type II Activin receptors (Cheng *et al.* 2004, Wang *et al.* 2016) as well as the Nodal co-receptor Oep (Yan *et al.* 2002), which I could co-immunoprecipitate in control experiments (Figure 11). It is possible that these proteins are of low abundance in the embryo and could therefore not be detected by MS. An important limitation of my CoIP/MS approach is that only peptides can be detected. Thus, it is possible that carbohydrates (Broussard and Boyce 2019) or lipids directly bind to Nodals/Leftys and act as diffusion regulators, but were not identified in the present analysis.

5. Conclusion and Outlook

There are several lines of evidence supporting the existence of diffusion regulators that restrict Nodal mobility in zebrafish embryos. These include the short Nodal signaling range (Section 4.1; van Boxtel *et al.* 2015) and low Nodal diffusion coefficients (Müller *et al.* 2012). The identification of endogenous Nodal regulators is crucial to understand the mechanisms that control Nodal signaling during vertebrate embryogenesis. Future MS screening projects could use proximity labeling based on APEX (Lobingier *et al.* 2017) or BioID (Roux *et al.* 2012) in order to identify transient Nodal interactions. An alternative approach to investigate the hindered diffusion of zebrafish Nodals is to characterize the kinetics underlying Nodal movement. For example, recently developed single-molecule imaging technology could be used with photoactivatable Nodal constructs to infer the *in vivo* binding kinetics between Nodals and their diffusion regulators (Reisser *et al.* 2018).

Moreover, the visualization of endogenous Nodal distribution and transport will be necessary to understand how Nodals function. Knock-in lines that encode fluorescent zebrafish Nodals and Leftys may allow *in vivo* imaging of their production, distribution and transport. Importantly, the morphotrap (Harmansa *et al.* 2015) or other membrane-tethered nanobodies (Section 4.2) could be expressed in these transgenic embryos to perturb the dispersal of GFP-tagged Nodals/Leftys and directly test the morphogen model.

Almost 20 years after the zebrafish Nodal Squint was proposed as a morphogen (Chen and Schier 2001), many important aspects of Nodal signaling have been characterized (Bennett *et al.* 2007a, Müller *et al.* 2012, Dubrulle *et al.* 2015, van Boxtel *et al.* 2015, Bisgrove *et al.* 2017, Montague and Schier 2017, Pelliccia *et al.* 2017, Rogers *et al.* 2017). Refining the understanding of extracellular Nodal interactions and transport will help to systematically test proposed Nodal signaling mechanisms in the future (Rogers and Müller 2019). In my doctoral studies, I have examined the endogenous Nodal signaling range and my results indicate that Nodal signaling does not require relay to signal to cells at a distance. Perturbing endogenous Nodal dispersal in future experiments will be required to test the importance of Nodal mobility for germ layer patterning. To modulate the extracellular diffusion of secreted proteins I have established weak membrane-tethered nanobodies that can be used as experimental diffusion regulators. They may allow the modulation of morphogen gradient range and the functional investigation of short-range activator/long-range inhibitor systems in the future. In combination with gene editing to generate endogenously tagged morphogens and modern live imaging these approaches promise exciting insights into morphogen function.

6. Supplementary Material

6.1 Supplementary data

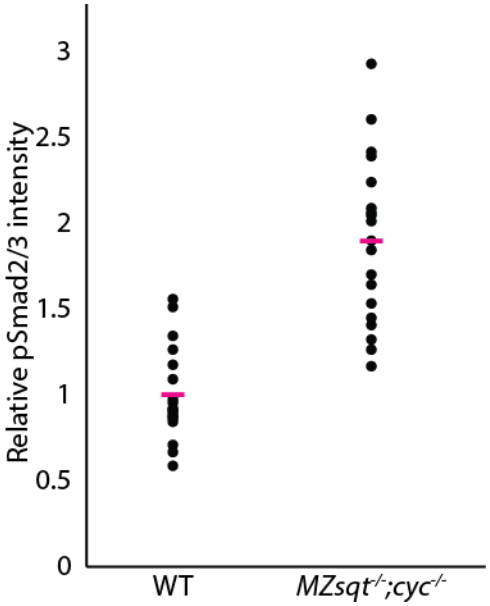

Supplementary Figure 1: Margin transplants exhibit higher pSmad2/3 intensities in *MZsqt*$^{-/-}$;*cyc*$^{-/-}$ mutants than in wildtype (WT) embryos. Fluorescence intensities were normalized to the mean WT fluorescence. The mean fluorescence intensities are 1.00±0.27 (WT) and 1.89±0.48 (*MZsqt*$^{-/-}$;*cyc*$^{-/-}$).

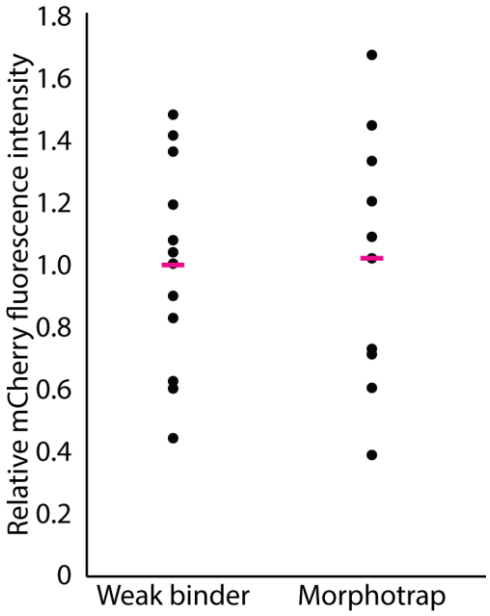

Supplementary Figure 2: mCherry fluorescence intensities are comparable between embryos that were injected with 50 pg of mRNA encoding either the weak binder or the morphotrap. Shown are mean mCherry fluorescence intensities (measured in the whole slice) from the samples in Figure 7A&B (black dots). The mean value of each group is shown as magenta bar. Fluorescence intensities were normalized to the mean weak binder fluorescence. The mean fluorescence intensities are 1.00±0.33 (Weak binder) and 1.02±0.41 (Morphotrap).

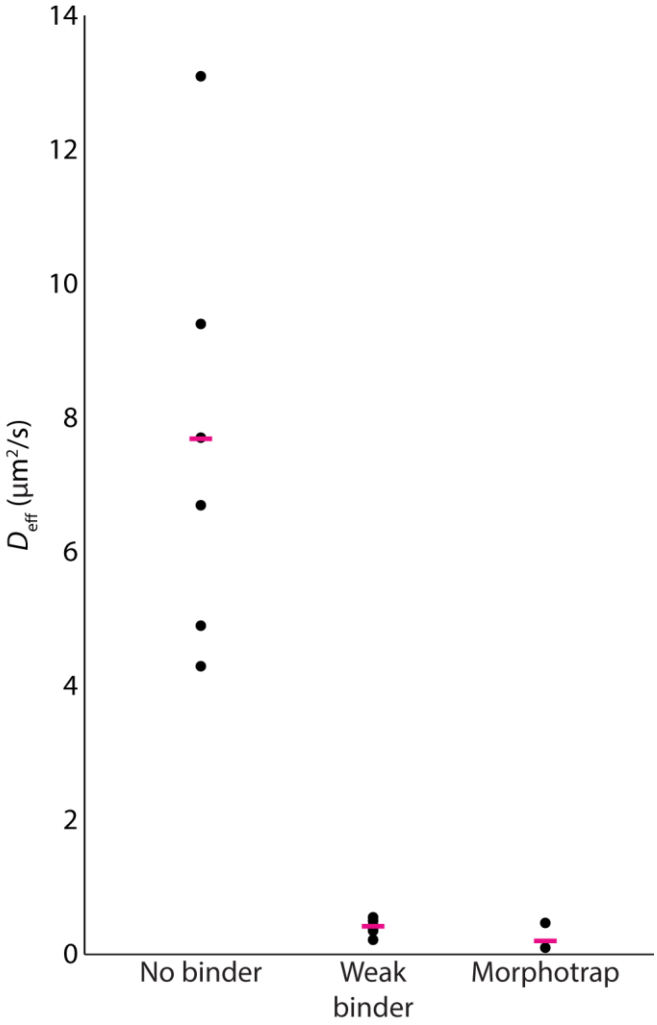

Supplementary Figure 3: The effective diffusion coefficient of Lefty1-GFP is reduced by membrane-tethered GFP binders. Black dots represent single FRAP experiments. The following mean effective diffusion coefficients (magenta bars) were determined: 7.7±3.2 µm²/s (No binder), 0.4±0.1 µm²/s (Weak binder) and 0.2±0.2 µm²/s (Morphotrap).

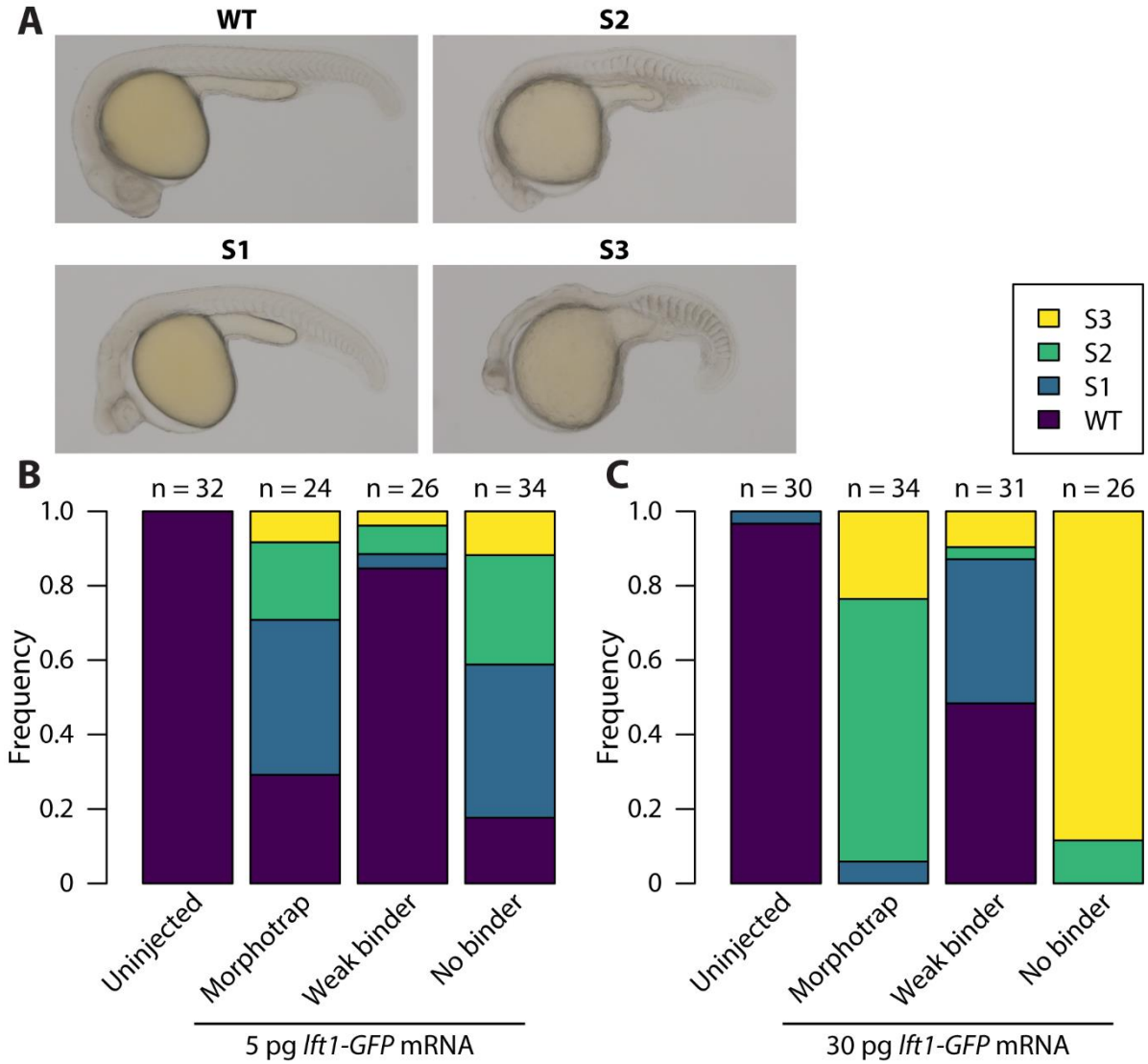

Supplementary Figure 4: The weak binder reduces Lefty1-GFP activity. A) Lefty1-GFP overexpression results in a range of phenotypes 1 day post fertilization (dpf). Images of representative embryos are shown for each phenotype class. Classes S1 through S3 indicate increasing severity of the phenotype. **B)** Phenotype statistics for embryos that were injected at the one-cell stage with 5 pg *lft1-GFP* mRNA. **C)** Phenotype statistics for embryos that were injected at the one-cell stage with 30 pg *lft1-GFP* mRNA. The embryos were co-injected with the indicated GFP binder. n is the number of embryos that were analyzed in the respective group.

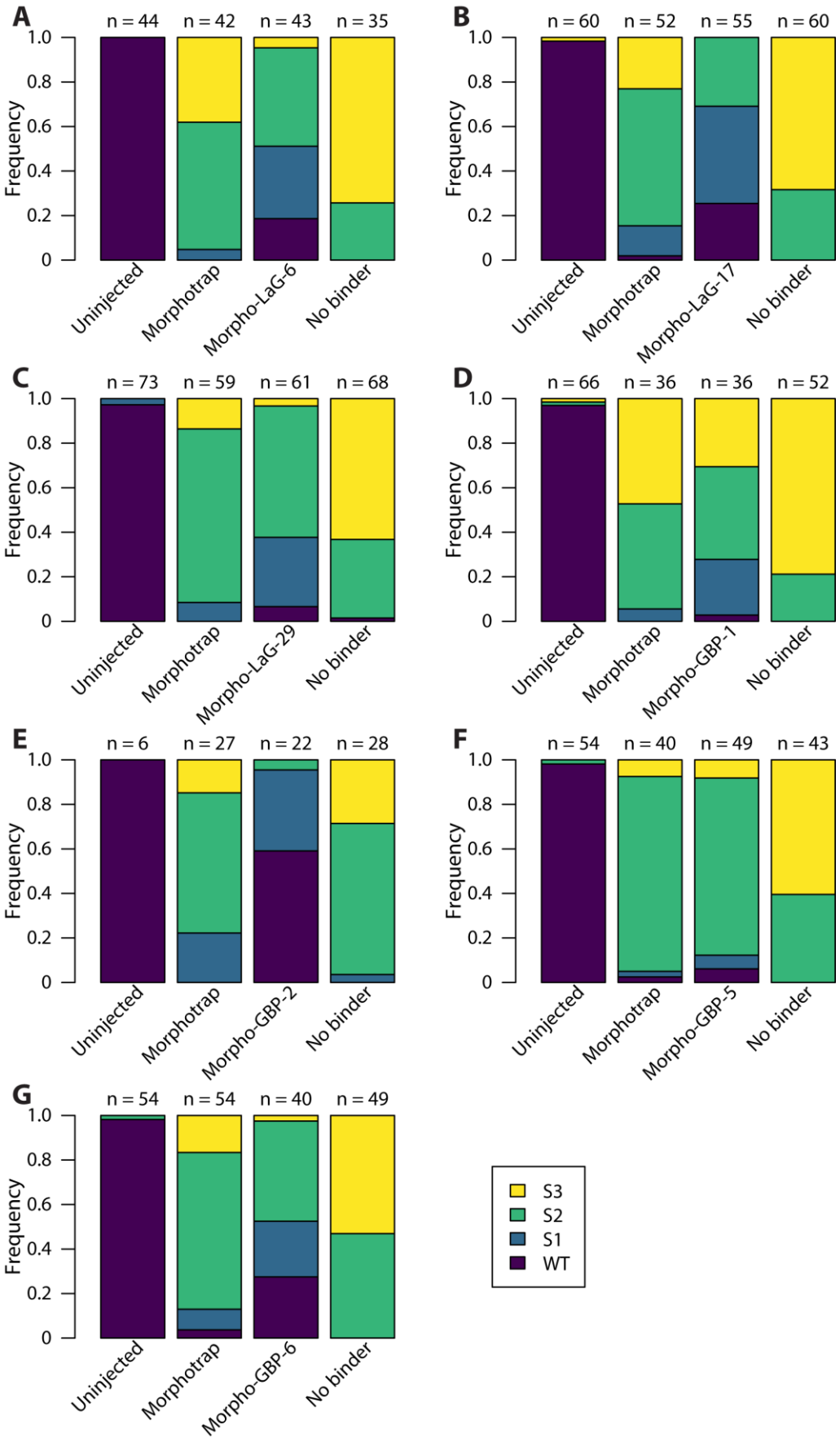

Supplementary Figure 5: Alternative GFP binders in the morphotrap scaffold have variable effects on Lefty1-GFP activity. Shown are the phenotypes that were observed when 30 pg Lefty1-GFP mRNA were injected

with morphotrap (Morphotrap) or an alternative binder (Morpho-…) mRNA or alone (No binder). Classes S1 through S3 indicate increasing severity of the phenotype. Note that the morpho-GBP-5 binder results in Lefty1-GFP activity that is comparable to the morphotrap (F). n is the number of embryos that were analyzed in the respective group.

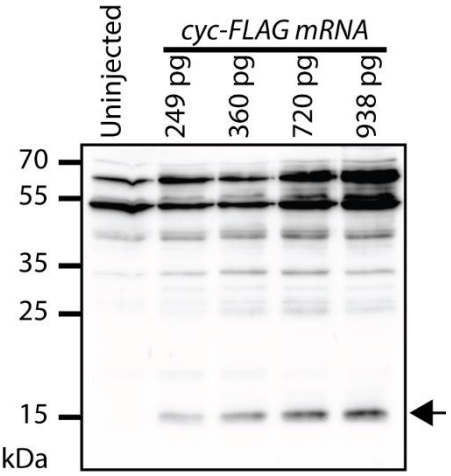

Supplementary Figure 6: Anti-FLAG western blot showing *cyclops-FLAG* mRNA titration. Increasing amounts of mature Cyclops-FLAG protein (arrow) are detected when higher amounts of mRNA are injected. Between 249 and 938 pg mRNA were injected per embryo. For each sample, protein sample corresponding to eight embryo caps was loaded.

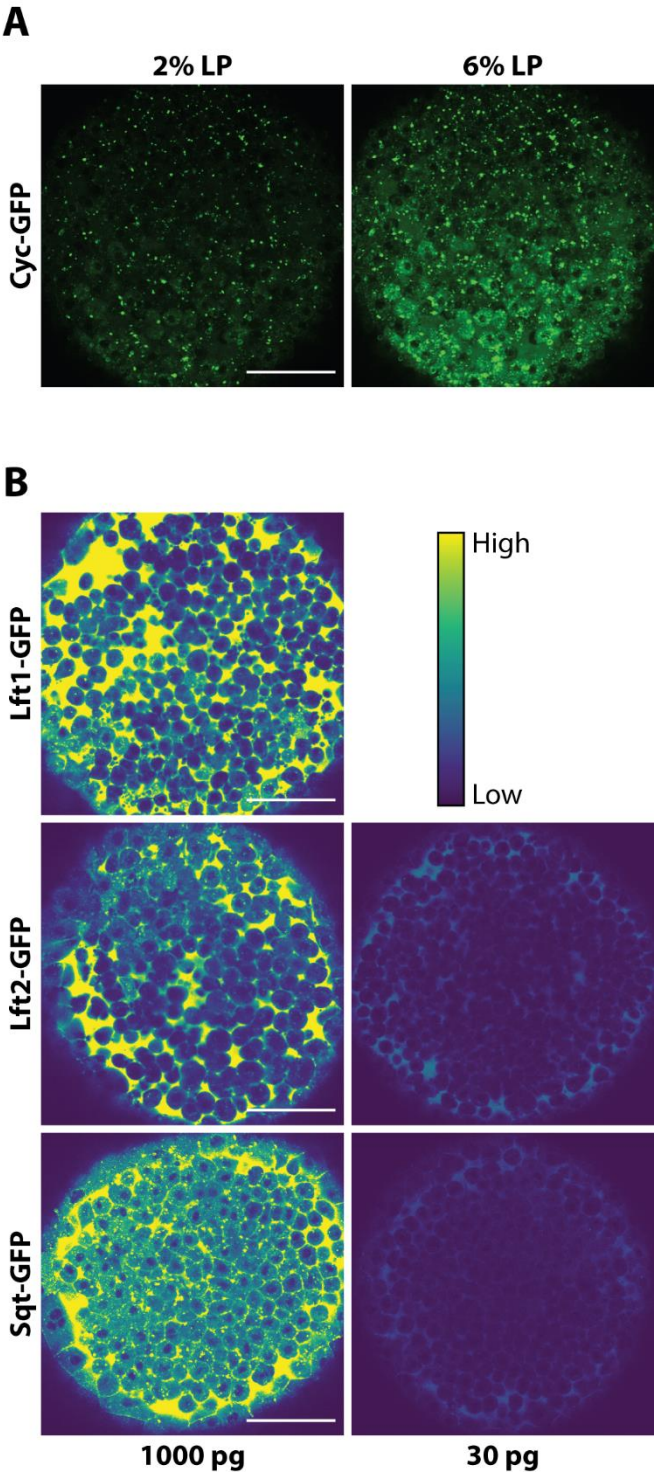

Supplementary Figure 7: Strong overexpression of GFP-tagged zebrafish Nodals and Leftys does not change their overall distribution. A) Embryos expressing 1025 pg *cyc-GFP* mRNA imaged at 30 µm depth. Although cytoplasmic GFP signal is evident at 6% laser power (LP), the majority of the GFP signal is in characteristic membrane-associated clusters (Müller 2012). **B)** Pseudo-colored GFP signal of embryos expressing either high (approximately 1000 pg) or low (30 pg) levels of *lefty1-GFP*, *lefty2-GFP* or *squint-GFP* mRNAs (imaged at 35 µm depth). In general, most of the GFP signal is extracellular. Note that membrane-associated clusters appear only when high levels of *squint-GFP* mRNA are expressed. Scale bars: 100 µm.

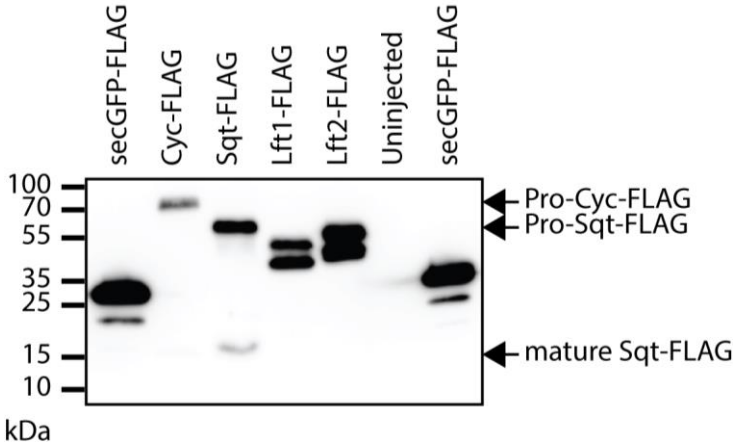

Supplementary Figure 8: Western blot shows that FLAG-tagged bait proteins are present in the samples used for MS analysis. 4% of the total CoIP eluates were analyzed by anti-FLAG western blot. Note that two secGFP-FLAG controls were used. Mature Nodals and the corresponding pro-proteins were detected, however the mature Cyc-FLAG signal is very weak.

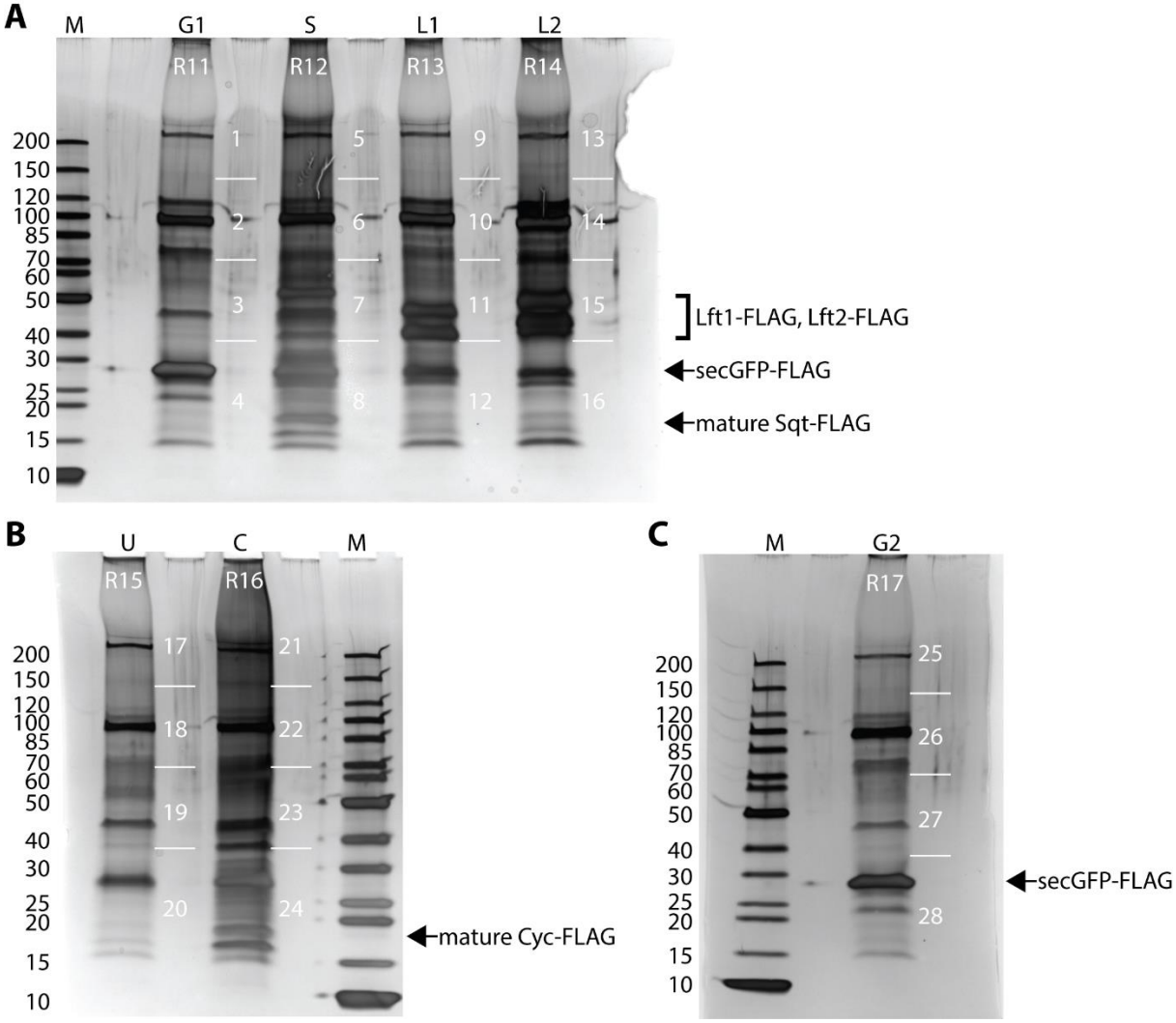

Supplementary Figure 9: Silver stained protein gels of CoIP eluates. The gel was cut as indicated by horizontal white lines and processed by the Proteome Center Tübingen. CoIP eluates were run on three different gels. **A)** Gel with secGFP-FLAG sample #1 (G1), Squint-FLAG (S), Lefty1-FLAG (L1) and Lefty2-FLAG (L2) samples. **B)** Gel with uninjected control (U) and Cyclops-FLAG (C) samples. **C)** Gel with secGFP-FLAG sample #2 (G2).

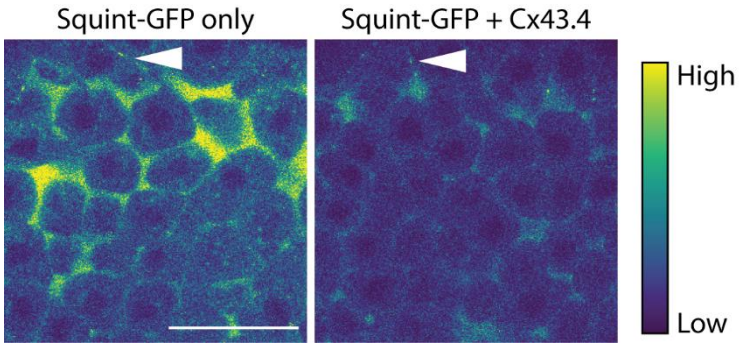

Supplementary Figure 10: Co-expression of Cx43.4 does not alter Squint-GFP localization. Left panel: Embryos expressing Squint-GFP have mostly extracellular GFP signal. Right panel: Co-expression of Cx43.4 does not alter the overall distribution of Squint-GFP. In general, Squint-GFP expression was weaker, when untagged MS candidates were co-expressed. Note that membrane-associated clusters in the embryo periphery (enveloping layer) are present in both conditions (arrowheads). Scale bar: 50 µm.

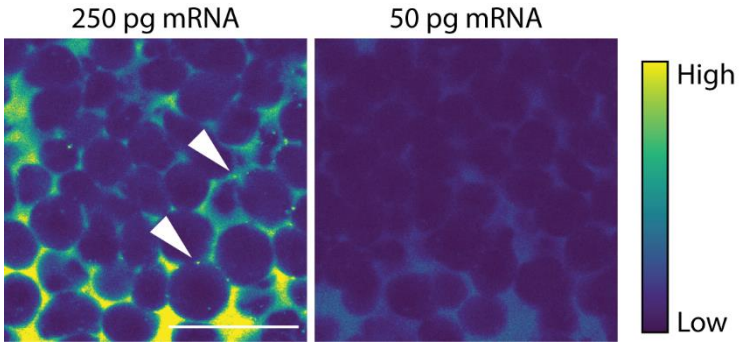

Supplementary Figure 11: Si:ch211-226h8.14-GFP forms membrane-associated clusters only at high expression levels. Embryos injected with 250 pg *si:ch211-226h8.14* mRNA exhibit membrane-associated clusters (arrowheads, left), but embryos injected wiht 50 pg mRNA do not (right). Scale bar: 50 µm.

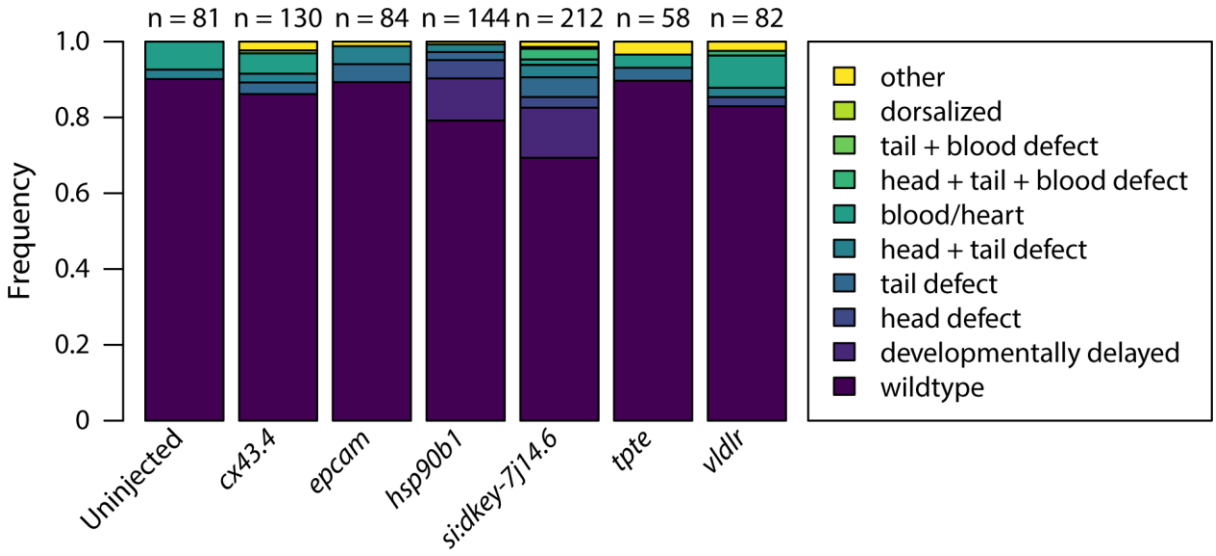

Supplementary Figure 12: Most MS candidates do not cause drastic phenotypes when overexpressed. 250 pg of each mRNA were microinjected into zebrafish embryos and the phenotypes assessed 1 dpf. A representative sample of uninjected embryos is shown. n is the number of embryos that were analyzed in the respective group.

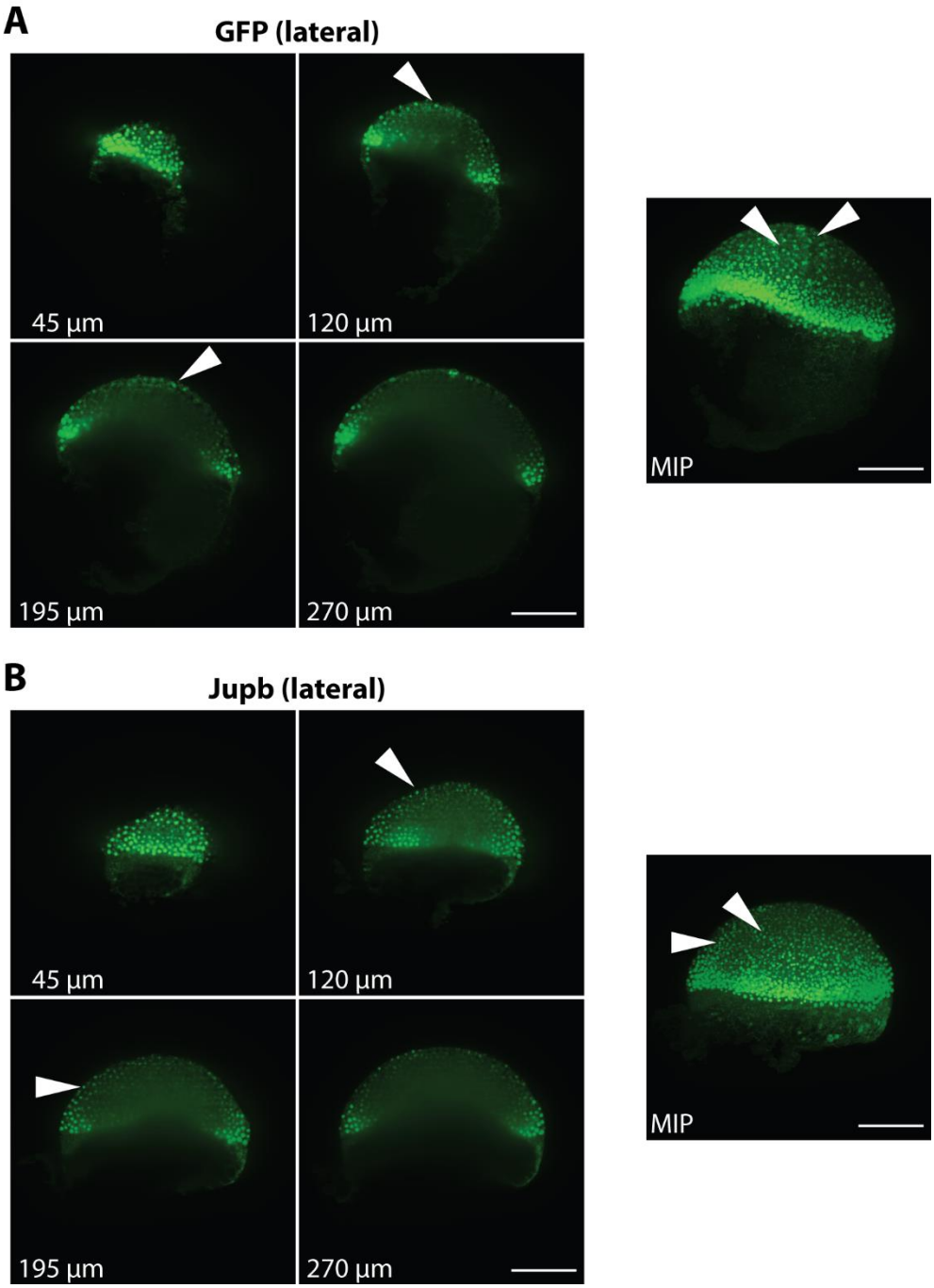

Supplementary Figure 13: pSmad2/3 immunofluorescence signal at the surface of the embryo appears as signal in the middle of the embryos in maximum intensity projections. Left panels show single slices of the acquired z-stacks at different distances from the embryo surface, right panels show maximum intensity projections (MIPs). Embryos injected with *GFP* **(A)** or *jupb* mRNA **(B)** are shown. The embryos are the same as in Figure 18. Scale bars: 200 µm

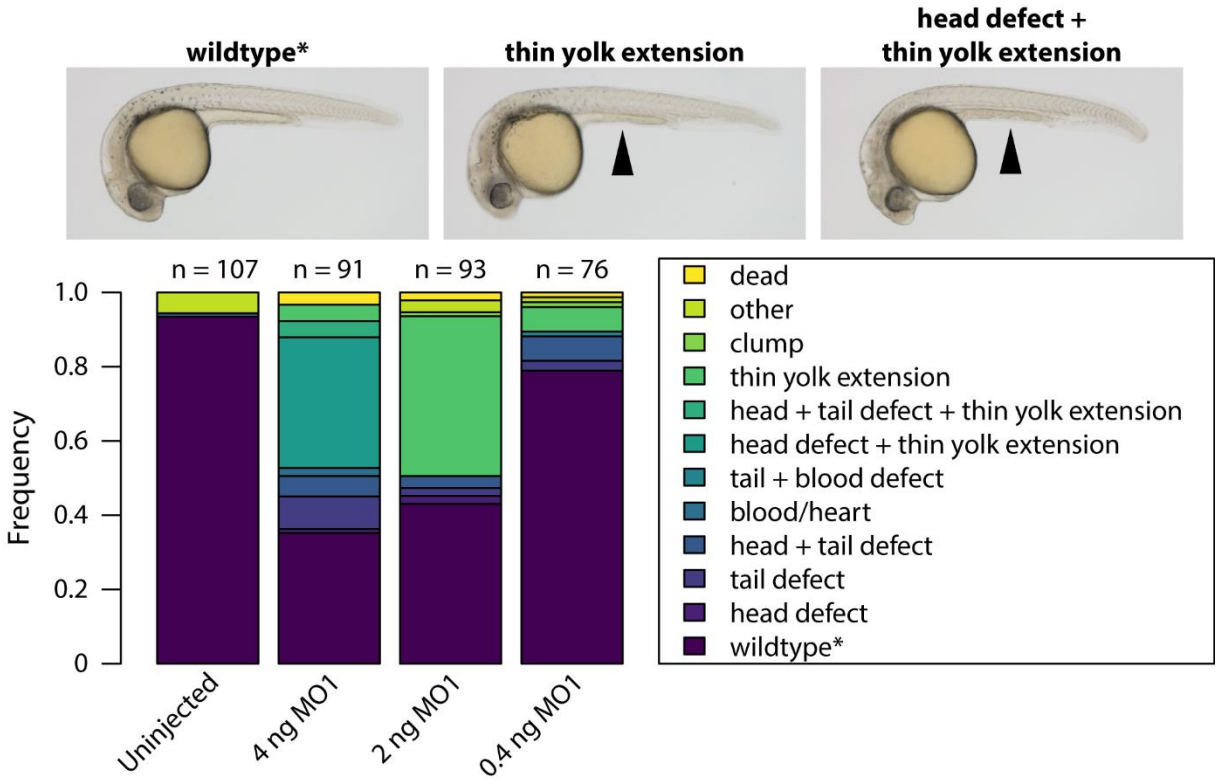

Supplementary Figure 14: Titration of MO1 induces only mild phenotypes. Top panel: Representative examples of the phenotypes. Lower panel: 2 ng MO1 cause mild yolk extension phenotypes in a large fraction of embryos. 4 ng MO1 result in additional head defects. Embryos with overall normal morphology, but necrotic tissue in the head are described as "wildtype*". n is the number of embryos that were analyzed in each group.

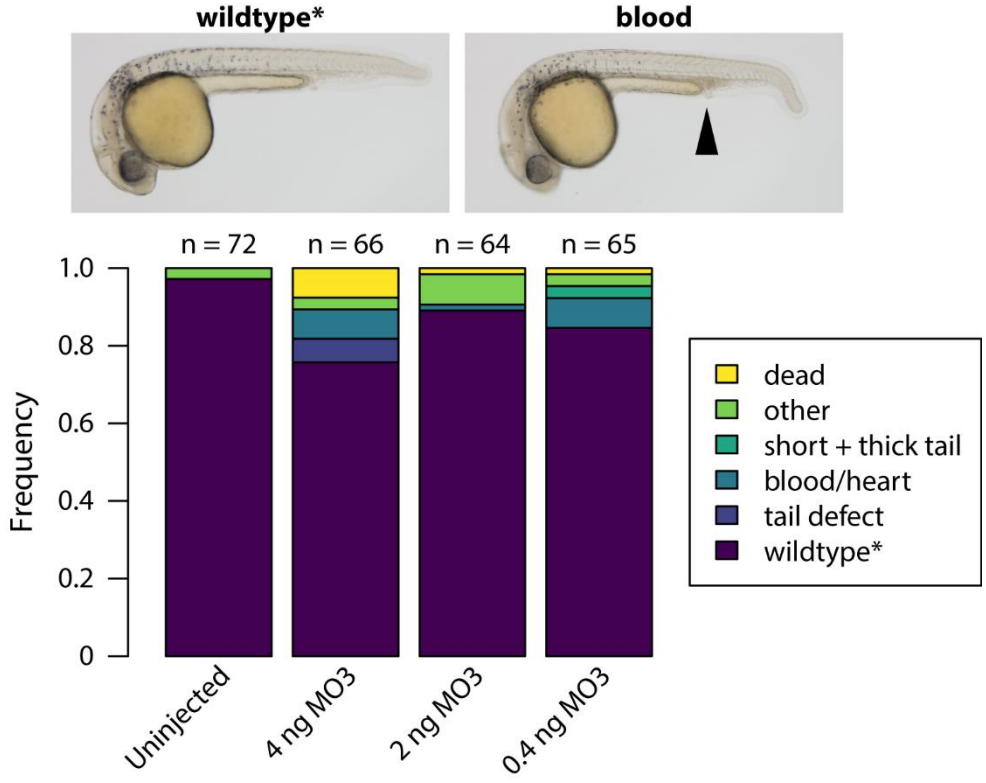

Supplementary Figure 15: Titration of MO3 induces phenotypes only in a small fraction of embryos. Top panel: Representative examples of the observed phenotypes. Lower panel: Titration shows that high amounts (4 ng) of MO3 cause diverse phenotypes. Embryos with overall normal morphology, but necrotic tissue in the head are described as "wildtype*. n is the number of embryos that were analyzed in each group.

Supplementary Table 1: MS identified 72 proteins in samples that were absent from controls. Shown are proteins where peptides were identified with a PEP<0.01 in the Nodal/Lefty samples, but not in the negative controls (excluding bait proteins).

		Sample			
Gene name	**UniProt ID(s)**	**Sqt**	**Cyc**	**Lft1**	**Lft2**
-	A0A0G2KG42		X		
pl10;ddx3	F1RCB2;B0S6P6;A0A0H2UJY3;X1WFB0		X		
rnf213b	A0A0R4I9Y1	X			
h1m	A0A0R4IAV0	X	X		
syncripl	A0A0R4ICN8;F1R8D7;Q6NYJ5		X		
capza1b;capza1a	Q6ZM50;A0A0R4IEP3;Q6NWK1				X
tuba1b;tuba8l4;tuba1a;si:ch211-114n24.6;tuba1c;tuba2	B8A516;Q6NWJ5;Q6NWK7;E7F244;B8A518;I3ISC4;Q6P972				X
gapdh	A0A0R4IG11;Q5XJ10;E9QIH5;E9QGA9			X	
vldlr	E9QBA5;E7FF13;A0A0R4IGN2	X			X
hspa8	Q1LY29;A0A0R4IVB0;A0A0R4IMF8;Q6NYR4	X			
si:ch211-244b2.1	Q1L881;A0A0R4IPS4	X	X	X	X
actr3b	F1QEB3;A0A0R4IPU5;F1QKV8				X
purba	A2BFY7;A0A0R4IS70		X		
camk2g1	Q4V9P8;A0A0R4IUL7;U3JAY8				X
igf2bp3	A0A0R4IYT0;Q9PW80		X		
eif2s3	A0A286Y8C2;F1QGW6;F1RBM8	X			
tuba7l	Q6GQM1;A0A286Y8F4				X
immt	A0A286Y9D5;Q6PFS4			X	X
hsp90b1	Q7T3L3;A0A286YAP4	X		X	X
ybx1	A1A605	X	X		X
gnb5a	A1L271				X
camk2b1	E9QDQ2;A2BGW3				X
cratb	A3KPZ2		X		
aldh18a1	A4IGC8	X			
zgc:171719;tpm1	A7E2K1;E7FBZ3				X
rfc3	A7MCR5	X	X		
atp5b	A8WGC6				X
cx43.4;gjc1	B0UYC0;Q92052	X			X
krt15	B0UYS0				X
ncl	E9QB18;B8JLQ3;F1R6L6	X	X	X	X
epcam	B8JM11		X		X
igbp1	B8JM93	X			
cap1	B8JMD0;Q6YBS2				X
kdf1a	E7F2A2				X
si:dkey-7j14.6	X1WE35;X1WCQ0;E7FD05	X			
ddx6;si:ch211-175g6.7	E7FD91;E7F1G8	X			
mrpl18	E9QDQ8;F1R1S5	X			
rpl17	E9QHB7;Q7T1K0	X	X	X	X
eno3	E9QJI6;Q6TH14				X
fmr1	F1Q664;F1Q663;F1R159		X		
zgc:110800	F1Q7J1				X
eif2s2	F1Q8P7		X		
hspa9	F1QFC0			X	
tpte	F1QG29	X			
si:ch211-226h8.14	F1QJD7	X	X		
zgc:56576	F1QKI4;Q7ZUH1	X			
zgc:114104	F1QKW1				X
adnpa	F1QLG5		X	X	
jupb	F8W4M8;F1QUV8	X			
si:ch211-69g19.2	F1QZD2			X	X
rfc2	F1R0T0		X		
prmt1	F1R3J9	X			
srpk1b	F1REN8		X		X
dvr1	P35621	X			
rpl36a	P61485		X		
rps7	P62084			X	
atp5a1	Q08BA1	X		X	X
rbb4;rbbp4	Q1LXD4;Q6P3H7		X		
rfc5	Q6DRK4		X		
tomm22	Q6IQJ1	X			
rbm4.3	Q6NXC1		X		X
ilf2	Q6NZ06		X		
rtcb	Q6NZS4		X		
rps5	Q6PC80	X			X
cct4	Q6PH46	X		X	
eif3d	Z4YIM6;Q6TH15		X		
zgc:56493	Q7ZUI4	X			
eif3i	Q7ZV55			X	
rpsa	Q803F6;J9JI05			X	
ywhaqb	Q803M8				X
fth1a	Q9DDT0	X			
ca15b	R4GDY8		X		X

6.2 Supplementary materials and methods

Zebrafish

The TE line was used as wildtype *Danio rerio*. For the described Nodal mutants, the *sqt*^{cz35} (Feldman *et al.* 1998) and *cyc*^{m294} (Schier *et al.* 1996) alleles were used. Zebrafish expressing H2A.F/Z-GFP (Pauls *et al.* 2001) are referred to as H2A-GFP line throughout the text. In all experiments, staging (Kimmel 1995) was based on the development of untreated control embryos. The control embryos were taken from the same batch (same sets of parents) as the treated samples.

Embryo medium (250 mg/l Instant Ocean sea salt mix) contained 1 mg/l methylene blue, except when used for confocal imaging. Embryos were dechorionated with pronase (Roche) as described previously (Müller *et al.* 2012, Rogers *et al.* 2015).

Margin transplantations

Donor embryos were obtained from an H2A-GFP incross. TE as well as *sqt*$^{-/-}$*;cyc*$^{-/-}$ host embryos were collected 1 h later. Note that *sqt*$^{-/-}$*;cyc*$^{-/-}$ embryos were obtained by incrossing *sqt*$^{-/-}$*;cyc*$^{-/-}$ germ line mutants (Ciruna *et al.* 2002; germ line transplantations were performed by Patrick Müller and Gary H. Soh). Only H2A-GFP embryos exhibiting strong fluorescence were used as donors. The embryos were transferred to Ringer's solution (116 mM NaCl, 2.9 mM KCl, 1.8 mM $CaCl_2$, 5 mM HEPES pH 7.2) for the margin transplantations. Margin cells were taken from donors around the 30-40% epiboly stage and transplanted into the animal pole of hosts (hosts were around sphere stage) using glass needles with an inner tip diameter of ~80-90 µm. Typically, two margin transplants were derived from each donor embryo (taken from opposing regions). In order to keep the experimental groups as similar as possible, transplantations were performed such that TE and *sqt*$^{-/-}$*;cyc*$^{-/-}$ embryos were used as hosts in an alternating manner. The embryos were kept in Ringer's solution for 30 min at room temperature (RT), transferred to embryo medium at 28°C afterwards and fixed 2 h post-transplantation.

Plasmids

Previously published FLAG-tagged and GFP-tagged zebrafish Nodals and Leftys in the *pCS2* vector were used (Müller *et al.* 2012). *pCS2-lefty1-RFP* and *pCS2-lefty2-RFP* (Rogers 2015) as well as *pCS2-cyclops-RFP* were generated by Katherine W. Rogers and are based on previous fluorescent fusion constructs (Müller *et al.* 2012; see also Montague and Schier 2017 for *pCS2-cyclops-RFP*). *pCS2-squint-mCherry* was kindly provided by Gary H. Soh who generated it based on previous fusion constructs (Müller *et al.* 2012). *pCS2-GFP* contains the GFP coding sequence and was used to make GFP mRNA. The *secGFP* construct was generated by adding the signal sequence of the secreted lectin-encoding *zgc:171717* to the GFP coding sequence by successive PCR with primers #1+#3 and #2+#3 (Supplementary Table 3). Based on this construct, *secGFP-FLAG* was generated by adding a FLAG-

tag-encoding sequence by PCR (primers #2+#4; Supplementary Table 3). Both *secGFP* and *secGFP-FLAG* were cloned into the *pCS2* vector.

In vitro transcription

To generate mRNAs for microinjection, the corresponding *pCS2* vectors were linearized by restriction digestion, purified and used in a 20 µl mMESSAGE mMACHINE SP6 reaction (Invitrogen) according to the manufacturer's instructions.

Microinjections

Approximately 1 nl injection mix, containing 0.1% phenol red (Sigma) and the indicated concentrations of mRNA or Morpholino (see sections below), was injected at the one- to two-cell stage.

Phenotypic analyses

The phenotypes of zebrafish embryos were assessed 1 dpf, between 26 and 30 hpf. If a small fraction of dead embryos was observed in both treated and control embryos, dead embryos were not considered in the phenotype statistics. The phenotype "clump" describes cases where the embryonic tissue exhibits neither recognizable body axis formation nor massive necrosis. Morpholino-injected embryos with necrotic tissue in the head are described as "wildtype*" if their gross morphology is that of a wildtype.

Cyclops-FLAG titration

For the titration of Cyclops-FLAG (Supplementary Figure 6), injection mixes containing 249, 360, 720 or 938 ng/µl *cyclops-FLAG* mRNA were microinjected into zebrafish embryos at the one-cell stage.

Testing Nodal/Lefty secretion at high expression levels

To compare the secretion of Nodals and Leftys at low and high expression levels (Supplementary Figure 7), either low (30 ng/µl) or high mRNA concentrations were injected. For high expression levels, the following mRNA concentrations, which are equimolar to 912 ng/µl *cyclops-FLAG* mRNA, were used: 1064 ng/µl *lefty1-GFP*, 1056 ng/µl *lefty2-GFP*, 1110 ng/µl *sqt-GFP*. For *cyclops-GFP*, the highest possible mRNA concentration (1025 ng/µl) was injected.

Anti-FLAG co-immunoprecipitation (CoIP)

This protocol uses the Anti-FLAG M2 Affinity Gel (Sigma, #A2220) and is based on the product information provided by the manufacturer.

120-180 µl of the original bead slurry (30 µl slurry corresponding to 15 µl resin per sample) were prepared by washing twice with TBS (50 mM Tris, 150 mM NaCl; pH 7.4), once with 0.1 M glycine (pH 3.5) and three times with TBS as described by the manufacturer. The resin was re-suspended in IP

buffer (50 mM Tris, 150 mM NaCl, 1% Triton X-100; pH 7.4; ½ Mini cOmplete EDTA-free protease inhibitor pill (Roche) was added per 10 ml) afterwards.

Dechorionated zebrafish embryos were transferred to 1.5 ml reaction tubes when control embryos were around sphere stage (4 hpf; Kimmel *et al.* 1995). They were lysed by pipetting ten times with a 200 µl pipette in cold IP buffer (typically 230 µl IP buffer were used to lyse embryos). All following steps were performed at 4°C. After removing the input control, IP buffer was added to the lysate such that after addition of the prepared agarose resin the total volume was 1 ml. The tubes were rotated axially at 4°C over night. The samples were centrifuged at 8,200 rcf for 1 min and the supernatant was discarded. 500 µl IP buffer were added to the agarose resin and the agarose was washed by carefully pipetting ten times with a 1 ml pipette. This wash step was repeated two more times. After centrifugation at 8,200 rcf for 1 min, the supernatant was discarded and 50 µl FLAG peptide (100 µg/ml in TBS, Sigma, #F3290) were added to the agarose. The samples were rotated axially at 4°C for 30 min, centrifuged at 8,200 rcf for 1 min and the supernatant was saved as eluate. The elution step was repeated with 50 µl FLAG peptide; the eluates were combined and dried in a speedvac concentrator before addition of SDS-PAGE loading buffer.

Sqt-FLAG/Oep-GFP CoIP with crosslinking

Zebrafish embryos were injected at the one-cell stage with approximately 1 nl of a mix containing 100 ng/µl *sqt-FLAG* mRNA and 100 ng/µl *oep-GFP* mRNA (sample) or 100 ng/µl *sqt-FLAG* mRNA and 100 ng/µl *secGFP* mRNA (negative control). 500 mM formaldehyde stock solution was prepared by dissolving 750 mg paraformaldehyde in 50 ml water at 85°C over night (Nadeau and Carlson 2007). 57 dechorionated embryos from each sample were transferred to 1.5 ml reaction tubes and 100 µl crosslinking buffer (50 mM HEPES, 116 mM NaCl, 2.9 mM KCl, 1.8 mM $CaCl_2$; pH 7.2) containing 1:20 formaldehyde stock solution or 1:20 water (negative control) were added. The tubes were incubated at 28°C for 30 min. 800 µl IP buffer were added and the embryos were lysed by pipetting. After quenching the crosslinking reaction at 37°C for 30 min, the lysate was used for anti-FLAG CoIP. Note that 20% of the lysate were used as input sample and were precipitated with acetone (Fic *et al.* 2010) before addition of SDS-PAGE loading buffer. Instead of eluting the proteins after the CoIP, 25 µl SDS-PAGE loading buffer were added to the agarose resin. All samples were boiled at 99°C for 20 min and vortexed before using them in SDS-PAGE.

CoIP for MS

mRNAs encoding FLAG-tagged Nodals/Leftys or secGFP-FLAG were injected at concentrations equimolar to 1000 ng/µl *cyclops-FLAG* mRNA. From each sample, 82 embryos were used for CoIP (without crosslinking) as described above.

SDS-PAGE, silver staining and western blot

For silver staining, proteins were separated on 4-15% Mini-PROTEAN TGX Stain-Free gels (Bio-Rad) and the Pierce Silver Stain Kit (Thermo Scientific) was used according to the manual.

For western blotting, embryos were deyolked manually around sphere stage (4 hpf), rinsed in embryo medium and lyzed by vortexing in SDS-PAGE loading buffer. Proteins were separated on 4-15% TGX Mini-PROTEAN TGX Stain-Free gels (Bio-Rad; Supplementary Figure 8) or home-made 10% (Figure 11) or 12% (Supplementary Figure 6) SDS-PAGE gels. Western blotting was performed in principle as in Almuedo-Castillo *et al.* (2018). The primary anti-GFP antibody (Life Technologies, A11122; dilution 1:5,000) was used with the secondary, peroxidase-conjugated AffiniPure anti-rabbit IgG antibody (Jackson ImmunoResearch, #111-035-003; dilution 1:10,000). The anti-FLAG M2 antibody (Sigma, #F3165; dilution 1:5,000) was used with the peroxidase-conjugated, secondary AffiniPure anti-mouse IgG antibody (Jackson ImmunoResearch, 715-035-150; dilution 1:10,000).

Mass spectrometry (MS)

In order to account for variability in unspecific binding between experiments, two secGFP-FLAG CoIP samples were analyzed.

Silver stained protein gels (Supplementary Figure 9) were submitted to the Proteome Center at the University of Tübingen for MS analysis. In brief, the following steps were performed. The gels were digested with trypsin (Borchert *et al.* 2010) and the peptides desalted with C_{18} StageTips (Rappsilber *et al.* 2007). After extracting the peptides, they were separated on an EASY-nLC 1200 System coupled to a Q Exactive HF mass spectrometer (Thermo Scientific) as in Kliza *et al.* (2017), with the following modifications: A 57 min segmented gradient from 10-33-50-90% solvent B (80% acetonitrile in 0.1% formic acid) in solvent A (0.1% formic acid) and a flow rate of 200 nl/min were used; the seven most intense precursor ions were sequentially fragmented by higher energy collisional dissociation in each scan cycle; for all measurements, the sequenced precursor masses were excluded from further selection for 30 s; target values for MS/MS fragmentation were 10^5 charges and for the MS scan $3 \cdot 10^6$ charges. The resulting spectra were processed using the MaxQuant software (version 1.5.2.8.; Cox and Mann 2008) with Andromeda (Cox *et al.* 2011). The peptides were searched against a target-decoy *Danio rerio* database, which was obtained from UniProt (The UniProt Consortium 2019). It contained 44,355 proteins, the FLAG-tagged bait protein sequences (Squint-FLAG, Cyclops-FLAG, Lefty1-FLAG, Lefty2-FLAG, sec-GFP-FLAG) as well as 285 commonly observed contaminants. Trypsin was defined as endoprotease with a maximum of two missed cleavages. N-terminal acetylation and methionine oxidation were set as variable modifications and cysteine carbamidomethylation was defined as fixed modification. The initial maximum allowed mass tolerance was 4.5 ppm for the survey scan and 20 ppm for the fragmentation by higher energy collisional dissociation. The false discovery rate was set to 1% at both the peptide and the protein level.

Identification of MS candidates

Among the identified proteins, those absent from the two secGFP controls and the uninjected control were considered specific to the Nodal/Lefty CoIPs. Proteins were only counted if at least one peptide with a posterior error probability (PEP; Käll *et al.* 2008) <0.01 was found. The following Gene Ontology (GO) "Cellular Component" terms (Ashburner *et al.* 2000, The Gene Ontology Consortium 2019) were used to identify MS candidates: "extrinsic to membrane" (*jupb*), "intrinsic to membrane" (*vldlr*, *cx43.4*, *si:dkey-7j14.6*), "membrane" (*tpte*, *si:ch211-226h8.14*, *epcam*), "extracellular region" (*dvr1*). *hsp90b1* was considered because it has a predicted signal sequence (Almagro Armenteros *et al.* 2019).

Note that a high number of peptides from the bait proteins were identified in the corresponding samples. Additionally, Nodal/Lefty peptides were identified in the following samples: Squint peptides in the secGFP-FLAG (R11) and Lefty1-FLAG (R13) samples, Lefty1 peptides in the Lefty2-FLAG (R14) sample and Lefty2 peptides in the Cyclops-FLAG (R16) sample. It is unclear, whether this results from cross-sample contamination of the highly abundant bait proteins or represents actual interactions.

Cloning MS candidates

Coding sequences for the MS candidates were either amplified by PCR from wildtype zebrafish cDNA (sphere stage; 4 hpf) or ordered as gBlock gene fragments (IDT; Supplementary Table 2). C-terminal GFP fusions were generated with splicing by overlap extension PCR (Higuchi *et al.* 1988, Ho *et al.* 1989, Heckman and Pease 2007) starting from two fragments (one encoding the MS candidate, one encoding GFP). All constructs were cloned into the *pCS2* vector. The primers that were used for cloning are shown in Supplementary Table 3.

Supplementary Table 2: Sequence information for cloning the MS candidates. *The amplified sequence encodes a protein with an R68C mutation compared to the shown reference.

Gene name	NCBI Reference Sequence	UniProt ID	Source
cx43.4	-	B0UYC0	cDNA
epcam	-	Q568H0*	cDNA
hsp90b1	NM_198210.2	Q7T3L3	cDNA
jupb	XM_002665476.6	-	gBlock
si:ch211-226h8.14	NM_001102392.3	-	cDNA
si:dkey-7j14.6	NM_001199721.1	E7FD05	gBlock
tpte	XM_005155259.4	F1QG29	gBlock
vldlr	NM_200923.2	E7FF13	gBlock

Supplementary Table 3: Primers used for cloning. Note that the *GFP* primers *GFP* R and *GFP* R #2 were used as reverse primers for multiple forward primers (indicated in brackets). frag. = fragment; Restr. = Restriction

#	Sequence	Purpose	Restr. site
1	CATTTTACTGAACTCAAGCCTGCTGATATCAGCGAGTGGTGGACATGGTCATATGGTGAGCAAGGGC	*secGFP* F1	-
2	TCCCATCGATGCGCCACCATGTTCTCTCTCAGTTTAGTGATCACCTTCATTTTACTGAACTCAAG	*secGFP* F2	ClaI
3	GAGGCCTTGAATTCTCACTTGTACAGCTCGTC	*GFP* R (1, 2, 13)	EcoRI
4	GGCCTTGAATTCTCACTTGTCGTCGTCGTCCTTGTAGTCGGAGCCCTTGTACAGCTCGTC	secGFP-FLAG R	EcoRI
5	TTTGCAGGATCCCGCCACCATGTCACTGCAAATGAG	*jupb* F	BamHI
6	GCCTTGAATTCTTAAAGAGGATTTGGATACAC	*jupb* R	EcoRI
7	GCTCACCATAGATCCAAGAGGATTTGGATAC	*jupb-GFP* frag. 1 R	-
8	GTATCCAAATCCTCTTGGATCTATGGTGAGC	*jupb-GFP* frag. 2 F	-
9	GGCCTTGAATTCTTACTTGTACAGCTCGTC	*jupb-GFP* frag. 2 R	EcoRI
10	GATCCCATCGATGCGCCACCATGTTCTCGCTCAGC	*si:ch211-226h8.14* F	ClaI
11	GCCTTGAATTCTCAGCTCCTACGACGTGTGCAGC	*si:ch211-226h8.14* R	EcoRI
12	CTTGCTCACCATGCTCCTACGACGTGTG	*si:ch211-226h8.14* frag. 1 R	-
13	CACACGTCGTAGGAGCATGGTGAGCAAG	*si:ch211-226h8.14* frag. 2 F	-
14	GATCCCATCGATGCGCCACCATGAGGCGGCTGTG	*hsp90b*1 F	ClaI
15	GCCTTGAATTCTTACAGCTCATCTTTGGATGTGGC	*hsp90b*1 R	EcoRI
16	CCCTTGCTCACCATCAGCTCATCTTTGG	*hsp90b*1 frag. 1 R	-
17	CCAAAGATGAGCTGATGGTGAGCAAGGG	*hsp90b*1 frag. 2 F	-
18	GCCTTGAATTCTTACTTGTACAGCTCGTCCATGC	*GFP* R #2 (17, 27, 36)	EcoRI
19	GGCCTCTCGAGGCCACCATGAGCTGGAGTTTTCTTACG	*cx43.4* F	XhoI
20	CTATAGTTCTAGATCAAGCATGGATCCCTTTTTC	*cx43.4* R	XbaI
21	CCTTGCTCACCATAGCATGGATCCCTTTTTC	*cx43.4* frag. 1 R	-
22	GAAAAAGGGATCCATGCTATGGTGAGCAAGG	*cx43.4* frag. 2 F	-
23	CTATAGTTCTAGACTCACTTGTACAGCTCGTC	*cx43.4* frag. 2 R	XbaI
24	GATCCCATCGATGCGCCACCATGAAGGTTTTAGTTGCC	*epcam* F	ClaI
25	GCCTTGAATTCTTAAGAAATTGTCTCCATCTCTCTGGC	*epcam* R	EcoRI
26	GCCCTTGCTCACCATAGAAATTGTCTCCATCTC	*epcam* frag. 1 R	-
27	GAGATGGAGACAATTTCTATGGTGAGCAAGGGC	*epcam* frag. 2 F	-
28	GATTCGAATTCGCCACCATGGTCAGGTCTATG	*vldlr* F	EcoRI
29	GAGGCTCGAGTTATGACAAGTCATCTTCTGTG	*vldlr* R	XhoI
30	GCCCTTGCTCACCATTGACAAGTCATCTTCTG	*vldlr* frag. 1 R	-
31	CAGAAGATGACTTGTCAATGGTGAGCAAGGGC	*vldlr* frag. 2 F	-
32	GAGGCTCGAGTTACTTGTACAGCTCGTC	*vldlr* frag. 2 R	XhoI
33	GATCCCATCGATGCGCCACCATGGCCTCTTCAATGACTAC	*si:dkey-7j14.6* F	ClaI
34	GCCTTGAATTCTTAAGAGCTGGAGATGGAATCCAG	*si:dkey-7j14.6* R	EcoRI
35	GCCCTTGCTCACCATAGAGCTGGAGATGGAATC	*si:dkey-7j14.6* frag. 1 R	-
36	GATTCCATCTCCAGCTCTATGGTGAGCAAGGGC	*si:dkey-7j14.6* frag. 2 F	-
37	GATTCGAATTCGCCACCATGACGTCTGTGCATTTTAAC	*tpte* F	EcoRI
38	GAGGCTCGAGTCAAGGCTCAGTGAAAGACAGCGTC	*tpte* R	XhoI
39	GCCCTTGCTCACCATAGGCTCAGTGAAAGAC	*tpte* frag. 1 R	-
40	GTCTTTCACTGAGCCTATGGTGAGCAAGGGC	*tpte* frag. 2 F	-
41	GAGGCTCGAGTCACTTGTACAGCTCGTCCATGC	*tpte* frag. 2 R	XhoI

Co-expression of GFP-tagged MS candidates with fluorescently-labeled Nodals/Leftys

To test for co-localization of GFP-tagged MS candidates with fluorescently-labeled Nodals/Leftys the injection mixes contained 250 ng/µl mRNA encoding the GFP-tagged MS candidate. mRNAs encoding fluorescent Nodals/Leftys were included in the mixes at the following concentrations: 250 ng/µl *squint-mCherry*, 60 ng/µl *cyclops-RFP*, 60 ng/µl *lefty1-RFP* or 60 ng/µl *lefty2-RFP*.

MS candidate overexpression for phenotypic analysis

mRNAs encoding untagged MS candidates were injected at 50 or 250 ng/µl for total amounts of 50 or 250 pg, respectively.

Fixation

At the indicated time points, the embryos were transferred to 2 ml reaction tubes with PBS (137 mM NaCl, 2.7 mM KCl, 10 mM Na_2HPO_4, 1.8 mM KH_2PO_4; pH 7.4) containing 4% formaldehyde and fixed at 4°C over night. The fixative was removed and the following wash steps were performed by shaking (back-and-forth) for 5 min at RT each: PBS, PBS-T (PBS containing 0.1% Tween 20), PBS-T:methanol (50:50), methanol, methanol. Fresh methanol was added and the embryos were stored at -20°C up to two months.

Digoxigenin-labeled RNA probes

The plasmid for the *gsc* probe (Müller *et al.* 2012) was linearized by restriction digest with EcoRI. This template was purified and used in a 20 µl T7 RNA Polymerase (Roche) reaction containing 2 µl enzyme, 2 µl DIG RNA Labeling Mix (Roche) and 1 µl RNase inhibitor (Applied Biosystems). After addition of 2 µl DNaseI (Roche) and 15 min incubation at 37°C, the RNA probe was purified with RNeasy Columns (Qiagen). It was diluted to 100 ng/µl with prehybridization solution (50% deionized formamide, 5X SSC (diluted from 20X UltraPure SSC; Invitrogen), 0.5 mg/ml RNA from torula yeast (Sigma), 50 µg/ml heparin, 0.1% Tween 20; in nuclease-free water) containing 5% dextran sulfate and stored at -20°C.

goosecoid Fluorescence in situ hybridization (FISH) followed by pSmad2/3 immunofluorescence

Approximately 20-30 fixed embryos were used per sample. *In situ* hybridization was performed in an InsituPro VSi robot (Intavis), similar to published protocols (Thisse and Thisse 2008, Almuedo-Castillo *et al.* 2018). For every wash/incubation step, 250 µl solution were used and the incubation temperature was RT if not mentioned otherwise.

The samples were washed in 70%, 50% and 30% methanol mixtures with PBS-T for 10 min each. After washing the samples six times for 10 min with PBS-T, they were incubated with PBS-T containing 4% formaldehyde for 30 min. The samples were rinsed with PBS-T; they were then washed four times with PBS-T for 10 min. After 1 h incubation with prehybridization solution at 70°C, the solution was replaced and the samples were incubated for another hour at 70°C. The samples were incubated with the RNA probes (1 ng/µl in prehybridization solution; heated to 80°C for 15 min before use) for 16 h at 70°C and then washed with posthybridization solution (50% deionized formamide, 5X SSC, 0.1% Tween 20; in nuclease-free water) at 70°C for 10 min. The following dilutions of posthybridization solution in 2X SSC were used for 15 min wash steps at 70°C: 75%, 50% and 25% posthybridization solution. The samples were washed three times in 2X SSC and three times in 0.2X SSC for 15 min at 70°C each. After cooling to RT, the samples were washed with the following dilutions of 0.2X SSC in

PBS-T for 15 min each: 75%, 50% and 25% 0.2X SSC. After two 15 min PBS-T washes the samples were removed from the robot and transferred to 2 ml reaction tubes containing PBS-T.

The staining procedure was performed manually and all following wash steps were performed by shaking the samples back-and-forth at RT. The PBS-T was replaced with 300 µl FISH blocking solution (2% blocking reagent (Roche) in MABTw (150 mM maleic acid, 100 mM NaCl, 0.1% Tween 20; pH 7.5)) and the samples were kept shaking for 2 h at RT. After removing the blocking solution, 200 µl of a 1:100 dilution of Anti-Digoxigenin-POD (Roche, #11207733910) in FISH blocking solution were added and the samples were kept shaking at 4°C over night. PBS-T was added to ~1.5 ml and removed right away. The samples were washed with ~1.5 ml PBS-T six times for 20 min each. The PBS-T was removed and 100 µl TSA Plus Working Solution containing 1:75 Cyanine 3 TSA Plus Stock Solution (Perkin Elmer) were added. The tubes were gently flicked and incubated for 45 min at RT in the dark (no shaking). To protect the samples from light, they were wrapped in aluminum foil for all following incubation steps. The samples were rinsed briefly by addition of PBS-T to ~1.5 ml. The solution was removed right away and the samples were washed for three times 10 min with ~1.5 ml PBS-T. After removing the PBS-T, the samples were briefly rinsed with quench solution (0.1 M glycine; pH 2.2). Fresh quench solution was added (~1.25 ml) and the samples were incubated for 30 min at RT (no shaking). After removal of the quench solution, the samples were rinsed with ~1.5 ml PBS-T. They were then washed with ~1.5 ml PBS-T for three times 10 min.

The pSmad2/3 immunofluorescence staining was performed as described below with the modification that the samples were washed in PBS-T six times for 20 min each after the incubation with anti-pSmad2/3 antibody. After the amplification reaction that visualizes the pSmad2/3 signal, the samples were washed five times with PBS-T for 20 min each and stored in PBS-T containing 1 mg/l DAPI at 4°C until they were imaged by lightsheet microscopy.

pSmad2/3 and GFP immunofluorescence

Fixed embryos (approximately 20-30) or FISH samples were transferred to a 2 ml reaction tube containing ice-cold acetone and kept at -20°C for 20 min. The acetone was removed and the samples were washed three times for 5 min with PBS-T. ~1.5 ml PBS-T were used for this and all following washes. If not stated otherwise, the wash and incubation steps were performed shaking (back-and-forth) at RT. After washing, the samples were incubated with 500 µl IF blocking solution (10% fetal bovine serum in PBS-T) for 1 h. The blocking solution was removed and replaced with 500 µl of a 1:5,000 dilution of anti-phospho-Smad2 (Ser465/467)/Smad3 (Ser423/425) antibody (Cell Signaling, #8828) in IF blocking solution. The samples were shaken (back-and-forth) at 4°C over night. To briefly rinse the samples, PBS-T was added to ~1.5 ml PBS-T and removed right away. The samples were washed eight times for 15 min each. They were then incubated with 500 µl IF blocking solution for 1 h. After removing the blocking solution, the samples were incubated with a 1:500 dilution of peroxidase-conjugated AffiniPure anti-rabbit IgG antibody (Jackson ImmunoResearch, #111-035-003) in IF

blocking solution, shaking at 4°C over night. The samples were rinsed briefly by adding PBS-T to ~1.5 ml and removing it right away. They were then washed six times for 20 min each. The PBS-T was removed and 100 µl TSA Plus working solution containing 1:75 Fluorescein TSA Plus Stock Solution (Perkin Elmer) were added. After gentle flicking of the tubes they were incubated for 45 min in the dark (no shaking). The samples were wrapped in aluminum foil for all following incubation steps. PBS-T was added to ~1.5 ml for a brief rinse and the samples were washed four times for 10 min each.

The PBS-T was removed, 500 µl IF blocking solution were added and the samples were incubated for 1 h. After removing the IF blocking solution, 500 µl IF blocking solution containing 1:1,000 anti-GFP antibody (Aves Labs, #GFP-1020) were added and the samples were shaken (back-and-forth) at 4°C over night. PBS-T was added to ~1.5 ml and the solution was removed right away. The samples were washed six times for 20 min each before blocking with 500 µl IF blocking solution for 1.5 h. The blocking solution was removed and a 1:500 dilution of Alexa Fluor 568-conjugated anti-chicken IgY (abcam 175477) in IF blocking solution was added to the samples which were then kept shaking at 4°C over night. PBS-T was added to ~1.5 ml to briefly rinse the samples and the samples were then washed twelve times for approximately 20 min each. They were stored in PBS-T containing 1 mg/l DAPI at 4°C until imaging by lightsheet microscopy.

Overexpression of MS candidates to test effects on Nodal signaling by FISH/immunofluorescence

mRNAs encoding untagged MS candidates or GFP were injected at a concentration of 250 ng/µl. *squint-FLAG* mRNA (positive control) was injected at a concentration of 50 ng/µl. *sqt*$^{-/-}$ control embryos were obtained from a *sqt*$^{-/-}$ incross. All embryos were fixed when the uninjected controls were at shield stage (6 hpf).

Morpholinos

Morpholinos were ordered from Gene Tools, LLC and diluted to1 mM stocks with water. Morpholino sequences are given in Supplementary Table 4. For microinjections, the Morpholinos were diluted to concentrations between 0.4 and 4 µg/µl, depending on the final dose as indicated.

Supplementary Table 4: Morpholino sequences.

Name	Target	Sequence	Target specifics
MO1	*si:ch211-226h8.14*	AAGCTGAGCGAGAACATGATTCTGC	Start codon
MO2	*si:ch211-226h8.14*	ACCCAAAAAGAAACTCACAGGTGAA	Exon1-Intron1
MO3	*si:ch211-226h8.14*	AGGTCTGTTAAATCCATACCATGAT	Exon4-Intron4

Widefield imaging of zebrafish embryos

To image the phenotypes of zebrafish embryos 1 dpf, they were mounted in 2% methylcellulose (in embryo medium). Images were acquired with an Axio Zoom.V16 (Zeiss) and a PlanNeoFluar Z 1x/0.25 objective. The white balance was auto-adjusted to the background for each sample.

Lightsheet microscopy

FISH and/or immunofluorescence samples were imaged on a Lightsheet Z.1 (Zeiss) with a W Plan-Apochromat 20x/1.0 objective. The samples were mounted in 1.5% NuSieve GTG Agarose (Lonza; in embryo medium) and imaged in water. All samples and controls from one experiment were imaged within the same day to ensure comparable fluorescence between embryos.

To image embryos after margin transplantations and immunofluorescence staining, the embryos were mounted with the animal-vegetal axis orthogonal to the agarose column. Z-stacks over 130 µm from the animal pole were acquired (10 µm steps; 13 slices) and maximum intensity projections over 110 µm (ignoring the two animal-most slices) were generated using Fiji (Schindelin *et al.* 2012). The outline of the transplants was drawn around cells that exhibited immunofluorescence signal for GFP. To measure pSmad2/3 intensities (Supplementary Figure 1), a circular region of interest was used to measure the mean pSmad2/3 immunofluorescence signal inside of the transplant. The shape and size of the region of interest was the same for all images.

To acquire dorsal and lateral views of embryos after MS candidate overexpression (FISH and immunofluorescence), they were mounted with the animal-vegetal axis parallel to the agarose column. The side with highest *gsc* FISH intensity was defined as the dorsal side. In the Jupb overexpression sample with distributed *gsc* signal around the margin, a part with strong *gsc* signal was defined as the dorsal side. In the *squint-FLAG* overexpression sample, where the *gsc* signal is homogenous throughout the embryo, a random side was defined as dorsal. For the acquisition of lateral views, the sample was rotated +90° with respect to the dorsal view. Z-stacks were acquired over 300 µm from the embryo surface (15 µm steps; 20 slices) and maximum intensity projections were generated using Fiji (Schindelin *et al.* 2012).

Confocal microscopy

Live zebrafish embryos were mounted in glass bottom dishes as described previously (Mörsdorf and Müller 2019), when uninjected controls were around sphere stage (4 hpf). An LSM 780 NLO (Zeiss) system was used to acquire animal pole views with an LD LCI Plan-Apochromat 25x/0.8 Imm Korr DIC objective. Images were acquired at a depth of approximately 35 µm from the animal pole, if not mentioned otherwise.

Fluorescence recovery after photobleaching (FRAP)

The FRAP experiments with the weak binder presented in Supplementary Figure 3 were performed as described for the morphotrap in Almuedo-Castillo *et al.* (2018).

For the FRAP experiments shown in Figure 20, zebrafish embryos were injected with injection mixes containing 30 ng/µl *squint-GFP* mRNA or 100 ng/µl *cyclops-GFP* mRNA. For co-expression of the secreted lectin, 250 ng/µl *si:ch211-226h8.14* mRNA were included in the injection mix. Embryos were mounted around sphere stage (4 hpf) and FRAP was performed as previously described (Müller *et al.* 2012). PyFRAP (Bläßle *et al.* 2018) was used to analyze the FRAP data. The default settings were used with two exceptions: A mesh with an element size of 25 pixels^3 was generated and the published decay rates of Squint and Cyclops (Müller *et al.* 2012) were used for fitting.

Characterization of additional weak GFP binders

The weak GFP binders that were used in the experiments for Supplementary Figure 5 were cloned using the strategy described in Mörsdorf & Müller 2019. The following binders were used: LaG-6, LaG-17, LaG-29 from Fridy *et al.* (2014) and PD-GBP-1, PD-GBP-2, PD-GBP-5 as well as PD-GBP-6 from Pellis *et al.* (2012).

The experiments testing the effects of the weak GFP binders on Lefty1-GFP activity (Supplementary Figures 4&5) were performed as the corresponding experiments in Almuedo-Castillo *et al.* (2018).

Statistics

Standard deviations are reported as errors.

7. References

Agathon A., Thisse C. and Thisse B. (2003). "The molecular nature of the zebrafish tail organizer." *Nature* **424**(6947): 448-452.

Alexandre C., Baena-Lopez A. and Vincent J. P. (2014). "Patterning and growth control by membrane-tethered Wingless." *Nature* **505**(7482): 180-185.

Almagro Armenteros J. J., Tsirigos K. D., Sønderby C. K., Petersen T. N., Winther O., Brunak S., von Heijne G. and Nielsen H. (2019). "SignalP 5.0 improves signal peptide predictions using deep neural networks." *Nat Biotechnol* **37**(4): 420-423.

Almuedo-Castillo M., Bläßle A., Mörsdorf D., Marcon L., Soh G. H., Rogers K. W., Schier A. F. and Müller P. (2018). "Scale-invariant patterning by size-dependent inhibition of Nodal signalling." *Nat Cell Biol* **20**(9): 1032-1042.

Andres J. L., Rönnstrand L., Cheifetz S. and Massagué J. (1991). "Purification of the transforming growth factor-β (TGF-β) binding proteoglycan betaglycan." *J Biol Chem* **266**(34): 23282-23287.

Annes J. P., Chen Y., Munger J. S. and Rifkin D. B. (2004). "Integrin $\alpha V\beta_6$-mediated activation of latent TGF-β requires the latent TGF-β binding protein-1." *J Cell Biol* **165**(5): 723-734.

Ashburner M., Ball C. A., Blake J. A., Botstein D., Butler H., Cherry J. M., Davis A. P., Dolinski K., Dwight S. S., Eppig J. T., Harris M. A., Hill D. P., Issel-Tarver L., Kasarskis A., Lewis S., Matese J. C., Richardson J. E., Ringwald M., Rubin G. M. and Sherlock G. (2000). "Gene ontology: tool for the unification of biology. The Gene Ontology Consortium." *Nat Genet* **25**(1): 25-29.

Baeg G. H. and Perrimon N. (2000). "Functional binding of secreted molecules to heparan sulfate proteoglycans in Drosophila." *Curr Opin Cell Biol* **12**(5): 575-580.

Belenkaya T. Y., Han C., Yan D., Opoka R. J., Khodoun M., Liu H. and Lin X. (2004). "Drosophila Dpp morphogen movement is independent of dynamin-mediated endocytosis but regulated by the glypican members of heparan sulfate proteoglycans." *Cell* **119**(2): 231-244.

Benham A. M. (2012). "Protein secretion and the endoplasmic reticulum." *Cold Spring Harb Perspect Biol* **4**(8): a012872.

Bennett J. T., Joubin K., Cheng S., Aanstad P., Herwig R., Clark M., Lehrach H. and Schier A. F. (2007a). "Nodal signaling activates differentiation genes during zebrafish gastrulation." *Dev Biol* **304**(2): 525-540.

Bennett J. T., Stickney H. L., Choi W. Y., Ciruna B., Talbot W. S. and Schier A. F. (2007b). "Maternal nodal and zebrafish embryogenesis." *Nature* **450**(7167): E1-2.

Bier E. and De Robertis E. M. (2015). "Embryo development. BMP gradients: A paradigm for morphogen-mediated developmental patterning." *Science* **348**(6242): aaa5838.

Bilandzic M. and Stenvers K. L. (2011). "Betaglycan: a multifunctional accessory." *Mol Cell Endocrinol* **339**(1-2): 180-189.

Bill B. R., Petzold A. M., Clark K. J., Schimmenti L. A. and Ekker S. C. (2009). "A primer for morpholino use in zebrafish." *Zebrafish* **6**(1): 69-77.

Bisgrove B. W., Su Y. C. and Yost H. J. (2017). "Maternal Gdf3 is an obligatory cofactor in Nodal signaling for embryonic axis formation in zebrafish." *Elife* **6**: e28534.

Bläßle A., Soh G., Braun T., Mörsdorf D., Preiss H., Jordan B. M. and Müller P. (2018). "Quantitative diffusion measurements using the open-source software PyFRAP." *Nat Commun* **9**(1): 1582.

Blum M., De Robertis E. M., Wallingford J. B. and Niehrs C. (2015). "Morpholinos: antisense and sensibility." *Dev Cell* **35**(2): 145-149.

Bökel C. and Brand M. (2013). "Generation and interpretation of FGF morphogen gradients in vertebrates." *Curr Opin Genet Dev* **23**(4): 415-422.

Borchert N., Dieterich C., Krug K., Schütz W., Jung S., Nordheim A., Sommer R. J. and Macek B. (2010). "Proteogenomics of Pristionchus pacificus reveals distinct proteome structure of nematode models." *Genome Res* **20**(6): 837-846.

Brivanlou A. H. and Darnell J. E., Jr. (2002). "Signal transduction and the control of gene expression." *Science* **295**(5556): 813-818.

Broussard A. C. and Boyce M. (2019). "Life is sweet: the cell biology of glycoconjugates." *Mol Biol Cell* **30**(5): 525-529.

Carrero G., McDonald D., Crawford E., de Vries G. and Hendzel M. J. (2003). "Using FRAP and mathematical modeling to determine the in vivo kinetics of nuclear proteins." *Methods* **29**(1): 14-28.

Chen C. and Shen M. M. (2004). "Two modes by which Lefty proteins inhibit nodal signaling." *Curr Biol* **14**(7): 618-624.

Chen Y. and Schier A. F. (2001). "The zebrafish Nodal signal Squint functions as a morphogen." *Nature* **411**(6837): 607-610.

Chen Y. and Schier A. F. (2002). "Lefty proteins are long-range inhibitors of squint-mediated nodal signaling." *Curr Biol* **12**(24): 2124-2128.

Cheng S. K., Olale F., Brivanlou A. H. and Schier A. F. (2004). "Lefty blocks a subset of TGFβ signals by antagonizing EGF-CFC coreceptors." *PLoS Biol* **2**(2): e30.

Ciruna B., Weidinger G., Knaut H., Thisse B., Thisse C., Raz E. and Schier A. F. (2002). "Production of maternal-zygotic mutant zebrafish by germ-line replacement." *Proc Natl Acad Sci U S A* **99**(23): 14919-14924.

Constam D. B. (2014). "Regulation of TGFβ and related signals by precursor processing." *Semin Cell Dev Biol* **32**: 85-97.

Cox J. and Mann M. (2008). "MaxQuant enables high peptide identification rates, individualized p.p.b.-range mass accuracies and proteome-wide protein quantification." *Nat Biotechnol* **26**(12): 1367-1372.

Cox J., Neuhauser N., Michalski A., Scheltema R. A., Olsen J. V. and Mann M. (2011). "Andromeda: a peptide search engine integrated into the MaxQuant environment." *J Proteome Res* **10**(4): 1794-1805.

Crank J. (1975). "The mathematics of diffusion." Oxford, Oxford University Press.

Crick F. (1970). "Diffusion in embryogenesis." *Nature* **225**(5231): 420-422.

de Boer T. P. and van der Heyden M. A. (2005). "Xenopus connexins: how frogs bridge the gap." *Differentiation* **73**(7): 330-340.

Derynck R. and Budi E. H. (2019). "Specificity, versatility, and control of TGF-β family signaling." *Sci Signal* **12**(570): eaav5183.

Di Donato V., De Santis F., Albadri S., Auer T. O., Duroure K., Charpentier M., Concordet J. P., Gebhardt C. and Del Bene F. (2018). "An attractive Reelin gradient establishes synaptic lamination in the vertebrate visual system." *Neuron* **97**(5): 1049-1062.

Dick A., Mayr T., Bauer H., Meier A. and Hammerschmidt M. (2000). "Cloning and characterization of zebrafish smad2, smad3 and smad4." *Gene* **246**(1-2): 69-80.

Dougan S. T., Warga R. M., Kane D. A., Schier A. F. and Talbot W. S. (2003). "The role of the zebrafish nodal-related genes squint and cyclops in patterning of mesendoderm." *Development* **130**(9): 1837-1851.

Downward J. (2001). "The ins and outs of signalling." *Nature* **411**(6839): 759-762.

Draper B. W., Morcos P. A. and Kimmel C. B. (2001). "Inhibition of zebrafish fgf8 pre-mRNA splicing with morpholino oligos: a quantifiable method for gene knockdown." *Genesis* **30**(3): 154-156.

Driever W. and Nüsslein-Volhard C. (1988). "The bicoid protein determines position in the Drosophila embryo in a concentration-dependent manner." *Cell* **54**(1): 95-104.

Dubrulle J., Jordan B. M., Akhmetova L., Farrell J. A., Kim S. H., Solnica-Krezel L. and Schier A. F. (2015). “Response to Nodal morphogen gradient is determined by the kinetics of target gene induction.” *Elife* **4**: e05042.

Dunn K. W., Kamocka M. M. and McDonald J. H. (2011). “A practical guide to evaluating colocalization in biological microscopy.” *Am J Physiol Cell Physiol* **300**(4): C723-742.

Eisen J. S. and Smith J. C. (2008). “Controlling morpholino experiments: don't stop making antisense.” *Development* **135**(10): 1735-1743.

Eldar A., Rosin D., Shilo B. Z. and Barkai N. (2003). “Self-enhanced ligand degradation underlies robustness of morphogen gradients.” *Dev Cell* **5**(4): 635-646.

Elson E. L. and Magde D. (1974). “Fluorescence correlation spectroscopy. I. Conceptual basis and theory.” *Biopolymers* **13**(1): 1-27.

Eon Kuek L., Leffler M., Mackay G. A. and Hulett M. D. (2016). “The MS4A family: counting past 1, 2 and 3.” *Immunol Cell Biol* **94**(1): 11-23.

Essner J. J., Laing J. G., Beyer E. C., Johnson R. G. and Hackett P. B., Jr. (1996). “Expression of zebrafish connexin43.4 in the notochord and tail bud of wild-type and mutant no tail embryos.” *Dev Biol* **177**(2): 449-462.

Fan X., Hagos E. G., Xu B., Sias C., Kawakami K., Burdine R. D. and Dougan S. T. (2007). “Nodal signals mediate interactions between the extra-embryonic and embryonic tissues in zebrafish.” *Dev Biol* **310**(2): 363-378.

Feldman B., Concha M. L., Saúde L., Parsons M. J., Adams R. J., Wilson S. W. and Stemple D. L. (2002). “Lefty antagonism of Squint is essential for normal gastrulation.” *Curr Biol* **12**(24): 2129-2135.

Feldman B., Gates M. A., Egan E. S., Dougan S. T., Rennebeck G., Sirotkin H. I., Schier A. F. and Talbot W. S. (1998). “Zebrafish organizer development and germ-layer formation require nodal-related signals.” *Nature* **395**(6698): 181-185.

Fic E., Kedracka-Krok S., Jankowska U., Pirog A. and Dziedzicka-Wasylewska M. (2010). “Comparison of protein precipitation methods for various rat brain structures prior to proteomic analysis.” *Electrophoresis* **31**(21): 3573-3579.

Fridy P. C., Li Y., Keegan S., Thompson M. K., Nudelman I., Scheid J. F., Oeffinger M., Nussenzweig M. C., Fenyö D., Chait B. T. and Rout M. P. (2014). “A robust pipeline for rapid production of versatile nanobody repertoires.” *Nat Methods* **11**(12): 1253-1260.

Fujise M., Takeo S., Kamimura K., Matsuo T., Aigaki T., Izumi S. and Nakato H. (2003). “Dally regulates Dpp morphogen gradient formation in the Drosophila wing.” *Development* **130**(8): 1515-1522.

Gagnon J. A., Valen E., Thyme S. B., Huang P., Akhmetova L., Pauli A., Montague T. G., Zimmerman S., Richter C. and Schier A. F. (2014). “Efficient mutagenesis by Cas9 protein-mediated oligonucleotide insertion and large-scale assessment of single-guide RNAs.” *PLoS One* **9**(5): e98186.

González-Méndez L., Gradilla A. C. and Guerrero I. (2019). “The cytoneme connection: direct long-distance signal transfer during development.” *Development* **146**(9): dev174607.

Gregor T., Bialek W., de Ruyter van Steveninck R. R., Tank D. W. and Wieschaus E. F. (2005). “Diffusion and scaling during early embryonic pattern formation.” *Proc Natl Acad Sci U S A* **102**(51): 18403-18407.

Gritsman K., Zhang J., Cheng S., Heckscher E., Talbot W. S. and Schier A. F. (1999). “The EGF-CFC protein one-eyed pinhead is essential for nodal signaling.” *Cell* **97**(1): 121-132.

Guiot E., Enescu M., Arrio B., Johannin G., G. R., Tosti S., Tfibel F., Mérola F., Brun A., Georges P. and P. F.-A. M. (2000). “Molecular dynamics of biological probes by fluorescence correlation microscopy with two-photon excitation.” *Journal of Fluorescence* **10**(4): 413-419.

Gupta M. and Brand M. (2013). “Identification and expression analysis of zebrafish glypicans during embryonic development.” *PLoS One* **8**(11): e80824.

Gurdon J. B., Standley H., Dyson S., Butler K., Langon T., Ryan K., Stennard F., Shimizu K. and Zorn A. (1999). “Single cells can sense their position in a morphogen gradient.” *Development* **126**(23): 5309-5317.

Häcker U., Nybakken K. and Perrimon N. (2005). “Heparan sulphate proteoglycans: the sweet side of development.” *Nat Rev Mol Cell Biol* **6**(7): 530-541.

Harland R. and Gerhart J. (1997). “Formation and function of Spemann's organizer.” *Annu Rev Cell Dev Biol* **13**: 611-667.

Harmansa S., Alborelli I., Bieli D., Caussinus E. and Affolter M. (2017). “A nanobody-based toolset to investigate the role of protein localization and dispersal in Drosophila.” *Elife* **6**: e22549.

Harmansa S., Hamaratoglu F., Affolter M. and Caussinus E. (2015). “Dpp spreading is required for medial but not for lateral wing disc growth.” *Nature* **527**(7578): 317-322.

Harvey S. A. and Smith J. C. (2009). “Visualisation and quantification of morphogen gradient formation in the zebrafish.” *PLoS Biol* **7**(5): e1000101.

Hatler J. M., Essner J. J. and Johnson R. G. (2009). “A gap junction connexin is required in the vertebrate left-right organizer.” *Dev Biol* **336**(2): 183-191.

Heckman K. L. and Pease L. R. (2007). “Gene splicing and mutagenesis by PCR-driven overlap extension.” *Nat Protoc* **2**(4): 924-932.

Heisenberg C. P., Houart C., Take-Uchi M., Rauch G. J., Young N., Coutinho P., Masai I., Caneparo L., Concha M. L., Geisler R., Dale T. C., Wilson S. W. and Stemple D. L. (2001). “A mutation in the Gsk3-binding domain of zebrafish Masterblind/Axin1 leads to a fate transformation of telencephalon and eyes to diencephalon.” *Genes Dev* **15**(11): 1427-1434.

Higuchi R., Krummel B. and Saiki R. K. (1988). “A general method of in vitro preparation and specific mutagenesis of DNA fragments: study of protein and DNA interactions.” *Nucleic Acids Res* **16**(15): 7351-7367.

Hill C. S. (2018). “Spatial and temporal control of NODAL signaling.” *Curr Opin Cell Biol* **51**: 50-57.

Hill C. S. and Treisman R. (1995). “Transcriptional regulation by extracellular signals: mechanisms and specificity.” *Cell* **80**(2): 199-211.

Ho S. N., Hunt H. D., Horton R. M., Pullen J. K. and Pease L. R. (1989). “Site-directed mutagenesis by overlap extension using the polymerase chain reaction.” *Gene* **77**(1): 51-59.

Imai H., Oomiya Y., Kikkawa S., Shoji W., Hibi M., Terashima T. and Katsuyama Y. (2012). “Dynamic changes in the gene expression of zebrafish Reelin receptors during embryogenesis and hatching period.” *Dev Growth Differ* **54**(2): 253-263.

Jessen J. R., Topczewski J., Bingham S., Sepich D. S., Marlow F., Chandrasekhar A. and Solnica-Krezel L. (2002). “Zebrafish trilobite identifies new roles for Strabismus in gastrulation and neuronal movements.” *Nat Cell Biol* **4**(8): 610-615.

Jia S., Ren Z., Li X., Zheng Y. and Meng A. (2008). “smad2 and smad3 are required for mesendoderm induction by Transforming Growth Factor-β/Nodal signals in zebrafish.” *J Biol Chem* **283**(4): 2418-2426.

Jiang J. and Hui C. C. (2008). “Hedgehog signaling in development and cancer.” *Dev Cell* **15**(6): 801-812.

Jing X. H., Zhou S. M., Wang W. Q. and Chen Y. (2006). “Mechanisms underlying long- and short-range nodal signaling in Zebrafish.” *Mech Dev* **123**(5): 388-394.

Jones C. M., Armes N. and Smith J. C. (1996). “Signalling by TGF-β family members: short-range effects of Xnr-2 and BMP-4 contrast with the long-range effects of activin.” *Curr Biol* **6**(11): 1468-1475.

Käll L., Storey J. D., MacCoss M. J. and Noble W. S. (2008). “Posterior error probabilities and false discovery rates: two sides of the same coin.” *J Proteome Res* **7**(1): 40-44.

Karnovsky A. and Klymkowsky M. W. (1995). “Anterior axis duplication in Xenopus induced by the over-expression of the cadherin-binding protein plakoglobin.” *Proc Natl Acad Sci U S A* **92**(10): 4522-4526.

Kerszberg M. and Wolpert L. (1998). “Mechanisms for positional signalling by morphogen transport: a theoretical study.” *J Theor Biol* **191**(1): 103-114.

Kicheva A., Pantazis P., Bollenbach T., Kalaidzidis Y., Bittig T., Jülicher F. and González-Gaitán M. (2007). “Kinetics of morphogen gradient formation.” *Science* **315**(5811): 521-525.

Kim C. H., Oda T., Itoh M., Jiang D., Artinger K. B., Chandrasekharappa S. C., Driever W. and Chitnis A. B. (2000). “Repressor activity of Headless/Tcf3 is essential for vertebrate head formation.” *Nature* **407**(6806): 913-916.

Kimmel C. B., Ballard W. W., Kimmel S. R., Ullmann B. and Schilling T. F. (1995). “Stages of embryonic development of the zebrafish.” *Dev Dyn* **203**(3): 253-310.

Kirchhofer A., Helma J., Schmidthals K., Frauer C., Cui S., Karcher A., Pellis M., Muyldermans S., Casas-Delucchi C. S., Cardoso M. C., Leonhardt H., Hopfner K. P. and Rothbauer U. (2010). “Modulation of protein properties in living cells using nanobodies.” *Nat Struct Mol Biol* **17**(1): 133-138.

Kliza K., Taumer C., Pinzuti I., Franz-Wachtel M., Kunzelmann S., Stieglitz B., Macek B. and Husnjak K. (2017). “Internally tagged ubiquitin: a tool to identify linear polyubiquitin-modified proteins by mass spectrometry.” *Nat Methods* **14**(5): 504-512.

Kolligs F. T., Kolligs B., Hajra K. M., Hu G., Tani M., Cho K. R. and Fearon E. R. (2000). “γ-catenin is regulated by the APC tumor suppressor and its oncogenic activity is distinct from that of β-catenin.” *Genes Dev* **14**(11): 1319-1331.

Kondo S. and Miura T. (2010). “Reaction-diffusion model as a framework for understanding biological pattern formation.” *Science* **329**(5999): 1616-1620.

Kornberg T. B. (2019). “Scripting a place in time.” *Dev Biol* **447**(1): 24-27.

Kuechlin S., Schoels M., Slanchev K., Lassmann S., Walz G. and Yakulov T. A. (2017). “EpCAM controls morphogenetic programs during zebrafish pronephros development.” *Biochem Biophys Res Commun* **487**(2): 209-215.

Lander A. D. (2007). “Morpheus unbound: reimagining the morphogen gradient.” *Cell* **128**(2): 245-256.

Lander A. D., Nie Q. and Wan F. Y. (2002). “Do morphogen gradients arise by diffusion?” *Dev Cell* **2**(6): 785-796.

Latimer A. and Jessen J. R. (2010). “Extracellular matrix assembly and organization during zebrafish gastrulation.” *Matrix Biol* **29**(2): 89-96.

Liebman P. A. and Entine G. (1974). “Lateral diffusion of visual pigment in photorecptor disk membranes.” *Science* **185**(4149): 457-459.

Liu B., Staron M., Hong F., Wu B. X., Sun S., Morales C., Crosson C. E., Tomlinson S., Kim I., Wu D. and Li Z. (2013). “Essential roles of grp94 in gut homeostasis via chaperoning canonical Wnt pathway.” *Proc Natl Acad Sci U S A* **110**(17): 6877-6882.

Lobingier B. T., Hüttenhain R., Eichel K., Miller K. B., Ting A. Y., von Zastrow M. and Krogan N. J. (2017). “An approach to spatiotemporally resolve protein interaction networks in living cells.” *Cell* **169**(2): 350-360.

Loomis W. F. (2014). “Cell signaling during development of Dictyostelium.” *Dev Biol* **391**(1): 1-16.

López-Casillas F., Cheifetz S., Doody J., Andres J. L., Lane W. S. and Massagué J. (1991). "Structure and expression of the membrane proteoglycan Betaglycan, a component of the TGF-β receptor system." *Cell* **67**(4): 785-795.

Lu H., Ma J., Yang Y., Shi W. and Luo L. (2013). "EpCAM is an endoderm-specific Wnt derepressor that licenses hepatic development." *Dev Cell* **24**(5): 543-553.

Maeda O., Usami N., Kondo M., Takahashi M., Goto H., Shimokata K., Kusugami K. and Sekido Y. (2004). "Plakoglobin (γ-catenin) has TCF/LEF family-dependent transcriptional activity in β-catenin-deficient cell line." *Oncogene* **23**(4): 964-972.

Magde D., Elson E. L. and Webb W. W. (1974). "Fluorescence correlation spectroscopy. II. An experimental realization." *Biopolymers* **13**(1): 29-61.

Marjoram L. and Wright C. (2011). "Rapid differential transport of Nodal and Lefty on sulfated proteoglycan-rich extracellular matrix regulates left-right asymmetry in Xenopus." *Development* **138**(3): 475-485.

Martin E. D., Moriarty M. A., Byrnes L. and Grealy M. (2009). "Plakoglobin has both structural and signalling roles in zebrafish development." *Dev Biol* **327**(1): 83-96.

Martinez Arias A. and Steventon B. (2018). "On the nature and function of organizers." *Development* **145**(5): dev159525.

Martyn I., Kanno T. Y., Ruzo A., Siggia E. D. and Brivanlou A. H. (2018). "Self-organization of a human organizer by combined Wnt and Nodal signalling." *Nature* **558**(7708): 132-135.

McGough I. J. and Vincent J. P. (2016). "Exosomes in developmental signalling." *Development* **143**(14): 2482-2493.

Meinhardt H. (2009). "Models for the generation and interpretation of gradients." *Cold Spring Harb Perspect Biol* **1**(4): a001362.

Meno C., Gritsman K., Ohishi S., Ohfuji Y., Heckscher E., Mochida K., Shimono A., Kondoh H., Talbot W. S., Robertson E. J., Schier A. F. and Hamada H. (1999). "Mouse Lefty2 and zebrafish antivin are feedback inhibitors of nodal signaling during vertebrate gastrulation." *Mol Cell* **4**(3): 287-298.

Miller J. R. and Moon R. T. (1997). "Analysis of the signaling activities of localization mutants of β-catenin during axis specification in Xenopus." *J Cell Biol* **139**(1): 229-243.

Miura T., Hartmann D., Kinboshi M., Komada M., Ishibashi M. and Shiota K. (2009). "The cyst-branch difference in developing chick lung results from a different morphogen diffusion coefficient." *Mech Dev* **126**(3-4): 160-172.

Mizutani C. M., Nie Q., Wan F. Y., Zhang Y. T., Vilmos P., Sousa-Neves R., Bier E., Marsh J. L. and Lander A. D. (2005). "Formation of the BMP activity gradient in the Drosophila embryo." *Dev Cell* **8**(6): 915-924.

Montague T. G. and Schier A. F. (2017). "Vg1-Nodal heterodimers are the endogenous inducers of mesendoderm." *Elife* **6**: e28183.

Mörsdorf D. and Müller P. (2019). "Tuning protein diffusivity with membrane tethers." *Biochemistry* **58**(3): 177-181.

Moussian B. and Roth S. (2005). "Dorsoventral axis formation in the Drosophila embryo - shaping and transducing a morphogen gradient." *Curr Biol* **15**(21): R887-899.

Müller P., Rogers K. W., Jordan B. M., Lee J. S., Robson D., Ramanathan S. and Schier A. F. (2012). "Differential diffusivity of Nodal and Lefty underlies a reaction-diffusion patterning system." *Science* **336**(6082): 721-724.

Müller P., Rogers K. W., Yu S. R., Brand M. and Schier A. F. (2013). "Morphogen transport." *Development* **140**(8): 1621-1638.

Müller P. and Schier A. F. (2011). “Extracellular movement of signaling molecules.” *Dev Cell* **21**(1): 145-158.

Mullins M. C., Hammerschmidt M., Kane D. A., Odenthal J., Brand M., van Eeden F. J., Furutani-Seiki M., Granato M., Haffter P., Heisenberg C. P., Jiang Y. J., Kelsh R. N. and Nüsslein-Volhard C. (1996). “Genes establishing dorsoventral pattern formation in the zebrafish embryo: the ventral specifying genes.” *Development* **123**: 81-93.

Nadeau O. W. and Carlson G. M. (2007). “Protein interactions captured by chemical cross-linking: one-step cross-linking with formaldehyde.” *CSH Protoc* **2007**(4): prot4634.

Nahmad M. and Lander A. D. (2011). “Spatiotemporal mechanisms of morphogen gradient interpretation.” *Curr Opin Genet Dev* **21**(6): 726-731.

Nellen D., Burke R., Struhl G. and Basler K. (1996). “Direct and long-range action of a DPP morphogen gradient.” *Cell* **85**(3): 357-368.

Ohi Y. and Wright C. V. (2007). “Anteriorward shifting of asymmetric Xnr1 expression and contralateral communication in left-right specification in Xenopus.” *Dev Biol* **301**(2): 447-463.

Olstad E. W., Ringers C., Hansen J. N., Wens A., Brandt C., Wachten D., Yaksi E. and Jurisch-Yaksi N. (2019). “Ciliary beating compartmentalizes cerebrospinal fluid flow in the brain and regulates ventricular development.” *Curr Biol* **29**(2): 229-241.

Ozeki Y., Yokota Y., Kato K. H., Titani K. and Matsui T. (1995). “Developmental expression of D-galactoside-binding lectin in sea urchin (Anthocidaris crassispina) eggs.” *Exp Cell Res* **216**(2): 318-324.

Pani A. M. and Goldstein B. (2018). “Direct visualization of a native Wnt in vivo reveals that a long-range Wnt gradient forms by extracellular dispersal.” *Elife* **7**: e38325.

Pauls S., Geldmacher-Voss B. and Campos-Ortega J. A. (2001). “A zebrafish histone variant H2A.F/Z and a transgenic H2A.F/Z:GFP fusion protein for in vivo studies of embryonic development.” *Dev Genes Evol* **211**(12): 603-610.

Pei W., Williams P. H., Clark M. D., Stemple D. L. and Feldman B. (2007). “Environmental and genetic modifiers of squint penetrance during zebrafish embryogenesis.” *Dev Biol* **308**(2): 368-378.

Pelegri F. and Maischein H. M. (1998). “Function of zebrafish β-catenin and TCF-3 in dorsoventral patterning.” *Mech Dev* **77**(1): 63-74.

Pelliccia J. L., Jindal G. A. and Burdine R. D. (2017). “Gdf3 is required for robust Nodal signaling during germ layer formation and left-right patterning.” *Elife* **6**: e28635.

Pellis M., Pardon E., Zolghadr K., Rothbauer U., Vincke C., Kinne J., Dierynck I., Hertogs K., Leonhardt H., Messens J., Muyldermans S. and Conrath K. (2012). “A bacterial-two-hybrid selection system for one-step isolation of intracellularly functional Nanobodies.” *Arch Biochem Biophys* **526**(2): 114-123.

Petrášek Z. and Schwille P. (2008). “Precise measurement of diffusion coefficients using scanning fluorescence correlation spectroscopy.” *Biophys J* **94**(4): 1437-1448.

Pomreinke A. P., Soh G. H., Rogers K. W., Bergmann J. K., Bläßle A. J. and Müller P. (2017). “Dynamics of BMP signaling and distribution during zebrafish dorsal-ventral patterning.” *Elife* **6**: e25861.

Poo M. M. and Cone R. A. (1973). “Lateral diffusion of phodopsin in Necturus rods.” *Exp Eye Res* **17**(6): 503-510.

Rappsilber J., Mann M. and Ishihama Y. (2007). “Protocol for micro-purification, enrichment, pre-fractionation and storage of peptides for proteomics using StageTips.” *Nat Protoc* **2**(8): 1896-1906.

Rebagliati M. R., Toyama R., Haffter P. and Dawid I. B. (1998). “cyclops encodes a nodal-related factor involved in midline signaling.” *Proc Natl Acad Sci U S A* **95**(17): 9932-9937.

Reeves G. T., Muratov C. B., Schüpbach T. and Shvartsman S. Y. (2006). “Quantitative models of developmental pattern formation.” *Dev Cell* **11**(3): 289-300.

Reilly K. M. and Melton D. A. (1996). “Short-range signaling by candidate morphogens of the TGFβ family and evidence for a relay mechanism of induction.” *Cell* **86**(5): 743-754.

Reisser M., Palmer A., Popp A. P., Jahn C., Weidinger G. and Gebhardt J. C. M. (2018). “Single-molecule imaging correlates decreasing nuclear volume with increasing TF-chromatin associations during zebrafish development.” *Nat Commun* **9**(1): 5218.

Reissmann E., Jörnvall H., Blokzijl A., Andersson O., Chang C., Minchiotti G., Persico M. G., Ibáñez C. F. and Brivanlou A. H. (2001). “The orphan receptor ALK7 and the Activin receptor ALK4 mediate signaling by Nodal proteins during vertebrate development.” *Genes Dev* **15**(15): 2010-2022.

Rodaway A., Takeda H., Koshida S., Broadbent J., Price B., Smith J. C., Patient R. and Holder N. (1999). “Induction of the mesendoderm in the zebrafish germ ring by yolk cell-derived TGF-β family signals and discrimination of mesoderm and endoderm by FGF.” *Development* **126**(14): 3067-3078.

Rodriguez E. A., Campbell R. E., Lin J. Y., Lin M. Z., Miyawaki A., Palmer A. E., Shu X., Zhang J. and Tsien R. Y. (2017). “The growing and glowing toolbox of fluorescent and photoactive proteins.” *Trends Biochem Sci* **42**(2): 111-129.

Rogers K. W. (2015). “Mesendoderm patterning by the Nodal/Lefty activator/inhibitor system.” *Doctoral dissertation, Harvard University, Graduate School of Arts & Sciences*.

Rogers K. W., Bläßle A., Schier A. F. and Müller P. (2015). “Measuring protein stability in living zebrafish embryos using fluorescence decay after photoconversion (FDAP).” *J Vis Exp*(95): 52266.

Rogers K. W., Lord N. D., Gagnon J. A., Pauli A., Zimmerman S., Aksel D. C., Reyon D., Tsai S. Q., Joung J. K. and Schier A. F. (2017). “Nodal patterning without Lefty inhibitory feedback is functional but fragile.” *Elife* **6**: e28785.

Rogers K. W. and Müller P. (2019). “Nodal and BMP dispersal during early zebrafish development.” *Dev Biol* **447**(1): 14-23.

Rogers K. W. and Schier A. F. (2011). “Morphogen gradients: from generation to interpretation.” *Annu Rev Cell Dev Biol* **27**: 377-407.

Ross S. and Hill C. S. (2008). “How the Smads regulate transcription.” *Int J Biochem Cell Biol* **40**(3): 383-408.

Routledge D. and Scholpp S. (2019). “Mechanisms of intercellular Wnt transport.” *Development* **146**(10): dev176073.

Roux K. J., Kim D. I., Raida M. and Burke B. (2012). “A promiscuous biotin ligase fusion protein identifies proximal and interacting proteins in mammalian cells.” *J Cell Biol* **196**(6): 801-810.

Saerens D., Pellis M., Loris R., Pardon E., Dumoulin M., Matagne A., Wyns L., Muyldermans S. and Conrath K. (2005). “Identification of a universal VHH framework to graft non-canonical antigen-binding loops of camel single-domain antibodies.” *J Mol Biol* **352**(3): 597-607.

Sagner A. and Briscoe J. (2017). “Morphogen interpretation: concentration, time, competence, and signaling dynamics.” *Wiley Interdiscip Rev Dev Biol* **6**(4): e271.

Santos E. M., Workman V. L., Paull G. C., Filby A. L., Van Look K. J., Kille P. and Tyler C. R. (2007). “Molecular basis of sex and reproductive status in breeding zebrafish.” *Physiol Genomics* **30**(2): 111-122.

Sasaki H. and Aketa K. (1981). “Purification and distribution of a lectin in sea urchin (Anthocidaris crassispina) egg before and after fertilization.” *Exp Cell Res* **135**(1): 15-19.

Schier A. F. (2003). “Nodal signaling in vertebrate development.” *Annu Rev Cell Dev Biol* **19**: 589-621.

Schier A. F. (2009). “Nodal morphogens.” *Cold Spring Harb Perspect Biol* **1**(5): a003459.

Schier A. F., Neuhauss S. C., Harvey M., Malicki J., Solnica-Krezel L., Stainier D. Y., Zwartkruis F., Abdelilah S., Stemple D. L., Rangini Z., Yang H. and Driever W. (1996). “Mutations affecting the development of the embryonic zebrafish brain.” *Development* **123**: 165-178.

Schier A. F. and Talbot W. S. (2001). “Nodal signaling and the zebrafish organizer.” *Int J Dev Biol* **45**(1): 289-297.

Schier A. F. and Talbot W. S. (2005). “Molecular genetics of axis formation in zebrafish.” *Annu Rev Genet* **39**: 561-613.

Schilling T. F., Nie Q. and Lander A. D. (2012). “Dynamics and precision in retinoic acid morphogen gradients.” *Curr Opin Genet Dev* **22**(6): 562-569.

Schindelin J., Arganda-Carreras I., Frise E., Kaynig V., Longair M., Pietzsch T., Preibisch S., Rueden C., Saalfeld S., Schmid B., Tinevez J. Y., White D. J., Hartenstein V., Eliceiri K., Tomancak P. and Cardona A. (2012). “Fiji: an open-source platform for biological-image analysis.” *Nat Methods* **9**(7): 676-682.

Schwille P., Meyer-Almes F. J. and Rigler R. (1997). “Dual-color fluorescence cross-correlation spectroscopy for multicomponent diffusional analysis in solution.” *Biophys J* **72**(4): 1878-1886.

Sekine R., Shibata T. and Ebisuya M. (2018). “Synthetic mammalian pattern formation driven by differential diffusivity of Nodal and Lefty.” *Nat Commun* **9**(1): 5456.

Shi M., Zhu J., Wang R., Chen X., Mi L., Walz T. and Springer T. A. (2011). “Latent TGF-β structure and activation.” *Nature* **474**(7351): 343-349.

Shi Y. and Massagué J. (2003). “Mechanisms of TGF-β signaling from cell membrane to the nucleus.” *Cell* **113**(6): 685-700.

Shih Y. H., Kuo C. L., Hirst C. S., Dee C. T., Liu Y. R., Laghari Z. A. and Scotting P. J. (2010). “SoxB1 transcription factors restrict organizer gene expression by repressing multiple events downstream of Wnt signalling.” *Development* **137**(16): 2671-2681.

Shimizu T., Yamanaka Y., Ryu S. L., Hashimoto H., Yabe T., Hirata T., Bae Y. K., Hibi M. and Hirano T. (2000). “Cooperative roles of Bozozok/Dharma and Nodal-related proteins in the formation of the dorsal organizer in zebrafish.” *Mech Dev* **91**(1-2): 293-303.

Slanchev K., Carney T. J., Stemmler M. P., Koschorz B., Amsterdam A., Schwarz H. and Hammerschmidt M. (2009). “The epithelial cell adhesion molecule EpCAM is required for epithelial morphogenesis and integrity during zebrafish epiboly and skin development.” *PLoS Genet* **5**(7): e1000563.

Soh G. H. and Müller P. (2018). “FRAP analysis of extracellular diffusion in zebrafish embryos.” *Methods Mol Biol* **1863**: 107-124.

Solnica-Krezel L., Stemple D. L., Mountcastle-Shah E., Rangini Z., Neuhauss S. C., Malicki J., Schier A. F., Stainier D. Y., Zwartkruis F., Abdelilah S. and Driever W. (1996). “Mutations affecting cell fates and cellular rearrangements during gastrulation in zebrafish.” *Development* **123**: 67-80.

Spemann H. and Mangold H. (1924). “Über Induktion von Embryonalanlagen durch Implantation artfremder Organisatoren.” *Archiv für mikroskopische Anatomie und Entwicklungsmechanik* **100**(3-4): 599-638.

Sprague B. L., Pego R. L., Stavreva D. A. and McNally J. G. (2004). “Analysis of binding reactions by fluorescence recovery after photobleaching.” *Biophys J* **86**(6): 3473-3495.

Stachel S. E., Grunwald D. J. and Myers P. Z. (1993). “Lithium perturbation and goosecoid expression identify a dorsal specification pathway in the pregastrula zebrafish.” *Development* **117**(4): 1261-1274.

Stainier D. Y. R., Raz E., Lawson N. D., Ekker S. C., Burdine R. D., Eisen J. S., Ingham P. W., Schulte-Merker S., Yelon D., Weinstein B. M., Mullins M. C., Wilson S. W., Ramakrishnan L., Amacher S. L., Neuhauss S. C. F., Meng A., Mochizuki N., Panula P. and Moens C. B. (2017). “Guidelines for morpholino use in zebrafish.” *PLoS Genet* **13**(10): e1007000.

Stejskal E. O. and Tanner J. E. (1965). “Spin diffusion measurements: spin echoes in the presence of a time-dependent field gradient.” *The Journal of Chemical Physics* **42**(1): 288-292.

Stern C. D. (2001). “Initial patterning of the central nervous system: how many organizers?” *Nat Rev Neurosci* **2**(2): 92-98.

Strigini M. and Cohen S. M. (1997). “A Hedgehog activity gradient contributes to AP axial patterning of the Drosophila wing.” *Development* **124**(22): 4697-4705.

Summerton J. and Weller D. (1997). “Morpholino antisense oligomers: design, preparation, and properties.” *Antisense Nucleic Acid Drug Dev* **7**(3): 187-195.

Swaminathan R., Hoang C. P. and Verkman A. S. (1997). “Photobleaching recovery and anisotropy decay of green fluorescent protein GFP-S65T in solution and cells: cytoplasmic viscosity probed by green fluorescent protein translational and rotational diffusion.” *Biophys J* **72**(4): 1900-1907.

Tabata T. and Takei Y. (2004). “Morphogens, their identification and regulation.” *Development* **131**(4): 703-712.

Tapparel C., Reymond A., Girardet C., Guillou L., Lyle R., Lamon C., Hutter P. and Antonarakis S. E. (2003). “The TPTE gene family: cellular expression, subcellular localization and alternative splicing.” *Gene* **323**: 189-199.

Tata J. R. (2005). “One hundred years of hormones.” *EMBO Rep* **6**(6): 490-496.

Tateno H. (2010). “SUEL-related lectins, a lectin family widely distributed throughout organisms.” *Biosci Biotechnol Biochem* **74**(6): 1141-1144.

Terry B. R., Matthews E. K. and Haseloff J. (1995). “Molecular characterisation of recombinant green fluorescent protein by fluorescence correlation microscopy.” *Biochem Biophys Res Commun* **217**(1): 21-27.

Tessadori F., Noël E. S., Rens E. G., Magliozzi R., Evers-van Gogh I. J., Guardavaccaro D., Merks R. M. and Bakkers J. (2015). “Nodal signaling range is regulated by proprotein convertase-mediated maturation.” *Dev Cell* **32**(5): 631-639.

The Gene Ontology Consortium (2019). “The Gene Ontology Resource: 20 years and still GOing strong.” *Nucleic Acids Res* **47**(D1): D330-338.

The UniProt Consortium (2019). “UniProt: a worldwide hub of protein knowledge.” *Nucleic Acids Res* **47**(D1): D506-515.

Thisse B. and Thisse C. (2015). “Formation of the vertebrate embryo: Moving beyond the Spemann organizer.” *Semin Cell Dev Biol* **42**: 94-102.

Thisse C. and Thisse B. (2008). “High-resolution in situ hybridization to whole-mount zebrafish embryos.” *Nat Protoc* **3**(1): 59-69.

Thisse C., Thisse B., Halpern M. E. and Postlethwait J. H. (1994). “Goosecoid expression in neurectoderm and mesendoderm is disrupted in zebrafish cyclops gastrulas.” *Dev Biol* **164**(2): 420-429.

Topczewski J., Sepich D. S., Myers D. C., Walker C., Amores A., Lele Z., Hammerschmidt M., Postlethwait J. and Solnica-Krezel L. (2001). “The zebrafish glypican knypek controls cell polarity during gastrulation movements of convergent extension.” *Dev Cell* **1**(2): 251-264.

Toyama R., O'Connell M. L., Wright C. V., Kuehn M. R. and Dawid I. B. (1995). “Nodal induces ectopic goosecoid and lim1 expression and axis duplication in zebrafish.” *Development* **121**(2): 383-391.

Turing A. M. (1952). “The Chemical Basis of Morphogenesis.” *Philosophical Transactions of the Royal Society of London Series B-Biological Sciences* **237**(641): 37-72.

van Boxtel A. L., Chesebro J. E., Heliot C., Ramel M. C., Stone R. K. and Hill C. S. (2015). “A temporal window for signal activation dictates the dimensions of a Nodal signaling domain.” *Dev Cell* **35**(2): 175-185.

van Boxtel A. L., Economou A. D., Heliot C. and Hill C. S. (2018). “Long-range signaling activation and local inhibition separate the mesoderm and endoderm lineages.” *Dev Cell* **44**(2): 179-191.

Waddington C. H. (1936). “The problems of embryology.” *Br Med J* **2**(3956): 862-864.

Walker S. M., Downes C. P. and Leslie N. R. (2001). “TPIP: a novel phosphoinositide 3-phosphatase.” *Biochem J* **360**(2): 277-283.

Wang X. F., Lin H. Y., Ng-Eaton E., Downward J., Lodish H. F. and Weinberg R. A. (1991). “Expression cloning and characterization of the TGF-β type III receptor.” *Cell* **67**(4): 797-805.

Wang Y., Wang X., Wohland T. and Sampath K. (2016). “Extracellular interactions and ligand degradation shape the nodal morphogen gradient.” *Elife* **5**: e13879.

Wartlick O., Kicheva A. and González-Gaitán M. (2009). “Morphogen gradient formation.” *Cold Spring Harb Perspect Biol* **1**(3): a001255.

Weiss A. and Attisano L. (2013). “The TGFbeta superfamily signaling pathway.” *Wiley Interdiscip Rev Dev Biol* **2**(1): 47-63.

West S. A., Winzer K., Gardner A. and Diggle S. P. (2012). “Quorum sensing and the confusion about diffusion.” *Trends Microbiol* **20**(12): 586-594.

Westmoreland J. J., Takahashi S. and Wright C. V. (2007). “Xenopus Lefty requires proprotein cleavage but not N-linked glycosylation to inhibit nodal signaling.” *Dev Dyn* **236**(8): 2050-2061.

White R. J., Collins J. E., Sealy I. M., Wali N., Dooley C. M., Digby Z., Stemple D. L., Murphy D. N., Billis K., Hourlier T., Füllgrabe A., Davis M. P., Enright A. J. and Busch-Nentwich E. M. (2017). “A high-resolution mRNA expression time course of embryonic development in zebrafish.” *Elife* **6**: e30860.

Whiteley M., Diggle S. P. and Greenberg E. P. (2017). “Progress in and promise of bacterial quorum sensing research.” *Nature* **551**(7680): 313-320.

Wilcockson S. G., Sutcliffe C. and Ashe H. L. (2017). “Control of signaling molecule range during developmental patterning.” *Cell Mol Life Sci* **74**(11): 1937-1956.

Williams B. O., Barish G. D., Klymkowsky M. W. and Varmus H. E. (2000). “A comparative evaluation of β-catenin and plakoglobin signaling activity.” *Oncogene* **19**(50): 5720-5728.

Williams M. L. K. and Solnica-Krezel L. (2019). “A mesoderm-independent role for Nodal signaling in convergence & extension gastrulation movements.” *bioRxiv* (posted July 11, 2019).

Wolpert L. (1968). The French Flag Problem: a contribution to the discussion on pattern development and regulation. Towards a Theoretical Biology. I. Prolegomena. C. H. Waddington. Edinburgh, Edinburgh University Press**:** 125-133.

Wolpert L. (1969). “Positional information and the spatial pattern of cellular differentiation.” *J Theor Biol* **25**(1): 1-47.

Wolpert L. (1989). “Positional information revisited.” *Development* **107**: Supplement 3-12.

Wolpert L. (2011). “Positional information and patterning revisited.” *J Theor Biol* **269**(1): 359-365.

Wolpert L. (2016). “Positional Information and Pattern Formation.” *Curr Top Dev Biol* **117**: 597-608.

Wu R. S., Lam, II, Clay H., Duong D. N., Deo R. C. and Coughlin S. R. (2018). “A rapid method for directed gene knockout for screening in G0 zebrafish.” *Dev Cell* **46**(1): 112-125.

Yan Y. T., Liu J. J., Luo Y., E C., Haltiwanger R. S., Abate-Shen C. and Shen M. M. (2002). “Dual roles of Cripto as a ligand and coreceptor in the nodal signaling pathway.” *Mol Cell Biol* **22**(13): 4439-4449.

Yang Y., Liu B., Dai J., Srivastava P. K., Zammit D. J., Lefrançois L. and Li Z. (2007). “Heat shock protein gp96 is a master chaperone for toll-like receptors and is important in the innate function of macrophages.” *Immunity* **26**(2): 215-226.

Yilmaz O., Patinote A., Nguyen T. V., Com E., Lavigne R., Pineau C., Sullivan C. V. and Bobe J. (2017). “Scrambled eggs: Proteomic portraits and novel biomarkers of egg quality in zebrafish (Danio rerio).” *PLoS One* **12**(11): e0188084.

Yu S. R., Burkhardt M., Nowak M., Ries J., Petrášek Z., Scholpp S., Schwille P. and Brand M. (2009). "Fgf8 morphogen gradient forms by a source-sink mechanism with freely diffusing molecules." *Nature* **461**(7263): 533-536.

Zecca M., Basler K. and Struhl G. (1996). "Direct and long-range action of a wingless morphogen gradient." *Cell* **87**(5): 833-844.

Zhou S., Lo W. C., Suhalim J. L., Digman M. A., Gratton E., Nie Q. and Lander A. D. (2012). "Free extracellular diffusion creates the Dpp morphogen gradient of the Drosophila wing disc." *Curr Biol* **22**(8): 668-675.

Zhurinsky J., Shtutman M. and Ben-Ze'ev A. (2000a). "Differential mechanisms of LEF/TCF family-dependent transcriptional activation by β-catenin and plakoglobin." *Mol Cell Biol* **20**(12): 4238-4252.

Zhurinsky J., Shtutman M. and Ben-Ze'ev A. (2000b). "Plakoglobin and β-catenin: protein interactions, regulation and biological roles." *J Cell Sci* **113**: 3127-3139.

Zinski J., Tajer B. and Mullins M. C. (2018). "TGF-β family signaling in early vertebrate development." *Cold Spring Harb Perspect Biol* **10**(6): a033274.

8. Original Publications

This chapter contains the original publications of this thesis including supplementary material:

1.) **Mörsdorf D.** and Müller P. (2019). “Tuning protein diffusivity with membrane tethers.” *Biochemistry* **58**(3): 177-181.

2.) Almuedo-Castillo M., Bläßle A., **Mörsdorf D.**, Marcon L., Soh G. H., Rogers K. W., Schier A. F. and Müller P. (2018). “Scale-invariant patterning by size-dependent inhibition of Nodal signalling.” *Nature Cell Biology* **20**(9): 1032-1042.

3.) Bläßle A., Soh G., Braun T., **Mörsdorf D.**, Preiss H., Jordan B. M. and Müller P. (2018). “Quantitative diffusion measurements using the open-source software PyFRAP.” *Nature Communications* **9**(1): 1582.

This is an open access article published under an ACS AuthorChoice License, which permits copying and redistribution of the article or any adaptations for non-commercial purposes.

Biochemistry

Communication

Cite This: Biochemistry 2019, 58, 177−181

pubs.acs.org/biochemistry

Tuning Protein Diffusivity with Membrane Tethers

David Mörsdorf and Patrick Müller*

Friedrich Miescher Laboratory of the Max Planck Society, Max-Planck-Ring 9, 72076 Tübingen, Germany

Supporting Information

ABSTRACT: Diffusion is essential for biochemical processes because it dominates molecular movement on small scales. Enzymatic reactions, for example, require fast exchange of substrate and product molecules in the local environment of the enzyme to ensure efficient turnover. On larger spatial scales, diffusion of secreted signaling proteins is thought to limit the spatial extent of tissue differentiation during embryonic development. While it is possible to measure diffusion *in vivo*, specifically interfering with diffusion processes and testing diffusion models directly remains challenging. The development of genetically encoded nanobodies that bind specific proteins has provided the opportunity to alter protein localization and reduce protein mobility. Here, we extend the nanobody toolbox with a membrane-tethered low-affinity diffusion regulator that can be used to tune the effective diffusivity of extracellular molecules over an order of magnitude in living embryos. This opens new avenues for future applications to functionally interfere with diffusion-dependent processes.

Downloaded via MPI FUR ENTWICKLUNGSBIOLOGIE on September 28, 2019 at 23:59:13 (UTC).
See https://pubs.acs.org/sharingguidelines for options on how to legitimately share published articles.

Diffusion is fast over short distances but slow over longer spatial scales. It can therefore theoretically limit the dispersal and action range of signaling proteins within tissues, for example during early development.[1,2] Most multicellular organisms develop from an embryo that initially consists of equivalent stem cell-like "naive" cells. A long-standing concept in developmental biology is that a subset of cells, the source, secretes signals that diffuse into the surrounding tissue and instruct naive cells to form embryonic organs. The idea that extracellular signaling molecules spread by diffusion appears to be straightforward due to the passive nature of diffusion,[3,4] but the relevance of extracellular diffusion for the dispersal of signaling molecules from source to target tissues is still largely unclear. Despite evidence for free diffusion of the *Drosophila melanogaster* bone morphogenetic protein (BMP) homolog Decapentaplegic (Dpp),[5] models of active Dpp transport have also been proposed.[6] Similarly, the extent to which extracellular diffusion of the vertebrate signaling molecules BMP[7−9] and Nodal[4,10−14] is required for their endogenous function is unclear. Thus, classical models in which diffusion determines signal dispersal and tissue patterning are still being debated.[1,15,16]

To examine the mechanisms underlying signal dispersal and to probe diffusion models, the Affolter lab has recently pioneered the morphotrap approach, in which a high-affinity anti-GFP nanobody[17] (reviewed in ref 18) is targeted to the cell surface with a transmembrane domain tagged with

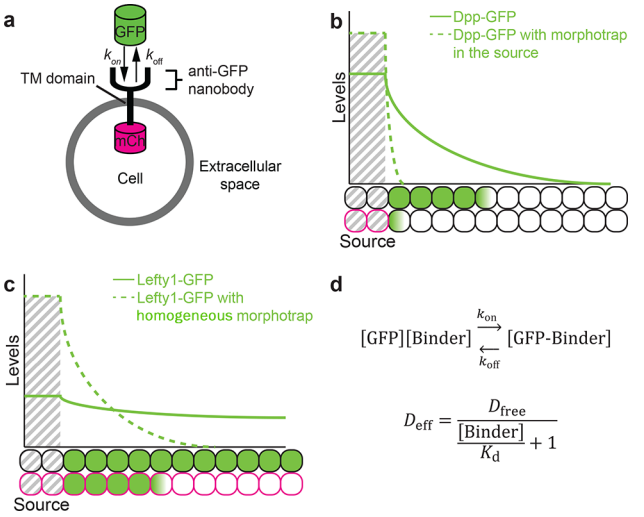

Figure 1. Using membrane-tethered nanobodies to immobilize extracellular GFP fusion proteins. (a) The morphotrap consists of a high-affinity anti-GFP nanobody, a transmembrane (TM) domain, and an intracellular mCherry (mCh) tag. Binding of extracellular GFP or GFP fusion proteins holds them on the plasma membrane.[19] (b) Illustration of the Dpp-GFP distribution in the *D. melanogaster* wing disc upon expression of the morphotrap from a localized source.[19] Normally, Dpp-GFP spreads from the source through the surrounding tissue (cells illustrated below the *x*-axis), forming a concentration gradient (green line). Cells that receive sufficiently high signal levels respond and induce downstream signaling (green cells). When the morphotrap is co-expressed in the source tissue (magenta cell outlines), Dpp-GFP is retained in the source and the formation of a relevant signaling gradient is abolished (green dashed line). Only cells in the immediate vicinity of the source receive signaling, whereas cells at a distance do not. (c) Illustration of the Lefty1-GFP distribution expressed from a localized source in zebrafish embryos.[24] Lefty1-GFP forms a long-range gradient from the source tissue (green solid line). When the morphotrap is homogeneously expressed in zebrafish embryos, Lefty1-GFP mobility is reduced, resulting in a steep gradient ∼2 h after the onset of Lefty1-GFP production (green dashed line). The range of Lefty1-GFP is illustrated by the green cells below the *x*-axis. (d). If GFP reversibly interacts with a binder such as an anti-GFP nanobody, GFP's effective diffusion coefficient D_{eff} is predicted to be modulated by the concentration of the binder as well as its GFP binding affinity,[21,22] K_d.

Special Issue: Future of Biochemistry: The International Issue

Received: October 31, 2018
Revised: December 9, 2018
Published: December 18, 2018

© 2018 American Chemical Society

DOI: 10.1021/acs.biochem.8b01150
Biochemistry 2019, 58, 177−181

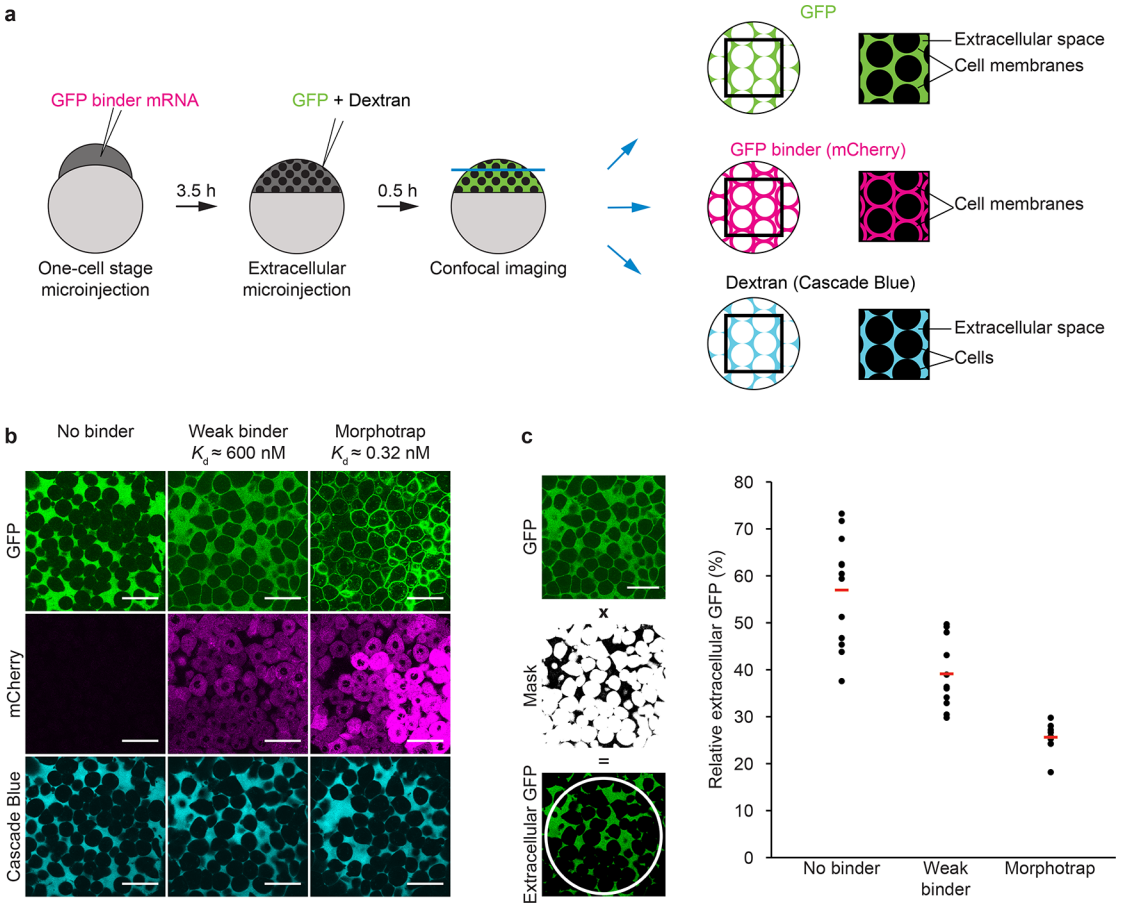

Figure 2. A low-affinity GFP binder partially tethers extracellular GFP to cell membranes in zebrafish embryos. (a) Schematic of the localization assay. GFP binders were expressed in zebrafish embryos by microinjecting 100 pg of the corresponding mRNAs at the one-cell stage. After 3.5 h of embryonic development, GFP and a fluorescent dextran were injected extracellularly followed by confocal microscopy to determine the localization of GFP, the GFP binder (mCherry), and dextran (Cascade Blue). The panel on the right illustrates the localization of the three fluorescent signals shown in panel b. (b) Without GFP binders, GFP is distributed homogeneously in the extracellular space. In embryos expressing the weak GFP binder, GFP can be detected both on cell membranes and in the extracellular space. In the presence of the morphotrap, the majority of GFP localizes to cell membranes. Scale bars correspond to 50 μm. (c) A mask was created from the extracellular dextran signal and used to extract the GFP signal in cell-free areas within a circular region of interest (ROI, white). The graph shows measurements of extracellular GFP normalized to total GFP in the ROI from single embryos (black dots). Red lines indicate mean values. The scale bar corresponds to 50 μm.

mCherry (Figure 1a, refs 19 and 20). The morphotrap binds extracellular GFP-tagged signaling molecules and thus tethers the signal to the cell membrane. In a tissue expressing the morphotrap, this presumably transient GFP−nanobody interaction slows the long-distance transport of the extracellular GFP-tagged population, resulting in a reduced "effective" diffusivity.[4,21,22] In the context of development, where signaling typically occurs in a defined time frame, decreasing the signal mobility results in a reduced signaling range, shortening the spatial domain in which signaling is active. Thus, the morphotrap provides a means to directly test the effect of decreasing the spatial range of GFP-tagged signaling molecules on the development of living systems.

Three examples have shown how the morphotrap can be used with GFP-tagged signals to test the importance of their mobility for biological functions. First, in the developing fly wing, Dpp-GFP normally exhibits a graded distribution away from producing cells, but co-expression of the morphotrap in these source cells abolished Dpp-GFP spreading[19] (Figure 1b) and resulted in a loss of Dpp-dependent signaling outside of the source. Second, a morphotrap was used in *Caenorhabditis elegans* to tether a fluorescently labeled Wnt homolog to membranes and prevent its extracellular spreading, resulting in a loss of cell migration.[23] Third, we have recently used the morphotrap in living zebrafish embryos to drastically slow the spreading of the normally highly mobile Nodal antagonist Lefty1-GFP, which leads to defective body size scaling after experimental shortening[24] (Figure 1c). The strong effect on the mobility of GFP fusion proteins can be explained by the high-affinity anti-GFP nanobody used in the morphotrap (*in vitro* dissociation constant K_d of approximately 0.32 nM[17]). However, to understand the extent to which signal diffusion determines the range over which the signal acts, it is crucial to decrease signal mobility in a gradual, fine-tuned manner.

To enable fine-tuned regulation of signaling molecule diffusivity, we have generated an alternative GFP binder by swapping the morphotrap nanobody[19] with an anti-GFP nanobody that has a dissociation constant of 600 nM *in vitro*.[25] The lower affinity of this GFP binder should result in a reduced degree of GFP membrane tethering compared to the morphotrap and thus a weaker effect on overall GFP

DOI: 10.1021/acs.biochem.8b01150
Biochemistry 2019, 58, 177−181

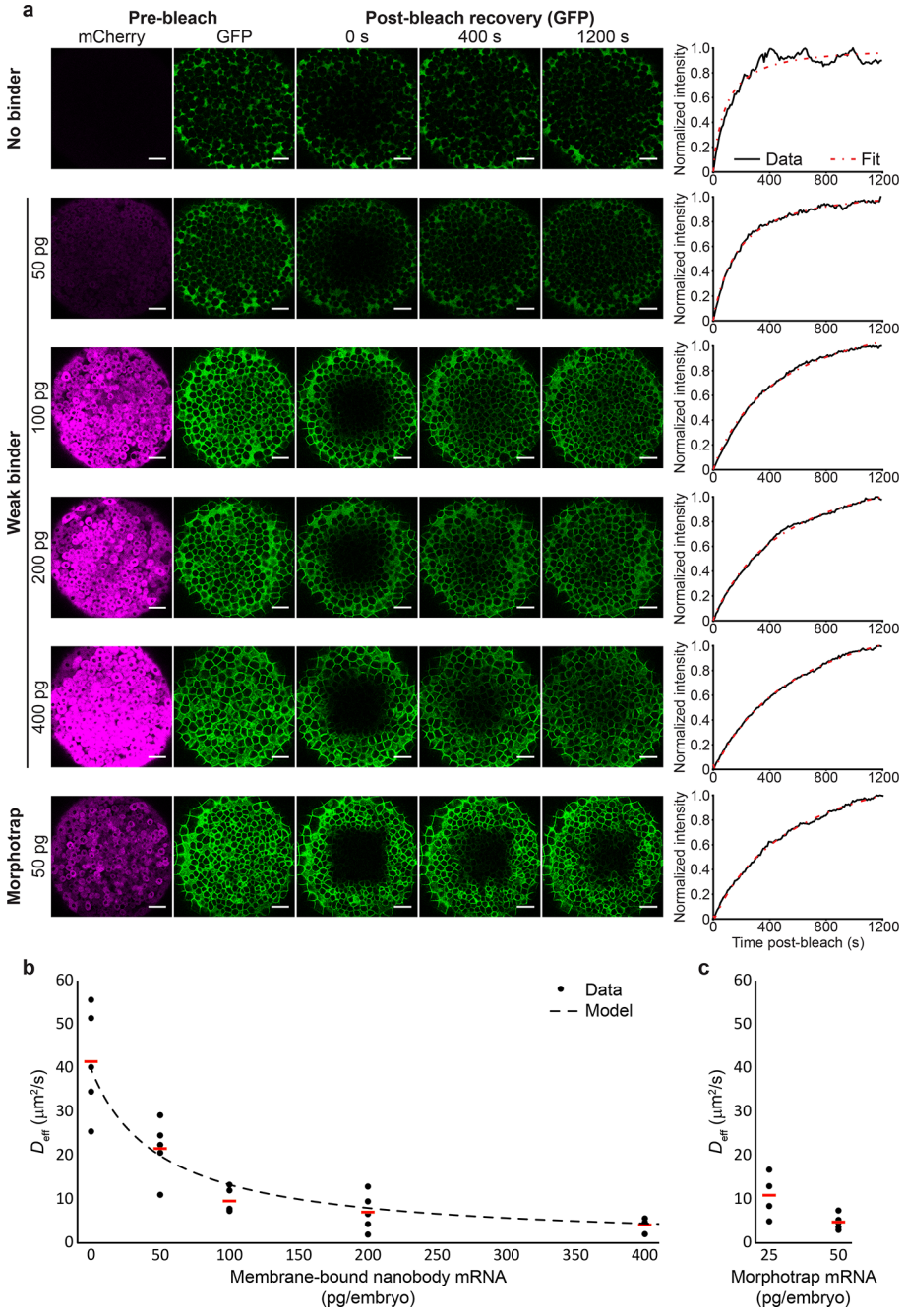

Figure 3. Titration of a low-affinity GFP binder modulates the mobility of extracellularly injected GFP in zebrafish embryos. (a) Different amounts of mRNA encoding the weak binder (K_d = 600 nM *in vitro*) were injected into zebrafish embryos at the one-cell stage (50, 100, 200, or 400 pg); negative controls were left uninjected (0 pg of mRNA), and positive controls were injected with 50 pg of mRNA encoding the morphotrap (K_d = 0.32 nM *in vitro*). Before the embryos were mounted for FRAP experiments at blastula stages, they were injected extracellularly with approximately 100 pg of recombinant GFP. FRAP experiments were performed as previously described[8,11] and analyzed using PyFRAP.[27] Scale bars correspond to 50 μm. (b and c) The effective diffusion coefficients (D_{eff}) of independent experiments executed as described for panel a are shown as black dots, and red lines indicate mean values. The dashed line in panel b shows an overlay with the effective diffusion model calculated from the equation in Figure 1d (see the Supporting Information for details).

mobility. Binding of GFP by membrane-tethered binders can be described by a second-order chemical reaction (Figure 1d). Because the binder and the GFP−binder complex are immobilized on the cell surface, formation of the GFP−binder complex decreases the amount of free GFP diffusing with the molecular diffusion coefficient D_{free}. If k_{on} and k_{off} (Figure 1d) of the GFP binding reaction are fast, the effective diffusion coefficient D_{eff}, which describes GFP mobility over tissue-wide scales, is decreased in the presence of the binder. D_{eff} depends on the concentration of the binder and the dissociation constant $K_d = k_{off}/k_{on}$ of the binding reaction[4,21,22,26] (Figure 1d).

The nanobody LaG-42 is a well-characterized GFP binder with an *in vitro* K_d of approximately 600 nM.[25] To test the effect this low-affinity GFP binder has on the localization of extracellular GFP, we expressed the weak GFP binder or the original morphotrap in zebrafish embryos and subsequently injected recombinant GFP into the extracellular space (Figure

DOI: 10.1021/acs.biochem.8b01150
Biochemistry 2019, 58, 177−181

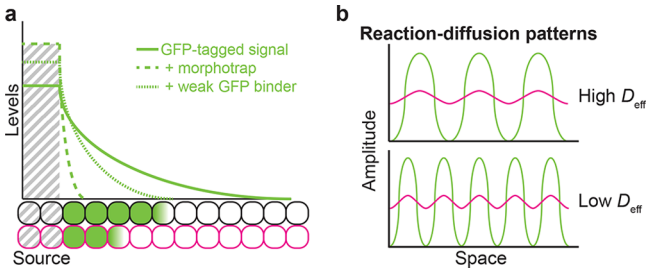

Figure 4. Potential future applications of weak GFP binders. (a) Homogeneous expression of weak GFP binders is predicted to moderately shorten gradients of GFP-tagged signaling molecules. (b) Potential use of weak GFP binders to change the characteristic wavelength of reaction−diffusion patterning systems.

2a). Assuming that the total levels of GFP and its binders are similar between experiments, a higher concentration of free GFP is expected for the weak binder compared to the morphotrap. Indeed, extracellular GFP levels were higher for the binder with a higher K_d in measurements in which independent masks for the extracellular space were used (see Figure 2b,c and the Supporting Information).

The relationship between D_{eff}, D_{free}, and binder levels in the equation of Figure 1d predicts that weak GFP binders could be used to fine-tune the effective diffusivity of extracellular GFP by using different binder concentrations. To test this prediction, we injected different amounts of mRNA encoding the low-affinity GFP binder into zebrafish embryos at the one-cell stage. Following extracellular injections of GFP at blastula stages, we performed FRAP experiments[8,11] and determined the resulting effective diffusion coefficients.[27,28] Our results show that the mobility of extracellular GFP can be fine-tuned by expressing different levels of the weak GFP binder (Figure 3). In good agreement with previous measurements in zebrafish embryos,[11,27] we found a mean effective diffusion coefficient of 42 $\mu m^2/s$ for extracellular GFP in the absence of a GFP binder. Strikingly, this effective diffusivity was reduced stepwise after microinjection of 50, 100, 200, and 400 pg of mRNA encoding the weak binder to 22, 10, 7, and 4 $\mu m^2/s$, respectively (Figure 3b). In contrast, just 50 pg of morphotrap-encoding mRNA reduced the effective GFP diffusivity to 5 $\mu m^2/s$ (Figure 3c). Although a reduced level of morphotrap expression resulted in a higher GFP mobility (Figure 3c), fine-tuning GFP mobility using even lower morphotrap expression levels may be difficult. GFP binders are expected to saturate more easily at low levels, and free diffusion may then dominate fluorescence recovery.[22] Interestingly, the difference in GFP mobilities with 50 pg of morphotrap mRNA [$D_{eff} \approx 5\ \mu m^2/s$ (Figure 3c)] and 50 pg of weak binder mRNA [$D_{eff} \approx 22\ \mu m^2/s$ (Figure 3b)] was weaker than expected on the basis of the *in vitro* dissociation constants, which differ by a factor of 2000. It is therefore possible that the *in vivo* dissociation constants of the nanobodies in zebrafish embryos are different from the values measured *in vitro*,[17,25] and fluorescence correlation spectroscopy (FCS) measurements might be able to dissect these potential differences in future experiments.[14,29,30]

Controlled expression of a GFP binder allowed us to tune the effective diffusivity of extracellular GFP over an order of magnitude, whereas alternative approaches that change the molecular weight of the attached fluorophore would be expected to have a much smaller effect size. Since the free diffusion of spherical molecules is proportional to their radii, even tripling the number of attached GFP molecules would at most lead to a 30% reduction in diffusivity,[3,11] for instance. To gradually reduce the mobility of a GFP-tagged signaling molecule, it is theoretically also possible to use distinct GFP binders with different affinities. In our experience, however, there are two caveats when comparing different GFP binders in combination with a GFP fusion protein. First, GFP binders can reduce the biological activity of a GFP fusion protein, depending on the nanobody used. Second, nanobody binding can increase or decrease GFP fluorescence.[31] We therefore chose to titrate a single GFP binder to obtain a gradual reduction of GFP mobility (Figure 3).

Long-range diffusion of ligands is responsible for the propagation of signaling in classical models of tissue patterning.[32,33] However, the requirement of signal mobility for patterning has so far only in a few cases been directly tested by tethering extracellular signaling molecules to cell membranes with a strong GFP binder.[19,20,23,24] Our proof-of-principle experiments demonstrate that a weak GFP binder can be used to reduce the effective diffusivity of extracellular GFP in a tunable manner between 2- and 10-fold. We expect that this control over signal mobility will allow the range of GFP-tagged signals to be shortened in future experiments, allowing a functional assessment of the extent to which diffusion controls signaling range during development (Figure 4a). Furthermore, this tool could be used to probe previously postulated self-organizing reaction−diffusion patterning systems,[11,34] whose characteristic wavelength should change with reduced effective diffusivities of the involved signaling molecules[35−37] (Figure 4b). For biological processes that are controlled by intracellular reaction kinetics, low-affinity anti-GFP nanobodies could be incorporated into the intracellular morphotrap[20] to generate weak binders that modulate the mobility of cytoplasmic proteins. For example, the kinetics of Pom1-GFP gradient formation in *Schizosaccharomyces pombe* could be perturbed to test the importance of Pom1-GFP distribution for symmetric cytokinesis.[38] Finally, purification of weak GFP binders might find useful applications in *in vitro* reaction−diffusion networks, such as the Min system,[39−41] to modulate pattern formation processes.

To date, nanobodies have been generated against various proteins and together with other types of small protein binders (recently reviewed in ref 42) could be used to alter the mobility of several signaling molecules. Future experiments combining these tools have the potential to revolutionize *in vivo* studies by testing the importance of signal diffusion in various biological settings.

■ ASSOCIATED CONTENT

Supporting Information

The Supporting Information is available free of charge on the ACS Publications website at DOI: 10.1021/acs.biochem.8b01150.

Experimental procedures (PDF)

■ AUTHOR INFORMATION

Corresponding Author

*E-mail: patrick.mueller@tuebingen.mpg.de.

DOI: 10.1021/acs.biochem.8b01150
Biochemistry 2019, 58, 177−181

ORCID

David Mörsdorf: 0000-0001-8982-2155
Patrick Müller: 0000-0002-0702-6209

Funding

This work was supported by the Max Planck Society, the International Max Planck Research School "From Molecules to Organisms", and an ERC Starting Grant (*QUANTPATTERN*).

Notes

The authors declare no competing financial interest.

■ ACKNOWLEDGMENTS

The authors are grateful to Martin Groß, Olga Matsarskaia, Autumn Pomreinke, Katherine W. Rogers, and Annamaria Sgromo for helpful discussions and comments. The authors also thank Aurora Panzera for technical help with imaging.

■ REFERENCES

(1) Crick, F. (1970) *Nature 225*, 420−422.
(2) Lander, A. D. (2007) *Cell 128*, 245−256.
(3) Müller, P., and Schier, A. F. (2011) *Dev. Cell 21*, 145−158.
(4) Müller, P., Rogers, K. W., Yu, S. R., Brand, M., and Schier, A. F. (2013) *Development 140*, 1621−1638.
(5) Zhou, S., Lo, W. C., Suhalim, J. L., Digman, M. A., Gratton, E., Nie, Q., and Lander, A. D. (2012) *Curr. Biol. 22*, 668−675.
(6) Roy, S., Huang, H., Liu, S., and Kornberg, T. B. (2014) *Science 343*, 1244624.
(7) Ramel, M. C., and Hill, C. S. (2013) *Dev. Biol. 378*, 170−182.
(8) Pomreinke, A. P., Soh, G. H., Rogers, K. W., Bergmann, J. K., Bläßle, A. J., and Müller, P. (2017) *eLife 6*, e25861.
(9) Zinski, J., Bu, Y., Wang, X., Dou, W., Umulis, D., and Mullins, M. (2017) *eLife 6*, e22199.
(10) Chen, Y., and Schier, A. F. (2001) *Nature 411*, 607−610.
(11) Müller, P., Rogers, K. W., Jordan, B. M., Lee, J. S., Robson, D., Ramanathan, S., and Schier, A. F. (2012) *Science 336*, 721−724.
(12) van Boxtel, A. L., Chesebro, J. E., Heliot, C., Ramel, M. C., Stone, R. K., and Hill, C. S. (2015) *Dev. Cell 35*, 175−185.
(13) van Boxtel, A. L., Economou, A. D., Heliot, C., and Hill, C. S. (2018) *Dev. Cell 44*, 179−191.
(14) Wang, Y., Wang, X., Wohland, T., and Sampath, K. (2016) *eLife 5*, e13879.
(15) Turing, A. M. (1952) *Philos. Trans. R. Soc., B 237*, 37−72.
(16) Rogers, K. W., and Müller, P. (2018) *Dev. Biol.*, 30925−30929.
(17) Saerens, D., Pellis, M., Loris, R., Pardon, E., Dumoulin, M., Matagne, A., Wyns, L., Muyldermans, S., and Conrath, K. (2005) *J. Mol. Biol. 352*, 597−607.
(18) Muyldermans, S. (2013) *Annu. Rev. Biochem. 82*, 775−797.
(19) Harmansa, S., Hamaratoglu, F., Affolter, M., and Caussinus, E. (2015) *Nature 527*, 317−322.
(20) Harmansa, S., Alborelli, I., Bieli, D., Caussinus, E., and Affolter, M. (2017) *eLife 6*, e22549.
(21) Crank, J. (1979) *The mathematics of diffusion*, Clarendon Press, Oxford, U.K.
(22) Sprague, B. L., Pego, R. L., Stavreva, D. A., and McNally, J. G. (2004) *Biophys. J. 86*, 3473−3495.
(23) Pani, A. M., and Goldstein, B. (2018) *eLife 7*, e38325.
(24) Almuedo-Castillo, M., Bläßle, A., Mörsdorf, D., Marcon, L., Soh, G. H., Rogers, K. W., Schier, A. F., and Müller, P. (2018) *Nat. Cell Biol. 20*, 1032−1042.
(25) Fridy, P. C., Li, Y., Keegan, S., Thompson, M. K., Nudelman, I., Scheid, J. F., Oeffinger, M., Nussenzweig, M. C., Fenyo, D., Chait, B. T., and Rout, M. P. (2014) *Nat. Methods 11*, 1253−1260.
(26) Miura, T., Hartmann, D., Kinboshi, M., Komada, M., Ishibashi, M., and Shiota, K. (2009) *Mech. Dev. 126*, 160−172.
(27) Bläßle, A., Soh, G. H., Braun, T., Mörsdorf, D., Preiß, H., Jordan, B. M., and Müller, P. (2018) *Nat. Commun. 9*, 1582.
(28) Soh, G. H., and Müller, P. (2018) *Methods Mol. Biol. 1863*, 107−124.
(29) Ries, J., Yu, S. R., Burkhardt, M., Brand, M., and Schwille, P. (2009) *Nat. Methods 6*, 643−645.
(30) Sigaut, L., Pearson, J. E., Colman-Lerner, A., and Ponce Dawson, S. (2014) *PLoS Comput. Biol. 10*, e1003629.
(31) Kirchhofer, A., Helma, J., Schmidthals, K., Frauer, C., Cui, S., Karcher, A., Pellis, M., Muyldermans, S., Casas-Delucchi, C. S., Cardoso, M. C., Leonhardt, H., Hopfner, K. P., and Rothbauer, U. (2010) *Nat. Struct. Mol. Biol. 17*, 133−138.
(32) Rogers, K. W., and Schier, A. F. (2011) *Annu. Rev. Cell Dev. Biol. 27*, 377−407.
(33) Sagner, A., and Briscoe, J. (2017) *Wiley Interdiscip. Rev.: Dev. Biol. 6*, e271.
(34) Raspopovic, J., Marcon, L., Russo, L., and Sharpe, J. (2014) *Science 345*, 566−570.
(35) Marcon, L., Diego, X., Sharpe, J., and Müller, P. (2016) *eLife 5*, e14022.
(36) Gierer, A. (1981) *Prog. Biophys. Mol. Biol. 37*, 1−47.
(37) Murray, J. D. (2003) *Mathematical Biology*, Springer, Berlin.
(38) Saunders, T. E., Pan, K. Z., Angel, A., Guan, Y., Shah, J. V., Howard, M., and Chang, F. (2012) *Dev. Cell 22*, 558−572.
(39) Denk, J., Kretschmer, S., Halatek, J., Hartl, C., Schwille, P., and Frey, E. (2018) *Proc. Natl. Acad. Sci. U. S. A. 115*, 4553−4558.
(40) Meinhardt, H., and de Boer, P. A. (2001) *Proc. Natl. Acad. Sci. U. S. A. 98*, 14202−14207.
(41) Kretschmer, S., Zieske, K., and Schwille, P. (2017) *PLoS One 12*, e0179582.
(42) Harmansa, S., and Affolter, M. (2018) *Development 145*, dev148874.

DOI: 10.1021/acs.biochem.8b01150
Biochemistry 2019, 58, 177−181

Supporting Information for:
Tuning protein diffusivity with membrane tethers

David Mörsdorf and Patrick Müller

Friedrich Miescher Laboratory of the Max Planck Society

Max-Planck-Ring 9

72076 Tübingen

Germany

Experimental Procedures

Molecular cloning

A DNA fragment encoding the low-affinity GFP binder LaG-42 (ref. *1*) was ordered as a gBlock gene fragment (IDT) such that the 5′ sequence was 5′-actagtATGGACCAGGTGCAGCTG-3′ (SpeI site in lower case), encoding the amino acid sequence TSMDQVQL, and the 3′ sequence was 5′-actagtGCTGCTCACGGTCACCTG-3′ (SpeI site in lower case), encoding the amino acid sequence QVTVSSTS. The gBlock was digested with SpeI, cloned into the plasmid pCS2(+)-morphotrap[2] (replacing the original nanobody sequence) and sequenced to confirm the correct orientation of the insert.

Microinjections

mRNAs for microinjections were synthesized using the mMessage mMachine SP6 Transcription Kit (Invitrogen) after linearization of the pCS2(+) plasmids with NotI. Approximately 1 nl of mRNA was injected into TE embryos at the one- or two-cell stage. If not mentioned otherwise, an injection mix containing 100 ng/µl mRNA was used. To inject higher amounts of mRNA, the mRNA concentration was adjusted (e.g. 400 ng/µl for 400 pg injections). All mRNA injection mixes contained 0.1% phenol red (Sigma). No toxicity was observed for the tested mRNA amounts, and the injected zebrafish embryos were phenotypically normal at 24 hours post fertilization.

For extracellular injections of GFP, recombinant EGFP (MBL) was diluted in PBS to a concentration of 200 ng/µl. Around oblong stage, five boli of approximately 100 pl were injected into the extracellular space at different positions of pronase-dechorionated embryos. When a mask for the extracellular space was needed (see "Quantification of extracellular GFP levels" below), 500 ng/µl Cascade Blue-conjugated 3 kDa dextran (Molecular Probes) was included in the extracellular injection mix.

Quantification of extracellular GFP levels

Dechorionated embryos were mounted for imaging around sphere stage[3] with the animal pole facing the objective using 1.5% low-melting point agarose in glass bottom culture dishes

(MatTek corporation). Imaging was performed on an Olympus FV1200 confocal microscope using a UPlanSApo 60 x W objective, approximately 20 µm deep from the animal pole.

To compare the relative levels of extracellular GFP when either the weak binder or the morphotrap was expressed, the Cascade Blue signal was used to define the extracellular space. A mask was generated from the Cascade Blue signal in Fiji[4] using the *Convert to Mask* function. The value 254 was subtracted from the resulting binary image to obtain a mask with values of 1 (extracellular space) or 0 (cells and region outside of embryo). Regions with extracellular GFP were then obtained by multiplying the GFP signal with the mask. To exclude cells in the periphery of the embryo, a large circular region of interest (ROI) was defined (Fig. 2c).

The following Fiji macro was used to measure extracellular GFP:

```
Current_Image=getTitle;
run("Split Channels");
selectWindow("C1-"+Current_Image);
setOption("BlackBackground", false);
run("Convert to Mask");
run("Subtract...", "value=254");
selectWindow("C2-"+Current_Image);
imageCalculator("Multiply create", "C2-"+Current_Image,"C1-"+Current_Image);
selectWindow("Result of C2-"+Current_Image);
makeOval(27, 35, 746, 746);
run("Measure");
```

The integrated density within the ROI was measured in the GFP channel before (total GFP) and after masking (extracellular GFP). For each sample ("no binder", "weak binder" or "morphotrap"), multiple embryos from three biological replicates (independent injections) were quantified and extracellular/total GFP ratios were calculated.

FRAP

Embryos were mounted for imaging around sphere or dome stages[3], and FRAP was performed on a Zeiss LSM 780 NLO confocal microscope as described previously[5]. A 20 min time series with 10 s intervals of spatially averaged data from the bleached region was used for model fitting to determine effective diffusion coefficients.

Comparison of FRAP measurements to a theoretical model of effective diffusion

The curve shown in Fig. 3b was calculated from the effective diffusion model

$$D_{\mathrm{eff}} = \frac{D_{\mathrm{free}}}{\frac{[\mathrm{Binder}]}{K_{\mathrm{d}}} + 1}$$

with D_{free} = 40 µm^2/s (refs. *5, 6*) and values for K_{d} and [Binder] that led to a good match with the experimental data. We assume a linear relationship between injected mRNA and the protein it encodes; however, the concentration of membrane-bound nanobody in our FRAP experiments is unknown. Furthermore, the *in vivo* affinity of the nanobody has not been determined in zebrafish embryos. Given these two unknown factors, the model curve in Fig. 3b can be interpreted in

multiple ways: Assuming that the *in vitro* and *in vivo* affinities of the nanobody are identical (K_d = 600 nM), the full scale of the x-axis from 0 pg to 400 pg mRNA in Fig. 3b would correspond to a range of 0 to 4.8 µM membrane-bound nanobody protein. In contrast, assuming that the *in vivo* affinity of the nanobody differs from its affinity *in vitro*, with a K_d of e.g. 50 nM the full scale of the x-axis in Fig. 3b would correspond to a range of 0 to 400 nM membrane-bound nanobody.

Supplementary References

[1] Fridy, P. C.; Li, Y.; Keegan, S.; Thompson, M. K.; Nudelman, I.; Scheid, J. F.; Oeffinger, M.; Nussenzweig, M. C.; Fenyo, D.; Chait, B. T.; Rout, M. P. *Nat Methods* **2014** *11*, 1253-1260.

[2] Almuedo-Castillo, M.; Bläßle, A.; Mörsdorf, D.; Marcon, L.; Soh, G. H.; Rogers, K. W.; Schier, A. F.; Müller, P. *Nat Cell Biol* **2018** *20*, 1032-1042.

[3] Kimmel, C. B.; Ballard, W. W.; Kimmel, S. R.; Ullmann, B.; Schilling, T. F. *Dev Dyn* **1995** *203*, 253-310.

[4] Schindelin, J.; Arganda-Carreras, I.; Frise, E.; Kaynig, V.; Longair, M.; Pietzsch, T.; Preibisch, S.; Rueden, C.; Saalfeld, S.; Schmid, B.; Tinevez, J. Y.; White, D. J.; Hartenstein, V.; Eliceiri, K.; Tomancak, P.; Cardona, A. *Nat Methods* **2012** *9*, 676-682.

[5] Bläßle, A.; Soh, G. H.; Braun, T.; Mörsdorf, D.; Preiß, H.; Jordan, B. M.; Müller, P. *Nature Communications* **2018** *9*, 1582.

[6] Müller, P.; Rogers, K. W.; Jordan, B. M.; Lee, J. S.; Robson, D.; Ramanathan, S.; Schier, A. F. *Science* **2012** *336*, 721-724.

ARTICLES
https://doi.org/10.1038/s41556-018-0155-7
nature cell biology

Scale-invariant patterning by size-dependent inhibition of Nodal signalling

María Almuedo-Castillo[1,3], Alexander Bläßle[1], David Mörsdorf[1], Luciano Marcon[1,3], Gary H. Soh[1], Katherine W. Rogers[1,2], Alexander F. Schier[2] and Patrick Müller[1*]

Individuals can vary substantially in size, but the proportions of their body plans are often maintained. We generated smaller zebrafish by removing 30% of their cells at the blastula stages and found that these embryos developed into normally patterned individuals. Strikingly, the proportions of all germ layers adjusted to the new embryo size within 2 hours after cell removal. As Nodal–Lefty signalling controls germ-layer patterning, we performed a computational screen for scale-invariant models of this activator–inhibitor system. This analysis predicted that the concentration of the highly diffusive inhibitor Lefty increases in smaller embryos, leading to a decreased Nodal activity range and contracted germ-layer dimensions. In vivo studies confirmed that Lefty concentration increased in smaller embryos, and embryos with reduced Lefty levels or with diffusion-hindered Lefty failed to scale their tissue proportions. These results reveal that size-dependent inhibition of Nodal signalling allows scale-invariant patterning.

Despite often substantial variability in size, embryos faithfully generate the correct tissue proportions[1–5]. During development, tissue patterning is achieved by gradients of signalling proteins that induce distinct differentiation programmes in discrete spatial domains[6–10]. To adjust tissue patterning and organ proportions to their body size, embryos need to appropriately scale the underlying signalling gradients[11]. Scaling mechanisms for individual tissue-specific signalling systems at different stages of development have been proposed, but how these mechanisms are integrated and coordinated during development to generate the correct proportions of all tissues is currently unclear[11–21]. Here, we analysed how signalling gradients adjust tissue proportions in differently sized zebrafish embryos and identified a size-dependent mechanism that mediates scale-invariant germ-layer patterning to provide the correct amount of progenitor cells for all future tissues.

Results

Scaling of tissue proportions in differently sized zebrafish embryos. We found that the removal of ~30% of cells by extirpation from the animal pole before gastrulation (Fig. 1a) generates zebrafish embryos that become normally patterned adults. Extirpated embryos developed into smaller individuals with the same number of proportionally thinner somites as untreated embryos (Fig. 1a). Consistently, the size of various organs, including the hatching gland (a mesodermal derivative, *hgg1* positive) and the eye (an ectodermal derivative, *vsx2* positive), was reduced in individuals developing from extirpated embryos (Fig. 1b). Strikingly, scaling of tissue proportions to embryo size already occurred during the gastrulation stages within 2 hours following extirpation. Using in situ hybridization, we quantified the extent of the presumptive ectoderm (*sox3* positive; Fig. 1c) and mesendoderm (*fascin* positive; Fig. 1d) and found that the germ-layer proportions adjusted progressively after extirpation: at 1-hour post-extirpation (1 hpe), extirpated embryos had excess mesendoderm and insufficient ectodermal progenitors as cells were removed from the animal pole containing presumptive ectoderm (Fig. 1c,d). Interestingly, 1 hour later (2 hpe), the ectoderm and mesendoderm proportions had adjusted in extirpated embryos (Fig. 1c,d). Using in toto light-sheet imaging, we confirmed that the mesendoderm scaled throughout the embryonic marginal zone (Fig. 1e–g). Even though cells were removed from the animal pole, the number of endodermal precursor cells (*sox17* and *sox32* positive) at the opposite side within the marginal zone of extirpated embryos was also proportionally reduced by the gastrulation stages (Fig. 1h).

Smaller embryos do not adjust developmental speed after extirpation. The cell density did not change (Fig. 2a) and the proliferation rates did not increase in extirpated embryos (Fig. 2b,c), indicating that neither changes in cell density nor compensatory proliferation underlie germ-layer scaling. Moreover, the spatial expression kinetics of *goosecoid*[22]—a highly sensitive indicator of developmental progression—were similar in untreated and extirpated embryos at different developmental time points (Supplementary Fig. 1). Even though smaller embryos displayed a reduced apparent epiboly due to the shortened blastoderm but unchanged yolk extent after extirpation, the spreading of the blastoderm during epiboly occurred at a similar pace (Fig. 2d–i). Thus, scaling can also not be explained by altered developmental speed in differently sized embryos.

Nodal signalling scales in smaller embryos. As the Nodal–Lefty activator–inhibitor system patterns the germ layers during early development[10,23], we hypothesized that Nodal signalling adjusts in smaller embryos to allow proportionate patterning. The activator Nodal is secreted from the marginal zone of the embryo and induces the endoderm and mesoderm, whereas the highly diffusive Nodal inhibitor Lefty[24], which is also expressed at the margin and induced by Nodal signalling, limits the mesendodermal domain[23,25–34]. To test whether Nodal signalling adjusts in smaller embryos, we measured the extent of Nodal activity by assessing the phosphorylation of the Nodal signal transducer Smad2/3 (pSmad2/3)[23,35,36] (Fig. 3a–d and

[1]Friedrich Miescher Laboratory of the Max Planck Society, Tübingen, Germany. [2]Department of Molecular and Cellular Biology, Harvard University, Cambridge, MA, USA. [3]Present address: Centro Andaluz de Biología del Desarrollo, Universidad Pablo de Olavide, Sevilla, Spain.
*e-mail: patrick.mueller@tuebingen.mpg.de

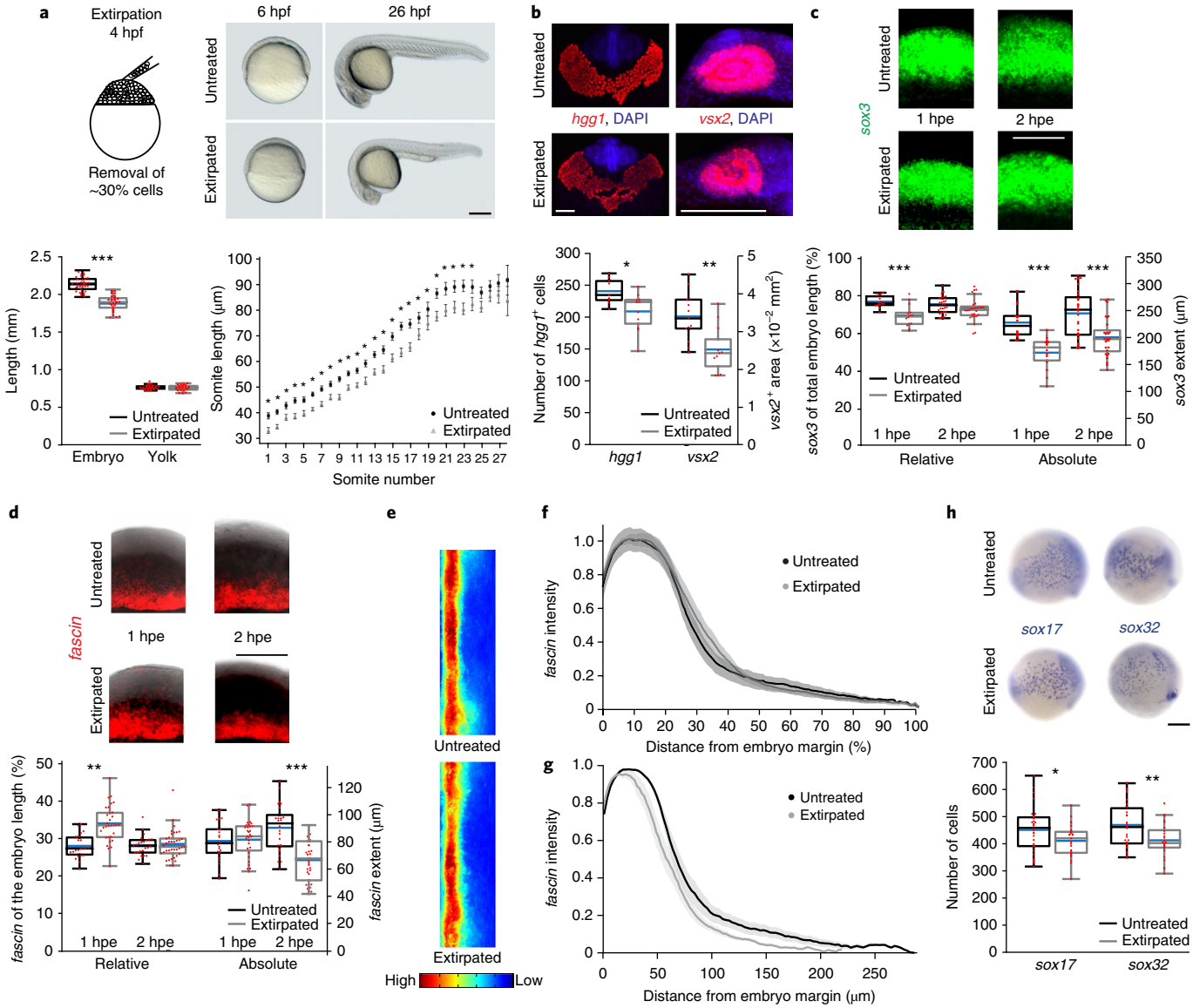

Fig. 1 | Scaling in smaller embryos after extirpation. a, Schematic of embryo extirpation (lateral views); hpf, hours post-fertilization. The total length of extirpated embryos at 1-day post-fertilization is smaller than untreated individuals (n of untreated = 40, n of extirpated = 37; ***$P < 0.00001$), whereas the yolk size remains unchanged (n of untreated = 23, n of extirpated = 24; $P > 0.05$) (bottom left). The length of the 24 posterior-most somites is proportionately smaller in extirpated embryos (bottom right, n of untreated = 15, n of extirpated = 13; *$P < 0.05$). The error bars in the 'Somite length' graph are the s.e.m. **b**, Maximum intensity projections of confocal FISH stacks (top) and the quantification of *hgg1*-positive cells (n of untreated = 9, n of extirpated = 11; *$P < 0.05$) and *vsx2*-positive cells (n of untreated = 13, n of extirpated = 11; **$P < 0.01$) (bottom). **c**,**d**, Maximum intensity projections of lateral confocal FISH stacks (top) and the quantification of the relative and absolute length of *sox3* (ectoderm; **c**) and *fascin* (mesendoderm; **d**) domains (bottom). The ectoderm proportions are smaller at 1 hpe (n of untreated = 14, n of extirpated = 14; ***$P < 0.001$) but scale by 2 hpe (n of untreated = 28, n of extirpated = 28; $P > 0.05$). Similarly, the mesendoderm proportions are too large at 1 hpe (n of untreated = 23, n of extirpated = 31; **$P < 0.01$) but scale by 2 hpe (n of untreated = 24, n of extirpated = 37; $P > 0.05$). **e**–**g**, 2D maps of 3D-reconstructed embryos imaged by light-sheet microscopy (**e**) and the quantification (**f**,**g**) of normalized *fascin* domains along the vegetal–animal axis show scaling (n of untreated = 9, n of extirpated = 9). The shaded regions in **f** and **g** are the s.e.m. **h**, Lateral views and the quantification of the number of endodermal cells positive for *sox17* (n of untreated = 30, n of extirpated = 27; *$P < 0.05$) or *sox32* (n of untreated = 26, n of extirpated = 28; **$P < 0.01$). The box plots show the median (blue line), the mean (black (untreated) and grey (extirpated) lines inside the box), the 25% and 75% quantiles (box) and all included data points (red markers). Whiskers extend to the smallest data point within the 1.5 interquartile range of the lower quartile and to the largest data point within the 1.5 interquartile range of the upper quartile. Two-sided Student's t-tests were performed ($\alpha = 0.05$). See Supplementary Table 1 for statistics source data. Scale bars, 200 μm.

Supplementary Fig. 2a,b). Similar to the mesendodermal domain (Fig. 1e,f), Nodal signalling scaled throughout the embryonic marginal zone by 2 hpe (Fig. 3b,c). Interestingly, Nodal signalling had already scaled by 1 hpe (Fig. 3a and Supplementary Fig. 2a,b), preceding the scaling of the presumptive ectoderm/mesendoderm (Fig. 1c,d) and the feedback-induced Nodals (*cyclops* and *squint*) and Leftys (*lefty1* (*lft1*) and *lefty2* (*lft2*)) (Fig. 3e–i).

A computational screen to identify scaling mechanisms. To identify the mechanism by which Nodal signalling might sense embryo size

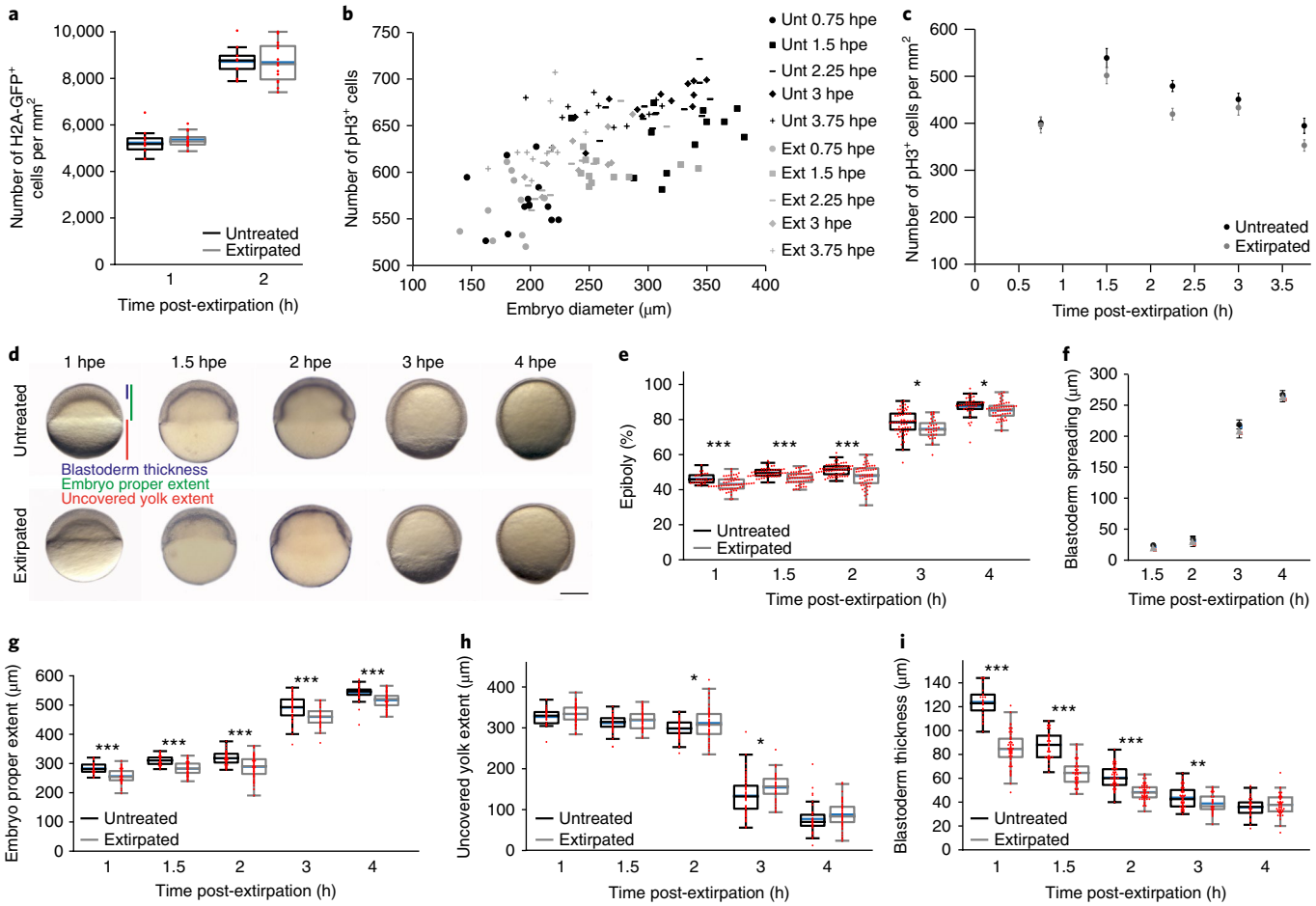

Fig. 2 | Germ-layer proportions scale in extirpated embryos without increases in cell proliferation or changes in cell density or developmental speed. a, Cell density measured in untreated and extirpated H2A-GFP embryos at different time points after extirpation. 1 hpe: *n* of untreated = 10, *n* of extirpated = 14, $P > 0.05$; 2 hpe: *n* of untreated = 9, n of extirpated = 14; $P > 0.05$. **b**,**c**, The number of proliferating cells (pH3 positive) relative to the embryo diameter (**b**) and the density of proliferating cells (**c**) in untreated (Unt) and extirpated (Ext) embryos at different time points after extirpation. 0.75 hpe: *n* of untreated = 13, *n* of extirpated = 11, $P > 0.05$; 1.5 hpe: *n* of untreated = 12, *n* of extirpated = 11, $P > 0.05$; 2.25 hpe: *n* of untreated = 12, *n* of extirpated = 12, $^{**}P < 0.01$; 3 hpe: *n* of untreated = 12, *n* of extirpated = 10, $P > 0.05$; 3.75 hpe: *n* of untreated = 12, *n* of extirpated = 11, $P > 0.05$. Individual data points are shown in **b**; the mean and s.e.m. of the same data are shown in **c**. **d**, Lateral views of untreated and extirpated embryos. The progression of gastrulation and epiboly spreading is unchanged after extirpation. Scale bar, 200 µm. **e**–**i**, Quantification of the epiboly (%) (that is, the ratio of the embryo proper extent to the total length (embryo proper + uncovered yolk) (**e**), blastoderm spreading (that is, the difference between the embryo proper extent at 1.5, 2, 3 and 4 hpe and the embryo proper extent at the first time point of analysis (1 hpe) (**f**), the extent of the embryo proper (**g**), the uncovered yolk (**h**) and the blastoderm thickness (**i**) at different time points after extirpation. 1 hpe: *n* of untreated = 28, *n* of extirpated = 59; 1.5 hpe: *n* of untreated = 51, *n* of extirpated = 55; 2 hpe: *n* of untreated = 62, *n* of extirpated = 58; 3 hpe: *n* of untreated = 59, *n* of extirpated = 33; 4 hpe: *n* of untreated = 38, *n* of extirpated = 55. $^{*}P < 0.05$; $^{**}P < 0.01$; $^{***}P < 0.001$. The mean and s.e.m. are shown in **f**. The box plots show the median (blue line), the mean (black (untreated) and grey (extirpated) lines), 25% and 75% quantiles (box) and all included data points (red markers). Whiskers extend to the smallest data point within the 1.5 interquartile range of the lower quartile and to the largest data point within the 1.5 interquartile range of the upper quartile. Two-sided Student's *t*-tests were performed ($\alpha = 0.05$). See Supplementary Table 1 for statistics source data.

and adjust tissue proportions, we performed a computational screen that included known positive and negative interactions in the Nodal–Lefty system[23,33,34] while keeping model complexity to a minimum (Fig. 4a,b and Supplementary Note 1). We constrained the screen with the measured biophysical properties, including Nodal/Lefty diffusivities and half-lives[33], and systematically varied the unknown parameters to identify systems that recapitulate the scaling observed during germ-layer patterning. To keep model complexity to a minimum, we did not account for spatial biases influencing the Nodal–Lefty system[37] and did not explicitly model receptor interactions[38].

We screened more than 400,000 parameter combinations representing the production of Lefty, the inhibition strength and the Nodal-mediated feedback on Nodal and Lefty production. By assessing the overlap between Nodal signalling in simulations of normally sized and shortened embryos, we found that systems that are capable of scaling require precise levels of highly diffusive Lefty, whose concentration increases in extirpated embryos to adjust the Nodal signalling gradient (Fig. 4c–e). In such systems, the boundary located more proximal to the marginal zone in shortened compared to normally sized embryos affects the long-range Lefty but not the short-range Nodal gradient (Fig. 4c). As we shortened embryos before the onset of Lefty protein secretion without removing *lft*-expressing cells from the marginal zone (Fig. 3e–i), the same amount of Lefty should be produced in early extirpated and untreated embryos. Thus, the concentration of Lefty should increase in smaller embryos, contracting the Nodal activity range to re-establish the correct tissue dimensions relative to the new size of the embryo.

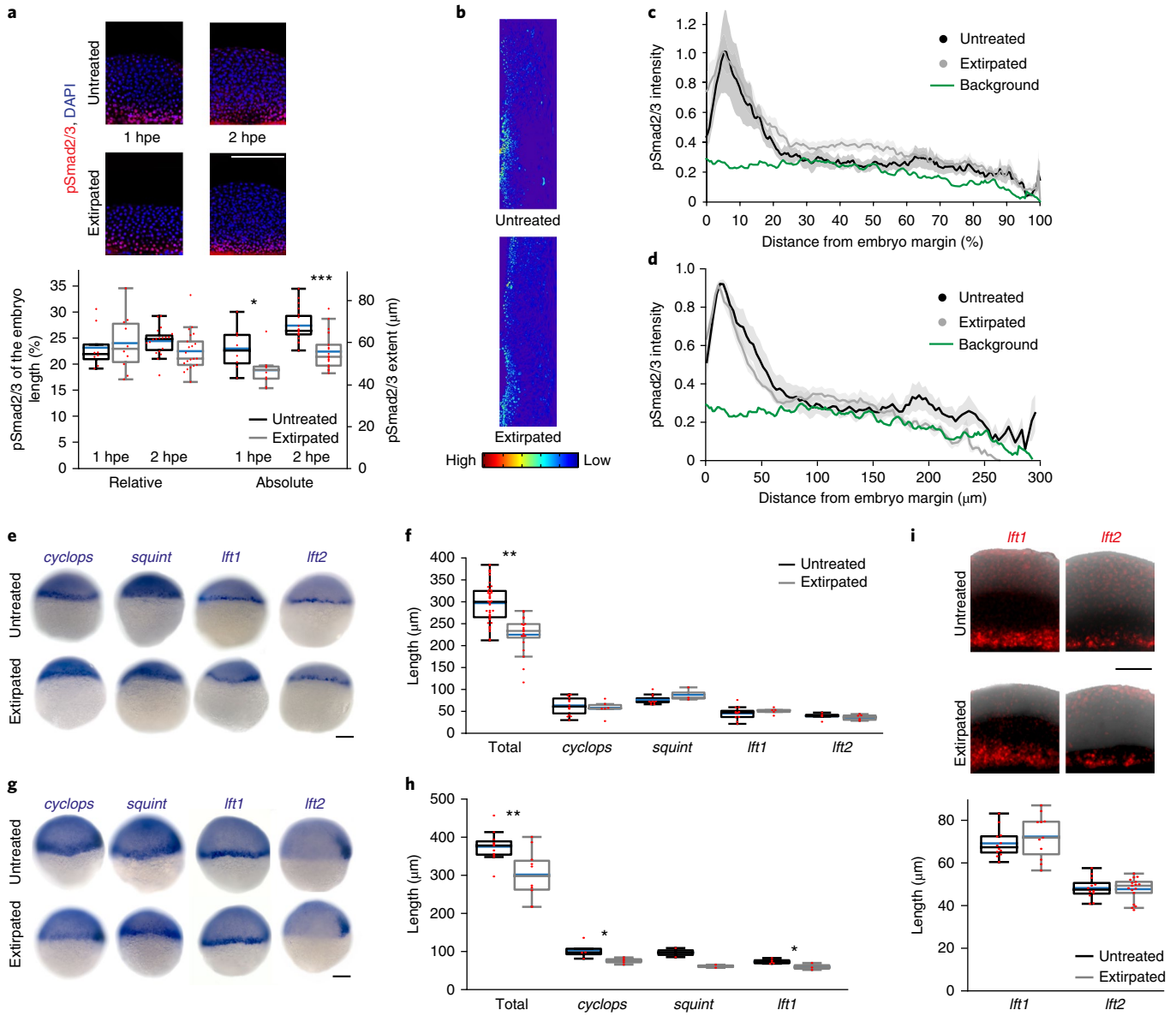

Fig. 3 | Scaling of Nodal-mediated patterning. a, Maximum intensity projections of lateral confocal pSmad2/3 immunostaining stacks (top) and the quantification of the absolute and relative length of the pSmad2/3 domain (bottom). 1 hpe: *n* of untreated = 7, *n* of extirpated = 10; 2 hpe: *n* of untreated = 19, *n* of extirpated = 21. **b**–**d**, 2D maps of 3D-reconstructed embryos imaged by light-sheet microscopy (**b**) and the quantification of normalized pSmad2/3 domains along the vegetal–animal axis show scaling (*n* of untreated = 5, *n* of extirpated = 6). Intensity as a function of embryo length (%) (**c**) and intensity as a function of the absolute distance from the margin (**d**) are shown. The shaded regions in **c** and **d** are the s.e.m. **e**–**h**, Lateral images showing the expression of *cyclops* and *squint* Nodals and *lft1* and *lft2* Leftys in untreated and extirpated embryos at 1 hpe (**e**) and 2 hpe (**g**), and the quantification of embryo length and expression domains at 1 hpe (**f**) and 2 hpe (**h**). 1 hpe: total: *n* of untreated = 42, *n* of extirpated = 20; *cyclops*: *n* of untreated = 14, *n* of extirpated = 6; *squint*: *n* of untreated = 11, *n* of extirpated = 3; *lft1*: *n* of untreated = 12, *n* of extirpated = 5; *lft2*: *n* of untreated = 5, *n* of extirpated = 6. 2 hpe: total: *n* of untreated = 11, *n* of extirpated = 10; *cyclops*: *n* of untreated = 4, *n* of extirpated = 5; *squint*: *n* of untreated = 2, *n* of extirpated = 2; *lft1*: *n* of untreated = 5, *n* of extirpated = 3. Nodal and Lefty domains are unchanged in differently sized embryos at 1 hpe but scale by 2 hpe. **i**, Maximum intensity projections of lateral confocal *lft1* and *lft2* FISH stacks in untreated and extirpated embryos at 1 hpe (top) and the quantification of expression domains (bottom). *lft1*: *n* of untreated = 12, *n* of extirpated = 11; *lft2*: *n* of untreated = 12, *n* of extirpated = 17. The box plots show the median (blue line), the mean (black (untreated) and grey (extirpated) lines), 25% and 75% quantiles (box) and all included data points (red markers). Whiskers extend to the smallest data point within the 1.5 interquartile range of the lower quartile and to the largest data point within the 1.5 interquartile range of the upper quartile. Two-sided Student's *t*-tests were performed ($\alpha = 0.05$). $^*P < 0.05$; $^{**}P < 0.01$; $^{***}P < 0.001$. See Supplementary Table 1 for statistics source data. Scale bars, 200 μm (**a**,**e**,**g**) and 100 μm (**i**).

In our simulations of the Nodal–Lefty system (Supplementary Video 1), scale-invariant germ-layer patterning only became apparent around 2 hpe, as observed experimentally (Fig. 1c,d). The simulations further closely matched the time window of germ-layer specification: Nodal signalling levels and mesendoderm specification expand as development proceeds, Nodal signalling levels peak around 2 hpe (6 hours post-fertilization (6 hpf)) and Nodal signalling rapidly decreases afterwards (Supplementary Video 1). Together, the experimental observations and computational simulations suggest that germ-layer scaling at 2 hpe results from

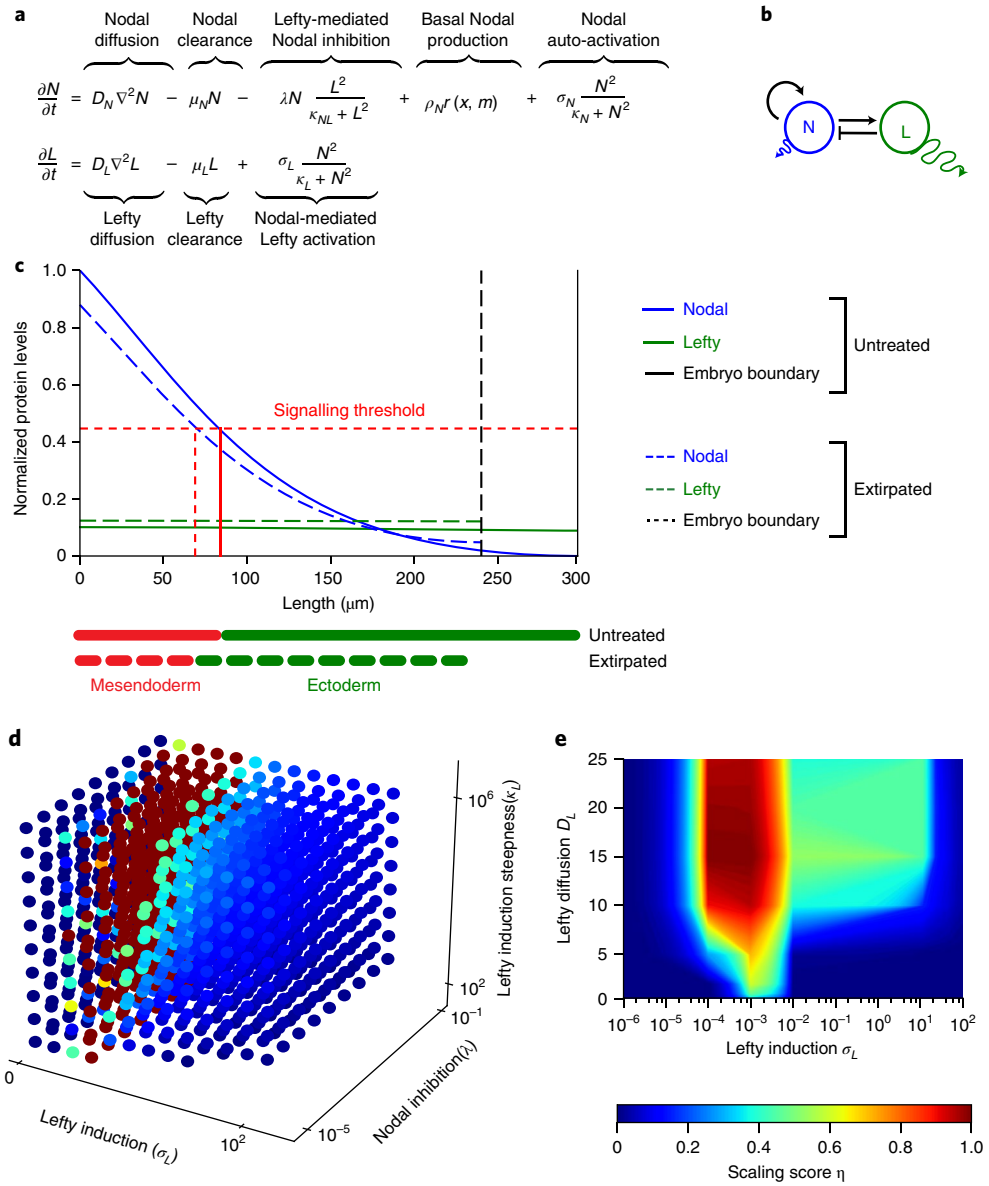

Fig. 4 | Computational screen for parameters conferring scale invariance. a,**b**, Equations (**a**) and network (**b**) describing the known interactions in the Nodal (N)–Lefty (L) activator–inhibitor system. The change in Nodal concentration over time (t) is a function of Nodal diffusion with the diffusion coefficient D_N, Nodal removal with the clearance rate constant μ_N, Lefty-mediated Nodal inhibition with the inhibition strength λ and the steepness parameter κ_{NL}, basal Nodal production described by the space (x)-dependent rectangular pulse function $r(x,m)$ representing the length m of the Nodal source, and Nodal auto-activation with the rate constant σ_N and the steepness parameter κ_N. Similarly, the change in Lefty concentration over time is a function of Lefty diffusion with the diffusion coefficient D_L, Lefty removal with the clearance rate constant μ_L, and Nodal-dependent Lefty induction with the rate constant σ_L and the steepness parameter κ_L. **c**, Example of a scale-invariant system identified by the screen, showing an increase in Lefty and dampening of Nodal signalling after extirpation. Simulations were fitted to the experimentally measured total length and mesendoderm extent (vertical red solid (untreated) and dashed (extirpated) lines). **d**, A parameter screen showing the influence of Lefty levels (σ_L), Nodal inhibition strength (λ) and Lefty induction steepness (κ_L) on scaling; the maximum projection through the six-dimensional parameter space is shown with the following discrete values: for σ_L: 0, 10^{-4}, 10^{-3}, 10^{-2}, 11.12, 22.23, 33.34, 44.45, 55.56, 66.67, 77.78, 88.89 and 10^2; for λ: 10^{-5}, 1.12×10^{-2}, 2.23×10^{-2}, 3.34×10^{-2}, 4.45×10^{-2}, 5.56×10^{-2}, 6.67×10^{-2}, 7.78×10^{-2}, 8.89×10^{-2} and 10^{-1}; for κ_L: 10^2, 1.12×10^5, 2.23×10^5, 3.34×10^5, 4.45×10^5, 5.56×10^5, 6.67×10^5, 7.78×10^5, 8.89×10^5 and 10^6. Parameter configurations that resulted in biologically unrealistic gradients were excluded. **e**, A parameter screen showing the influence of Lefty diffusivity on scaling; the maximum projection through the six-dimensional parameter space is shown. The model predicts that scaling should fail if Lefty induction (σ_L) or diffusion (D_L) is too low (that is, less than ~7 μm^2 s^{-1}).

adjustments in mesendoderm expansion dynamics over time rather than from shrinking an initially too broadly specified mesendodermal domain.

Scaling depends on Lefty levels. Our model predicted that scaling crucially depends on the levels of Lefty (Figs. 4d and 5a,b). To test this prediction, we assessed mesendoderm proportions in embryos with varying numbers of functional *lft* alleles (*lft1* and *lft2*)[36]. As expected, both untreated and extirpated double-homozygous *lft1*$^{-/-}$; *lft2*$^{-/-}$ mutants showed dramatically increased Nodal signalling and an expanded mesendoderm[36] (Fig. 5c–g and Supplementary Fig. 3a–c). By contrast, untreated and shortened double-heterozygous

lft1$^{+/-}$;*lft2*$^{+/-}$ embryos exhibited nearly normal Nodal signalling and mesendoderm and ectoderm proportions, indicating that one functional allele of each *lft* is sufficient for proper spatial Nodal signalling and scaling, possibly due to dosage adjustments that result in similar amounts of protein (Fig. 5c–h and Supplementary Fig. 3a–c). Normally sized and extirpated single-homozygous *lft2*$^{-/-}$ mutants had excess Nodal signalling and mesendoderm at the expense of the ectoderm (Fig. 5c–h and Supplementary Fig. 3a–c). By striking contrast, single-homozygous *lft1*$^{-/-}$ embryos displayed expanded Nodal signalling and mesendoderm and a reduced ectoderm only after extirpation (Fig. 5c–h and Supplementary Fig. 3a–c). Interestingly, Lefty1 is less inhibitory than its paralogue Lefty2 (Supplementary Fig. 3d,e); thus, although highly active Lefty2 is sufficient for germ-layer patterning in normally sized embryos, the correct levels of less-active Lefty1 are required for scale-invariant patterning in substantially smaller embryos. These experimental findings support the simulations of our size-dependent inhibition model (Figs. 4d and 5a,b), showing that a small reduction in Lefty production, which does not significantly affect mesendoderm formation, abrogates scaling.

Scaling depends on highly diffusive Lefty. The second prediction of our model is that scaling depends on the high diffusivity of Lefty, which must reach the end of the patterning field (Figs. 4e and 6a,b). To test this prediction, we decreased Lefty diffusivity and determined the consequences on scaling. To obtain a patterning system in which the diffusion of Lefty1 can be experimentally manipulated, we first generated embryos in which the only source of Lefty was Lefty1-GFP (green fluorescent protein). We rescued *lft1*$^{-/-}$;*lft2*$^{-/-}$ double mutants by injecting highly precise and physiologically relevant amounts (see Methods for details) of *lft1-GFP* mRNA into the yolk syncytial layer (YSL) to mimic the secretion of endogenous Lefty from the marginal zone (Fig. 6c). Consistent with the high diffusivity of Lefty[33,39], Lefty1-GFP reached the end of the patterning field within 60 minutes after YSL injection (Fig. 6d,e and Supplementary Video 2). A large proportion of *lft1*$^{-/-}$;*lft2*$^{-/-}$ mutant embryos was rescued to adulthood with this method in normally sized (~70% fully or partially rescued) and extirpated (~60% fully or partially rescued) embryos (Fig. 6f–h and Supplementary Fig. 4a–d). Thus, Lefty1-GFP provided from the marginal zone is sufficient not only to pattern germ layers but also to allow scaling. Next, to hinder Lefty1-GFP diffusion, we used a 'morphotrap'—an mCherry-labelled membrane-localized GFP-binding nanobody[40]. Co-injection of mRNA encoding the morphotrap and *lft1-GFP* mRNA into one-cell-stage embryos changed the localization of Lefty1-GFP from uniform extracellular to strongly membrane associated (Supplementary Fig. 4e). Crucially, the diffusion coefficient (D) of Lefty1-GFP in embryos expressing the morphotrap was significantly lower ($D = 7.7 \pm 3.2\,\mu m^2\,s^{-1}$ for Lefty1-GFP and $0.2 \pm 0.2\,\mu m^2\,s^{-1}$ for Lefty1-GFP + morphotrap (mean ± s.d.); Fig. 6i,j). In addition, the activity of Lefty was decreased by morphotrap binding (Supplementary Fig. 4f,g).

We then injected mRNA encoding the morphotrap into *lft1*$^{-/-}$;*lft2*$^{-/-}$ mutant embryos at the one-cell stage and generated local sources of Lefty1-GFP at the marginal zone (Fig. 6d,e). The expression of the morphotrap dramatically changed the range of Lefty1-GFP from a nearly uniform distribution to a short-range gradient that did not reach the end of the embryo (Fig. 6d,e and Supplementary Videos 2 and 3). In normally sized embryos, hindered Lefty diffusion did not significantly affect germ-layer patterning (Fig. 6f–h), possibly owing to decreased Lefty activity in the presence of morphotrap (Supplementary Fig. 4f,g). The change in Lefty distribution correlated with a steep drop in the rescue of extirpated embryos (Fig. 6f,g) and with an expanded mesendoderm (Fig. 6h and Supplementary Fig. 4c,d). Simulations of the size-dependent inhibition model with hindered Lefty diffusion recapitulated the experimentally observed change in Lefty distribution (Fig. 6a,b,d,e): the decreased Lefty range precludes scaling of Nodal signalling as Lefty cannot reach the distal end of the patterning field. Together, these observations show that hindering Lefty diffusion prevents scaling in extirpated embryos, supporting the prediction of the size-dependent inhibition model.

Lefty concentration increases in smaller embryos. The third prediction of our model is that the inhibitor concentration increases to reduce Nodal signalling in extirpated embryos (Figs. 4c and 7a), whereas the total amount of Lefty should slightly decrease over time due to feedback regulation (Fig. 7b). To test this prediction, we used quantitative immunoblotting and measured the amount of endogenous Lefty1 and histone H3 as a proxy for cellular mass. Histone H3 levels were reduced by approximately one-third after extirpation (Supplementary Fig. 5a–c). Importantly, the histone H3 signal intensity increased proportionally when 5, 10 or 15 embryos were loaded, showing that changes in total protein can be detected reliably (Supplementary Fig. 5c). The decrease in Lefty1 amounts in extirpated embryos was less pronounced than histone H3 levels, resulting in an increased Lefty1 concentration as predicted by the model (Supplementary Fig. 5b). However, Lefty1 intensities detected by the only currently available antibody against a zebrafish Lefty[35] were low (Supplementary Fig. 5a and see Supplementary Fig. 8 for unprocessed data); sufficient Lefty1 levels could only be reliably detected after 50% epiboly stages, so that earlier dynamics of potential changes in Lefty1 levels could not be analysed. To corroborate these findings and to uncouple the rise in Lefty concentration from feedback regulation, we quantified the GFP intensity after injection of physiologically relevant amounts of *lft1-GFP* mRNA in the YSL and found that extirpated embryos exhibited a higher GFP intensity than normally sized embryos (Fig. 7c).

Exogenous inhibitor can mediate scaling in lieu of Lefty. To assess whether this increase in inhibitor concentration is required for germ-layer scaling, we analysed mesendoderm patterning in untreated and extirpated *lft1*$^{-/-}$;*lft2*$^{-/-}$ mutants upon exposure to the small-molecule Nodal inhibitor SB-505124 (ref. [36]). In contrast to the YSL injection rescue approach, a reduction in embryo size should not affect the concentration of the tonic Nodal inhibitor in this experimental setup (Supplementary Fig. 6a–d). A large fraction of untreated *lft1*$^{-/-}$;*lft2*$^{-/-}$ mutants (~90%; Fig. 7d,e) was rescued by 4.8 µM of Nodal inhibitor exposure. By contrast, exposure of extirpated *lft1*$^{-/-}$;*lft2*$^{-/-}$ mutants to the same inhibitor concentration resulted in abnormal mesendoderm proportions and only ~30% displayed some phenotypic rescue (Fig. 7d,e and Supplementary Fig. 6e,f). These results show that tonic size-independent inhibition levels that are effective in normally sized embryos do not allow scaling, as the inhibitor concentration cannot increase in shortened embryos.

Our model implies that increasing tonic Nodal inhibitor levels should restore the appropriate Nodal signalling range in extirpated embryos. Consistent with this prediction, increasing the exposure of the small-molecule Nodal inhibitor from 4.8 µM to 6–7 µM significantly improved the rescue of extirpated *lft1*$^{-/-}$;*lft2*$^{-/-}$ mutants from ~26% to ~64% (Fig. 7e and Supplementary Fig. 6g), demonstrating that increased inhibitor levels are required for scaling in extirpated embryos.

Discussion

Together, four lines of evidence suggest that scale-invariant germ-layer patterning is achieved by size-dependent inhibition of Nodal signalling. First, the reduction of Lefty levels (Fig. 5) precludes scaling. Second, decreasing Lefty diffusivity interferes with scale-invariant patterning (Fig. 6). Third, the concentration of the Nodal inhibitor Lefty increases in extirpated embryos (Fig. 7c and

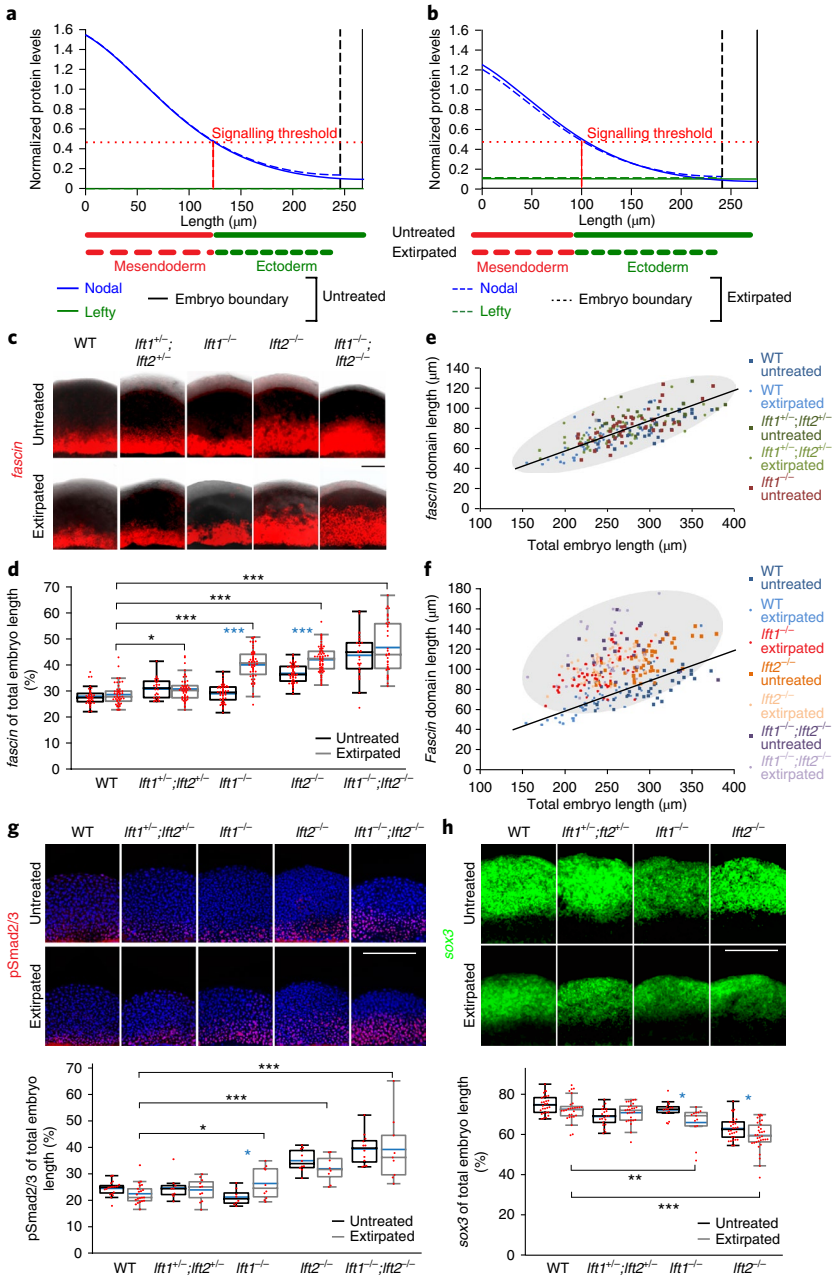

Fig. 5 | Germ-layer scaling depends on Lefty levels. a,**b**, Simulations of the size-dependent inhibition predict that, in the absence of Lefty, the mesendoderm is extended and does not scale (**a**), whereas reduced Lefty induction should prevent scaling in shortened embryos without a significant change in mesendoderm specification in normally sized individuals (**b**). **c**, Maximum intensity projections of lateral confocal stacks of *fascin* FISH in untreated and extirpated embryos with different numbers of *lft* alleles. **d**, Quantification of *fascin*-positive mesendoderm proportions. The asterisks show differences between untreated and extirpated embryos (blue asterisks) and between WT and *lft* mutant extirpated embryos (black asterisks) (*$P<0.05$, ***$P<0.001$). **e**,**f**, Quantification of *fascin* relative to embryo length. The data for WT untreated and extirpated are plotted in both **e** and **f**. For the *lft* mutants, the encircled domains cluster two groups: group 1 shows a similar mesendoderm proportion as WT individuals and a linear increase of mesendoderm with embryo size (**e**), whereas group 2 clusters in a wider domain with larger mesendodermal proportions, indicating an absence of scaling (**f**). In **c**–**f**, WT: *n* of untreated = 38, *n* of extirpated = 49; *lft1*$^{+/-}$;*lft2*$^{+/-}$: *n* of untreated = 26, *n* of extirpated = 55; *lft1*$^{-/-}$: *n* of untreated = 50, *n* of extirpated = 58; *lft2*$^{-/-}$: *n* of untreated = 50, *n* of extirpated = 63; *lft1*$^{-/-}$;*lft2*$^{-/-}$: *n* of untreated = 29, *n* of extirpated = 34. **g**,**h**, Maximum intensity projections of lateral confocal pSmad2/3 immunostaining (**g**) and *sox3* FISH stacks (**h**), and quantification in 2 hpe embryos with different numbers of *lft* alleles. For pSmad2/3: WT: *n* of untreated = 19, *n* of extirpated = 21; *lft1*$^{+/-}$;*lft2*$^{+/-}$: *n* of untreated = 10, *n* of extirpated = 11; *lft1*$^{-/-}$: *n* of untreated = 8, *n* of extirpated = 10; *lft2*$^{-/-}$: *n* of untreated = 9, *n* of extirpated = 8; *lft1*$^{-/-}$;*lft2*$^{-/-}$: *n* of untreated = 12, *n* of extirpated = 9. For *sox3*: WT: *n* of untreated = 28, *n* of extirpated = 28; *lft1*$^{+/-}$;*lft2*$^{+/-}$: *n* of untreated = 21, *n* of extirpated = 27; *lft1*$^{-/-}$: *n* of untreated = 14, *n* of extirpated = 13; *lft2*$^{-/-}$: *n* of untreated = 30, *n* of extirpated = 33. The asterisks show differences between untreated and extirpated embryos (blue asterisks) and between extirpated WT and *lft* mutant embryos (black asterisks) (*$P<0.05$; **$P<0.01$; ***$P<0.001$). The box plots show the median (blue line), the mean (black (untreated) and grey (extirpated) lines), 25% and 75% quantiles (box) and all included data points (red markers). Whiskers extend to the smallest data point within the 1.5 interquartile range of the lower quartile and to the largest data point within the 1.5 interquartile range of the upper quartile. Two-sided Student's *t*-tests were performed ($\alpha = 0.05$). See Supplementary Table 1 for statistics source data. Scale bars, 70 μm (**c**) and 200 μm (**g**,**h**).

Supplementary Fig. 5b). Fourth, the rescue of extirpated *lft1*$^{-/-}$;*lft2*$^{-/-}$ mutants requires higher amounts of a Nodal inhibitor drug than non-extirpated mutants (Fig. 7e and Supplementary Fig. 6g). In agreement with our mathematical model (Fig. 4, Supplementary Fig. 7 and Supplementary Note 1), these results support the idea that the concentration and high diffusivity of Lefty are essential to adjust germ-layer proportions.

The initial computational screen used *fascin* as a proxy for mesendoderm formation, which, in addition to Nodal, is also under the control of fibroblast growth factor (FGF) signalling[10,35]. For the simplified screening model, we subsumed the action of Nodal and FGF into one effective signalling gradient, as the induction of both *fgf* and *fascin* depends on Nodal signalling[35,41–44], Nodal and FGF signals have similar effective mobilities in zebrafish embryos[33,39], and the range of *fascin* can be changed by Lefty-dependent modulation of Nodal signalling[32,33]. Thus, our conclusions are not affected by how FGF, acting downstream of Nodal signalling, helps to regulate *fascin* expression together with Nodal. In more-refined simulations, we demonstrate the plausibility of our model for Nodal signalling based on pSmad2/3 activity (Supplementary Fig. 7m,n), a direct readout of Nodal activity. Although tissue proportions might be further refined by interactions with other signalling pathways, such as bone morphogenetic protein (BMP) and FGF[10,35,43,45] (Supplementary Fig. 7o,p and Supplementary Note 1), the scaled distribution of the Nodal signal transducer pSmad2—which is independent of BMP and FGF—and the scaled tissue proportions in *lft* mutants rescued by feedback-uncoupled Lefty—in which Lefty production is not under any transcriptional regulation—demonstrate the central role of Lefty in germ-layer scaling.

In agreement with previous findings[10,36,46,47], our results suggest that Nodal-mediated germ-layer patterning is robust to variations in signalling. Although the mesendoderm is significantly expanded in *lft1*$^{-/-}$ extirpated and *lft2*$^{-/-}$ untreated embryos (Supplementary Fig. 3c), most of them develop with normal morphology (Fig. 5 and

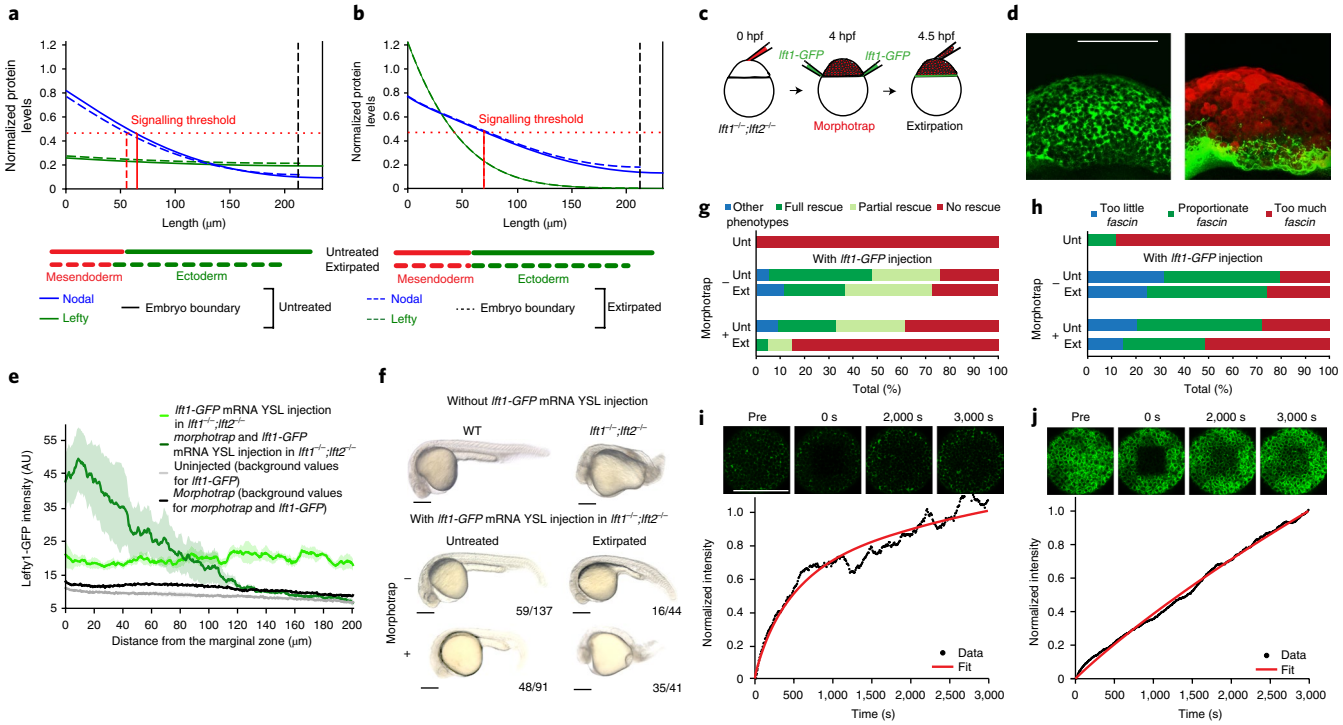

Fig. 6 | High Lefty diffusivity is required for scaling. a,**b**, Simulations of the model without feedback inhibition (*lft1-GFP* injected in the YSL; **a**) and hindered Lefty diffusion (morphotrap binds to *lft1-GFP*; **b**) predict that a reduction in Lefty diffusivity—preventing Lefty from reaching the animal pole—should preclude scaling. **c**, Schematic of morphotrap-mediated Lefty1-GFP diffusion hindrance in extirpated embryos. **d**, Maximum intensity projections of confocal stacks of *lft1*$^{-/-}$;*lft2*$^{-/-}$ embryos injected with (right panel) or without (left panel) morphotrap (injected at the one-cell stage) and *lft1-GFP* mRNA in the YSL (injected at the sphere stage). Lateral views are shown. **e**, Spatial distribution of Lefty1-GFP secreted from the YSL. The morphotrap prevents spreading of Lefty1-GFP towards the animal pole of the embryo. *n* of *lft1-GFP* mRNA injection = 6, *n* of *morphotrap* + *lft1-GFP* mRNA injection = 3, *n* of background values = 1, *n* of background values for morphotrap = 2. The experimentally determined distributions of Lefty1-GFP with morphotrap-mediated diffusion hindrance resemble the simulation of the scenario in **b**. The shaded regions are the s.e.m. **f**, Lateral views of representative 26 hpf *lft1*$^{-/-}$;*lft2*$^{-/-}$ embryos with different treatments. The numbers in the figure panel indicate the fraction of these representative embryos. **g**, Phenotype distributions in *lft1*$^{-/-}$;*lft2*$^{-/-}$ embryos after different treatments (*n* of *lft1*$^{-/-}$;*lft2*$^{-/-}$ = 39; *lft1*$^{-/-}$;*lft2*$^{-/-}$ + *lft1-GFP*: *n* of untreated (Unt) = 137, *n* of extirpated (Ext) = 44; *lft1*$^{-/-}$;*lft2*$^{-/-}$ + *morphotrap* + *lft1-GFP*: *n* of untreated = 91, *n* of extirpated = 44). Embryos with partial rescue display imperfect tails and reduced cephalic structures (that is, very mild Lefty mutant phenotypes). **h**, The fraction of treated *lft1*$^{-/-}$;*lft2*$^{-/-}$ embryos with low (<22%), normal (22–33%) and high (>34%) mesendoderm proportions (*n* of *lft1*$^{-/-}$;*lft2*$^{-/-}$ = 44; *lft1*$^{-/-}$;*lft2*$^{-/-}$ + *lft1-GFP*: *n* of untreated = 67, *n* of extirpated = 66; *lft1*$^{-/-}$;*lft2*$^{-/-}$ + *morphotrap* + *lft1-GFP*: *n* of untreated = 35, *n* of extirpated = 37). The fraction of rescued and non-rescued *lft1*$^{-/-}$;*lft2*$^{-/-}$ embryos correlates with the fraction of normal and high mesendoderm proportions in **g** and **h**. **i**,**j**, FRAP experiments demonstrate that Lefty1-GFP diffusion is hindered by the morphotrap. Representative FRAP data for Lefty1-GFP (**i**) and Lefty1-GFP with morphotrap (**j**) are shown. Microscopy images are shown before photobleaching (Pre), immediately after (0 s), as well at 2,000 s and 3,000 s after photobleaching. Diffusion coefficients and production rates were fitted to the recovery curves using previously published values for Lefty1-GFP protein stability[33]. The mean (±s.d.) diffusion coefficients were 7.7 ± 3.2 μm^2 s^{-1} for Lefty1-GFP (from *n* = 6 independent experiments) and 0.2 ± 0.2 μm^2 s^{-1} for Lefty1-GFP with morphotrap (from *n* = 4 independent experiments). See Supplementary Table 1 for statistics source data. Scale bars, 200 μm (**d**,**f**,**i**,**j**).

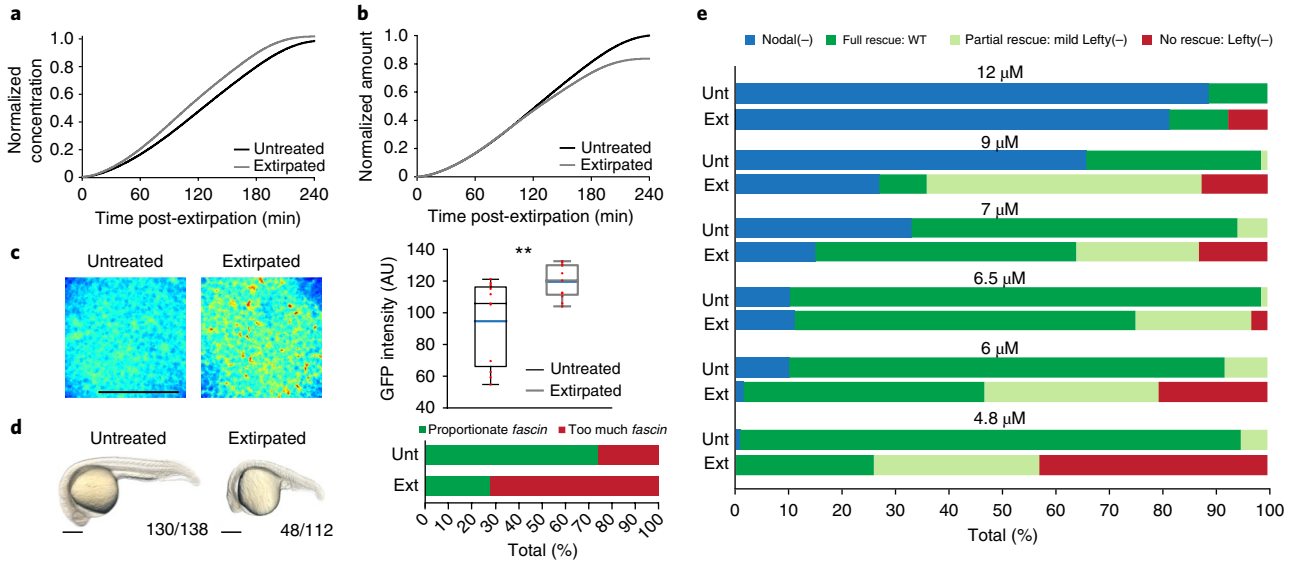

Fig. 7 | Lefty concentration increases in smaller embryos to allow scaling. a, The increase in Lefty concentration over time in smaller embryos predicted by the size-dependent inhibition model. **b**, The decrease in Lefty amount over time in smaller embryos predicted by the size-dependent inhibition model. **c**, Animal pole views of the maximum intensity confocal stack projections of WT untreated and extirpated embryos injected with *lft1-GFP* mRNA in the YSL (left) and the quantification of GFP intensity; $^{**}P < 0.01$; *n* of untreated = 11, *n* of extirpated = 11 (right). The box plot shows the median (blue line), the mean (black (untreated) and grey (extirpated) lines), 25% and 75% quantiles (box) and all included data points (red markers). Whiskers extend to the smallest data point within the 1.5 interquartile range of lower quartile and to the largest data point within the 1.5 interquartile range of the upper quartile. Two-sided Student's *t*-test were performed ($\alpha = 0.05$). **d**, Lateral views of representative 26 hpf *lft1*$^{-/-}$;*lft2*$^{-/-}$ embryos exposed to 4–4.8 µM of the Nodal inhibitor SB-505124. The numbers in the figure panel indicate the fraction of these representative embryos. Mesendoderm quantification (right panel) of *lft1*$^{-/-}$;*lft2*$^{-/-}$ embryos exposed to 4–4.8 µM of the Nodal inhibitor SB-505124 (*n* of untreated (Unt) = 27, *n* of extirpated (Ext) = 18). **e**, Phenotype quantification in *lft1*$^{-/-}$;*lft2*$^{-/-}$ embryos exposed to different concentrations of the Nodal inhibitor SB-505124. Untreated: 4.8 µM: *n* = 138, 6 µM: *n* = 160, 6.5 µM: *n* = 80, 7 µM: *n* = 106, 9 µM: *n* = 85, 12 µM: *n* = 36. Extirpated: 4.8 µM: *n* = 77, 6 µM: *n* = 146, 6.5 µM: *n* = 64, 7 µM: *n* = 108, 9 µM: *n* = 56, 12 µM: *n* = 27. Exposure to higher concentrations of the Nodal inhibitor SB-505124 increases *lft1*$^{-/-}$;*lft2*$^{-/-}$ mutant rescue after extirpation. The fraction of rescued and non-rescued *lft1*$^{-/-}$;*lft2*$^{-/-}$ embryos correlates with the fraction of normal and high mesendoderm proportions in **d**. See Supplementary Table 1 for statistics source data. Scale bars, 200 µm (**c**,**d**).

Supplementary Fig. 3b). This suggests that embryos can adapt to a certain degree of mesendoderm expansion, possibly up to ~42% (Supplementary Fig. 3a–c). However, this margin of tolerance is reduced in *lft1*$^{-/-}$;*lft2*$^{-/-}$ embryos rescued with YSL-expressed Lefty1-GFP, and an increase in the mesendoderm domain above ~35% in this context seems to invariably prevent phenotypic rescue. Thus, patterning robustness might arise from Nodal–Lefty regulatory feedback, which is absent in *lft1*$^{-/-}$;*lft2*$^{-/-}$ mutant embryos but present in embryos with at least one intact Lefty paralogue.

Previously postulated feedback-dependent scaling systems rely on modulators whose concentrations change depending on tissue size to adjust the signalling activity range by modulating the diffusion or clearance of the signal[11,14,48–56]. The Nodal–Lefty activator–inhibitor system is an excellent candidate for a modulator-based scaling mechanism: (1) Lefty (modulator) inhibits Nodal activity by binding and preventing it from activating its receptors, (2) the Nodal activity range is unaffected by the size reduction in extirpated embryos, as the Nodal distribution is restricted to the marginal zone owing to its low diffusivity[33], (3) Lefty diffuses significantly faster than Nodal and exhibits a nearly uniform distribution[33,36] (Figs. 4c and 6d,e,i and Supplementary Video 2), and (4) the production of Lefty is largely independent of the changes in size as Lefty-producing cells are located at the margin, which remains unaffected immediately following extirpation (Fig. 3e–i). An example of a modulator-based scaling mechanism is the recently proposed 'expansion–repression' model, in which scaling of signalling gradients is achieved by an expander that increases the range of the signal and that is itself repressed by the signal[51]. Superficially, our model can be interpreted as a mirror image of the 'expansion–repression' model—that is, a 'contraction–activation' system—as the 'inhibitor' (or the 'contractor') Lefty restricts the range of the signal (Nodal) and is activated by the signal. However, our theoretical model does not depend on feedback between the signal and the modulator. Because in our system the modulator inhibits the signal, it is sufficient to couple the changes in the concentration of the inhibitor to size to confer proportionate patterning. Similarly, we showed experimentally that Nodal-mediated Lefty activation is dispensable for scaling (Figs. 6 and 7 and Supplementary Figs. 4 and 6). This suggests that scale-invariant patterning is purely based on size-dependent Nodal inhibition that is mediated by Lefty, providing a foundation for the proportionate allocation of all future tissues.

The scaling mechanism that we found crucially depends on the coupling of the inhibitor concentration to embryo size, which is conferred by the high diffusivity of Lefty. Strikingly, a similar mechanism based on the coupling of cell volume to the concentration of a cell-cycle inhibitor has recently been found to control cell size in yeast[57]. Thus, it is possible that this simple mechanism might be widespread across various levels of biological organization to coordinate growth with cellular functions and patterning.

Methods

Methods, including statements of data availability and any associated accession codes and references, are available at https://doi.org/10.1038/s41556-018-0155-7.

Received: 2 August 2017; Accepted: 27 June 2018;
Published online: 30 July 2018

References

1. Morgan, T. H. Half embryos and whole embryos from one of the first two blastomeres. *Anat. Anz.* **10**, 623–685 (1895).
2. Cooke, J. Control of somite number during morphogenesis of a vertebrate, *Xenopus laevis*. *Nature* **254**, 196–199 (1975).
3. Inomata, H. Scaling of pattern formations and morphogen gradients. *Dev. Growth Differ.* **59**, 41–51 (2017).
4. Garcia, M., Nahmad, M., Reeves, G. T. & Stathopoulos, A. Size-dependent regulation of dorsal–ventral patterning in the early *Drosophila* embryo. *Dev. Biol.* **381**, 286–299 (2013).
5. Lauschke, V. M., Tsiairis, C. D., Francois, P. & Aulehla, A. Scaling of embryonic patterning based on phase-gradient encoding. *Nature* **493**, 101–105 (2013).
6. Kicheva, A. et al. Kinetics of morphogen gradient formation. *Science* **315**, 521–525 (2007).
7. Wartlick, O., Kicheva, A. & González-Gaitán, M. Morphogen gradient formation. *Cold Spring Harb. Perspect. Biol.* **1**, a001255 (2009).
8. Yu, S. R. et al. Fgf8 morphogen gradient forms by a source–sink mechanism with freely diffusing molecules. *Nature* **461**, 533–536 (2009).
9. Rogers, K. W. & Schier, A. F. Morphogen gradients: from generation to interpretation. *Annu. Rev. Cell Dev. Biol.* **27**, 377–407 (2011).
10. Rogers, K. W. & Müller, P. Nodal and BMP dispersal during early zebrafish development. *Dev. Biol.* https://doi.org/10.1016/j.ydbio.2018.04.002 (2018).
11. Umulis, D. M. & Othmer, H. G. Mechanisms of scaling in pattern formation. *Development* **140**, 4830–4843 (2013).
12. Gregor, T., Bialek, W., de Ruyter van Steveninck, R. R., Tank, D. W. & Wieschaus, E. F. Diffusion and scaling during early embryonic pattern formation. *Proc. Natl Acad. Sci. USA* **102**, 18403–18407 (2005).
13. Gregor, T., McGregor, A. P. & Wieschaus, E. F. Shape and function of the bicoid morphogen gradient in dipteran species with different sized embryos. *Dev. Biol.* **316**, 350–358 (2008).
14. Ben-Zvi, D., Shilo, B.-Z., Fainsod, A. & Barkai, N. Scaling of the BMP activation gradient in *Xenopus* embryos. *Nature* **453**, 1205–1211 (2008).
15. Ben-Zvi, D., Pyrowolakis, G., Barkai, N. & Shilo, B. Z. Expansion–repression mechanism for scaling the Dpp activation gradient in *Drosophila* wing imaginal discs. *Curr. Biol.* **21**, 1391–1396 (2011).
16. Hamaratoglu, F., de Lachapelle, A. M., Pyrowolakis, G., Bergmann, S. & Affolter, M. Dpp signaling activity requires pentagone to scale with tissue size in the growing *Drosophila* wing imaginal disc. *PLoS Biol.* **9**, e1001182 (2011).
17. Wartlick, O. et al. Dynamics of Dpp signaling and proliferation control. *Science* **331**, 1154–1159 (2011).
18. Cheung, D., Miles, C., Kreitman, M. & Ma, J. Scaling of the bicoid morphogen gradient by a volume-dependent production rate. *Development* **138**, 2741–2749 (2011).
19. Wartlick, O., Jülicher, F. & González-Gaitán, M. Growth control by a moving morphogen gradient during *Drosophila* eye development. *Development* **141**, 1884–1893 (2014).
20. Kicheva, A. et al. Coordination of progenitor specification and growth in mouse and chick spinal cord. *Science* **345**, 1254927 (2014).
21. Uygur, A. et al. Scaling pattern to variations in size during development of the vertebrate neural tube. *Dev. Cell* **37**, 127–135 (2016).
22. Schulte-Merker, S. et al. Expression of zebrafish goosecoid and no tail gene products in wild-type and mutant no tail embryos. *Development* **120**, 843–852 (1994).
23. Schier, A. F. Nodal morphogens. *Cold Spring Harb. Perspect. Biol.* **1**, a003459 (2009).
24. Chen, C. & Shen, M. M. Two modes by which Lefty proteins inhibit Nodal signaling. *Curr. Biol.* **14**, 618–624 (2004).
25. Feldman, B. et al. Zebrafish organizer development and germ-layer formation require Nodal-related signals. *Nature* **395**, 181–185 (1998).
26. Rebagliati, M. R., Toyama, R., Fricke, C., Haffter, P. & Dawid, I. B. Zebrafish Nodal-related genes are implicated in axial patterning and establishing left–right asymmetry. *Dev. Biol.* **199**, 261–272 (1998).
27. Sampath, K. et al. Induction of the zebrafish ventral brain and floorplate requires Cyclops/Nodal signalling. *Nature* **395**, 185–189 (1998).
28. Meno, C. et al. Mouse Lefty2 and zebrafish antivin are feedback inhibitors of nodal signaling during vertebrate gastrulation. *Mol. Cell* **4**, 287–298 (1999).
29. Feldman, B. et al. Lefty antagonism of Squint is essential for normal gastrulation. *Curr. Biol.* **12**, 2129–2135 (2002).
30. Chen, Y. & Schier, A. F. Lefty proteins are long-range inhibitors of Squint-mediated Nodal signaling. *Curr. Biol.* **12**, 2124–2128 (2002).
31. Cheng, S. K., Olale, F., Brivanlou, A. H. & Schier, A. F. Lefty blocks a subset of TGFβ signals by antagonizing EGF-CFC coreceptors. *PLoS Biol.* **2**, e30 (2004).
32. Choi, W. Y., Giraldez, A. J. & Schier, A. F. Target protectors reveal dampening and balancing of Nodal agonist and antagonist by miR-430. *Science* **318**, 271–274 (2007).
33. Müller, P. et al. Differential diffusivity of Nodal and Lefty underlies a reaction-diffusion patterning system. *Science* **336**, 721–724 (2012).
34. Wang, Y., Wang, X., Wohland, T. & Sampath, K. Extracellular interactions and ligand degradation shape the Nodal morphogen gradient. *eLife* **5**, e13879 (2016).
35. van Boxtel, A. L. et al. A temporal window for signal activation dictates the dimensions of a Nodal signaling domain. *Dev. Cell* **35**, 175–185 (2015).
36. Rogers, K. W. et al. Nodal patterning without Lefty inhibitory feedback is functional but fragile. *eLife* **6**, e28785 (2017).
37. Xu, C. et al. Nanog-like regulates endoderm formation through the Mxtx2–Nodal pathway. *Dev. Cell* **22**, 625–638 (2012).
38. Marcon, L., Diego, X., Sharpe, J. & Müller, P. High-throughput mathematical analysis identifies Turing networks for patterning with equally diffusing signals. *eLife* **5**, e14022 (2016).
39. Müller, P., Rogers, K. W., Yu, S. R., Brand, M. & Schier, A. F. Morphogen transport. *Development* **140**, 1621–1638 (2013).
40. Harmansa, S., Hamaratoglu, F., Affolter, M. & Caussinus, E. Dpp spreading is required for medial but not for lateral wing disc growth. *Nature* **527**, 317–322 (2015).
41. Gritsman, K. et al. The EGF-CFC protein one-eyed pinhead is essential for Nodal signaling. *Cell* **97**, 121–132 (1999).
42. Mathieu, J. et al. Nodal and Fgf pathways interact through a positive regulatory loop and synergize to maintain mesodermal cell populations. *Development* **131**, 629–641 (2004).
43. Bennett, J. T. et al. Nodal signaling activates differentiation genes during zebrafish gastrulation. *Dev. Biol.* **304**, 525–540 (2007).
44. Liu, Z. et al. Fscn1 is required for the trafficking of TGF-β family type I receptors during endoderm formation. *Nat. Commun.* **7**, 12603 (2016).
45. van Boxtel, A. L., Economou, A. D., Heliot, C. & Hill, C. S. Long-range signaling activation and local inhibition separate the mesoderm and endoderm lineages. *Dev. Cell* **44**, 179–191 (2018).
46. Dougan, S. T. The role of the zebrafish Nodal-related genes squint and cyclops in patterning of mesendoderm. *Development* **130**, 1837–1851 (2003).
47. Pei, W., Williams, P. H., Clark, M. D., Stemple, D. L. & Feldman, B. Environmental and genetic modifiers of squint penetrance during zebrafish embryogenesis. *Dev. Biol.* **308**, 368–378 (2007).
48. Gierer, A. & Meinhardt, H. A theory of biological pattern formation. *Kybernetik* **12**, 30–39 (1972).
49. Othmer, H. G. & Pate, E. Scale-invariance in reaction-diffusion models of spatial pattern formation. *Proc. Natl Acad. Sci. USA* **77**, 4180–4184 (1980).
50. Francois, P., Vonica, A., Brivanlou, A. H. & Siggia, E. D. Scaling of BMP gradients in *Xenopus* embryos. *Nature* **461**, E1 (2009).
51. Ben-Zvi, D. & Barkai, N. Scaling of morphogen gradients by an expansion–repression integral feedback control. *Proc. Natl Acad. Sci. USA* **107**, 6924–6929 (2010).
52. Umulis, D. M. Analysis of dynamic morphogen scale invariance. *J. R. Soc. Interface* **6**, 1179–1191 (2009).
53. Inomata, H., Shibata, T., Haraguchi, T. & Sasai, Y. Scaling of dorsal–ventral patterning by embryo size-dependent degradation of Spemann's organizer signals. *Cell* **153**, 1296–1311 (2013).
54. Ben-Zvi, D., Fainsod, A., Shilo, B. Z. & Barkai, N. Scaling of dorsal–ventral patterning in the *Xenopus laevis* embryo. *Bioessays* **36**, 151–156 (2014).
55. Werner, S. et al. Scaling and regeneration of self-organized patterns. *Phys. Rev. Lett.* **114**, 138101 (2015).
56. Rasolonjanahary, M. & Vasiev, B. Scaling of morphogenetic patterns in reaction-diffusion systems. *J. Theor. Biol.* **404**, 109–119 (2016).
57. Schmoller, K. M., Turner, J. J., Koivomagi, M. & Skotheim, J. M. Dilution of the cell cycle inhibitor Whi5 controls budding-yeast cell size. *Nature* **526**, 268–272 (2015).

Acknowledgements

We thank C. Hill for providing the Lefty1 antibody, M. Affolter for providing the morphotrap construct and J. Raspopovic and N. Lord for helpful comments. This work was supported by EMBO (M.A.-C., L.M. and P.M.) and HFSP (P.M.) long-term fellowships, the NSF Graduate Research Fellowship Program (K.W.R.), NIH grant GM56211 (A.F.S.), and funding from the Max Planck Society, ERC Starting Grant 637840 and HFSP Career Development Award CDA00031/2013-C (P.M.).

Author contributions

M.A.-C., A.F.S. and P.M. conceived the study. P.M. developed the extirpation assay and supervised the project. G.H.S. developed the extirpation device and the 2D map visualization workflow and optimized the pSmad2/3 immunostaining protocol. D.M. performed the experiments in Fig. 6i,j, Supplementary Figs. 4f,g, 5 and 8 and contributed to experiments in Fig. 6f,h. K.W.R. and A.F.S. contributed the data in Supplementary

Fig. 3d,e and provided the *lft* mutants before publication. M.A.-C. performed all other experiments. M.A.-C., A.B., D.M. and P.M. analysed the data. A.F.S. and P.M. conceptualized the scaling model. A.B. performed the mathematical analysis and simulations with assistance from L.M. and P.M. M.A.-C. and P.M. wrote the manuscript with input from all authors.

Competing interests

The authors declare no competing interests.

Additional information

Supplementary information is available for this paper at https://doi.org/10.1038/s41556-018-0155-7.

Reprints and permissions information is available at www.nature.com/reprints.

Correspondence and requests for materials should be addressed to P.M.

Publisher's note: Springer Nature remains neutral with regard to jurisdictional claims in published maps and institutional affiliations.

Methods

Generating smaller embryos by extirpation. All procedures involving animals were executed in accordance with the guidelines of the State of Baden-Württemberg (Germany) and approved by the Regierungspräsidium Tübingen (35/9185.46-5 and 35/9185.81-5).

Extirpation assays were performed using a glass capillary holder mounted on a Hamilton syringe and fixed in a micromanipulator (Narishige). Extirpations were performed in 4-hpf pronase-dechorionated sphere-stage embryos in Ringer's solution (116 mM NaCl, 2.8 mM KCl, 1 mM $CaCl_2$ and 5 mM HEPES). To allow wound healing after extirpation, embryos were left undisturbed for 30 min at 28 °C. The wound typically healed within 15 min after extirpation and the extirpated embryos were then transferred to normal embryo medium. To assess the survival of extirpated embryos without considering other mechanical disruptions of the extirpation assay (such as wound-healing failure or mechanical constraints due to changes in the embryo/yolk ratio), embryos that did not survive extirpation or that did not proceed to gastrulation were discarded.

For the quantification of cell numbers, extirpated cells from pools of ten embryos were transferred to individual PCR tubes containing 0.05% trypsin solution (Gibco) and incubated for 15 min at 37 °C. Dissociated cells were then quantified using a Neubauer chamber on an Olympus CKX41 microscope. Pools (10–20) of extirpated cells from 10 embryos were quantified per extirpation experiment. The average number of extirpated cells per embryo was 820 ± 130 cells, which corresponds to ~30% of the cells of an embryo at the sphere stage with ~3,000 cells.

Whole-mount in situ hybridization. *fascin*, *hgg1*, *vsx2*, *sox3*, *sox17* and *sox32* RNA probes for in situ hybridization assays were synthesized using SP6 or T7 polymerase (Roche) and digoxigenin (DIG)-modified (Roche) or dinitrophenol (DNP)-modified (Perkin Elmer) ribonucleotides. RNA probes were purified by ethanol precipitation with 7.5 M lithium chloride. For chromogenic in situ hybridizations, embryos were fixed overnight at 4 °C in 4% formaldehyde and then processed using an In situ Pro hybridization robot (Abimed/Intavis) and, as previously described[58], with the following modifications: no proteinase K treatment before the 90% epiboly stage; no pre-absorption of the anti-DIG antibody (11093274910, Roche); 5% dextran sulfate (Sigma) added to the hybridization solution[59]; riboprobes were denatured at 80 °C for 15 min and chilled on ice prior to hybridization using a final concentration of 1–2 ng µl^{-1}.

For fluorescent in situ hybridization (FISH), the following modifications were used: the blocking solution contained 2% Blocking Reagent (Roche) in 1× MABTw; incubation with anti-DIG (Roche) or anti-DNP-POD (FP1129, Perkin-Elmer) antibodies at a dilution of 1:150 in blocking solution was carried out overnight with shaking at 4 °C; after antibody incubation, embryos were washed six times for 20–30 min at room temperature with PBS containing 0.1% Tween (PBST) and the signal was developed with 100 µl TSA Cy3 or Cy5 at a dilution of 1:75 in amplification buffer (Perkin Elmer) for 1 h at room temperature without shaking.

For imaging, embryos were embedded in 1% low-melting point agarose, transferred to glass-bottom culture dishes (MatTek corporation) and oriented manually. Only embryos that were mounted with the vegetal–animal axis completely parallel to the cover glass were used for analysis. For chromogenic in situ samples, images were captured using an Axio Zoom.V16 (Zeiss). For fluorescent in situ samples, confocal laser scanning microscopy was performed using an LSM 780 NLO microscope (Zeiss). Images were processed using Fiji[60]. The number of *hgg1*-, *sox17*- and *sox32*-positive cells was quantified using the 'multi-point selection' tool[60]. *fascin* and *sox3* expression domains[44,61] in the central-most embryo regions were quantified using the 'measure' tool in Fiji. *fascin* was quantified from the margin of the embryo to the end of the domain with high expression values. *sox3* was quantified from the animal pole to the end of the domain with high expression values. The shield was excluded in the selection due to a higher expression of mesendodermal markers in this region. The size of embryos (from the margin to the animal pole) was measured similarly using bright-field images.

Immunostaining. For immunostainings, anti-phospho-histone H3 (anti-pH3; 3377S, Cell Signaling Technologies) and anti-pSmad2/3 (8828, Cell Signaling Technologies) antibodies were used.

Immunostaining for pH3 was carried out as described previously[62] with a 1:500 dilution of the primary antibody. For pSmad2/3, specimens were incubated in cold acetone at −20 °C for 20 min before blocking[35]. To ensure staining specificity, samples were exposed to low concentrations of anti-pSmad2/3 antibody (1:2,000 or 1:5,000) and samples were washed for 24 h with PBST before adding the secondary antibody. The signal was then amplified using horseradish peroxidase (HRP)-conjugated anti-rabbit antibodies (111-035-003, Jackson ImmunoResearch) and TSA Cy3 or Cy5 at a dilution of 1:75 in amplification buffer (Perkin Elmer) for 45 min at room temperature without shaking. Embryos were mounted for imaging as described above for FISH, but with the dorsal–ventral axis parallel to the cover glass in the case of pH3 staining. Confocal laser scanning microscopy was performed using an LSM 780 NLO (Zeiss) confocal microscope and images were processed using Fiji. The number of pH3-positive cells was quantified over a depth of 140 µm using the 'find maxima' plug-in in Fiji, with a fixed noise tolerance of 10,000 and manual correction. pSmad2/3 distributions were quantified from the margin of the embryo to the end of the pSmad2/3 nuclear staining using the 'measure' tool in Fiji. Non-nuclear staining was excluded. The extent of pSmad2/3 signalling was variable along the embryonic margin, and the mean of the pSmad2/3 domain at ten different points along the marginal zone is shown in all figures. The size of embryos from the margin to the animal pole was measured similarly using 4,6-diamidino-2-phenylindole (DAPI)-stained images.

Cell density quantification. Cell density measurements were performed in untreated and extirpated H2A-GFP[63] transgenic embryos. Embryos were mounted at 1 hpe and 2 hpe as described above for pH3 immunostaining. The number of cells was quantified as described above for pH3-positive cells but over a depth of 80 µm. The automatic segmentation and assignment of nuclei within the highly dense field of cells were carefully inspected visually and manually corrected.

Epiboly measurements. Untreated and extirpated embryos were imaged every 30 min after extirpation. Lateral images were taken. The extent of the embryo proper, the uncovered yolk, the blastoderm thickness and the total length (embryo proper + yolk) were measured. To calculate the percentage of epiboly, the percentage of the total length that was covered by the embryo proper was calculated. Blastoderm spreading during epiboly was calculated by subtracting the extent of the embryo proper at 1.5, 2, 3 and 4 hpe from the embryo proper extent at the first time point of analysis (1 hpe).

Light-sheet imaging for 3D reconstructions of *fascin* and pSmad2/3 domains. For 3D imaging, a Light-sheet Z.1 microscope (Zeiss) was used. Embryos were embedded in 1% low-melting point agarose and mounted in glass capillaries. For merging of the different views, far-red or green fluorescent beads (Thermo Fischer Scientific) were added to the agarose at a 1:200,000 dilution. After 3D reconstruction, 2D maps were generated as described previously[64] and rotated to the correct perspective using Hugin panorama photo stitcher software (http://hugin.sourceforge.net).

To quantify the signal distribution in the resulting 2D maps, images were opened in Fiji and rotated by 90°. The region corresponding to the whole embryo was selected, and the average intensity of *fascin* or pSmad2/3 from every point of the embryonic vegetal–animal axis was obtained using the 'plot profile' plug-in in Fiji. Distances in pixels were transformed into percentages of the total embryo length with the vegetal-most side defined as 0% and the animal-most side as 100%. Intensity was then normalized by subtracting background values (that is, the lowest intensity value closest to the animal pole of the embryo) and setting the highest intensity value to 1. For the quantification of pSmad2/3 distributions, background values were obtained by imaging *lefty* mRNA-injected embryos after pSmad2/3 immunostaining and normalized using the highest intensity value from the uninjected experimental data sets. 2D maps of DAPI were used as controls to rule out spatial inhomogeneities along the embryonic vegetal–animal axis. The graphs in Figs. 1e and 3b represent scaled average maps obtained from several embryos.

To re-dimensionalize the scaled 2D maps (Figs. 1g and 3d), distances were multiplied by the measured embryo diameter and divided by π/2. Intensities were averaged in bins of 2 µm, and the mean and standard error of different individuals were calculated piece wise.

Assessment of Lefty1 and Lefty2 activity. mRNA encoding Lefty1-GFP or Lefty2-GFP[33] was generated by plasmid linearization with NotI (NEB), purification with a Qiagen PCR clean-up kit and in vitro transcription using SP6 mMessage mMachine kits (Ambion). Pronase-dechorionated wild-type (WT; TLAB) embryos at the one-cell stage were injected with different amounts of *lft1-GFP* (22 pg, 43 pg and 86 pg) or *lft2-GFP* (5 pg, 10 pg and 20 pg) mRNA along with 100 pg of 10 kDa Alexa546-dextran (Life Technologies). At the sphere stage, three to five embryos per condition were imaged on an LSM 780 (Zeiss) confocal laser scanning microscope, and eight embryos with three replicates per condition were collected for qRT–PCR at 50% epiboly. Extracellular fluorescence intensity quantifications and qRT–PCR measurements with Promega Go-Taq qPCR Master Mix were executed as described previously[33] using the zebrafish elongation factor *ef1a* as a normalization control.

Immunoblotting. WT (TE strain) zebrafish embryos around the 50% epiboly stage were deyolked manually with tweezers and a dissection needle. 'Negative control' embryos were treated from 4-cell to 8-cell stages onward with the Nodal inhibitor SB-505124 (S4696, Sigma Aldrich) at 50 µM as described previously[35]. The efficiency of inhibitor treatment was confirmed by assessing the phenotypes of inhibitor-treated and dimethylsulfoxide-treated embryos at 24 hpf. 'Positive control' embryos were injected with 10 pg Squint-encoding mRNA[33] to induce endogenous *lft1* expression and were staged according to the development of uninjected siblings. Deyolked embryo caps were transferred to microcentrifuge tubes, excess embryo medium was removed, embryos were mixed with sample buffer (94 mM Tris pH 6.8, 3% SDS, 15% glycerol, 150 mM dithiothreitol and 0.003% bromophenol blue; 1 µl per embryo) and lysed by vortexing and incubation at 95 °C for 10 min. Before loading, the samples were vortexed again and cleared by brief centrifugation.

The Lefty1 and H3 signals originated from different SDS–polyacrylamide gels and polyvinylidene difluoride (PVDF) membranes owing to differences in the abundance and molecular weights of these proteins. For anti-Lefty1 western blots 5, 10 or 15 embryos were loaded on 10% SDS–polyacrylamide gels (5 µl, 10 µl or 15 µl, respectively). The loading of samples at the concentration used for Lefty1 blots resulted in a saturated H3 signal; thus, samples were diluted fivefold to quantify H3 levels using 12% SDS–polyacrylamide gels. To resolve Lefty1 well and separate it from unspecific bands, we let proteins with a molecular weight of less than 25 kDa run off the gels for Lefty1 immunoblots, making subsequent detection of H3 (~15 kDa) impossible.

Proteins were blotted onto PVDF membranes using the Trans-Blot Turbo Transfer System (Bio-Rad) in 'mixed molecular weight' mode. Blotted membranes were blocked in PBST containing 5% milk powder for 1 h at room temperature and incubated with the primary antibody (diluted in PBST containing 5% milk powder; 1:2,000 for the Lefty1 antibody[35] and 1:10,000 for the histone H3 antibody (ab1791, Abcam)) at 4 °C overnight. The membranes were briefly rinsed with PBST, washed twice with PBST for 5 min and washed two more times with PBST for 10 min at room temperature. Membranes were then incubated with HRP-coupled anti-rabbit antibody (111-035-003, Jackson ImmunoResearch; diluted 1:10,000 in PBST containing 5% milk powder) for 1.5 h at room temperature, followed by a brief rinse with PBST, two washes with PBST for 5 min and two washes for 10 min at room temperature. Fresh PBST was added to the membranes before application of SuperSignal West Dura Extended Duration Substrate (Thermo Fisher Scientific). Chemiluminescence was detected with a Fusion Solo imaging system (Vilber Lourmat).

TIFF images were analysed in Fiji. Regions of interest were drawn around Lefty1 or H3 bands and the mean intensity values were used for further analysis. For lanes without clear Lefty1 bands, the signal intensity was measured at the position of the expected molecular weight based on embryos overexpressing *squint*. The region of interest dimensions were constant for all lanes measured on a given membrane (Supplementary Fig. 8). We did not subtract background intensities for the quantifications in Supplementary Fig. 5, which seemed to be higher in untreated than in extirpated embryos (Supplementary Fig. 8), although single bands in the untreated or extirpated samples did not consistently follow this general trend (perhaps representing yolk proteins[65] and possibly reflecting sample-related differences in deyolking efficiency). The Lefty1 signal from samples with 10 embryos provided the most reliable signal, whereas the signal for samples with 5 embryos was not robustly detectable and the signal from samples with 15 embryos might be close to saturation (Supplementary Fig. 5c).

Injection of *lft1-GFP* mRNA into the YSL. mRNA encoding Lefty1-GFP[33] was generated by plasmid linearization with NotI-HF (NEB), purification with a Qiagen PCR clean-up kit and in vitro transcription using SP6 mMessage mMachine kits (Ambion). To mimic endogenous Lefty secretion, a physiologically relevant amount of 100 pg *lft1-GFP* mRNA was precisely injected into 4 hpf (the sphere stage) pronase-dechorionated embryos at two equidistant points (1 nl of 50 ng µl^{-1} *lft1-GFP* mRNA per point) within the embryonic YSL. To identify physiologically relevant amounts, 40, 60, 80, 100, 160 and 200 pg *lft1-GFP* mRNA were tested in a careful titration series, and 100 pg *lft1-GFP* mRNA were found to most efficiently rescue *lft1*$^{-/-}$;*lft2*$^{-/-}$ mutants.

Extirpations were performed 20–30 min after YSL injections. Embryos were divided into three groups: one group was fixed at the shield stage and processed for FISH, the second was incubated in embryo medium at 28 °C in 24-well plates covered with 2% agarose (1 embryo per well) for phenotypic analysis at 24 hpf, and the third group was processed for imaging 45–60 min after YSL injections. Mounting for imaging was done as described above for FISH samples. Movies were recorded with identical imaging conditions. Embryos were imaged for a total of approximately 100 min and Fiji was used to generate the movies. For measurements of Lefty1-GFP intensity, injections of *lft1-GFP* mRNA in the YSL and extirpations were performed as described above, but imaging was carried out 1.5–2 h after injection. Samples were captured with identical imaging conditions. Twenty confocal slices were used for *z*-projections over a depth of 53 µm, and the intensity of equivalent areas of the images was quantified using the 'measure' plug-in in Fiji.

Hindering Lefty1-GFP diffusion. The morphotrap construct[40] comprises a strong GFP binder (K_d: ~0.3 nM)[66]. The morphotrap construct was digested with *Xho*I and *Xba*I to insert the morphotrap into a pCS2$^+$ expression plasmid. mRNA was generated as described above for *lft1-GFP*. One nanolitre containing 100–150 pg mRNA encoding the morphotrap was injected into one-cell-stage embryos for experiments shown in the middle panel of Supplementary Fig. 4e. Transplantation of cells expressing the morphotrap (bottom panel of Supplementary Fig. 4e) was performed as described above for the extirpation experiments. Briefly, 50–100 cells were transplanted from a sphere-stage donor previously injected with 200 pg morphotrap-encoding mRNA into the sphere-stage host embryos previously injected with 50 pg *lft1-GFP* mRNA.

Time-lapse imaging experiments (Supplementary Videos 2 and 3) showed that Lefty1-GFP mobility from the YSL is strongly affected by the presence of the morphotrap. However, Lefty1-GFP mobility is not abolished entirely. This outcome is expected—even for a high-affinity GFP binder—if binding is reversible and the on/off kinetics are fast[39]. The strong membrane localization of Lefty1-GFP in embryos expressing the morphotrap confirmed the high affinity. The movement of the Lefty1-GFP signal appeared to follow the membranes in these embryos and is slow, consistent with a low fraction of mobile Lefty1-GFP. However, morphogenetic movements during epiboly might play an additional role in Lefty1-GFP transport, possibly facilitating Lefty spreading towards the animal pole.

Testing the effect of morphotrap binding on Lefty1-GFP activity. WT (TE) embryos were injected at the one-cell stage with 1 nl injection mix containing 5 pg or 30 pg *lft1-GFP* mRNA and 0.05% phenol red. To test the effect of the morphotrap on Lefty1-GFP activity, 150 pg *morphotrap* mRNA was included in the injection mix. Lefty overexpression phenotypes were evaluated at 24 hpf. Three groups of Nodal loss-of-function phenotypes were defined according to their strength (Supplementary Fig. 4f,g): mild (S1), intermediate (S2) and severe (S3). For imaging, embryos were mounted in 2% methylcellulose in embryo medium. Bright-field images were acquired with an Axio Zoom.V16 (Zeiss).

Lefty1-GFP gradient measurements. A physiologically relevant amount of 100 pg mRNA encoding Lefty1-GFP was injected into the YSL of *lft1*$^{-/-}$;*lft2*$^{-/-}$ embryos. One group of embryos was additionally injected with 150 pg *morphotrap* mRNA at the one-cell stage. Ninety minutes after YSL injections, embryos were mounted and imaged using an LSM 780 NLO (Zeiss) confocal laser scanning microscope. Embryos were imaged between 90 min and 140 min after YSL injections. To measure the gradients of secreted Lefty1-GFP from the YSL, maximum intensity projections were generated from 28 confocal slices over a depth of 194 µm, and the 'plot profile' plug-in in Fiji was used to obtain the intensity of Lefty1-GFP from every point of the vegetal–animal axis in a central region of the embryo. Background values were obtained by imaging *lft1*$^{-/-}$;*lft2*$^{-/-}$ uninjected embryos (for the group injected with *lft1-GFP* mRNA) or *lft1*$^{-/-}$;*lft2*$^{-/-}$ injected with morphotrap (for the group injected with *morphotrap* + *lft1-GFP* mRNA).

Fluorescence recovery after photobleaching. WT (TE) embryos were injected at the one-cell stage with 1 nl injection mix containing 50 pg *lft1-GFP* mRNA and 0.05% phenol red. In experiments in which the effect of the morphotrap on Lefty1-GFP diffusivity was measured, 200 pg mRNA encoding the morphotrap were included in the injection mix. Pronase-dechorionated embryos were selected for homogeneous expression of the morphotrap using an Axio Zoom.V16 (Zeiss). Embryos were mounted around the oblong to the sphere stage in 1% low-melting agarose using 35-mm glass-bottom microwell dishes (MatTek). Fluorescence recovery after photobleaching (FRAP) was performed and analysed as described previously[33,67,68] using an LSM 780 NLO (Zeiss) confocal microscope at an imaging depth of 30–40 µm. Diffusion coefficients and production rates were fitted to the recovery curves using previously published values for Lefty1-GFP protein stability[33]. The fit was constrained with a minimal diffusion coefficient of 0.1 µm^2 s^{-1}, which is on the order of the speed of cell movements during early zebrafish development[33].

***lft1*$^{-/-}$;*lft2*$^{-/-}$ mutant rescue with the small-molecule Nodal inhibitor SB-505124.** Rescue experiments were performed as recently described[36]. Extirpations were performed in 4 hpf pronase-dechorionated embryos at the sphere stage as described above. Thirty to forty minutes after extirpation, embryos were transferred to 24-well plates covered with 2% agarose (1 embryo per well) and treated with 4.8 µM SB-505124 in embryo medium starting 40 min after extirpation (~30% epiboly stage). Embryos were then separated into two groups: one group was fixed 2–2.5 h after extirpation (the shield stage) and processed for FISH, and the second group was further incubated with the inhibitor at 28 °C until 24 hpf (20 h after extirpation) for phenotypic analysis. For the experiments with increasing Nodal inhibitor exposure, different concentrations from 6 µM to 12 µM SB-505124 in embryo medium were tested.

Mathematical modelling. Details of the computational screen and the parameters used for modelling of the size-dependent inhibition system are described in Supplementary Note 1 and Supplementary Table 2.

Statistics and reproducibility. Two tests were performed to assess whether experimental data were normally distributed: the Kolmogorov–Smirnov ($\alpha = 0.05$) and the Shapiro–Wilk tests ($\alpha = 0.05$). To analyse whether experimental groups were significantly different, two-sided Student's t-tests ($\alpha = 0.05$) were performed.

Embryos from zebrafish crosses were randomly allocated into experimental groups for extirpation, injections and drug treatments. Most experiments were carried out at least twice, and the findings of all key experiments were reliably reproduced. All replicates and precise *P* values are documented in the 'Summary' sheet of Supplementary Table 1, which states the number of independent samples, embryos and independent experiments.

Reporting Summary. Further information on experimental design is available in the Nature Research Reporting Summary linked to this article.

Code availability. The source code for the custom scripts used for data analysis in this study is available from the corresponding author on reasonable request.

Data availability. Supplementary Table 1 contains the source data for Figs. 1a,c,d,h, 2b,c,e–i, 3a, 5c–h, 6f–j and 7e and Supplementary Figs. 2a,b, 3a–c and 4a–d. The data that support the findings of this study are available from the corresponding author on reasonable request.

References

58. Thisse, C. & Thisse, B. High-resolution in situ hybridization to whole-mount zebrafish embryos. *Nat. Protoc.* **3**, 59–69 (2008).
59. Lauter, G., Soll, I. & Hauptmann, G. Two-color fluorescent in situ hybridization in the embryonic zebrafish brain using differential detection systems. *BMC Dev. Biol.* **11**, 43 (2011).
60. Schindelin, J. et al. Fiji: an open-source platform for biological-image analysis. *Nat. Methods* **9**, 676–682 (2012).
61. Dee, C. T. et al. A change in response to BMP signalling precedes ectodermal fate choice. *Int J. Dev. Biol.* **51**, 79–84 (2007).
62. Feng, X., Adiarte, E. G. & Devoto, S. H. Hedgehog acts directly on the zebrafish dermomyotome to promote myogenic differentiation. *Dev. Biol.* **300**, 736–746 (2006).
63. Pauls, S., Geldmacher-Voss, B. & Campos-Ortega, J. A. A zebrafish histone variant H2A.F/Z and a transgenic H2A.F/Z:GFP fusion protein for in vivo studies of embryonic development. *Dev. Genes Evol.* **211**, 603–610 (2001).
64. Schmid, B. et al. High-speed panoramic light-sheet microscopy reveals global endodermal cell dynamics. *Nat. Commun.* **4**, 2207 (2013).
65. Link, V., Shevchenko, A. & Heisenberg, C. P. Proteomics of early zebrafish embryos. *BMC Dev. Biol.* **6**, 1 (2006).
66. Saerens, D. et al. Identification of a universal VHH framework to graft non-canonical antigen-binding loops of camel single-domain antibodies. *J. Mol. Biol.* **352**, 597–607 (2005).
67. Pomreinke, A. P. et al. Dynamics of BMP signaling and distribution during zebrafish dorsal–ventral patterning. *eLife* **6**, e25861 (2017).
68. Blässle, A. et al. Quantitative diffusion measurements using the open-source software PyFRAP. *Nat. Commun.* **9**, 1582 (2018).

nature research

Corresponding author(s): Patrick Müller

Reporting Summary

Nature Research wishes to improve the reproducibility of the work that we publish. This form provides structure for consistency and transparency in reporting. For further information on Nature Research policies, see Authors & Referees and the Editorial Policy Checklist.

Statistical parameters

When statistical analyses are reported, confirm that the following items are present in the relevant location (e.g. figure legend, table legend, main text, or Methods section).

n/a	Confirmed	
☐	☒	The exact sample size (*n*) for each experimental group/condition, given as a discrete number and unit of measurement
☐	☒	An indication of whether measurements were taken from distinct samples or whether the same sample was measured repeatedly
☐	☒	The statistical test(s) used AND whether they are one- or two-sided *Only common tests should be described solely by name; describe more complex techniques in the Methods section.*
☒	☐	A description of all covariates tested
☐	☒	A description of any assumptions or corrections, such as tests of normality and adjustment for multiple comparisons
☐	☒	A full description of the statistics including central tendency (e.g. means) or other basic estimates (e.g. regression coefficient) AND variation (e.g. standard deviation) or associated estimates of uncertainty (e.g. confidence intervals)
☐	☒	For null hypothesis testing, the test statistic (e.g. *F*, *t*, *r*) with confidence intervals, effect sizes, degrees of freedom and *P* value noted *Give P values as exact values whenever suitable.*
☒	☐	For Bayesian analysis, information on the choice of priors and Markov chain Monte Carlo settings
☒	☐	For hierarchical and complex designs, identification of the appropriate level for tests and full reporting of outcomes
☒	☐	Estimates of effect sizes (e.g. Cohen's *d*, Pearson's *r*), indicating how they were calculated
☐	☒	Clearly defined error bars *State explicitly what error bars represent (e.g. SD, SE, CI)*

Our web collection on statistics for biologists may be useful.

Software and code

Policy information about availability of computer code

Data collection	For data acquisition on a Lightsheet Z.1 microscope, we used ZEN 2014 SP1 Black Version 9.2.0.0 (ZEISS). For data collection on an Axio Zoom.V16 microscope, we used ZEN Blue Version 2.0.0.0 (ZEISS). For data acquisition on an LSM 780 NLO microscope, we used ZEN 2.3 SP1 Black version 14.0.0.201 (ZEISS).
Data analysis	For image analysis, we used Fiji/ImageJ version 1.51. 2D maps were re-aligned using the Hugin panorama photo stitcher software 2016.0.0. Most simulations were executed in Python 2.7.8 with scipy 0.19.0, numpy 1.14.0, fipy 3.1, and matplotlib 1.5.3. Simulations in Fig. 7a,b were performed in COMOL Multiphysics version 3.5a. FRAP data was analysed using MATLAB 7.10.0 (R2010a), COMSOL Multiphysics version 3.5a, and custom scripts. The source code for custom scripts used for data analysis in this study is available from the corresponding author.

For manuscripts utilizing custom algorithms or software that are central to the research but not yet described in published literature, software must be made available to editors/reviewers upon request. We strongly encourage code deposition in a community repository (e.g. GitHub). See the Nature Research guidelines for submitting code & software for further information.

Data

Policy information about availability of data

All manuscripts must include a data availability statement. This statement should provide the following information, where applicable:

- Accession codes, unique identifiers, or web links for publicly available datasets
- A list of figures that have associated raw data
- A description of any restrictions on data availability

The data that support the findings of this study are available from the corresponding author.

Field-specific reporting

Please select the best fit for your research. If you are not sure, read the appropriate sections before making your selection.

☒ Life sciences ☐ Behavioural & social sciences ☐ Ecological, evolutionary & environmental sciences

For a reference copy of the document with all sections, see nature.com/authors/policies/ReportingSummary-flat.pdf

Life sciences study design

All studies must disclose on these points even when the disclosure is negative.

Sample size	At least three biological replicates were estimated to provide an adequate sample size based on previous analyses (Müller et al., Science 2012; Müller et al., Development 2013, Pomreinke et al., eLife 2017). For most experiments, we exceeded this minimal sample size to reduce the relative standard error.
Data exclusions	Data was excluded using pre-established criteria. To assess the survival of extirpated embryos without considering other mechanical disruptions of the extirpation assay (such as wound healing failure or mechanical constraints due to changes in the embryo/yolk ratio), embryos that did not survive extirpation or that did not proceed to gastrulation were discarded. For FRAP experiments, we discarded embryos with a non-uniform distribution of Lefty1-GFP since the model to fit the data assumes a uniform fluorescence distribution around the bleached domain.
Replication	Most experiments were carried out at least twice, and the experimental findings were reliably reproduced.
Randomization	Embryos from zebrafish crosses were randomly allocated into experimental groups for extirpation, injections, and drug treatments.
Blinding	Since embryos from zebrafish crosses were genetically uniform and indistinguishable, blinding of the investigators was not necessary.

Reporting for specific materials, systems and methods

Materials & experimental systems

n/a	Involved in the study
☐	☒ Unique biological materials
☐	☒ Antibodies
☒	☐ Eukaryotic cell lines
☒	☐ Palaeontology
☐	☒ Animals and other organisms
☒	☐ Human research participants

Methods

n/a	Involved in the study
☒	☐ ChIP-seq
☒	☐ Flow cytometry
☒	☐ MRI-based neuroimaging

Unique biological materials

Policy information about availability of materials

Obtaining unique materials	There are no restrictions on the availability of materials, which can be obtained from standard commercial sources or from the corresponding author. The only exception is the antibody directed against zebrafish Lefty1, which was obtained from Dr. Caroline Hill (The Francis Crick Institute).

Antibodies

Antibodies used

We used anti-DIG-AP (Roche, 11093274910) at a dilution of 1:3000, anti-DIG-POD (Roche, 11207733910) at a dilution of 1:150, anti-DNP-POD (Perkin-Elmer, FP1129) at a dilution of 1:150, anti-phospho-Histone H3 (Cell Signaling Technologies, 3377S) at a dilution of 1:500, anti-pSmad2/3 (Cell Signaling Technologies, 8828) at a dilution of 1:2000 or 1:5000, HRP-conjugated anti-rabbit (Jackson ImmunoResearch, 111-035-003) at a dilution of 1:500, anti-Lefty1 (van Boxtel et al., Dev Cell 2015) at a dilution of 1:2000, and anti-Histone H3 (Abcam, ab1791) at a dilution of 1:10000.

Validation

We used validated primary antibodies from standard commercial sources (for validation see Moens, Cold Spring Harb Protoc 2008; Lauter et al., BMC Dev Biol 2011; Brend and Holley, JoVE 2009; van Boxtel et al., Dev Cell 2018; https://www.cellsignal.com/products/primary-antibodies/phospho-histone-h3-ser10-d2c8-xp-rabbit-mab/3377; https://www.cellsignal.com/products/primary-antibodies/phospho-smad2-ser465-467-smad3-ser423-425-d27f4-rabbit-mab/8828; Vastenhouw et al., Nature 2010). The only exception is the antibody directed against zebrafish Lefty1, which was validated by Dr. Caroline Hill's laboratory (The Francis Crick Institute) in van Boxtel et al., Dev Cell 2015. We also validated the specificity of this antibody by generating "negative control" embryos treated with the Nodal inhibitor SB-505124 (which inhibits lefty1 expression) and "positive control" embryos injected with Squint-encoding mRNA (which induces endogenous lefty1 expression).

Animals and other organisms

Policy information about studies involving animals; ARRIVE guidelines recommended for reporting animal research

Laboratory animals

All procedures involving animals were executed in accordance with the guidelines of the State of Baden-Württemberg (Germany) and approved by the Regierungspräsidium Tübingen (35/9185.46-5, 35/9185.81-5). We performed experiments exclusively on zebrafish embryos and larvae that were at most two days old and were not yet freely feeding. We used wild type (TE and TLAB strains) and Lefty mutant zebrafish embryos generated by TALEN-mediated targeted mutagenesis (Rogers et al., eLife 2017).

Wild animals

We did not use wild animals.

Field-collected samples

We did not use field-collected samples.

nature cell biology

SUPPLEMENTARY INFORMATION

https://doi.org/10.1038/s41556-018-0155-7

In the format provided by the authors and unedited.

Scale-invariant patterning by size-dependent inhibition of Nodal signalling

María Almuedo-Castillo[1,3], Alexander Bläßle[1], David Mörsdorf[1], Luciano Marcon[1,3], Gary H. Soh[1], Katherine W. Rogers[1,2], Alexander F. Schier[2] and Patrick Müller[1]*

[1]Friedrich Miescher Laboratory of the Max Planck Society, Tübingen, Germany. [2]Department of Molecular and Cellular Biology, Harvard University, Cambridge, MA, USA. [3]Present address: Centro Andaluz de Biología del Desarrollo, Universidad Pablo de Olavide, Sevilla, Spain.
*e-mail: patrick.mueller@tuebingen.mpg.de

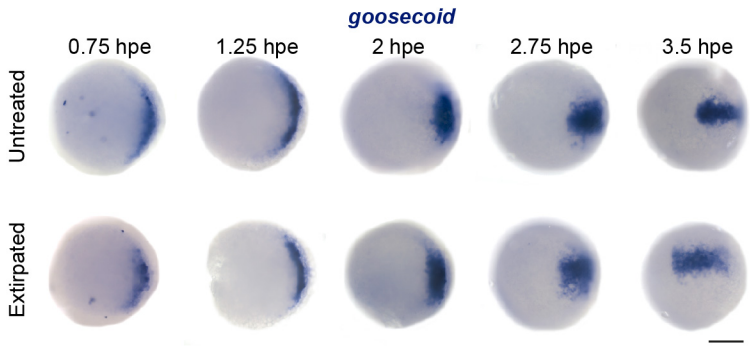

Supplementary Figure 1

Similar developmental speed in untreated and extirpated embryos.

Animal pole view images of *goosecoid* expression. Changes in the *goosecoid* expression domain during development proceed with a similar speed in untreated and extirpated embryos. Unt: Untreated; Ext: Extirpated. 0.75 hpe: n[untreated]=9, n[extirpated]=7; 1.25 hpe: n[untreated]=12, n[extirpated]=11; 2 hpe: n[untreated]=9, n[extirpated]=11; 2.75 hpe: n[untreated]=7, n[extirpated]=13; 3.5 hpe: n[untreated]=10, n[extirpated]=14. Scale bar: 200 μm.

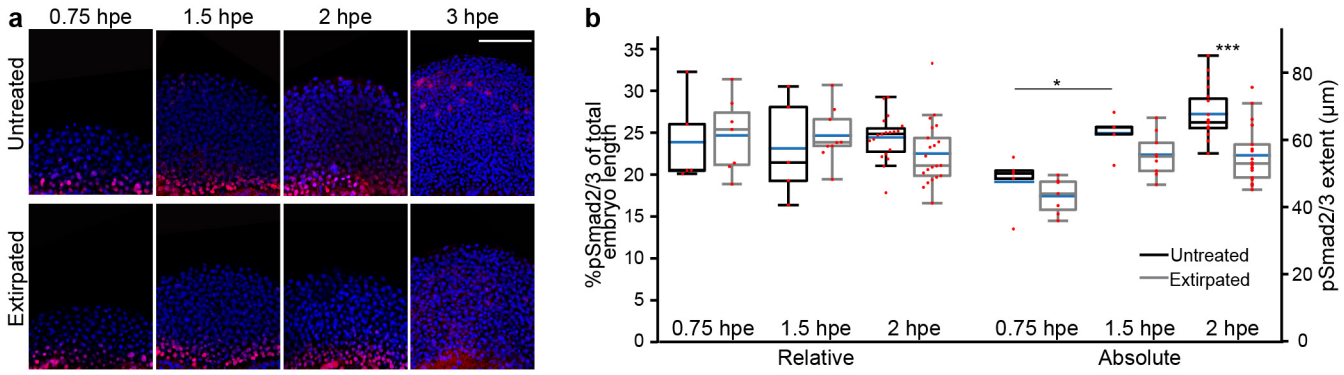

Supplementary Figure 2

Scaling of Nodal signaling after extirpation.

(a) Maximum intensity projections of lateral confocal pSmad2/3 immunostaining stacks, and **(b)** quantification of relative and absolute pSmad2/3 domains in untreated and extirpated embryos at different times after extirpation. 0.75 h post extirpation (hpe): n[untreated]=5, n[extirpated]=7; 1.5 hpe: n[untreated]=5, n[extirpated]=9; 2 hpe: n[untreated]=19, n[extirpated]=21. *p<0.05, ***p<0.001. Two-sided Student's t-tests were performed (α=0.05). See Supplementary Table 1 for statistics source data. Box plots show median (blue line), mean (untreated: black; extirpated: grey lines), 25% quantiles (box), and all included data points (red markers). Whiskers extend to the smallest data point within the 1.5 interquartile range of the lower quartile, and to the largest data point within the 1.5 interquartile range of the upper quartile. Scale bar: 200 μm.

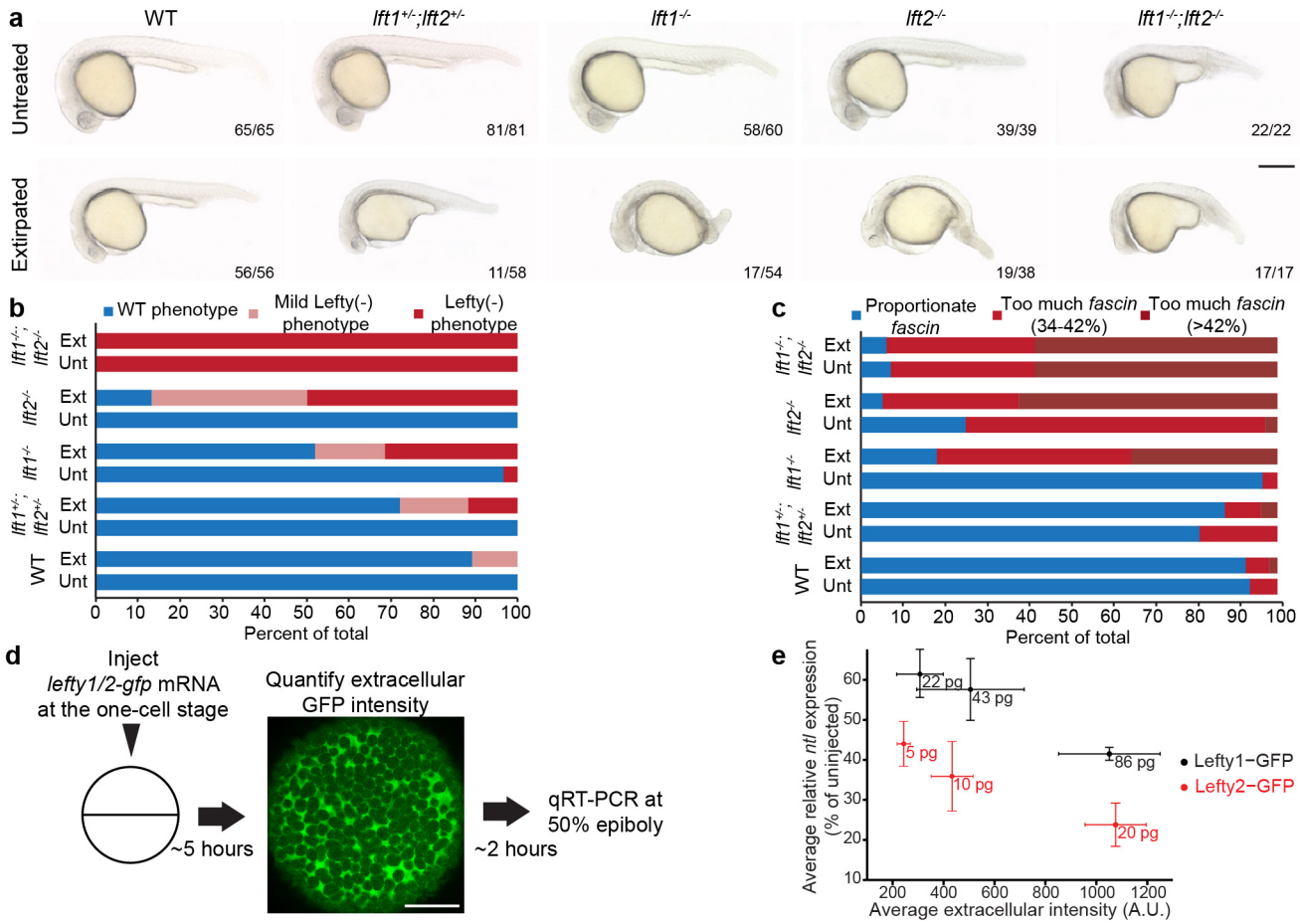

Supplementary Figure 3

Lack of Lefty1 precludes germ layer scaling.

(a) Lateral views of representative 24 hpf untreated and extirpated embryos with different numbers of functional *lefty* alleles. Numbers in the figure panel represent the fraction of these representative embryos. **(b)** Chart showing the fraction of phenotypes in different *lefty* mutants. "Mild *lft1*$^{-/-}$;*lft2*$^{-/-}$ phenotype" refers to embryos that do not exhibit the severe *lft1*$^{-/-}$;*lft2*$^{-/-}$ phenotype but show shorter or thicker tails or slightly reduced cephalic structures. **(c)** Fraction of *lefty* mutants with normal mesendoderm proportion (22-33%), high mesendoderm proportion (34-42%), and very high mesendoderm proportion (>= 42%). **(d)** Schematic of experiments to assess the activity of Lefty1 and Lefty2. Embryos were injected at the one-cell stage with different amounts of *lefty1*- or *lefty2-gfp* mRNA as indicated in figure panel (e). Some embryos were also injected with 100 pg Alexa546-dextran for subsequent generation of intracellular masks for extracellular intensity measurements. Extracellular GFP intensity was quantified at 5 hpf, and sibling embryos were collected at 50% epiboly. qRT-PCR using primers for the Nodal target gene *no tail* (*ntl*) was used to assess inhibitory activity. **(e)** Average *ntl* expression is plotted against average extracellular intensity. At similar intensities, Lefty2-GFP consistently repressed *ntl* expression more effectively than Lefty1-GFP. For fluorescence measurements: n[5 pg Lefty2-GFP]=5, n[10 pg Lefty2-GFP]=4, n[20 pg Lefty2-GFP]=3, n[22 pg Lefty1-GFP]=4, n[43 pg Lefty1-GFP]=5, n[86 pg Lefty1-GFP]=4. For qRT-PCR measurements, 3 samples with 8 embryos each were analysed per condition. Error bars: SEM. See Supplementary Table 1 for statistics source data. Scale bars: 200 μm (a) and 100 μm (d).

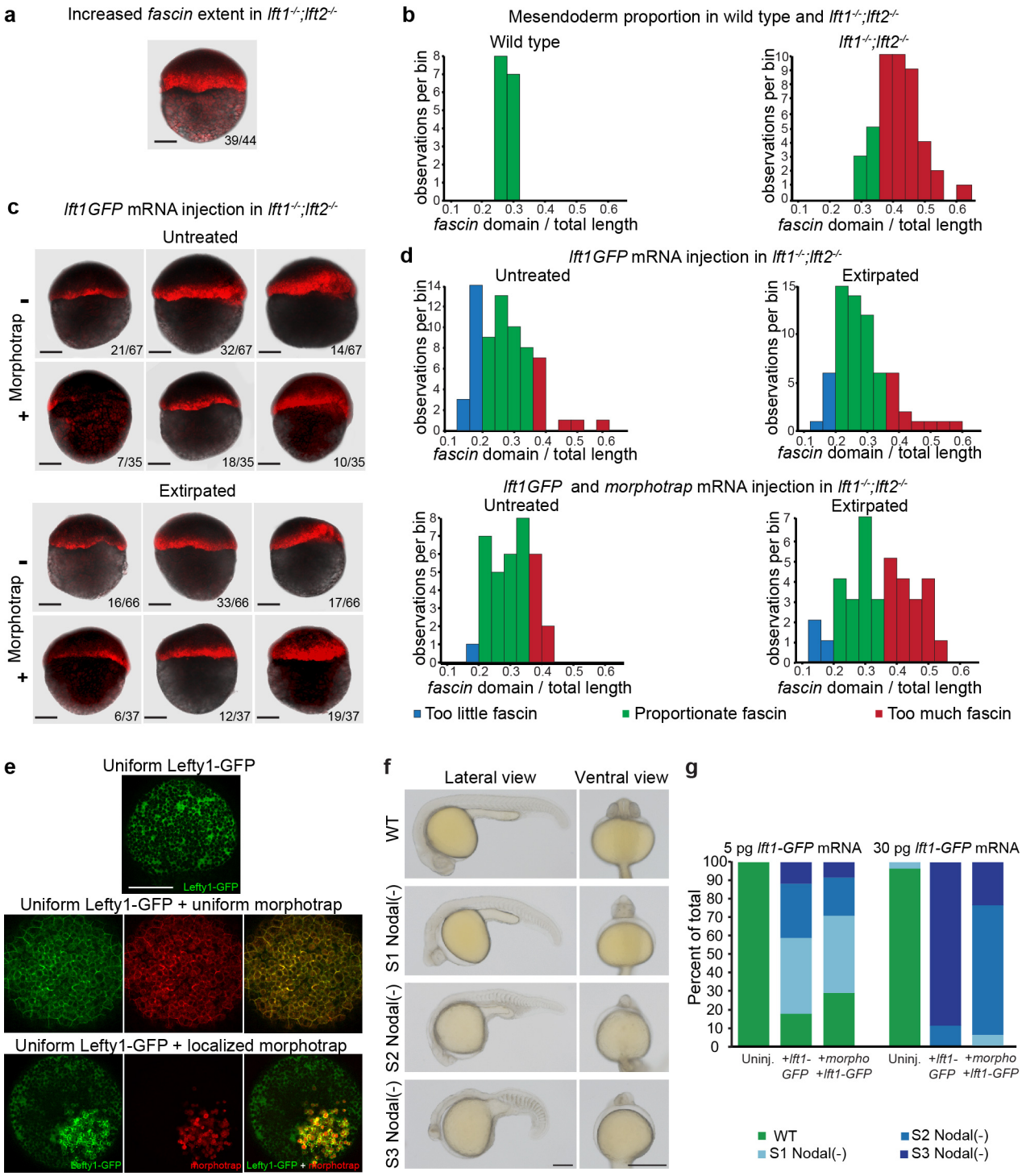

Supplementary Figure 4

Manipulation of Lefty1-GFP diffusion in zebrafish embryos.

(a,c) Maximum intensity projections of lateral confocal stacks of *fascin* expression in *lft1*$^{-/-}$;*lft2*$^{-/-}$ embryos subjected to different treatments. Representative embryos for each treatment are shown. Numbers in the figure panel represent the fraction of these representative embryos. **(b,d)** Mesendoderm proportions in differently sized embryos. Note that the fraction of embryos with normal mesendoderm extent is equivalent to the fraction of rescued *lft1*$^{-/-}$;*lft2*$^{-/-}$ embryos shown in Fig. 6. **(e)** Maximum intensity projections of

confocal stacks of 30-50% epiboly stage embryos. Animal pole views. The upper image shows an embryo injected with *lefty1-GFP* mRNA at the one-cell stage. The middle panel shows an embryo co-injected with morphotrap-encoding mRNA and *lefty1-GFP* mRNA at the one-cell stage. The lower panel shows an embryo injected with *lefty1-GFP* mRNA at the one-cell stage and transplanted with a morphotrap-expressing clone at sphere stage. The morphotrap changes the distribution of Lefty1-GFP from uniform extracellular to strongly membrane-associated. **(f,g)** Morphotrap binding affects Lefty activity. Lateral and ventral views of 24 hpf wild type embryos injected with morphotrap and different concentrations of *lefty1-GFP* mRNA. Representative embryos for each phenotypic category are shown (f). Distribution of phenotypes after different treatments (g). Three groups of Nodal loss-of-function phenotypes were defined according to their strength: mild (S1), intermediate (S2), and severe (S3). For 5 pg of *lft1-GFP* mRNA: n[uninjected]=32, n[+*lft1-GFP*]=34, n[+*morphotrap*+*lft1-GFP*]=24. For 30 pg of *lft1-GFP* mRNA: n[uninjected]=30, n[+*lft1-GFP*]=26, n[+*morphotrap*+*lft1-GFP*]=34. See Supplementary Table 1 for statistics source data. Scale bars: 200 μm.

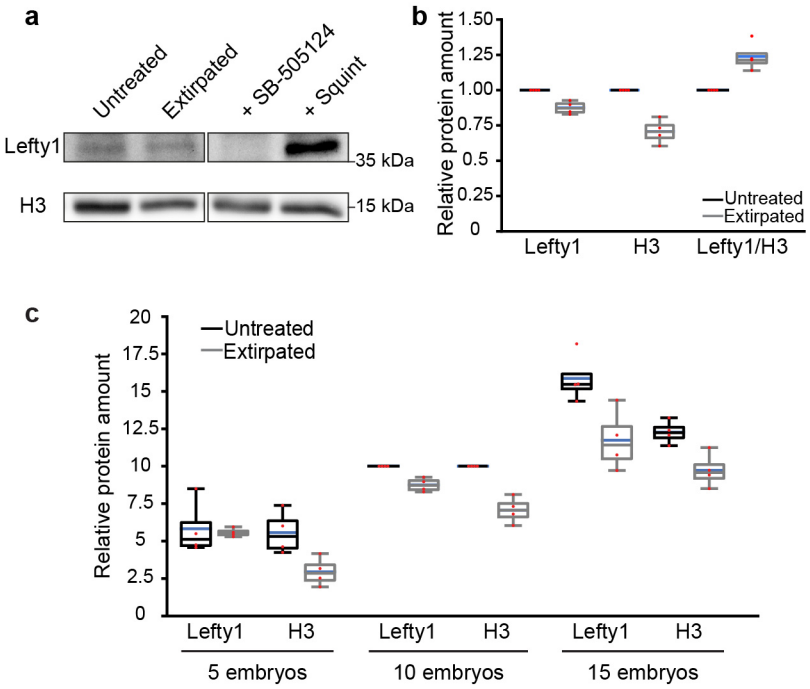

Supplementary Figure 5

Endogenous Lefty1 concentration increases in smaller embryos.

(a,b) Immunoblot analysis indicates a more pronounced decrease of the cellular marker Histone H3 compared to Lefty1, suggesting an increase in Lefty concentration in extirpated embryos (b). The samples derive from the same experiment, but for technical reasons (see Methods) Lefty1 and H3 levels were determined from independent immunoblots (see Supplementary Fig. 8 for raw data). **(c)** Quantification of Lefty1 and Histone H3 levels in the blots shown in Supplementary Fig. 8. All Lefty1 levels were normalised to the Lefty1 levels in the “10 embryos” sample, and all H3 levels were normalised to the H3 levels in the “10 embryos”. The Lefty1 and H3 levels in the “10 embryos” sample were set to 10. Note the approximately linear increase in Lefty1 and H3 levels between samples with different embryo numbers. On average, the decrease in H3 levels in extirpated compared to untreated embryos is more pronounced than the decrease in Lefty1 levels, similar to the model prediction in Fig. 7b. Box plots shows median (blue line), mean (untreated: black; extirpated: grey lines), 25% quantiles (box) and all included data points (red markers). Whiskers extend to the smallest data point within the 1.5 interquartile range of the lower quartile, and to the largest data point within the 1.5 interquartile range of the upper quartile.

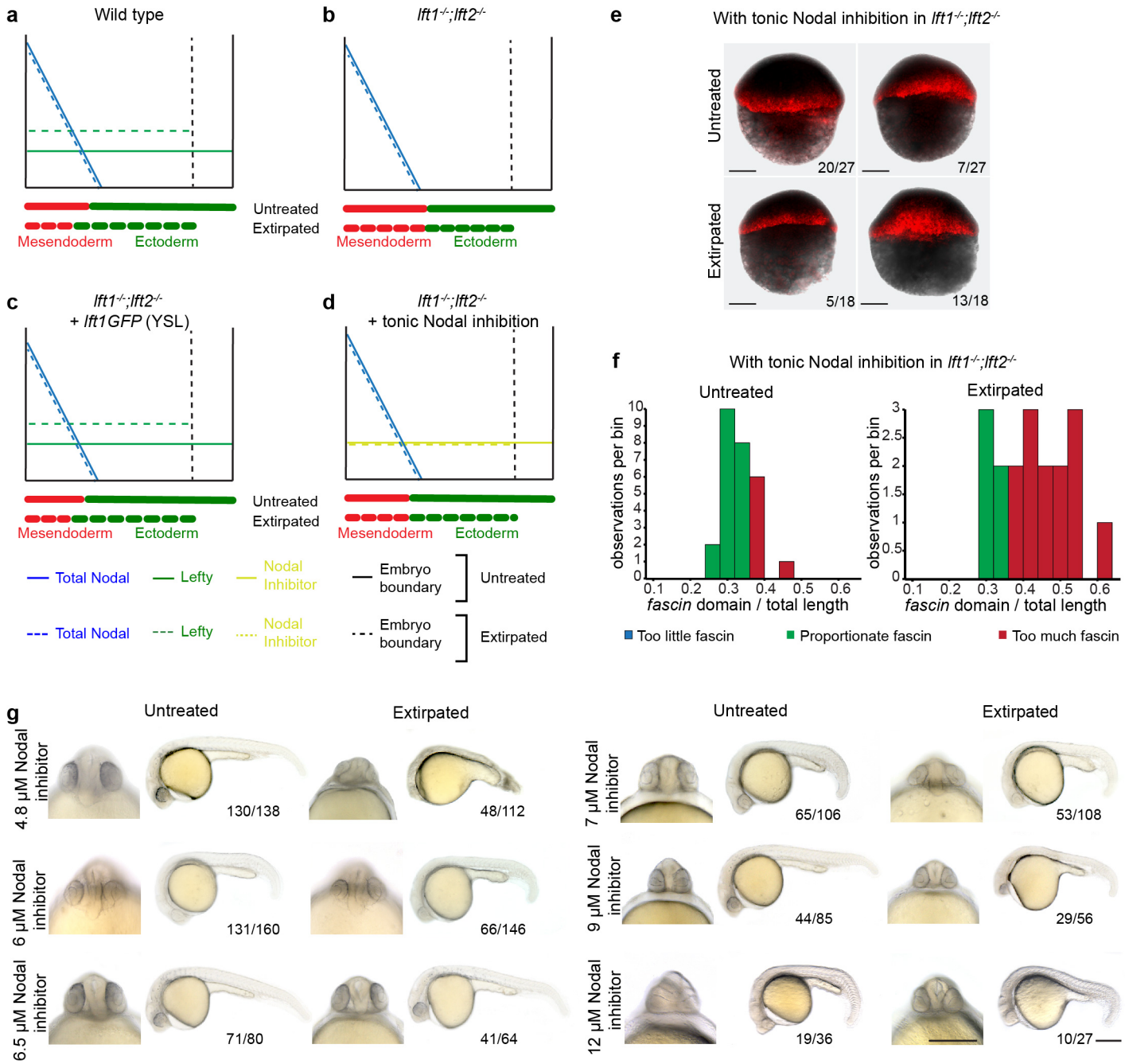

Supplementary Figure 6

An increase in Lefty concentration is required for scale-invariant patterning.

(a-d) Simplified qualitative models of Nodal (i.e. total Nodal, in contrast to the free Nodal shown in the simulations throughout the paper) and Lefty gradients in different scenarios to explain experimental observations. In contrast to our approach using ectopic Lefty gradients, most of the extirpated *lft1*$^{-/-}$;*lft2*$^{-/-}$ mutants exposed to levels of the Nodal inhibitor SB-505124 that rescue normally sized embryos are unable to restore normal mesendoderm proportions. In contrast to ectopic Lefty proteins (c), the Nodal inhibitor is provided tonically, and its concentration does not increase after a reduction in embryo size (d). **(e)** Maximum intensity projections of confocal stacks of *fascin* expression in *lft1*$^{-/-}$;*lft2*$^{-/-}$ embryos exposed to 4.8 µM of the Nodal inhibitor SB-505124. Lateral views. Representative embryos for each treatment are shown. Numbers in the figure panel represent the proportion of these representative embryos. **(f)** Mesendoderm proportions in embryos treated with 4.8 µM of the Nodal inhibitor SB-505124. **(g)** Lateral views of 26 hpf *lft1*$^{-/-}$;*lft2*$^{-/-}$ embryos exposed to different concentrations of the Nodal inhibitor SB-505124. Embryos representing the majority of phenotypes are

shown for each treatment. Numbers in the figure panel indicate the number of these representative phenotypes out of all analysed embryos. Scale bars: 200 μm.

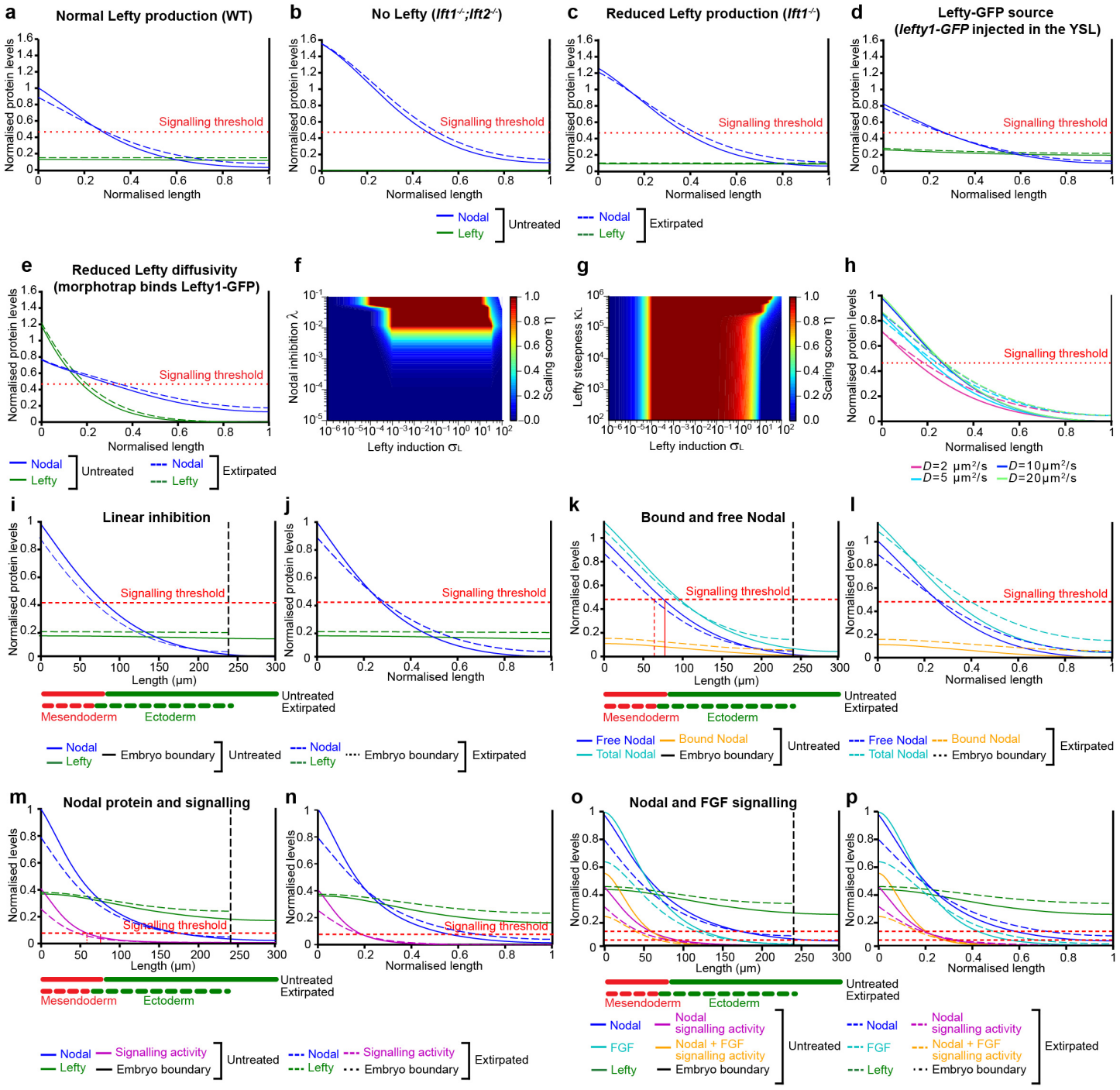

Supplementary Figure 7

Summary and extensions of the size-dependent inhibition model for scale-invariant patterning.

(a-e) Normalised Nodal and Lefty protein profiles scaled to embryo size for simulations of the size-dependent inhibition model with normal Lefty production (a), no Lefty production (b), reduced Lefty production (c), and feedback-less Lefty inhibition in the absence (d) or presence of morphotrap (e). In contrast to the graphs shown in Fig. 4, Fig. 5, and Fig. 6, these graphs show normalised length for both untreated and extirpated embryos. Here, models scale when the dashed and solid lines overlap at the intercept with the signaling threshold. In (c), Lefty induction was reduced by 30%. Normal Lefty diffusivity was set to D_L = 15 $\mu m^2/s$, and Lefty diffusivity in the presence of morphotrap (e) was set to D_L = 0.35 $\mu m^2/s$. All simulation parameter values are listed in Supplementary Table 2 [Parameter

Tables 3 and 4]. **(f,g)** Relationship between the maximum rate of Lefty induction and the strength of Lefty-mediated Nodal inhibition (f) or between the maximum rate of Lefty induction and Lefty induction steepness (g). The plots show maximum projections through the six-dimensional parameter space of the size-dependent inhibition model. **(h)** Simulation of the full model with different values for Lefty diffusivities. A minimal diffusion coefficient of approximately 7-10 $\mu m^2/s$ is required for scale-invariant patterning. **(i,j)** Implementation of the size-dependent inhibition model with linear Lefty inhibition. Scaling solutions are also found with a linear inhibition term, showing that the general mechanism of the size-dependent inhibition model is not dependent on the assumption of non-linear inhibition. (k-p) Extensions of the size-dependent inhibition model. **(k,l)** Simulations of the size-dependent inhibition system explicitly modelling total, free, and Lefty-bound (inhibited) Nodal protein, showing results for absolute (k) and normalised (l) embryo length. **(m,n)** Simulations with separate variables for signalling and protein levels showing results for absolute (m) and normalised (n) embryo length. **(o,p)** Simulations with separate variables for Nodal and FGF proteins and signalling.

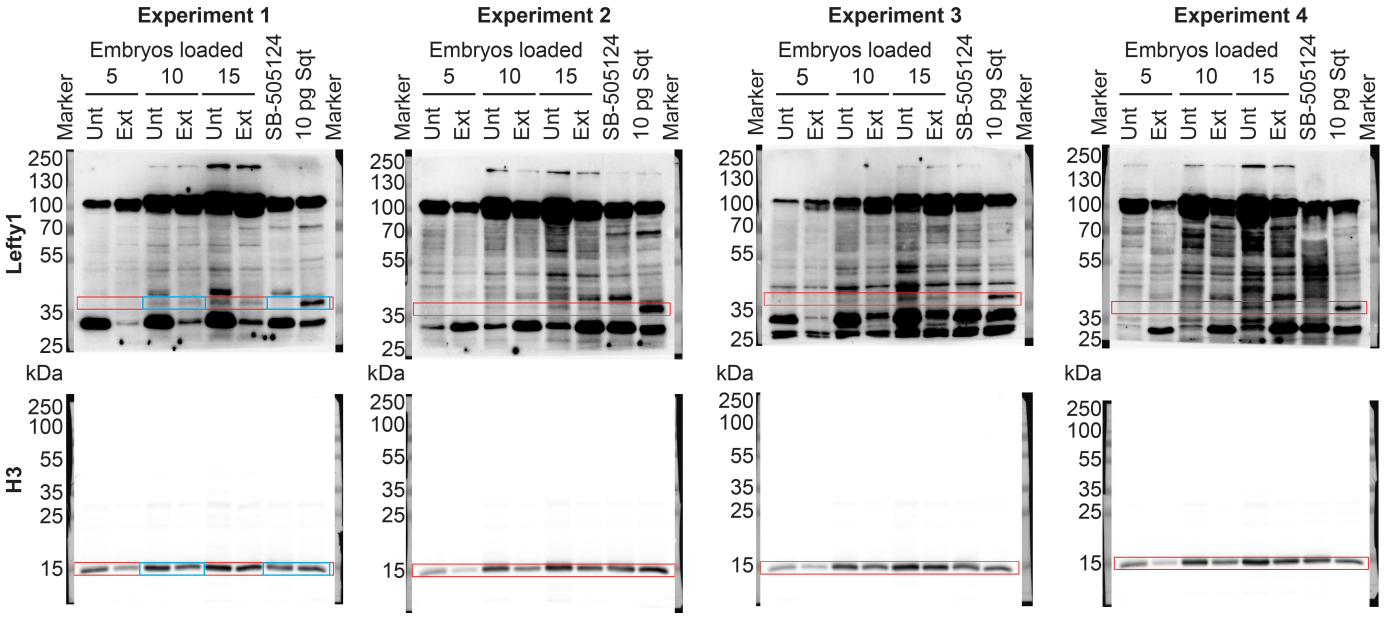

Supplementary Figure 8

Raw immunoblot data.

(a) Marker lanes are shown as overlay of the white light image at the edge of the membranes. Experiments 1, 2, and 4 are biological replicates, whereas experiment 3 is a technical replicate of experiment 1. Turquoise boxes indicate the regions shown in Supplementary Fig. 5a, and red boxes outline the regions used for quantification in Supplementary Fig. 5b,c. Unt: Untreated, Ext: Extirpated.

Supplementary Note 1
Screening for models of scale-invariant patterning. This note includes details about the mathematical modelling of Nodal/Lefty spatio-temporal dynamics, the execution of computational screens to identify the size-dependent inhibition system, and possible model extensions.

Supplementary Table 1
Statistics source data. The "Summary" sheet contains information about the number (n) of biologically independent samples / embryos / independent experiments, and precise p values from statistical tests. The other sheets contain the source data for all instances where the figures show representative experiments of multiple independent repeats, or averages of two independent experiments.

Supplementary Table 2
Simulation parameters. The file contains Parameter Tables 1-8, organized into individual sheets.

Supplementary Movie 1
Temporal dynamics of the scaling model. Nodal signalling levels (blue, solid line: normally sized embryo, dashed line: extirpated embryo) peak at the time of Nodal readout (red). Nodal signalling levels decrease rapidly afterwards, matching the time window of germ layer specification. Grey bars indicate the extent of the mesendodermal domain, and green lines show Lefty levels (solid line: normally sized embryo, dashed line: extirpated embryo).

Supplementary Movie 2
Lefty1-GFP diffusion from the marginal zone in *lefty1*$^{-/-}$;*lefty2*$^{-/-}$ embryos. Time-lapse imaging over 70 min after yolk syncytial layer (YSL) injections reveals high mobility of Lefty1-GFP emerging from the YSL. Lefty1-GFP levels increase in the YSL and over time localize to the extracellular space. Lefty1-GFP moves over a long distance to the animal pole within ≈40 min. Maximum intensity projection of a 60 μm *z*-stack. The animal pole is at the top, and Lefty1-GFP signal is shown in green. The experiment was repeated three times independently with similar results.

Supplementary Movie 3
Lefty1-GFP diffusion from the marginal zone in *lefty1*$^{-/-}$;*lefty2*$^{-/-}$ embryos expressing the GFP binding morphotrap. Time-lapse imaging over 70 min after YSL injections reveals hindered movement of Lefty1-GFP from the YSL in the presence of morphotrap. The morphotrap drastically changes the distribution of Lefty1-GFP from diffuse extracellular to membrane-bound. Maximum intensity projection of a 60 μm *z*-stack. The animal pole is at the top, and an overlay of the Lefty1-GFP signal (green) with the morphotrap signal (red) is shown. The experiment was repeated three times independently with similar results.

Supplementary Movie 4
Temporal dynamics of the extended scaling model. Nodal signalling, i.e. pSmad2/3 levels (magenta, solid line: normally sized embryo, dashed line: extirpated embryo), peaks at the time of Nodal readout (red). Dashed-dotted lines indicate the extent of the pSmad2/3 domain, blue lines show Nodal, and green lines show Lefty levels (solid line: normally sized embryo, dashed line: extirpated embryo).

nature COMMUNICATIONS

ARTICLE

DOI: 10.1038/s41467-018-03975-6 OPEN

Quantitative diffusion measurements using the open-source software PyFRAP

Alexander Bläßle[1], Gary Soh[1], Theresa Braun[1,3], David Mörsdorf[1], Hannes Preiß[1], Ben M. Jordan[2] & Patrick Müller[1]

Fluorescence Recovery After Photobleaching (FRAP) and inverse FRAP (iFRAP) assays can be used to assess the mobility of fluorescent molecules. These assays measure diffusion by monitoring the return of fluorescence in bleached regions (FRAP), or the dissipation of fluorescence from photoconverted regions (iFRAP). However, current FRAP/iFRAP analysis methods suffer from simplified assumptions about sample geometry, bleaching/photoconversion inhomogeneities, and the underlying reaction-diffusion kinetics. To address these shortcomings, we developed the software PyFRAP, which fits numerical simulations of three-dimensional models to FRAP/iFRAP data and accounts for bleaching/photoconversion inhomogeneities. Using PyFRAP we determined the diffusivities of fluorescent molecules spanning two orders of magnitude in molecular weight. We measured the tortuous effects that cell-like obstacles exert on effective diffusivity and show that reaction kinetics can be accounted for by model selection. These applications demonstrate the utility of PyFRAP, which can be widely adapted as a new extensible standard for FRAP analysis.

[1] Friedrich Miescher Laboratory of the Max Planck Society, Max-Planck-Ring 9, 72076 Tübingen, Germany. [2] Department of Organismic and Evolutionary Biology, Harvard University, 26 Oxford Street, Cambridge, MA 02138, USA. [3] Present address: University of Konstanz, Universitätsstraße 10, 78457 Konstanz, Germany. Correspondence and requests for materials should be addressed to P.Mül. (email: patrick.mueller@tuebingen.mpg.de)

The diffusion of molecules is important for almost any process across all scales of biological organisation, from transcription factors finding their targets on DNA to signalling molecules spreading through tissues during development and homoeostasis[1–3]. The biological function of a molecule is affected by its action range and therefore its mobility; however, effective diffusion of molecules moving through complex tissues is difficult to measure quantitatively. More than 40 years ago, Poo & Cone[4] and Liebman & Entine[5] developed a method to assess the diffusivities of fluorescent molecules. In these fluorescence recovery after photobleaching (FRAP) experiments, the fluorescence of molecules in a small region of the sample is bleached by exposure to a strong laser pulse[6]. The dynamics of fluorescence recovery in the bleached region can then be used to infer the mobility of the fluorescent molecules (Fig. 1a). Inverted FRAP (iFRAP) assays have recently been developed as an extension of FRAP experiments[7–10], which eliminate the often harsh bleaching conditions used in FRAP experiments. iFRAP assays utilise photoconvertible molecules that can be induced to alter their fluorescence excitation/emission properties after exposure to 'photoconverting' light. In iFRAP experiments, the spread of signal from a small photoconverted domain into the neighbouring regions of the sample is monitored over time and thus represents an experimental mirror image of FRAP (Fig. 1b).

Diffusion coefficients are commonly extracted from FRAP experiments by fitting analytical solutions computed from theoretical models to the measured recovery curves[11–18], and a few simulation-based analysis methods have been developed[19–21]. Although this allows for a rapid assessment of qualitative mobility differences in identical experimental settings, current approaches rely on several assumptions that can affect the accuracy of the analysis. First, most current methods reduce the FRAP analysis to one-dimensional or two-dimensional simplifications[11–21], often assuming that the fluorescent pool is infinitely large[11–14,16,17], or ignoring more complex geometries of biological samples that could play important roles in molecule movement (Fig. 1c). Recent studies have argued that geometry is crucial for dynamic biological processes[22,23], and must be taken into account for accurate analysis of FRAP data. Indeed, false assumptions about the FRAP sample geometry can drastically affect diffusion coefficient estimates (Fig. 1d).

Second, the bleaching process in FRAP experiments is often inaccurately modelled. Bleaching is posited to be homogeneous or to follow a Gaussian distribution throughout bleached circular or rectangular regions, while the molecules outside of the bleached region are assumed to remain unbleached[11–13, 15–18]. However, molecules diffusing during the bleaching process can create inhomogeneities both inside and outside of the bleached region; moreover, a delay between bleaching and the start of the recovery measurement can lead to further inhomogeneities (Fig. 1c). Incorrect assumptions about the bleaching process can thus lead to a severe misestimation of diffusion coefficients[14, 24–27] (Fig. 1e).

Third, in vivo FRAP experiments can be strongly influenced by reaction kinetics such as production or degradation of fluorescent molecules, which can contribute to the observed recovery curve (Fig. 1c). However, this is mostly neglected in classical FRAP analysis models and can lead to erroneous diffusion estimates (Fig. 1f)[11–17].

To address these shortcomings, we developed the versatile Python-based FRAP analysis software PyFRAP (available at https://mueller-lab.github.io/PyFRAP). To facilitate data analysis, PyFRAP is equipped with an intuitive graphical user interface (GUI, Fig. 2a), which gives users without a computational background access to a sophisticated FRAP data analysis workflow from image analysis to statistical model comparison methods (Fig. 2b). PyFRAP applies the first post-bleach image as initial condition (Fig. 2c), and numerically simulates the FRAP experiment in realistic two-dimensional or three-dimensional experiment geometries (Fig. 2d, e); the solution from this simulation is then fitted to the experimental data. Furthermore, PyFRAP can accurately account for both uniform production and degradation during FRAP experiments. PyFRAP saves all analysed data and settings in a logical data structure that can be shared with collaborators or re-used for later analyses (Fig. 2f). The software is freely available, and the open-source environment allows for rapid expansion through collaborative work[28] to adjust analysis methods to the users' needs.

To demonstrate the utility of PyFRAP, we conducted several typical in vitro and in vivo FRAP experiments (Supplementary Fig. 1). PyFRAP accurately determines the diffusion coefficients of fluorescent molecules ranging from 3 to 500 kDa in both artificial and biological contexts. In contrast to currently available software, PyFRAP's flexible initial conditions also allow analysis of iFRAP experiments, producing results comparable to FRAP. We used PyFRAP to measure the influence that obstacles such as cells exert on the movement of diffusing molecules, and found that such geometric hindrance decreases diffusivity by about one-third. Moreover, PyFRAP provides accurate modelling of reaction kinetics, including production and degradation. Finally, to test the impact of extracellular binding on protein diffusivity, we measured the diffusion of signalling molecules in living zebrafish embryos. We found that the effective diffusivity of a signalling molecule in developing zebrafish was reduced to about one-tenth of its predicted value, in agreement with hindered diffusion models postulating interactions of embryonic signals with diffusion regulators[22,29]. Altogether, our analyses highlight how detailed examination of FRAP data can be used to determine the contribution of individual factors to the movement of molecules in controlled artificial and biological contexts[30].

Results

PyFRAP is a versatile FRAP/iFRAP analysis package. Current FRAP analysis methods often make simplified assumptions about FRAP experimental conditions to aid in the derivation of analytical solutions[11–16,18], and to facilitate numerical simulations[20,21]. Such assumptions include reducing complex sample geometries to lower dimensions, idealising the initial bleaching profile, or ignoring additional reaction kinetics potentially underlying fluorescence recovery (Fig. 1c). Unless the experiment is well approximated by these assumptions (e.g., simple geometry, small bleach spot compared to a large sample volume, sharp bleach profile, no reactions), this can lead to erroneous diffusion estimates (Fig. 1d–f). To address these shortcomings, we developed PyFRAP. PyFRAP numerically simulates FRAP experiments in realistic three-dimensional geometries using an interpolation of the first post-bleach image as initial condition. This simulation is then fitted to the experimental data, incorporating reaction kinetics such as uniform production and degradation.

PyFRAP is an open-source Python-based FRAP analysis software that runs on the major operating systems Microsoft Windows, Mac OSX and Linux. Over the past 20 years, Python has become the standard programming language for scientific research because of the availability of versatile add-on packages and its intuitive and simple syntax[31]. Building on the resourcefulness of Python, PyFRAP is based on commonly used packages such as PyQT, SciPy and FiPy[32–36]. PyFRAP comes with an intuitive graphical user interface (GUI, Fig. 2a) and a fully documented application programming interface (API) allowing

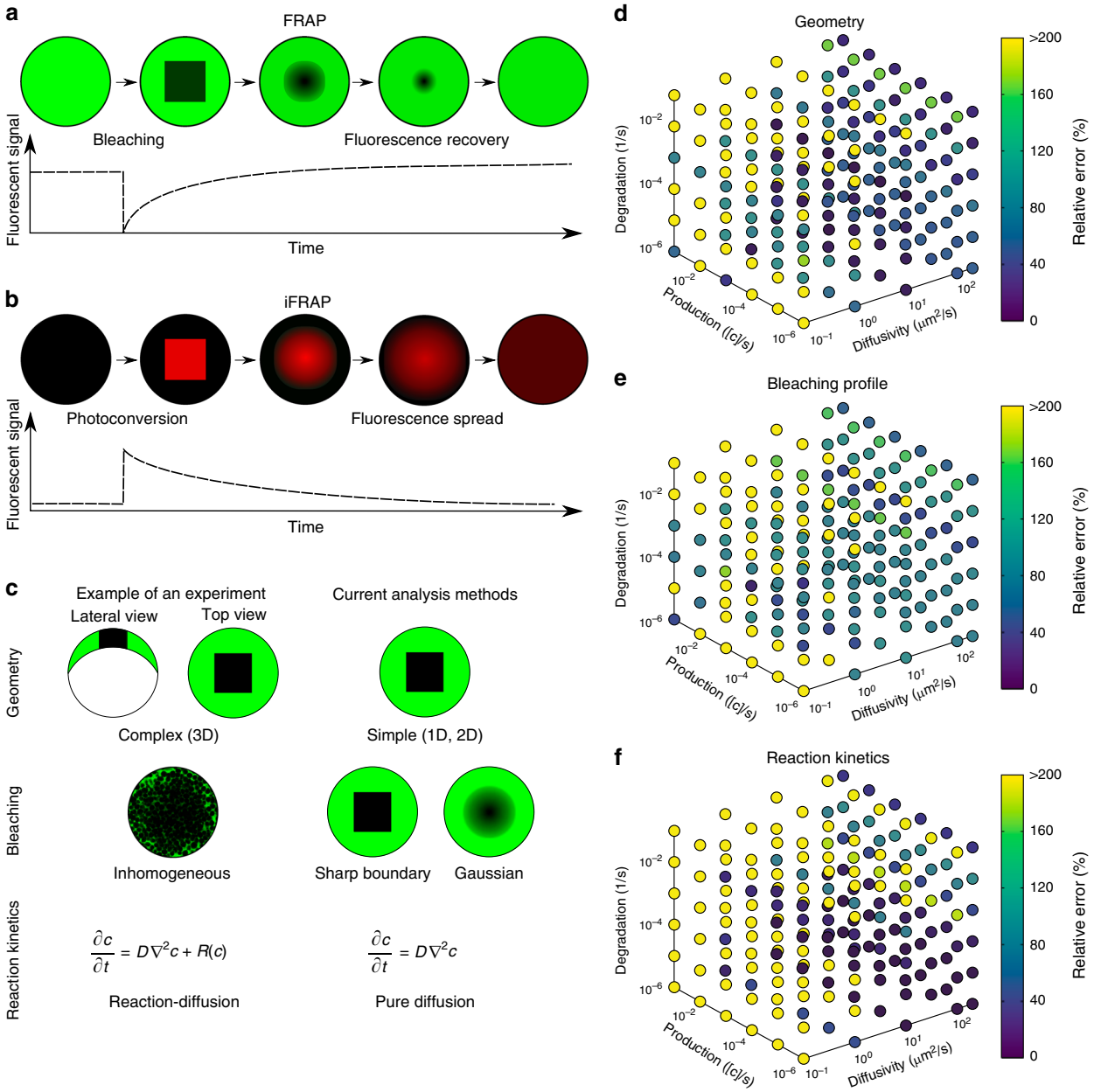

Fig. 1 Fluorescence perturbation techniques used for effective diffusion measurements, and drawbacks of current analysis methods. **a** In fluorecence recovery after photobleaching (FRAP) experiments, a small region in the sample is bleached. After bleaching, the diffusion-driven recovery in the bleached region is monitored. **b** Inverse FRAP (iFRAP) is an experimental mirror image of FRAP: Molecules in a given region are photoconverted and then spread throughout the sample, resulting in the loss of fluorescent signal in the region of photoconversion. **c** Drawbacks of current analysis methods exemplified with zebrafish development at late blastula stages. Current analysis methods simplify sample geometry, idealise bleaching profiles, or ignore underlying reaction kinetics. **d**–**f** Possible relative error in diffusion coefficient estimates that can occur if false assumptions are made about sample geometry (**d**), bleaching conditions (**e**), or reaction kinetics (**f**), respectively. The maximum displayed error was capped to a value of 200%, but can be up to 1000%

quick development of scripts or modifications of the PyFRAP code. PyFRAP's functionalities include sophisticated image processing functions useful for FRAP analysis, customisable geometry and analysis region definitions, a finite element partial differential equation (PDE) solver that simulates FRAP/iFRAP experiments with adjustable options, statistical tools for averaging and model comparison, and multiple plotting and input/output functions (see Methods section and Supplementary Note 1 for details). To make the software easily accessible, dialogue boxes (software wizards) guide the user step-by-step through data import, image analysis, simulation and fitting.

We programmed PyFRAP to import image data from most common microscope formats, such as .tif, .lsm and .czi. Users can define arbitrary regions of interests (ROIs) that are then used for image analysis, simulation and fitting (Supplementary Fig. 2a). For some experimental setups, the imaged sample might be larger than the field of view. In these cases, the concentration of molecules in regions outside of the image can be estimated from selected areas in the first image of the recovery image series (Supplementary Fig. 2b). Uneven illumination is a common artefact in FRAP experiments. PyFRAP can correct this artefact by normalisation using pre-bleach images or using a correction matrix computed from a secondary data set generated with a

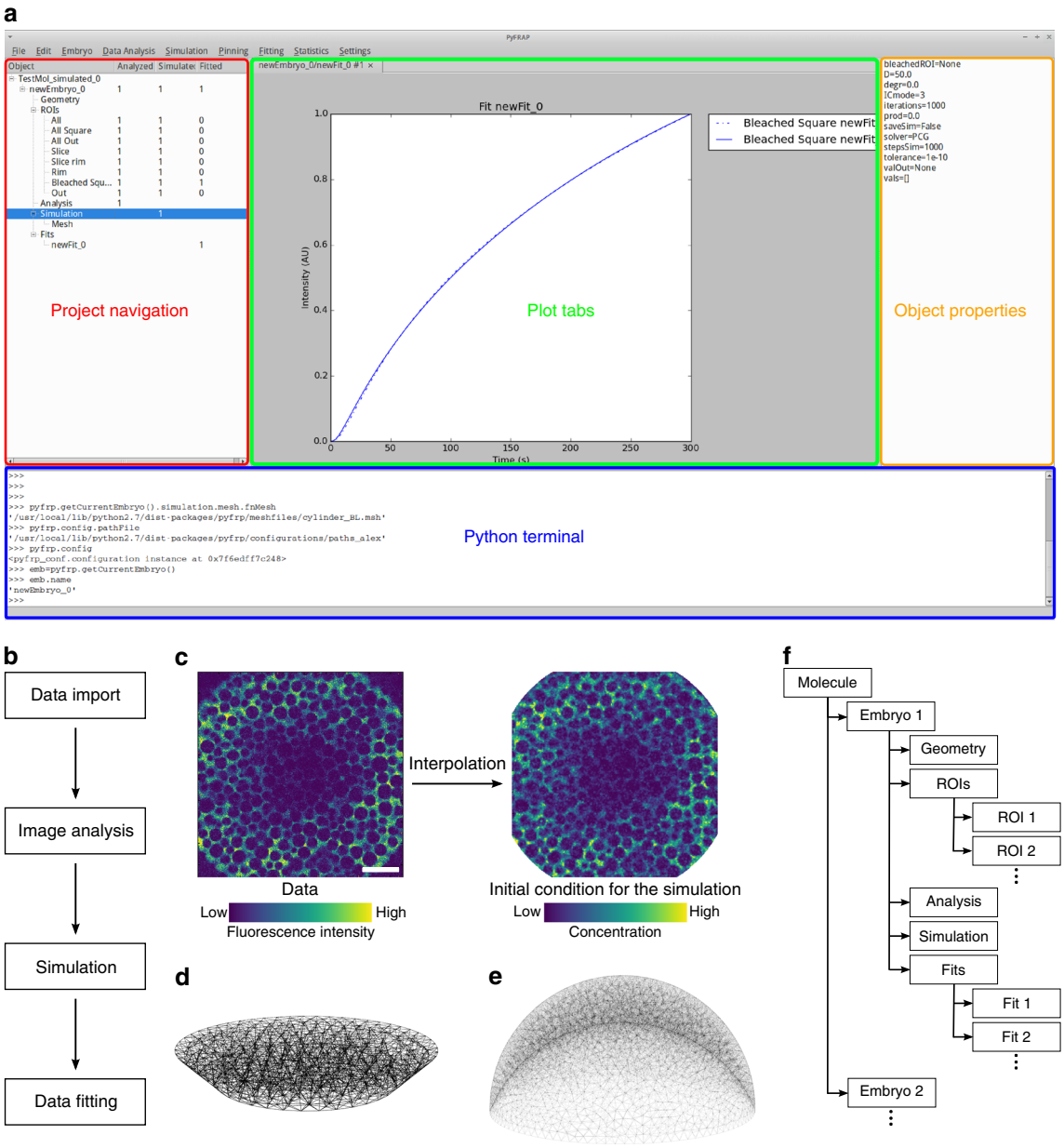

Fig. 2 The PyFRAP software package. **a** Annotated snapshot of the PyFRAP main GUI with project navigation tree (red), plot tabs (green), object property display (orange), and integrated Python terminal (blue). **b** PyFRAP work flow. **c** PyFRAP's interpolation of the first post-bleach image as initial condition for FRAP simulations. The length of the white scale bar represents 100 µm. **d**, **e** Spatial discretisation of geometries resembling **d** a frustum and **e** a zebrafish embryo at late blastula stages (dome stage). **f** PyFRAP's data structure

homogeneously distributed fluorophore[37–39] (see Methods section and Supplementary Fig. 2c for details). To avoid numerical instabilities, PyFRAP allows the user to smooth or denoise the image data using a Gaussian or median filter (see Methods section, Supplementary Note 1, Supplementary Fig. 3, and Supplementary Table 1 for details).

FRAP and iFRAP experiments have been performed in a variety of contexts, from the cigar-shaped *Drosophila* embryo and the relatively flat *Drosophila* wing disc to the dome-shaped pre-gastrula stage zebrafish embryo[10,22,29, 40–42]. These structures have distinct geometries that could impact fluorescence recovery. In fact, we found that simplifying the three-dimensional zebrafish embryo to a two-dimensional disc can frequently lead up to a >200% error in estimated diffusion coefficients (Fig. 1d). In PyFRAP, users can define arbitrary two-dimensional and three-dimensional geometries using Gmsh[43] or CAD STereoLithography (.stl) files that are then spatially discretised into tetrahedral meshes by Gmsh in combination with TetGen[44]. PyFRAP provides various meshing options, such as local mesh refinements, boundary layer meshes and attractor meshes, allowing users to adapt the mesh to experimental details (see Fig. 2d, e and Supplementary Fig. 4c for example geometries and meshes).

In current FRAP analysis methods, the initial condition of the FRAP experiment is often simplified to a simple rectangular function or a Gaussian profile to approximate sharp or blurred bleach boundaries, respectively[11,12, 14–18, 45–47]. However, light scattering, imperfect bleaching and diffusion during the bleaching process can lead to more complex bleaching profiles and thus need to be considered during FRAP analysis to avoid misestimation of diffusion coefficients[24,25,30,48]. To overcome this issue, PyFRAP uses a bilinear interpolation between pixels of the first

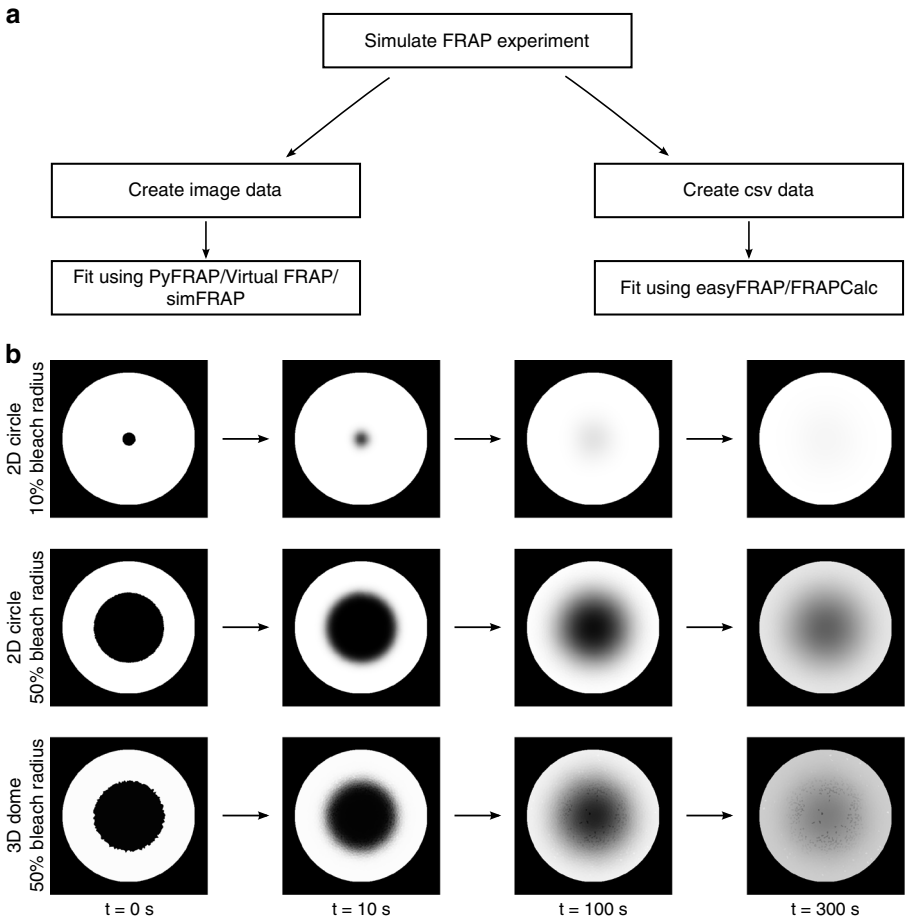

c

Geometry	Bleach domain radius (%)	Simulated D (μm²/s)	PyFRAP D (μm²/s)	FrapCalc D (μm²/s)	easyFRAP* D (μm²/s)	simFRAP D (μm²/s)	virtualFRAP D (μm²/s)
2D circle	5	10	9.8	9.0	14.0	9.3	9.1
2D circle	10	10	9.7	9.7	21.5	9.5	9.1
2D circle	50	10	9.8	10.4	89.1	13.1	10.3
2D circle	5	50	47.5	37.2	38.2	39.8	44.2
2D circle	10	50	49.5	45.2	70.7	47.9	44.3
2D circle	50	50	48.4	63.6	260.5	19.0	42.0
2D circle	5	200	245.0	112.7	67.3	n.a.	39.3
2D circle	10	200	179.0	157.6	161.0	8.7	177.8
2D circle	50	200	197.1	503.1	910.0	n.a.	191.7
3D dome	5	10	11.9	n.a.	17.2	9.7	11.3
3D dome	10	10	9.0	n.a.	23.8	10.1	9.0
3D dome	50	10	10.3	24.0	83.3	12.7	13.3
3D dome	5	50	56.9	n.a.	61.5	47.7	41.8
3D dome	10	50	44.2	n.a.	90.7	49.5	43.4
3D dome	50	50	47.4	n.a.	310.4	48.7	34.1
3D dome	5	200	211.6	n.a.	139.2	185.6	40.5
3D dome	10	200	172.4	n.a.	264.5	192.5	188.0
3D dome	50	200	191.1	n.a.	1021.9	177.3	113.5

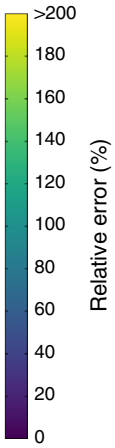

Fig. 3 PyFRAP benchmarking simulation experiment. **a** Workflow of PyFRAP benchmarking. **b** Examples of simulated data sets for different bleach spot sizes and geometries. **c** Benchmarking results of PyFRAP against currently available software packages using simulated FRAP experiments. Simulation experiments varied in bleached region size, diffusion coefficient and experiment geometry. All diffusion coefficients and estimates are given in units of μm²/s. n.a. indicates that the software was not able to fit the simulated data. Colours indicate relative estimation error in %. Diffusion coefficients determined by easyFRAP (asterisk) were computed in combination with an equation providing a relationship between recovery rate, bleached domain size and diffusivity[45]

post-bleach image to estimate the initial condition for mesh cells. This initial condition closely resembles initial experimental bleaching profiles and concentration distributions (Fig. 2c). Moreover, in contrast to most current FRAP analysis methods[11–18,46,47], PyFRAP does not fit a mathematical expression based on simplified assumptions to the data; instead, PyFRAP uses FiPy[32] to simulate the experiment numerically, resulting in a solution that incorporates the realistic three-dimensional geometry and initial conditions. The numerical simulation is then fitted to the FRAP data by minimising the sum of squared differences using classical optimisation algorithms[49–51] (see Methods section for details).

In typical FRAP and iFRAP experiments, a protein of interest is tagged with a fluorescent protein and expressed within a tissue. In such an experiment, the fusion protein is often actively produced at the same time that FRAP is carried out; additionally, fusion proteins undergo degradation over time. Depending on how the fusion protein is expressed (promoter-driven expression, mRNA injection, etc.), its degradation kinetics, and the timescale of the FRAP/iFRAP experiment, production and degradation can dramatically influence recovery curves. Ignoring reaction kinetics in FRAP experiments could therefore lead to erroneous diffusion coefficient estimates. Indeed, recovery curves with pure diffusion fitted to a simulated reaction-dominant data set often resulted in a >200% error in the estimated diffusion coefficients (Fig. 1f). To ensure that the appropriate reaction kinetics are considered when analysing FRAP data, PyFRAP is equipped with four models: (1) Pure diffusion, (2) diffusion with production, (3) diffusion with degradation and (4) diffusion with production and degradation (see Methods section for details). The model can be constrained with previous reaction rate measurements from assays such as fluorescence decay after photoconversion (FDAP) [52,53]; alternatively, production and degradation rates can be directly obtained from fitting the FRAP data. Below, we discuss methods to determine which approaches are most appropriate for a given data set.

An advantage of PyFRAP is its ability to assess FRAP data using multiple models of varying complexity, from pure diffusion to combined reaction-diffusion kinetics. However, determining which model is appropriate for a given data set can be challenging. Choosing the incorrect model can lead to overfitting and potentially false diffusion coefficients[54]. The Akaike information criterion (AIC) is a statistical tool that can aid in model selection[55]. PyFRAP's implementation of the AIC allows users to compare the models mentioned above and determines the most likely model based on a relative weighted measure that includes both the model's log-likelihood and its degrees of freedom, i.e., the number of model parameters. Moreover, PyFRAP provides several statistical tests (Supplementary Table 2) to assess differences between measurements and obtained fits, such as Student's *t*-test[56] for normally distributed data or the Mann–Whitney-U-test[57], which does not require normally distributed data. The Shapiro–Wilk-test can be used to assess whether the measured diffusivities follow a normal distribution[58] and whether application of Student's *t*-test or the Mann–Whitney-U-test is justified.

PyFRAP's object-oriented data structure (Fig. 2f) can be saved into serialised objects and easily loaded for further analysis or shared with collaborators. In addition, PyFRAP lets users visualise every aspect of PyFRAP's analysis work flow and save plots and images into publication-ready figures.

Benchmarking PyFRAP. To validate PyFRAP, we first determined whether it can recover true diffusion coefficients and reaction kinetics from simulated data. We used our previous in-house solution[22,29,42] based on the commercial programs MATLAB and COMSOL multiphysics to simulate 24 FRAP experiments with different reaction kinetics and diffusion coefficients. Using PyFRAP, the simulated data sets were fitted with all four possible reaction-diffusion models (see above). We determined a maximal error of 10% (average error: 2%, Supplementary Table 3) between simulated and estimated diffusion coefficients, demonstrating that PyFRAP recovers correct diffusion coefficients within the error tolerance of the numerical simulations.

Next, we tested whether PyFRAP's implementation of the AIC allows identification of the models used to create the simulated data. When the data were simulated with models describing either pure diffusion, diffusion and degradation, or diffusion and production, the AIC predicted the correct underlying model (Supplementary Table 3). However, the model selection based on the AIC did not favour the correct model for data sets that included diffusion combined with both production and degradation, since models with fewer degrees of freedom provided smaller Akaike weight values. Simulations involving diffusion, production and degradation can generate data effectively indistinguishable from data simulated with only diffusion and production or diffusion and degradation, explaining why the AIC cannot predict the correct model in this case.

To assess PyFRAP's performance in comparison with other available software packages based on analytical[17,46,47,59] or numerical[20,21,60] approaches (Supplementary Table 4), we used easyFRAP[47], Virtual FRAP[20], FrapCalc[46], simFRAP[21] and PyFRAP itself to analyse simulated FRAP experiments (Supplementary Note 2, Fig. 3). We simulated 18 experiments in which geometry, relative bleach window size, and diffusion coefficients differed. Simulations were conducted either in a simple circular two-dimensional domain or a complex three-dimensional zebrafish embryo-like geometry (Fig. 2e). FrapCalc and easyFRAP assume circular bleach windows[12,46,47]; to facilitate comparison, we therefore simulated FRAP experiments with circular bleach windows. Bleach window sizes comprised 5, 10 or 50% of the slice diameter, representing different proportions between fluorescent and bleached pools (Fig. 3b). Simulations were performed with three biologically relevant diffusion coefficients: 10, 50 and 200 $\mu m^2/s$.

Simulation-based programs (PyFRAP, virtualFRAP and simFRAP) generally provided better results than analytical solutions (easyFRAP and FrapCalc): FrapCalc and easyFRAP were either unable to determine diffusion coefficients, or provided diffusivities that were off by at least 20% for most experiments (Fig. 3c). Fast recovery dynamics were challenging for all tested software. One reason for this is that fewer data points were recorded during the actual recovery process of highly diffusive molecules due to a fixed frame rate of 1 frame/s in the simulated test data sets, leading to larger errors; moreover, for fast recovery dynamics errors from interpolating simulations onto images are more severe. The analytical software packages provided better results for the two-dimensional compared to three-dimensional geometries, while simulation-based approaches showed no clear trend regarding geometry. In terms of bleach window radius, the analytical solutions performed worst if the window diameter was 50% of the slice diameter. This effect might be due to the assumption of an infinite pool of fluorescent molecules outside of the bleached region[12]—when the bleach window is very large, the pool of unbleached fluorescent molecules is small, which conflicts with the assumption of an infinite pool. In contrast, PyFRAP outperformed all current software packages and exhibited the smallest error between predicted and simulated diffusion coefficients (Fig. 3c).

Applications of PyFRAP to measure diffusion hindrance. In vivo, it is thought that the overall movement of molecules is affected by binding interactions and by the presence of obstacles such as cells, resulting in a reduced effective diffusion coefficient of secreted proteins that move through tissues[22]. However, the effects of these interactions have not been rigorously tested experimentally. We therefore employed PyFRAP to examine the effects of obstacles and binding partners on the effective diffusivity of dextrans and proteins in experimentally controlled in vitro geometries and in living zebrafish embryos.

First, we measured diffusion coefficients of a wide range of differently sized molecules (Supplementary Table 5) in a simple in vitro context in the absence of binding partners or obstacles. We performed FRAP experiments with different bleach

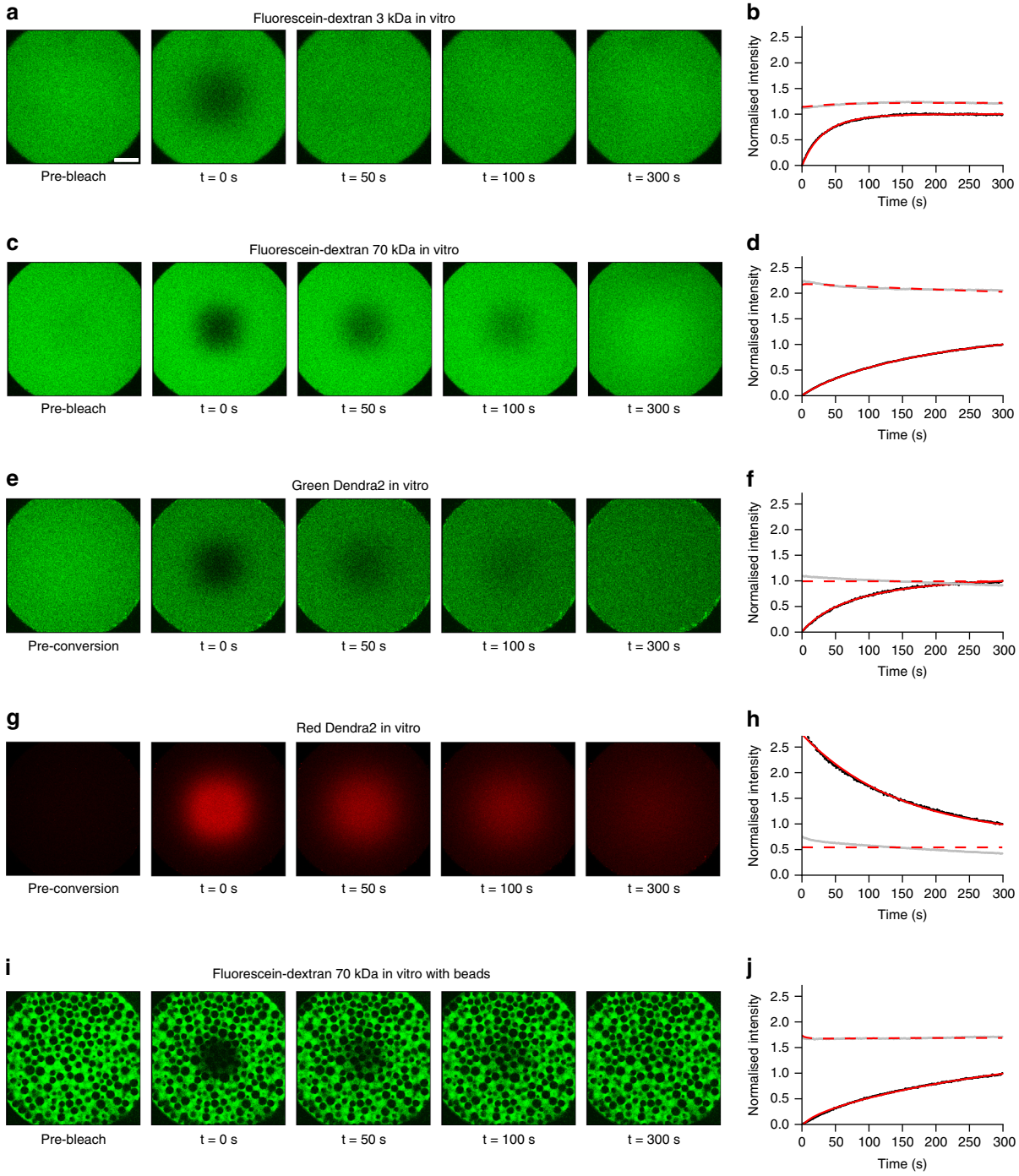

Fig. 4 Examples of in vitro FRAP and iFRAP experiments and the resulting fits to measure free diffusion. **a**, **c**, **e**, **g**, **i** In vitro FRAP and iFRAP experiment images and **b**, **d**, **f**, **h**, **j** fits with PyFRAP. Black and grey dots represent data points of bleached and slice ROI, respectively. Red solid and dashed lines show the respective fits. **a**–**d** FRAP experiments with 3 and 70 kDa fluorescent dextrans (see Supplementary Fig. 5 for the full data set with fluorescent dextrans between 3 and 500 kDa). **e**–**h** iFRAP experiment with photoconverted Dendra2 protein showing data for the green (**e**, **f**) and the red (**g**, **h**) channel. **i**, **j** FRAP experiment with 70 kDa fluorescent dextran in the presence of polyacrylamide beads. Recovery curves were normalised between 0 (intensity in the bleached ROI at the first post-bleach time point) and 1 (intensity in the bleached ROI at the last post-bleach time point) to allow comparison across data sets. The length of the white scale bar in **a** represents 100 μm, and all images were acquired with the same magnification

geometries using fluorophore-coupled dextrans ranging from 3 to 500 kDa in molecular weight (Fig. 4a–d, Supplementary Figs. 5 and 6), and compared the results with theoretical predictions and literature values. Fluorescence recovery in these in vitro experiments should be purely defined by diffusion, and the theoretical diffusivities D of spherical molecules can be calculated from their radii r based on the relationship $D \sim 1/r$ as postulated by the Einstein–Stokes equation (Supplementary Note 3). The diffusion coefficients determined by PyFRAP were in good agreement with literature values and theoretical predictions (Fig. 5a, Supplementary Tables 6 and 7).

A variant of FRAP that allows exclusion of reaction kinetics, such as production, and thus decrease the number of unknown experimental parameters is iFRAP (Fig. 1b). To perform in vitro iFRAP experiments, we used the green-to-red photoconvertible protein Dendra2[61]. Since photoconverting Dendra2 from green to red can also be interpreted as bleaching the original green fluorescence, measuring unconverted and converted protein distributions produces both FRAP and iFRAP experiments at the same time. To test whether PyFRAP correctly analyses iFRAP data, we used the experimental FRAP and iFRAP sets independently and assessed whether the obtained diffusion values are equal (Fig. 4e–h). Using FRAP we measured a Dendra2 diffusivity of 52.9 ± 5.2 (standard deviation) $\mu m^2/s$, and using iFRAP we obtained a similar value of $53.3 \pm 3.1\ \mu m^2/s$ (Fig. 5b, average difference between the two diffusivities per data set: $2.6 \pm 1.5\ \mu m^2/s$).

Next, we examined the effect of tortuosity on diffusion. In biological samples, the path length that molecules take increases as they move around obstacles such as cells. The effect of this

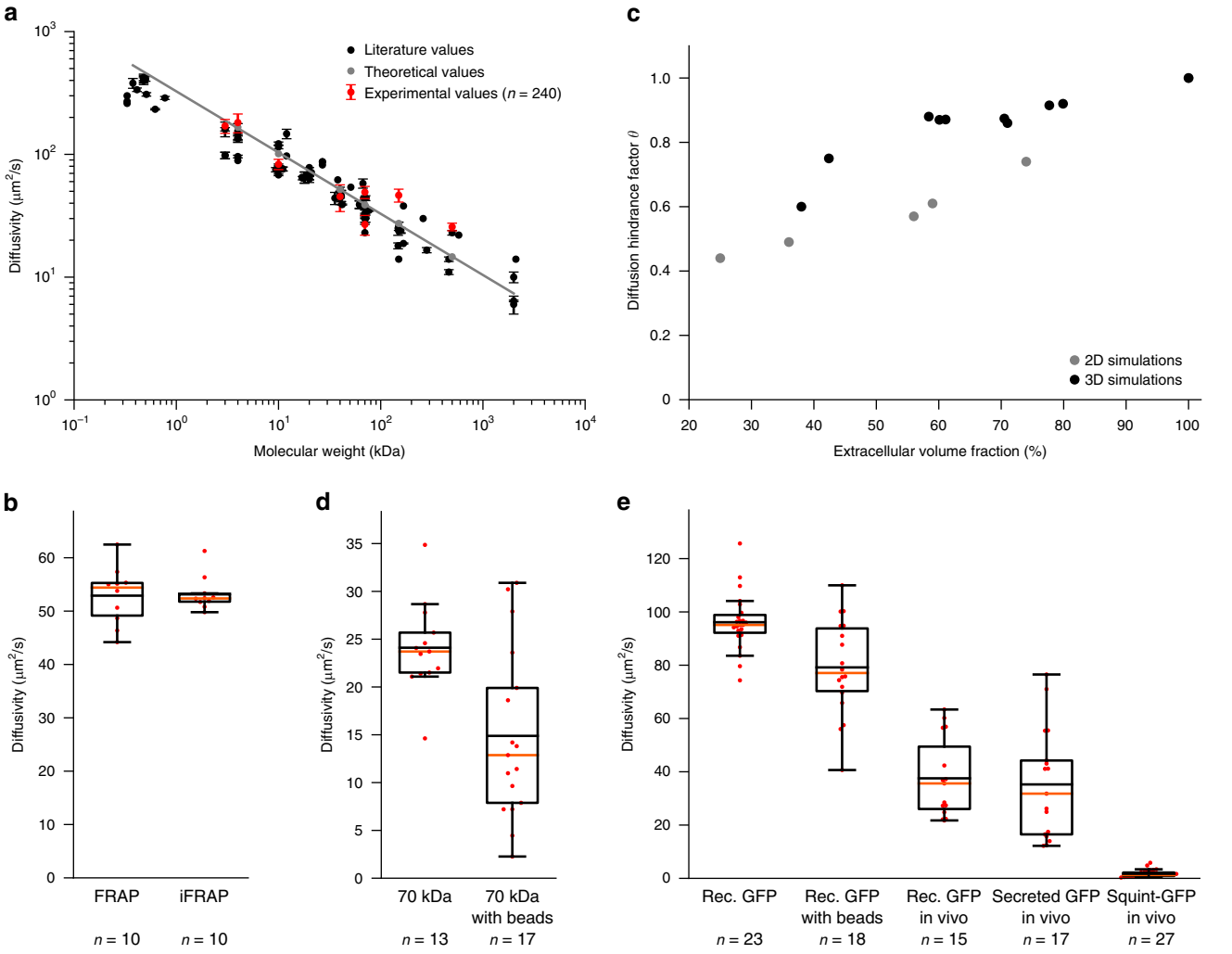

Fig. 5 Effective diffusion coefficients determined by PyFRAP. **a** Results of in vitro experiments and PyFRAP analysis for freely diffusing fluorescent dextrans of different molecular weights. Black markers indicate literature values for fluorescent dextrans, red markers the mean effective diffusion estimates obtained by in vitro experiments and PyFRAP analysis, and grey markers the theoretical estimates derived from the Einstein-Stokes equation (see Supplementary Note 3). Red error bars show the standard deviation of PyFRAP's effective diffusion estimates, and black error bars show the standard deviation of the literature values listed in Supplementary Table 7. The grey line represents a linear regression fit to the theoretical values. **b** Results of FRAP/iFRAP experiments for the photoconvertible protein Dendra2. **c** Results of simulations investigating the influence of tortuosity on effective diffusion for differently packed bead experiments. Grey and black markers indicate 2D and 3D simulation results, respectively. **d** Results of fluorescent dextran experiments demonstrating the impact of tortuosity on effective diffusivities. **e** Results of GFP experiments to analyse the impact of tortuosity, embryonic extracelluar environment, protein production, and extracellular binding on effective diffusion estimates. Box plots in **b**, **d**, **e** show median (orange line), mean (black horizontal line inside box), 25% quantiles (box), and all included data points (red markers). Whiskers extend to the smallest data point within the 1.5 interquartile range of the lower quartile, and to the largest data point within the 1.5 interquartile range of the upper quartile

tortuous movement can be described by the diffusion hindrance factor (also known as diffusion permeability[62]) $\theta = 1/\lambda^2 = D^*/D$, where λ is the tortuosity, D^* is the effective diffusion coefficient (with obstacles), and D is the free diffusion coefficient (without obstacles). To assess the expected magnitude of tortuosity on altering effective diffusivity, we first performed numerical simulations of FRAP experiments with and without radial obstacles in two- and three-dimensional geometries. Radial obstacles were either placed regularly, randomly, or following a nearly-ideal packing scheme, resulting in an extracellular volume fraction (EVF, i.e., the space available for molecules to diffuse) ranging from 78% down to 25% (Supplementary Fig. 7). These simulations demonstrated that recovery rates are slowed down as the EVF decreases (Fig. 5c, Supplementary Table 8). If the geometry is two-dimensional, an EVF of 25% results in an expected reduction in effective diffusivity of approximately 66%. In three-dimensional simulation experiments, we obtained a reduction of effective diffusion coefficients by 40% when the EVF was decreased to 38% (Supplementary Note 3).

To determine whether the presence of obstacles decreases effective diffusivity as predicted by our simulations, we performed FRAP assays in vitro with a fluorescein-coupled 70 kDa dextran (Fig. 4i, j) or recombinant GFP (Supplementary Fig. 8) in the presence of polyacrylamide beads. Consistent with our predictions, recovery was slower in the presence of beads, and the effective diffusivity of fluorescein-coupled 70 kDa dextran dropped from 24.1 ± 0.4 (standard error) μm^2/s to 14.9 ± 0.5 μm^2/s, suggesting an EVF of 39% ($\theta = 0.61$) (Fig. 5c, d, Supplementary Tables 8 and 9). Similarly, for recombinant GFP effective diffusivity dropped by 18% (Fig. 5e, Supplementary Table 10, Supplementary Fig. 8a–d).

To assess diffusion hindrance in vivo, we injected recombinant GFP protein into the extracellular space of living zebrafish embryos. We found that the effective diffusivity in vivo was 60% lower than for freely diffusing GFP, and 53% lower than in in vitro experiments with beads (Fig. 5e, Supplementary Table 10, Supplementary Fig. 8e, f). This suggests that tortuosity in zebrafish embryos is higher than in the in vitro bead assay. Importantly, we found similar diffusion coefficients of 36 μm^2/s in vivo for extracellularly injected recombinant GFP and secreted GFP constantly produced from injected mRNA, showing that PyFRAP can properly account for both diffusion and production (Fig. 5e, Supplementary Table 10, Supplementary Fig. 8g, h).

Finally, we examined the effects of binding interactions on effective diffusivity. GFP presumably does not experience significant binding interactions with extracellular molecules in zebrafish embryos, although its movement is affected by obstructions like cells and cellular extensions. In contrast, secreted signalling molecules are expected to interact with extracellular molecules such as receptors and extracellular matrix components[22]. To assess the effect that interactions with extracellular molecules might have on secreted signalling molecules, we injected mRNA encoding the TGFβ-superfamily member Squint fused to GFP into zebrafish embryos[29]. Squint-GFP is approximately 1.5 times larger than GFP and according to the Einstein-Stokes equation (Supplementary Note 3) would be predicted to have an approximately 1.14 times smaller diffusion coefficient than GFP (effective diffusivity D(GFP) = 36 μm^2/s, expected effective diffusivity D(Squint-GFP) = 31 μm^2/s). However, we measured an effective diffusion coefficient of approximately 2 μm^2/s for Squint-GFP in living zebrafish embryos, ~90% lower than the predicted diffusion coefficient (Fig. 5e, Supplementary Table 10, Supplementary Figs. 8i, j and 9). These findings are consistent with previous measurements[29] and with the idea that interactions with so far unidentified binding partners slow down the effective diffusion of embryonic signalling molecules like Squint-GFP[22,29].

Discussion

Although FRAP analyses have long been used to measure relative differences in mobilities between macromolecules, analysis tools to accurately and quantitatively determine effective diffusion coefficients from FRAP data are lacking. Current analysis tools impose several simplifications including one-dimensional or two-dimensional reductions of complex three-dimensional geometries, idealised bleaching conditions, and the absence of important reaction kinetics. When the experimental conditions closely resemble the simplified assumptions, e.g., small bleach domains and negligible reaction kinetics, these tools can rapidly provide reasonable diffusion estimates (Fig. 3c). However, experimental conditions are often more complex, and the use of simplified assumptions may yield drastically divergent diffusion coefficients (Fig. 1d–f). PyFRAP addresses these shortcomings by providing a simulation-based analysis that incorporates realistic geometries, bleaching conditions and reaction kinetics.

We found that PyFRAP's data analysis pipeline is numerically reliable, recovered the correct diffusion coefficients and reaction kinetics, and additionally predicted the correct underlying reaction-diffusion models for simulated test data sets with known diffusion, production, and degradation parameters. PyFRAP consistently outperformed all other tested software packages, demonstrating its strength as a novel FRAP analysis method. Furthermore, PyFRAP was able to determine diffusion coefficients comparable to both theoretical and previously experimentally measured estimates for macromolecules with molecular weights ranging over two orders of magnitude. Since PyFRAP can analyse data independently of any assumptions about the initial conditions, it is suitable to analyse both FRAP and iFRAP experiments. iFRAP has recently been developed as an alternative to FRAP due the increasing availability of photoconvertible proteins and allows ignoring reaction kinetics such as production. We performed tandem FRAP/iFRAP experiments to analyse the diffusion of the photoconvertible protein Dendra2 and found equal diffusion coefficients in vitro with both methods.

FRAP experiments are typically performed in tissues in which macromolecules need to move around cellular obstacles, resulting in slower fluorescence recovery. To determine how this tortuosity might affect diffusion coefficients estimated from FRAP experiments, we first simulated FRAP experiments in two- and three-dimensional geometries introducing radial beads at different densities to vary the extracellular volume fraction (EVF). Our simulations showed a strong correlation between tortuosity and effective diffusivity and agree with previous theoretical work including Monte-Carlo simulations and homogenisation theory[62–65]. We then tested the predictions from these simulations with in vitro experiments using polyacrylamide beads to mimic cells. Compared to experiments without beads, the effective diffusion coefficient decreased by 39% (diffusion hindrance factor $\theta = 0.61$) for 70 kDa fluorescein-dextran and 18% ($\theta = 0.82$) for recombinant GFP. In living zebrafish embryos, effective diffusivity is much further reduced (Fig. 5e). It is unlikely that this is due to different viscosity of the extracellular medium in vivo, since free GFP diffusion is only marginally reduced in zebrafish embryos[22]. Instead, it is plausible that the complex geometries of real extracelluar environments—which include filopodia, extracellular matrix, and cavities that might act as dead end pores—could further increase tortuosity[62]. Finally, most in vivo FRAP experiments are affected by biochemical reactions such as

production and degradation of proteins, which must be taken into account for accurate diffusion coefficient estimates (Fig. 1c, f). PyFRAP offers various models for different reaction kinetics and can accurately estimate diffusion coefficients from data sets that include constant production and degradation.

PyFRAP measures effective diffusion, but due to its built-in PDE solver it could be extended in the future to consider spatially inhomogeneous kinetics and advective fluxes and to perhaps even determine the diffusivities of individual species in polydisperse mixtures of fluorescent molecules[66,67]. While PyFRAP can simulate three-dimensional FRAP experiments, FRAP data is currently almost exclusively obtained from two-dimensional confocal microscopy. In recent years, the development of light-sheet microscopy made fast three-dimensional imaging with low phototoxicity feasible[68]. In the future, PyFRAP's image analysis tools could be extended to fit light-sheet microscopy data, which might provide deeper insights into the three-dimensional dynamics of molecule movement including convective flows or spatially inhomogeneous diffusion.

Methods

FRAP/iFRAP experiments in vitro. FRAP experiments to measure pure diffusion and tortuosity effects were conducted in a frustum-like plexiglass hole. Holes around 700 µm in diameter and about 100 µm in depth were drilled into a plexiglass block using a dental drill. Due to the small depth, the resulting shape was frustum-like with an upper base of 510 µm diameter.

Holes were filled with aqueous solutions of FITC-/fluorescein-labelled dextrans of different sizes, recombinant GFP, or Dendra2 protein (Supplementary Table 5) using a micro-pipette. Dendra2 protein was centrifuged at 16,000 × *g* for 30 min at 4 °C to remove protein aggregates. Excess liquid was removed from the hole by pipetting under observation with a stereo microscope.

To model the effect of tortuosity in the in vitro FRAP experiments, polyacrylamide beads were added to the sample solution. The microbeads (Bio-Gel P-2 Gel, <45 µm wet bead size) were first soaked in distilled water overnight for hydration. The beads were then centrifuged at 300 × *g*, the supernatant removed, and the required quantity of beads transferred to another tube for resuspension in fluorescein-dextran or GFP+BSA solution. This was repeated and followed by removal of the supernatant, leaving a concentrated slurry of beads and fluorescent solution for the experiments. The beads were transferred into the plexiglass template and settled within 1–2 min.

To prevent evaporation, mineral oil (Sigma) was placed around the solution before sealing the hole with a cover slip (No 1.5). Supplementary Fig. 1a outlines the sample preparation process for in vitro experiments. The sample was upended carefully and mounted on an inverted confocal microscope. Images were taken using an LSM 780 NLO microscope (ZEISS) with an LD LCI Plan-Apochromat 25×/0.8 Imm Korr DIC objective (ZEISS) and immersion oil (Immersol TM W, $n = 1.334$ at 23 °C, ZEISS). First, a plane approximately in the middle of the hole was chosen and the *z*-position set to zero. Then, the position of the highest and lowest point was determined. Cuboid volumes (141.42 µm × 141.42 µm × 100 µm) were bleached by imaging a *z*-stack at highest laser power (488 nm) or photoconverted at moderate laser power. Time series of 300 images (512 pixels × 512 pixels) were taken with a speed of 1 frame/s (pixel dwell time: 3.15 µs) over a duration of 5 min. The zoom was set to 0.7, and the resulting images had a size of 566.79 µm × 566.79 µm.

After the FRAP experiment, the template was cleaned using distilled water, soap, and an interdental toothbrush.

FRAP experiments in vivo. Zebrafish embryos (*Danio rerio*) were collected 10 min after mating and proteolytically dechorionated[22,29,42]. For the experiments with recombinant GFP, 100 pg of recombinant GFP were injected into the extracelluar space when zebrafish embryos reached high stage[22,29,69] (Supplementary Table 10). For experiments with secreted GFP[29], 100 pg of the mRNA encoding the fluorescent protein were injected at the one-cell stage. For experiments with Squint-GFP[29], either 30 or 200 pg of mRNA were injected at the one-cell stage. At dome stage, embryos were mounted in drops of 1% low-melting-point agarose animal pole down onto a glass-bottom dish (MatTek Corp. P35G-1.5-20-C), and as soon as the drops solidified covered with Danieau's medium[29,42] to prevent the embryos from drying out. Supplementary Fig. 1b outlines the in vivo sample preparation process.

Confocal images were taken roughly at a depth of 40 µm from the animal pole into the embryo. For data sets injected with 200 pg of Squint-GFP-encoding mRNA, images were acquired with the same settings as described for the in vitro experiments either with 1 frame/s for 300 s, or 1 frame/10 s for 3000 s. Images of embryos injected with 30 pg of Squint-GFP-encoding mRNA were taken with a spatial resolution of 340.08 µm × 340.08 µm and 1 frame/10 s for 3000 s. Data sets for recombinant GFP in vivo were acquired with the same microscope settings as the experiments conducted in vitro.

ROI selection. PyFRAP's image analysis depends on defining specific ROIs for the experimental data and simulations. Users can define multiple different geometrical shapes of ROIs in three-dimensional space such as cylinders, prisms, and any kind of addition or subtraction between ROIs. The specified ROIs are then used for image analysis, estimating concentrations outside the field of view, evaluating the simulation, and fitting to the analysed data. PyFRAP is equipped with an ROI manager and wizards for several standard sets of ROIs.

Image analysis. Let Ω_i (with $i \in \{1, 2, \ldots, n_\Omega\}$ and n_Ω the number of ROIs) be the list of ROIs specified for PyFRAP's analysis. The mean intensity over the ROI Ω_i at time t_j (with $j \in \{1, 2, \ldots, n_t\}$ and n_t the number of images) is then calculated by

$$\bar{I}_{\Omega_i}(t_j) = \frac{1}{A_i} \sum_{(x_k, y_l) \in \Omega_i} I(x_k, y_l, t_j) \quad (1)$$

where A_i is the area of Ω_i, and $I(x_k, y_l, t_j)$ is the intensity at pixel (x_k, y_l) (with $k \in \{1, 2, \ldots, n_x\}$ and n_x the number of rows in the images, and with $l \in \{1, 2, \ldots, n_y\}$ and n_y the number of columns in the images).

FRAP image data were analysed within the ROIs Ω_{bleached} and Ω_{slice}. Ω_{slice} was defined as a circular domain with centre C_{slice} and radius r_{slice}. Since the imaging depth varied between experiments, both C_{slice} and r_{slice} were cropped for each data set. The bleached ROI Ω_{bleached} was defined as a square with sidelength s_{bleached} and left-lower corner at $O_{\text{bleached}} = C_{\text{slice}} - \frac{1}{2}(s_{\text{bleached}}, s_{\text{bleached}})$. The definition of both ROIs is shown in Supplementary Fig. 2a.

Accounting for uneven illumination. Uneven imaging due to inhomogeneous sample illumination is a common problem in microscopy[37–39]. We implemented two solutions in PyFRAP to address this problem: (1) Normalisation by an image acquired before bleaching, and (2) applying a flattening mask derived from imaging a homogeneous fluorescent sample. The pixel-wise mean image over n_t images can be defined as

$$M(x_k, y_l, t_j) = \frac{1}{n_t} \sum_{j=1}^{n_t} I(x_k, y_l, t_j) \quad (2)$$

To avoid noise-induced singularities when normalising, PyFRAP computes a mean normalisation mask M_{pre} over multiple pre-bleach images, and then divides each image of the recovery time series pixel-wise by the computed mask

$$\tilde{I}(x_k, y_l, t_j) = \frac{I(x_k, y_l, t_j) + O_{\text{norm}}}{M_{\text{pre}}(x_k, y_l) + O_{\text{norm}}} \quad (3)$$

where O_{norm} is the optimal data offset computed via

$$O_{\text{norm}} = \max\left\{ \min_{k,j}\left(I(x_k, y_l, t_j)\right), \min_{k,j}\left(M_{\text{pre}}(x_k, y_l, t_j)\right) \right\} + 1 \quad (4)$$

Similarly, the flattening mask F is computed using the mean over multiple images of a fluorophore spread homogeneously across a cover slip, M_{flat}:

$$F(x_k, y_l) = \frac{\max_k(M_{\text{flat}}(x_k, y_l)) + O_{\text{flat}}}{M_{\text{flat}}(x_k, y_l) + O_{\text{flat}}} \quad (5)$$

Similar to the normalisation in Eq. (4), the optimal data offset O_{flat} is obtained by taking the maximum over all minimum intensities of images in both recovery and flattening data sets. The recovery data set is obtained by pixel-wise multiplication of the recovery image with the flattening mask obtained in Eq. (5):

$$\tilde{I}(x_k, y_l, t_j) = F(x_k, y_l) \cdot I(x_k, y_l, t_j) \quad (6)$$

An outline of both correction methods is shown in Supplementary Fig. 2c.

In the present study, two pre-bleach images were acquired per sample for the normalisation mask, and two images of fluorescein conjugated to a 40 kDa dextran or recombinant GFP homogeneously spread on a cover slip were acquired for the flattening approach. The effects of flattening and normalisation on data analysis are described in Supplementary Note 1.

Accounting for background fluorescence. Background subtraction is a standard procedure to extract the true signal of microscope images[38,39]. Similar to the flattening and normalisation masks, PyFRAP takes the average over multiple pixels to obtain a background mask and then subtracts it pixel-wise[38,39]:

$$\tilde{I}(x_k, y_l, t_j) = I(x_k, y_l, t_j) - M_{\text{bkgd}}(x_k, y_l) \quad (7)$$

The mean of two images without a sample was determined to compute a background mask. The effect of background subtraction is discussed in Supplementary Note 1.

Application of filters for noise reduction. Microscope data sets are often noisy, causing problems for normalisation and simulation. PyFRAP smooths noisy pixels by either applying a Gaussian blur with standard deviation σ_{gauss}, or a median filter with filter window radius r_{median}. We found that $\sigma_{gauss} = 2$ and $r_{median} = 5$ provided good results for the data in the present study (see Supplementary Note 1).

Accounting for fluorescence outside of the imaging view. In some cases it is not possible to capture the whole sample in one field of view under the microscope, and the concentration in the non-imaged regions needs to be estimated. PyFRAP solves this by letting users define an ROI Ω_{rim} to select an approximation of the average unbleached intensity from the first image of the recovery image series:

$$c_{rim} = \frac{1}{A_{rim}} \sum_{(x_k, y_l) \in \Omega_{rim}} I(x_k, y_l, t_0) \tag{8}$$

Ω_{rim} is defined by $\Omega_{rim} = \Omega_{slice} - \Omega_{centre}$, where

$$\Omega_{center} = \left\{ (x_k, y_l) | \sqrt{(x_k - x_c)^2 + (y_l - yc)^2} < \rho_{rim} r_{slice} \right\} \tag{9}$$

with (x_c, y_c) the centre pixel coordinates of the image. Ω_{rim} thus defines a small annulus comprising all pixels (x_k, y_l) inside Ω_{slice} that have a distance of at least $\rho_{rim} r_{slice}$ from the centre of the image (Supplementary Fig. 2b). $\rho_{rim} = 0.66$ and $\rho_{rim} = 0.4585$ were found to provide good values for the in vitro and in vivo experiments, respectively.

Simulations. PyFRAP simulates FRAP experiments numerically. Ignoring reaction kinetics, a FRAP experiment can be described by the diffusion equation

$$\frac{\partial c(\mathbf{x}, t)}{\partial t} = D \nabla^2 c(\mathbf{x}, t), \mathbf{x} \in \Omega \tag{10}$$

where $c(\mathbf{x}, t)$ is the concentration of the measured molecule at position $\mathbf{x} = \langle x, y, z \rangle$ and time t inside the domain Ω, and D is its scalar diffusion coefficient. The diffusion coefficient is assumed to be constant and homogeneous.

Since the sample is assumed to be a closed system, no-flux Neumann boundary conditions were defined as

$$\frac{\partial c(\mathbf{x}, t)}{\partial \mathbf{n}} = 0, \mathbf{x} \in \partial\Omega \tag{11}$$

where $\mathbf{n}$ is the normal vector of the boundary $\partial\Omega$ at position $\mathbf{x}$.

Initial conditions for simulations. The initial conditions are given by the bilinear interpolation P between pixels of the initial post-bleaching image:

$$P(x, y) = \frac{(x_2 - x, x - x_1)}{(x_1 - x_2)(y_2 - y_1)} \cdot \begin{pmatrix} I(x_1, y_1) & I(x_1, y_2) \\ I(x_2, y_1) & I(x_2, y_2) \end{pmatrix} \cdot \begin{pmatrix} y_2 - y \\ y - y_1 \end{pmatrix} \tag{12}$$

$I(x_{k'}, y_{l'})$ with $k', l' \in \{1, 2\}$ represents the intensities in the initial image of the four pixels surrounding (x, y). If (x, y) is outside of the visible ROI in the initial image (Ω_1), the rim concentration c_{rim} given in Eq. (8) is combined piece-wise with Eq. (12) to give the initial condition

$$c(\mathbf{x}, 0) = \begin{cases} P(x, y) & \text{if} (x, y) \in \Omega_1 \forall z \\ c_{rim} & \text{otherwise} \end{cases} \tag{13}$$

Simulation geometry. PyFRAP comes with its own geometry definition tool. Geometry definitions can then be converted into the Gmsh format[43] for meshing. PyFRAP can read Gmsh's geometry definition files, use Gmsh's mesh files, or import STereoLithography (.stl) files, allowing users to define arbitrary two- and three-dimensional geometries. This gives users the ability to describe a realistic FRAP experiment geometry with the necessary precision.

The simulation geometry Ω for the in vitro experiments was a conical frustum with upper radius $r_{upper} = 317.65$ pixels, lower radius $r_{lower} = 224.25$ pixels, and height $h \approx 90.33$ pixels (Supplementary Fig. 4b). For the in vivo experiments, the simulation geometry resembled a zebrafish embryo at dome stage, i.e., the intersection of two hemispheres intersecting each other at the equator of the outer hemisphere. Since the geometry depends on the radius of the embryo in the initial image, $r_{imaging}$ was calculated separately for each experiment[29,70]. Assuming that the radius of the inner hemisphere r_{inner} is 10% larger than the one of the outer hemisphere, r_{outer}, the geometry can be computed by

$$\begin{aligned} r_{outer} &= \frac{r_{imaging}^2 + h_{imaging}^2}{-2h_{imaging}} \\ r_{inner} &= 1.1 \cdot r_{outer} \\ d_{center} &= \sqrt{r_{inner}^2 - r_{outer}^2} \end{aligned} \tag{14}$$

where d_{centre} is the distance between the two centres of the hemispheres. Supplementary Fig. 4a shows a schematic of the zebrafish dome stage geometry.

Meshing for simulations. PyFRAP discretises simulation geometries using Gmsh[43] in combination with TetGen[44] into tetrahedral meshes. PyFRAP utilises almost all functionalities of Gmsh—such as boundary layer meshes, attractor meshes, mesh merging and mesh refinement—allowing users to apply fine meshes where they are needed.

The overall default element size in the present study was $\nu = 25$ pixels^3. To overcome numerical instabilities, such as Gibbs phenomena at the boundary of $\Omega_{bleached}$, the mesh around the bleached area boundary was refined using a boundary layer mesh of thickness $w_{BL} = 30$ pixels and element size $\nu_{BL} = 15$ pixels^3. Since only the simulation inside Ω_{slice} and $\Omega_{bleached}$ is used to fit the FRAP experiments, the mesh inside Ω_{slice} was also refined to an element size of $\nu_{slice} = 15$ pixels^3. Supplementary Fig. 4c, e shows an example of a tetrahedral mesh with both slice refinement and boundary layer meshes for the zebrafish dome geometry described in the previous section.

PDE solver. All partial differential equations (PDEs) were simulated using the FiPy toolbox[32]. The LU factorisation algorithm or the Preconditioned-Conjugated-Gradient algorithm implemented in PySparse were used to solve the linear system at each time step.

Simulation parameters. All simulations were performed with a reference diffusion coefficient of $D = 50$ pixels^2/s. To ensure that the simulations run long enough to capture the full recovery of the FRAP experiment, the end time point of the simulation was set to $t_{sim,end} = 1680$ s for experiments conducted with an acquisition interval of $\Delta t = 1$ s. Since the recovery is steepest at the beginning of the simulations, a logarithmic time-stepping scheme was used, making early time steps shorter to achieve greater accuracy. A summary of all simulation parameters used to analyse the FRAP data in the present study is given in Supplementary Table 11.

Fitting. To avoid the need to re-simulate the FRAP experiment for each choice of diffusion coefficient D, PyFRAP uses the self-similarity property of the solution to Eq. (10). For example, a simulated FRAP experiment with the diffusion coefficient $D = 50$ pixels^2/s results in the same recovery behaviour as an experiment with the diffusion coefficient $D = 200$ pixels^2/s, just four times slower. This can be described as

$$c(\mathbf{x}, t, D) = c\left(\mathbf{x}, \frac{D_{ref}}{D} t, D_{ref}\right) \tag{15}$$

where D_{ref} is the reference diffusion coefficient, i.e., the diffusion coefficient used for the simulation of Eq. (10). Supplementary Fig. 4d shows simulated recovery curves for various diffusion coefficients illustrating this self-similarity property.

PyFRAP allows users to fit four different models to FRAP data: (1) Pure diffusion, (2) diffusion and production, (3) diffusion and degradation, (4) diffusion with degradation and production, and each of these models with an additional set of equalisation parameters (see below). In case of pure diffusion, the solution for the diffusion coefficient D over a given ROI Ω_i is simply given by the volume integral of the solution in Eq. (15):

$$\bar{c}(\Omega_i, t, D) \equiv \int_{\mathbf{x} \in \Omega_i} c(\mathbf{x}, t, D) \mathrm{d}V \tag{16}$$

A summary of all parameters used to fit the FRAP data in the present study is given in Supplementary Table 12.

Extending the diffusion model with reaction kinetics. Spatially uniform production was added to the scaled FRAP model defined in Eq. (15) or in Eq. (20) by

$$\bar{c}(\Omega_i, t, D) = c(\Omega_i, t, D) + k_2 t \tag{17}$$

where k_2 is the production rate. To add spatially uniform degradation, the resulting solution is given by

$$\bar{c}(\Omega_i, t, D) = c(\Omega_i, t, D) e^{-k_1 t} \tag{18}$$

The parameter k_1 represents the degradation rate constant. Adding both degradation and production to the system results in the following superposition of solutions:

$$\bar{c}(\Omega_i, t, D) = c(\Omega_i, t, D) e^{-k_1 t} + \left(1 + e^{-k_1 t}\right) \frac{k_2}{k_1} \tag{19}$$

Accounting for varying fluorophore fractions by equalisation. FRAP experiments can vary in intensity during the experiment due to, for example, an increase or decrease in extracellular volume fraction, due to molecules moving in and out of the imaging plane, or due to an immobile fraction of fluorescent molecules. These effects are accounted for by equalisation, which normalises both simulation and data recovery curves to an equivalent scale between 0 and 1. During

the fitting process, the simulated recovery curves are slightly lifted or lowered to better resemble overall fluorescence levels. This can be written as

$$\tilde{c}(\Omega_i, t, D) = \frac{1}{\bar{c}_{\max} E_i}\left(\int_{\mathbf{x}\in\Omega_i} \bar{c}(\mathbf{x}, t, D)\mathrm{d}V - \bar{c}_{\min}\right) \quad (20)$$

where E_i is the equalisation factor for ROI Ω_i. The background $\bar{c}_{\min}$ was chosen to be the smallest concentration of the bleached ROI inside the imaging region (Ω_{bleached}), over the whole time series

$$\bar{c}_{\min} = \min_t \int_{\mathbf{x}\in\Omega_{\text{bleached}}} \bar{c}(\mathbf{x}, t)\mathrm{d}V \quad (21)$$

and the normalisation value $\bar{c}_{\max}$ to be the maximum concentration inside the whole imaging ROI (Ω_{slice}), over the whole time series

$$\bar{c}_{\max} = \max_t \int_{\mathbf{x}\in\Omega_{\text{slice}}} \bar{c}(\mathbf{x}, t)\mathrm{d}V \quad (22)$$

Minimisation and parameter estimation. Choosing one of the models defined in Eqs. (15), (16), (17), (18) and (19), the sum of squared differences, SSD, was calculated by

$$\mathrm{SSD} = \sum_{\mathrm{i}}\sum_{\mathrm{t_j}}\left(\mathrm{e}\left(\Omega_{\mathrm{i}}, \mathrm{t_j}, \mathrm{D}\right) - \mathrm{I}_{\Omega_{\mathrm{i}}}\left(\mathrm{t_j}\right)\right)^2 \quad (23)$$

where $t_j \in 0, .., T$ are all time points of the FRAP data set, and $\Omega_i \in \Omega_{\text{bleached}}, \Omega_{\text{slice}}$ are the two ROIs of interest yielding a mean optimal fit between all fitted ROIs. The minimisation of Eq. (23) was carried out using a constrained Nelder–Mead algorithm[49]. Since especially for a larger number of degrees of freedom the minimisation algorithm tended to stop in local minima, initial guesses for the diffusion coefficient D were tested over two orders of magnitude, and the fit yielding the minimum SSD was considered optimal.

Analysis speed. Details of the method to determine PyFRAP's performance in terms of analysis speed are described in Supplementary Note 4 and Supplementary Tables 13 and 14.

Statistics. PyFRAP offers four statistical tools (Supplementary Table 2) allowing users to test whether the estimated diffusion coefficient for one experimental group is significantly different from another one. The statistical tools include the two most prominent parametric significance tests, the Student's t-test[56] and a modification of this test, Welch's t-test[71], which both assume normally distributed test groups. PyFRAP also provides the Shapiro–Wilk test, allowing PyFRAP users to quickly assess whether the estimated diffusion coefficients follow a normal distribution. The Shapiro–Wilk test was recently found to have the best sensitivity compared to other common normality tests[72]. If normality cannot be guaranteed, PyFRAP offers two non-parametric ranked hypothesis tests: The Wilcoxon signed-rank test[73] and the Mann–Whitney U test[57].

Often, the underlying reaction kinetics of FRAP experiments or the relevance of their contribution might be unknown[54]. However, models with more parameters generally provide better fits than simpler models. The AIC[55] allows users to evaluate which model fits the data the best while keeping model complexity low. For this, let

$$\Theta := (k_1, k_2, D, E_1, E_2, \dots) \quad (24)$$

be the vector of unknown diffusion coefficient D, reaction rates k_1 and k_2, and E_1, E_2, … a list of equalisation factors. Moreover, let $m = m(\Theta)$ be the model prediction using Θ. Assuming that the data is distributed normally around the model

$$d_i - m_i \sim \mathcal{N}(\mu, \sigma) \quad (25)$$

the log-likelihood function at data point i, L_i becomes

$$L_i(\Theta|d_i - m_i) = (d_i - m_i)^2 \quad (26)$$

and is thus identical with the sum of squared differences used for optimisation in Eq. (23):

$$L(\Theta) = \sum_i L_i(\Theta) = \mathrm{SSD} \quad (27)$$

The AIC is then given by

$$\mathrm{AIC} = 2\mathrm{k} - 2\mathrm{L}\left(\hat{\Theta}\right) \quad (28)$$

where k is the number of parameters of model m and

$$\hat{\Theta} = \mathrm{argmin}(L(\Theta|d_i - m_i, i = 1...n)) \quad (29)$$

is the parameter configuration Θ minimising the log-likelihood function (Eq. (27)), i.e., the parameter configuration returned from fitting the model to data. The best model according to the AIC is then $m(\mathrm{argmin}(\mathrm{AIC}_i - \mathrm{AIC}_{\min}))$. If the number of sample points is small, the corrected AIC (AICc) provides a more accurate model selection technique:

$$\mathrm{AICc} = \mathrm{AIC} + \frac{2\mathrm{k}(\mathrm{k}+1)}{\mathrm{n}-\mathrm{k}-1} \quad (30)$$

where n is the number of data points. A rule of thumb for when the AIC (Eq. (28)) or its corrected version (Eq. (30)) should be used is

$$\frac{n}{k} > 40 \quad (31)$$

PyFRAP automatically selects which statistical model is more appropriate if not specified differently.

PyFRAP also provides R^2-values for each fit: An R^2-value for each fitted ROI and the product and mean of these values. In general, PyFRAP computes an R^2-value of an ROI by

$$R^2 = 1 - \frac{\sum_i m_i - d_i}{\sum_i d_i - \bar{d}} \quad (32)$$

where m_i and d_i are model and data at time i, and $\bar{d}$ is the mean over all data points.

Data exclusion. We performed a rigorous screen of all data sets, and we excluded data sets that showed strong radial inhomogeneities in the first post-bleach image due to inhomogeneous distribution of fluorescent molecules. Moreover, we excluded in vitro data sets that showed unstable distributions in the overall fluorescence intensity levels, indicating incomplete bleaching through the depth of the sample.

Code availability. PyFRAP is freely available from https://mueller-lab.github.io/PyFRAP.

Data availability. All data is available from the corresponding author upon request.

Received: 24 September 2017 Accepted: 26 March 2018
Published online: 20 April 2018

References

1. Crick, F. Diffusion in embryogenesis. *Nature* **255**, 420–422 (1970).
2. Lander, A. D., Nie, Q. & Wan, F. Y. M. Do morphogen gradients arise by diffusion? *Dev. Cell.* **2**, 785–796 (2002).
3. Müller, P. & Schier, A. F. Extracellular movement of signaling molecules. *Dev. Cell.* **21,**145-158 (2011).
4. Poo, M. M. & Cone, R. A. Lateral diffusion of rhodopsin in Necturus rods. *Exp. Eye Res.* **17**, 503–507 (1973).
5. Liebman, P. A. & Entine, G. Lateral diffusion of visual pigment in photoreceptor disk membranes. *Science* **185**, 457–459 (1974).
6. Loren, N. et al. Fluorescence recovery after photobleaching in material and life sciences: putting theory into practice. *Q. Rev. Biophys.* **48**, 323–387 (2015).
7. Lippincott-Schwartz, J., Altan-Bonnet, N. & Patterson, G. H. Photobleaching and photoactivation: following protein dynamics in living cells. *Nat. Cell Biol.* **5**, S7–S14 (2003).
8. Bancaud, A., Huet, S., Rabut, G. & Ellenberg, J. Fluorescence perturbation techniques to study mobility and molecular dynamics of proteins in live cells: FRAP, photoactivation, photoconversion, and FLIP. *Cold Spring Harb. Protoc.* **12**, 1303–1325 (2010).
9. Griffin, E. E., Odde, D. J. & Seydoux, G. Regulation of the MEX-5 gradient by a spatially segregated kinase/phosphatase cycle. *Cell* **146**, 955–958 (2011).
10. Zhou, S. et al. Free extracellular diffusion creates the Dpp morphogen gradient of the *Drosophila* wing disc. *Curr. Biol.* **22**, 668–675 (2012).
11. Axelrod, D., Koppel, D. E., Schlessinger, J., Elson, E. & Webb, W. W. Mobility measurement by analysis of fluorescence photobleaching recovery kinetics. *Biophys. J.* **16**, 1055–1069 (1976).

12. Soumpasis, D. Theoretical analysis of fluorescence photobleaching recovery experiments. *Biophys. J.* **41**, 95–97 (1983).
13. Sprague, B. L. & McNally, J. G. FRAP analysis of binding: proper and fitting. *Trends Cell Biol.* **15**, 84–91 (2005).
14. Kang, M., Day, C. A., Drake, K., Kenworthy, A. K. & DiBenedetto, E. A generalization of theory for two-dimensional Fluorescence Recovery After Photobleaching applicable to confocal laser scanning microscopes. *Biophys. J.* **97**, 1501–1511 (2009).
15. Deschout, H. et al. Straightforward FRAP for quantitative diffusion measurements with a laser scanning microscope. *Opt. Express* **18**, 22886–22905 (2010).
16. Kang, M., Day, C. A., Kenworthy, A. K. & DiBenedetto, E. Simplified equation to extract diffusion coefficients from confocal FRAP data. *Traffic* **13**, 1589–1600 (2012).
17. Kraft, L. J., Dowler, J. & Kenworthy, A. K. *Frap-toolbox: Software for the Analysis of Fluorescence Recovery after Photobleaching*. http://www.fraptoolbox.com Accessed 12 Dec 2016 (2014).
18. Lin, L. & Othmer, H. G. Improving parameter inference from FRAP data: an analysis motivated by pattern formation in the *Drosophila*wing disc. *Bull. Math. Biol.* **79**, 448–497 (2017).
19. Beaudouin, J., Mora-Bermúdez, F., Klee, T., Daigle, N. & Ellenberg, J. Dissecting the contribution of diffusion and interactions to the mobility of nuclear proteins. *Biophys. J.* **90**, 1878–1894 (2006).
20. Schaff, J. C., Cowan, A. E., Loew, L. M. & Moraru, I. I. Virtual FRAP-an experiment-oriented simulation tool. *Biophys. J.* **96**, 30a (2009).
21. Blumenthal, D., Goldstien, L., Edidin, M. & Gheber, L. A. Universal approach to FRAP analysis of arbitrary bleaching patterns. *Sci. Rep.* **5**, 11655 (2015).
22. Müller, P., Rogers, K. W., Yu, S. R., Brand, M. & Schier, A. F. Morphogen transport. *Development* **140**, 1621–1638 (2013).
23. Umulis, D. M. & Othmer, H. G. The importance of geometry in mathematical models of developing systems. *Curr. Opin. Genet. Dev.* **22**, 547–552 (2012).
24. Weiss, M. Challenges and artifacts in quantitative photobleaching experiments. *Traffic* **5**, 662–671 (2004).
25. Mazza, D., Cella, F., Vicidomini, G., Krol, S. & Diaspro, A. Role of three-dimensional bleach distribution in confocal and two-photon fluorescence recovery after photobleaching experiments. *Appl. Opt.* **46**, 7401–7411 (2007).
26. Machán, R., Foo, Y. H. & Wohland, T. On the equivalence of FCS and FRAP: simultaneous lipid membrane measurements. *Biophys. J.* **111**, 152–161 (2016).
27. Braga, J., Desterro, J. M. & Carmo-Fonseca, M. Intracellular macromolecular mobility measured by Fluorescence Recovery After Photobleaching with confocal laser scanning microscopes. *Mol. Biol. Cell.* **10**, 4749–4760 (2004).
28. Blischak, J. D., Davenport, E. R. & Wilson, G. A quick introduction to version control with Git and GitHub. *PLoS. Comput. Biol.* **12**, e1004668 (2016).
29. Müller, P. et al. Differential diffusivity of Nodal and Lefty underlies a reaction-diffusion patterning system. *Science* **336**, 721–724 (2012).
30. Sigaut, L., Ponce, M. L., Colman-Lerner, A. & Dawson, S. P. Optical techniques provide information on various effective diffusion coefficients in the presence of traps. *Phys. Rev. E* **82**, 051912 (2010).
31. Millman, K. J. & Aivazis, M. Python for scientists and engineers. *Comput. Sci. Eng.* **13**, 9–12 (2011).
32. Guyer, J. E., Wheeler, D. & Warren, J. A. FiPy: partial differential equations with Python. *Comput. Sci. Eng.* **11**, 6–15 (2009).
33. van der Walt, S. et al. scikit-image: Image processing in Python. *PeerJ* **2**, e453 (2014).
34. Jones, E. et al. *SciPy: Open source scientific tools for Python* (2001). http://www.scipy.org/
35. van der Walt, S., Colbert, C. & Varoquaux, G. The numpy array: a structure for efficient numerical computation. *Comput. Sci. Eng.* **13**, 22–30 (2011).
36. Hunter, J. D. Matplotlib: a 2D graphics environment. *Comput. Sci. Eng.* **9**, 90–95 (2007).
37. Lindblad, J. & Bengtsson, E. in *Proceedings of the 12th Scandinavian Conference on Image Analysis (SCIA)*, 264–271 (2001).
38. Waters, J. C. Accuracy and precision in quantitative fluorescence microscopy. *J. Cell. Biol.* **185**, 1135–1148 (2009).
39. Schwarzfischer, M. et al. in *Proceedings of Microscopic Image Analysis with Applications in Biology* (2011).
40. Gregor, T., Bialek, W., de Ruyter van Steveninck, R. R., Tank, D. W. & Wieschaus, E. F. Diffusion and scaling during early embryonic pattern formation. *Proc. Natl Acad. Sci. USA* **102**, 18403–18407 (2005).
41. Kicheva, A. et al. Kinetics of morphogen gradient formation. *Science* **5811**, 521–525 (2007).
42. Pomreinke, A. P. et al. Dynamics of BMP signaling and distribution during zebrafish dorsal-ventral patterning. *eLife* **6**, e25861 (2017).
43. Geuzaine, C. & Remacle, J.-F. Gmsh: a 3-D finite element mesh generator with built-in pre- and post-processing facilities. *Int. J. Numer. Methods Eng.* **79**, 1309–1331 (2009).
44. Si, H. Tetgen, a delaunay-based quality tetrahedral mesh generator. *ACM Trans. Math. Softw.* **41**, 11:1–11:36 (2015).
45. Sprague, B. L., Pego, R. L., Stavreva, D. A. & McNally, J. G. Analysis of binding reactions by fluorescence recovery after photobleaching. *Biophys. J.* **86**, 3473–3495 (2004).
46. Miura, K. *Frapcalc*. http://wiki.cmci.info/downloads/frap_analysis Accessed 12 Dec 2016 (2016).
47. Rapsomaniki, M. A. et al. EasyFRAP: an interactive, easy-to-use tool for qualitative and quantitative analysis of FRAP data. *Bioinformatics* **28**, 1800–1801 (2012).
48. Castle, B. T., Howard, S. A. & Odde, D. J. Assessment of transport mechanisms underlying the Bicoid morphogen gradient. *Cell. Mol. Bioeng.* **4**, 116–121 (2011).
49. Nelder, J. A. & Mead, R. A simplex method for function minimization. *Comput. J.* **7**, 308–313 (1965).
50. Nash, S. G. Newton-type minimization via the Lanczos method. *SIAM J. Numer. Anal.* **21**, 770–788 (1984).
51. Nocedal, J. & Wright, S. J. *Numerical optimization*. 2nd edn, (Springer, NY, 2006).
52. Bläßle, A. & Müller, P. PyFDAP: automated analysis of fluorescence decay after photoconversion (FDAP) experiments. *Bioinformatics* **6**, 972–974 (2015).
53. Rogers, K. W., Bläßle, A., Schier, A. F. & Müller, P. Measuring protein stability in living zebrafish embryos using fluorescence decay after photoconversion (FDAP). *J. Vis. Exp.* **95**, e52266 (2015).
54. Mai, J. et al. Are assumptions about the model type necessary in reaction-diffusion modeling? A FRAP application. *Biophys. J.* **100**, 1178–1188 (2011).
55. Akaike, H. A new look at the statistical model identification. *IEEE Trans. Autom. Control* **19**, 716–723 (1974).
56. Student. The probable error of a mean. *Biometrika* **6**, 1–25 (1908).
57. Mann, H. B. & Whitney, D. R. On a test of whether one of two random variables is stochastically larger than the other. *Ann. Math. Stat.* **18**, 50–60 (1947).
58. Shapiro, S. S. & Wilk, M. B. An analysis of variance test for normality (complete samples). *Biometrika* **52**, 591–611 (1965).
59. Aaron, J. *FRAP* https://de.mathworks.com/matlabcentral/fileexchange/47327-frap-zip Accessed 12 Dec 2016 (2016).
60. Ulrich, M. et al. Tropical-parameter estimation and simulation of reaction-diffusion models based on spatio-temporal microscopy images. *Bioinformatics* **22**, 2709–2710 (2006).
61. Gurskaya, N. G. et al. Engineering of a monomeric green-to-red photoactivatable fluorescent protein induced by blue light. *Nat. Biotechnol.* **24**, 461–465 (2006).
62. Hrabe, J., Hrabetová, S. & Segeth, K. A model of effective diffusion and tortuosity in the extracellular space of the brain. *Biophys. J.* **87**, 1606–1617 (2004).
63. Tao, L. & Nicholson, C. Maximum geometrical hindrance to diffusion in brain extracellular space surrounding uniformly spaced convex cells. *J. Theor. Biol.* **229**, 59–68 (2004).
64. Novak, I. L., Kraikivski, P. & Slepchenko, B. M. Diffusion in cytoplasm: effects of excluded volume due to internal membranes and cytoskeletal structures. *Biophys. J.* **97**, 758–767 (2009).
65. Donovan, P., Chehreghanianzabi, Y., Rathinam, M. & Zustiak, S. P. Homogenization theory for the prediction of obstructed solute diffusivity in macromolecular solutions. *PLoS ONE* **11**, e0146093 (2016).
66. Periasamy, N. & Verkman, A. S. Analysis of fluorophore diffusion by continuous distributions of diffusion coefficients: application to photobleaching measurements of multicomponent and anomalous diffusion. *Biophys. J.* **75**, 557–567 (1998).
67. Xiong, R. et al. Sizing nanomaterials in bio-fluids by cFRAP enables protein aggregation measurements and diagnosis of bio-barrier permeability. *Nat. Commun.* **7**, 12982 (2016).
68. Höckendorf, B., Thumberger, T. & Wittbrodt, J. Quantitative analysis of embryogenesis: a perspective for light sheet microscopy. *Dev. Cell.* **23**, 1111–1120 (2012).
69. Yu, S. R. et al. Fgf8 morphogen gradient forms by a source-sink mechanism with freely diffusing molecules. *Nature* **461**, 533–536 (2009).
70. Kimmel, C. B., Ballard, W. W., Kimmel, S. R., Ullmann, B. & Schilling, T. F. Stages of embryonic development of the zebrafish. *Dev. Dyn.* **203**, 253–310 (1995).
71. Welch, B. L. The generalisation of Student's problems when several different population variances are involved. *Biometrika* **34**, 28–35 (1947).
72. Razali, N. M. & Wah, Y. B. Power comparisons of Shapiro-Wilk, Kolmogorov-Smirnov, Lilliefors and Anderson-Darling tests. *J. Stat. Model. Anal.* **2**, 21–33 (2011).
73. Wilcoxon, F. Individual comparisons by ranking methods. *Biom. Bull.* **1**, 80–83 (1945).

Acknowledgements

We thank Ekkehard Kröwerath (University Hospital Tübingen, Centre for Dentistry, Oral Medicine, and Maxillofacial Surgery) for the preparation of plexiglass holes, Katherine Rogers and Fabian Fröhlich for discussions and suggestions, and Sarah Keim and Katherine Rogers for testing PyFRAP. This work was supported by the Emmy Noether Programme of the Deutsche Forschungsgemeinschaft, the Max Planck Society, and an ERC Starting Grant to P.M.

Author contributions

A.B., B.M.J. and P.M. conceived the study. A.B. and P.M. designed the software and performed data analysis and simulations. A.B. implemented the software. G.S., T.B., D.M. and H.P. conducted experiments. A.B. and P.M. wrote the manuscript.

Additional information

Supplementary Information accompanies this paper at https://doi.org/10.1038/s41467-018-03975-6.

Competing interests: The authors declare no competing interests.

Reprints and permission information is available online at http://npg.nature.com/reprintsandpermissions/

Publisher's note: Springer Nature remains neutral with regard to jurisdictional claims in published maps and institutional affiliations.

Open Access This article is licensed under a Creative Commons Attribution 4.0 International License, which permits use, sharing, adaptation, distribution and reproduction in any medium or format, as long as you give appropriate credit to the original author(s) and the source, provide a link to the Creative Commons license, and indicate if changes were made. The images or other third party material in this article are included in the article's Creative Commons license, unless indicated otherwise in a credit line to the material. If material is not included in the article's Creative Commons license and your intended use is not permitted by statutory regulation or exceeds the permitted use, you will need to obtain permission directly from the copyright holder. To view a copy of this license, visit http://creativecommons.org/licenses/by/4.0/.

© The Author(s) 2018

Supplementary Information for

Quantitative diffusion measurements using the open-source software PyFRAP

Alexander Bläßle[1], Gary Soh[1], Theresa Braun[1,2], David Mörsdorf[1], Hannes Preiß[1], Ben M. Jordan[3], and Patrick Müller[1,*]

[1]Friedrich Miescher Laboratory of the Max Planck Society, Tübingen, Germany
[2]Present address: University of Konstanz, Konstanz, Germany
[3]Department of Organismic and Evolutionary Biology, Harvard University, Cambridge, USA

[*]Correspondence to: patrick.mueller@tuebingen.mpg.de (P.M.)

This PDF includes:
Supplementary Notes 1-4
Supplementary Tables 1-14
Supplementary Figures 1-9
Supplementary References 1-43

Supplementary Note 1: Analysis method selection

To assess how image correction by flattening, normalisation, background subtraction, Gaussian blur, and median filter application affects effective diffusion estimates from FRAP experiments, we tested the 24 analysis combinations listed in Supplementary Table 1. We assessed whether 1) the resulting diffusion estimate D is affected, 2) the standard deviation σ of the estimated diffusion coefficients is affected (i.e. whether correcting and smoothing the images makes the diffusion estimates more exact), and 3) the goodness of the fits (i.e. R^2-values) is affected. We quantified the effect of an analysis option by

$$H(v, \alpha) = \frac{v(\alpha)}{v(\alpha_0)} \tag{1}$$

where $\alpha = \{n, f, b, g, m\}$ represents an analysis option defined by five binary entries indicating whether normalisation n, flattening f, background subtraction b, Gaussian blur g, or a median filter m was used. If we did not correct images, we denote this by α_0. The variable v describes the quantified result, such as the mean diffusion coefficient. Supplementary Fig. 3 shows a subset of this analysis for three different variables v: The mean diffusion coefficient D, the variance of diffusion coefficients σ, and the fit quality R^2. FRAP experiments performed in the present study were grouped by condition (*in vitro* experiments with free diffusion, *in vitro* experiments with beads, and *in vivo* experiments) to isolate condition-specific effects. We did not correct for potential illumination inhomogeneities in *in vivo* experiments, since these only covered a small centered area of the total image, and illumination is homogeneous in this region. Moreover, normalisation cannot be used for the analysis of *in vitro* experiments containing beads, since normalisation would introduce artificially high intensity areas at the locations of the beads.

If only normalisation and flattening were applied, we observed an increase of the apparent diffusion coefficients and an improvement in fit quality for free diffusion (Supplementary Fig. 3a,c). Both techniques only mildly affected the variance of diffusion coefficients (Supplementary Fig. 3b). Background subtraction had no effect on any measure (Supplementary Fig. 3a-c). Moreover, noise reduction or smoothing via median filter or Gaussian blur application tended to decrease the variance in all conditions (Supplementary Fig. 3b) and improve the fits for free diffusion (Supplementary Fig. 3b).

We also tested whether a combination of an illumination correction technique (n or f) with the remaining three manipulation techniques (b, g and m) can further improve the analysis. Supplementary Fig. 3d shows that this can lead to an increase in mean apparent diffusion estimates similar to those observed in Supplementary Fig. 3a. Moreover, applying a median filter or Gaussian blur in combination with flattening improves fit quality and decreases diffusion estimate variance (Supplementary Fig. 3e,f).

To keep the extent of image manipulation as minimal as possible while obtaining comparable low-variance estimates from high-quality fits, we only applied flattening to correct the images from *in vitro* experiments. Since both Gaussian blur and median filter treatments appeared to stabilise diffusion coefficient estimates (i.e. reducing their variance) to a similar extent, we restricted image smoothing to the application of a median filter for all other analyses.

Supplementary Note 2: Comparison of PyFRAP to other FRAP analysis software

We selected four current FRAP analysis software packages for comparison with PyFRAP: The two analytical programs easyFRAP[1] and FrapCalc[2], and the two numerical packages virtualFRAP[3] and simFRAP[4] (Supplementary Table 4).

To assess the performance of PyFRAP in comparison with other FRAP analysis software solutions, we created simulated FRAP data sets using PyFRAP's simulation toolbox. We found that PyFRAP and our in-house software based on MATLAB and COMSOL Multiphysics[5–7] produced identical simulated data, and we subsequently chose to use PyFRAP to simulate the experiments due to the ease of PyFRAP's scripting abilities. We simulated two-dimensional or three-dimensional FRAP experiments with circular bleaching spots of various sizes for a 300 s time-course. Two-dimensional simulated experiments were conducted in a circle with radius 215 μm, and three-dimensional experiments resembled a zebrafish at dome stage with $r_{\text{imaging}} = 215$ μm and $h_{\text{imaging}} = 80$ μm (see Methods section for details). Molecules were allowed to move with diffusion coefficients of 10 μm^2/s, 50 μm^2/s, or 200 μm^2/s, covering a range of typical diffusivities in biological samples. Bleached spots were placed in the center of the simulation geometry and comprised 5%, 10%, or 50% of the slice radius. We chose the boundary layer mesh described in the Methods section to envelope the bleached spot, guaranteeing numerical accuracy of the simulation experiments. PDEs were simulated over 4000 logarithmically-spaced time steps. The simulations were saved in a csv sheet specifically formatted for the use of easyFRAP or FrapCalc, or in 301 images by interpolation of the numerical solution onto a 512 μm $\times$ 512 μm grid. We then either imported and analysed the csv sheet using FrapCalc (`https://github.com/miura/FrapCalc` for IgorPro7) or easyFRAP, or read in and analysed the simulated images using simFRAP or virtualFRAP. The benchmarking analysis was performed using Microsoft Windows 8.1.

In contrast to other programs that determine absolute diffusion coefficients, easyFRAP only provides recovery half times ($1/\tau_{\frac{1}{2}}$). Thus, to compute diffusion coefficients from easyFRAP, we used the well-established[8] equation

$$D = \frac{-\omega^2 \ln\left(\frac{1}{2}\right)}{\tau_{\frac{1}{2}}}$$

with various dimensions of the bleached spot ω.

We used PyFRAP's standard pipeline to analyse the saved simulated FRAP images files in an unbiased manner, only constraining imaging depth and radius.

As mentioned in the main text, PyFRAP outperformed all tested software packages and exhibited the smallest error between predicted and simulated diffusion coefficients (Fig. 3c).

Supplementary Note 3: Data analysis and control experiments

Computation of theoretical diffusion coefficients

We compared our *in vitro* FRAP results for differently sized fluorescein-labeled dextrans to predictions derived from the Einstein-Stokes equation

$$D = \frac{k_{\mathrm{B}}T}{6\pi\eta r} \tag{2}$$

where $k_{\mathrm{B}} = 1.380\,648\,52 \times 10^{-23}\ \mathrm{m^2\,kg\,s^{-2}\,K^{-1}}$ is the Boltzmann constant. The FRAP experiments were conducted in an aqueous solution with viscosity $\eta = 0.9321 \times 10^{-3}\ \mathrm{kg\,s^{-1}\,m^{-1}}$ at $T = 296\ \mathrm{K}$. Stokes radii r of the fluorescent molecules were obtained from the manufacturers' websites and are listed along with the calculated theoretical diffusion coefficients in Supplementary Table 5.

FRAP experiments with different bleach window sizes

To test whether different bleach window size might lead to different diffusion coefficient estimates, we performed FRAP experiments with three different bleach window sizes: 34.01 $\mu\mathrm{m}$, 141.7 $\mu\mathrm{m}$, and 242.91 $\mu\mathrm{m}$. Using fluorescein-labeled dextrans of 40 kDa and 70 kDa molecular weight, we found that different bleach window sizes do not affect diffusion coefficient estimates determined by PyFRAP (Supplementary Fig. 6).

FRAP experiments can be executed over different spatial scales, from subcellular to tissue-level measurements. Our experiments were performed on spatial scales that are three orders of magnitude larger than the microscope's resolution limit. However, it is possible that FRAP experiments in very small samples with subcellular bleach areas may be affected by the imaging resolution, and future deconvolution-based approaches could be helpful to improve the measurement accuracy of PyFRAP in these cases.

Simulating tortuosity

The movement of molecules during FRAP experiments in biological samples is affected by obstacles such as cells, nuclei, or filopodia, and such tortuous molecule movements have been suggested to alter recovery rates and diffusion estimates[6].

To obtain a better understanding of how obstacles alter effective diffusion coefficients, we performed a simulation study in two- and three-dimensional geometries. We placed objects with a radius of $r_{\mathrm{Bead}} \approx 20\ \mu\mathrm{m}$ (similar to the dimensions of cells and beads used in the present study) in each geometry in three different ways: 1) Equally sized beads aligned as a regular grid (Supplementary Fig. 7a), 2) randomly placed within the domain with radii drawn from a cut-off normal distribution (Supplementary Fig. 7b,d), and 3) equally sized beads placed according to a hexagonal close-packing (Supplementary Fig. 7c). Beads were placed with different minimal gaps between them, ranging from 0.05 $\mu\mathrm{m}$ to 10 $\mu\mathrm{m}$. For 2D simulations, the overall geometry was a circle with radius 300 $\mu\mathrm{m}$. We chose a cylinder with equal radius and height of 100 $\mu\mathrm{m}$ or a cuboid with dimensions 600 $\mu\mathrm{m} \times 600\ \mu\mathrm{m} \times 100\ \mu\mathrm{m}$ for all 3D simulations experiments. The combination between various placement methods and gap sizes allowed us to vary the extracellular volume fraction (EVF) – i.e. the space available for the diffusing molecules – from 25% to 78%.

Confirming previous analyses[9–12], we found that the introduction of beads delayed molecule recovery in the bleached ROI, and the effect of tortuosity increased as the EVF decreased (Fig. 5b, Supplementary Fig. 7e,f, Supplementary Table 8). Moreover, the effect in two-dimensional experiments was more severe. For example, FRAP simulations with EVF $= 36\%$ reduced diffusion by 51% compared to only 40% for EVF $= 38\%$ in a three-dimensional simulation. Both observations are in line with theoretical predictions and previous results[9–12].

BSA does not affect fluorophore diffusivity

We found a stronger effect of bead-mediated tortuosity on 70 kDa fluorescein-labeled dextran molecules than on GFP *in vitro* (Fig. 5d,e). BSA was added to the aqueous solution with GFP to prevent the fluorescent protein from interacting with the plexiglass surface of the drilled hole in the *in vitro* experiments. To test whether BSA might also interact with the polyacrylamide beads and thus distort FRAP results, we repeated the experiments with 70 kDa fluorescein-labeled dextran both for pure diffusion with beads in addition to experiments with 70 kDa fluorescein-labeled dextran + BSA + beads. We found that BSA had no influence on the recovery rates, yielding equal results within standard error, i.e. 14.9 ± 2.1 μm^2/s for bead experiments and 15.1 ± 2.4 μm^2/s for experiments with additional BSA (Supplementary Fig. 9a).

Varying the experimental settings for Squint-GFP FRAP experiments does not consistently affect measured diffusion coefficients

For the FRAP experiments with Squint-GFP produced from injected mRNA, we acquired data sets varying the amount of injected mRNA, the frame rate and length of image acquisition, and the zoom factor of the microscope. Results were partitioned into three experimental groups, i.e. images recorded with 1) a frame rate of 1 frames/10 s for 3000 s with 30 pg of injected mRNA and a spatial resolution of 340.08 $\mu m \times 340.08$ μm, 2) a frame rate of 1 frame/10 s for 3000 s with 200 pg of injected mRNA and a spatial resolution of 566.79 $\mu m \times 566.79$ μm, and 3) a frame rate of 1 frame/s for 300 s with 200 pg of injected mRNA and a spatial resolution of 566.79 $\mu m \times 566.79$ μm.

There were no clear trends between different acquisition methods (Supplementary Fig. 9b). However, acquiring images at a higher frame rate for a shorter period of time appeared to make experiments and thus apparent diffusion coefficients more noisy, possibly resulting from the slow transport process underlying Squint-GFP diffusion.

Supplementary Note 4: PyFRAP analysis speed

To evaluate PyFRAP's analysis speed, we tested several analysis settings on different operating systems and computers. We designed three test cases: 1) A two-dimensional circular geometry similar to those used for the benchmarking simulations described in Supplementary Note 2, 2) a three-dimensional frustum geometry identical to the ones used to analyse the *in vitro* FRAP experiments described in the present work, and 3) a three-dimensional geometry resembling a zebrafish embryo at dome stage similar to our analysis of the *in vivo* experiments. The test data sets had identical properties as the data described for the respective experiments. A summary of all relevant test parameters can be found in Supplementary Table 13. All cases were tested on the three common operating systems Mac OSX, Microsoft Windows, and Ubuntu Linux, and the time from analysing the image data to mesh generation, simulation, and model fitting was measured for each test case. The results of these tests are summarised in Supplementary Table 14.

Note that PyFRAP does not allow parallel processing and only uses a single core of a CPU.

Supplementary Table 1. Combinations of image correction and smoothing methods used to analyse FRAP experiments. See Supplementary Fig. 3 for the results of this analysis. Note that flattening and normalisation were never applied at the same time since this would have distorted the image data.

Combination	Normalisation	Flattening	Background subtraction	Gaussian filter	Median filter
1	Off	Off	Off	Off	Off
2	Off	Off	Off	Off	On
3	Off	Off	Off	On	Off
4	Off	Off	Off	On	On
5	Off	Off	On	Off	Off
6	Off	Off	On	Off	On
7	Off	Off	On	On	Off
8	Off	Off	On	On	On
9	Off	On	Off	Off	Off
10	Off	On	Off	Off	On
11	Off	On	Off	On	Off
12	Off	On	Off	On	On
13	Off	On	On	Off	Off
14	Off	On	On	Off	On
15	Off	On	On	On	Off
16	Off	On	On	On	On
17	On	Off	Off	Off	Off
18	On	Off	Off	Off	On
19	On	Off	Off	On	Off
20	On	Off	Off	On	On
21	On	Off	On	Off	Off
22	On	Off	On	Off	On
23	On	Off	On	On	Off
24	On	Off	On	On	On

Supplementary Table 2. Statistical tools available in PyFRAP.

Method	Purpose	Type	Publication
Student's t-test	Significance testing	Parametric	[13]
Welch's t-test	Significance testing	Parametric	[14]
Wilcoxon signed-rank test	Significance testing	Non-parametric	[15]
Mann-Whitney U test	Significance testing	Non-parametric	[16]
Shapiro-Wilk test	Normality testing	Parametric	[17]
Akaike Information Criterion (AIC)	Model comparison	Parametric	[18]

Supplementary Table 3. Benchmarking PyFRAP against an in-house software combination of MATLAB and COMSOL Multiphysics. Data was simulated with MATLAB and COMSOL Multiphysics[5–7], and then fitted with PyFRAP for each of the four available reaction-diffusion models.

MATLAB + COMSOL Multiphysics			***PyFRAP***			***R^2-value***		***AIC***
D (μm^2/s)	**Degradation (10^{-4}/s)**	**Production (10^{-4} [c]/s)**	**D (μm^2/s)**	**Degradation (10^{-4}/s)**	**Production (10^{-4} [c]/s)**	**Bleached window**	**Slice**	**Correct model prediction**
Pure diffusion								
1	0	0	1.0	0	0	0.998	0.972	yes
5	0	0	4.8	0	0	1.000	0.910	yes
10	0	0	9.5	0	0	1.000	0.932	yes
40	0	0	39.1	0	0	0.999	0.870	yes
110	0	0	109.4	0	0	0.999	0.984	yes
200	0	0	199.1	0	0	0.999	0.990	yes
Diffusion + degradation								
1	5.0	0	1.0	5.8	0	0.998	0.921	yes
5	5.0	0	4.9	5.5	0	1.000	0.959	yes
10	5.0	0	9.7	5.4	0	1.000	0.972	yes
40	5.0	0	39.0	5.0	0	0.999	0.950	yes
110	5.0	0	108.1	4.9	0	0.999	0.943	yes
200	5.0	0	198.0	5.0	0	0.999	0.982	yes
Diffusion + production								
1	0	5.0	1.0	0	4.4	0.999	0.950	yes
5	0	5.0	5.0	0	4.6	1.000	0.972	yes
10	0	5.0	9.8	0	4.7	1.000	0.978	yes
40	0	5.0	38.9	0	5.0	1.000	0.991	yes
110	0	5.0	108.3	0	5.1	1.000	0.998	yes
200	0	5.0	198.4	0	5.0	1.000	0.999	yes
Diffusion + production + degradation								
1	5.0	7.0	1.1	4.8	6.2	0.992	0.845	no
5	5.0	7.0	5.0	4.8	6.4	1.000	0.894	no
10	5.0	7.0	9.5	5.9	7.5	1.000	0.910	no
40	5.0	7.0	39.2	4.1	6.3	1.000	0.979	no
110	5.0	7.0	105.2	9.7	12.0	0.999	0.995	no
200	5.0	7.0	192.6	11.6	13.3	1.000	0.996	no

Supplementary Table 4. Selection of current FRAP analysis software packages.

Software	Fit type	Result type	Input data	Publication	Platform	Tested	Comments
easyFRAP	Analytical	Qualitive	CSV	[1]	Windows, Mac OSX	Yes	Requires MATLAB Runtime, only produces $\tau_{1/2}$
FrapCalc	Analytical	Qualitive	CSV	[2]	Windows, Mac OSX	Yes	Requires IgorPro
FRAP	Analytical	Qualitive	Image files	[19]	Cross-platform	No	Requires specialised MATLAB toolboxes
simFRAP	Simulation	Quantitive	Image files	[4]	Cross-platform	Yes	Fiji Plugin
virtualFRAP	Simulation	Quantitive	Image files	[3]	Windows	Yes	
FRAPToolbox	Simulation	Quantitive	Image files	[20]	Cross-platform	No	Unable to read non-OME formats
Tropical	Simulation	Quantitive	Image files	[21]	Windows, Linux	No	Software unavailable

Supplementary Table 5. Fluorescent samples used for *in vitro* experiments, and their calculated theoretical diffusion coefficients. Theoretical values were only computed if an estimate of the molecule's Stokes radius could be found (see Supplementary Note 3 for details).

Fluorophore	**Molecular weight (kDa)**	**Concentration (µM)**	**Manufacturer**	**Stokes radius (nm)**	**Theoretical D ($\mu m^2/s$)**
Fluorescein-dextran	3	1	Thermo Fisher	1.36	171
Fluorescein-dextran	4	1, 15, 100	Sigma-Aldrich	1.4	166
Fluorescein-dextran	10	1	Thermo Fisher	2.3	101
Fluorescein-dextran	40	1	Thermo Fisher	4.5	52
Fluorescein-dextran	70	1	Sigma-Aldrich	6.0	39
Fluorescein-dextran	70	1	Thermo Fisher	6.0	39
Fluorescein-dextran	150	1	Sigma-Aldrich	8.5	27
Fluorescein-dextran	500	1	Thermo Fisher	15.8	15
GFP	32.7	4	Biovision	n.a.	n.a.
Dendra2	27.5	0.5	Hoelzel Diagnostics	n.a	n.a.

Supplementary Table 6. Diffusion coefficients determined by *in vitro* experiments and PyFRAP analysis. Theoretical values were only computed if an estimate of the molecule's Stokes radius could be found. Mean D values determined by PyFRAP as well as literature values are given with standard deviation.

			PyFRAP		***Literature***		
Dextran size (kDa)	**Manufacturer**	**D ($\mu m^2/s$) theoretical**	**D ($\mu m^2/s$) experimental**	**n**	**D ($\mu m^2/s$) experimental**	**Technique**	**Reference**
3	Thermo Fisher	171	170.3 ± 21.9	19	161 ± 22	FCS	[22]
4	Sigma-Aldrich	166	181.1 ± 31.6	44	135 ± 10	FRAP	[23]
10	Thermo Fisher	101	83.1 ± 8.0	12	122 ± 4	FCS	[22]
40	Thermo Fisher	52	45.3 ± 11.1	57	47 ± 2	FCS	[22]
70	Thermo Fisher	39	26.9 ± 4.9	35	37 ± 7	FCS	[22]
70	Sigma-Aldrich	39	49.2 ± 5.6	31	30 ± 2	FRAP	[24]
150	Sigma-Aldrich	27	46.4 ± 5.6	31	26 ± 2	FRAP	[24]
500	Thermo Fisher	15	25.7 ± 1.8	11	23.2 ± 1.1	FRAP	[25]

Supplementary Table 7. Literature values used for Fig. 5.

Molecule	MW (kDa)	Temperature during measurement (°C)	Manufacturer	D ($\mu m^2/s$)	Stdev ($\mu m^2/s$)	Technique	Reference
Fluorescein	0.33	22	Sigma-Aldrich	300	n.a.	FCS	[24]
Fluorescein	0.33	23	n.a.	270	n.a.	FRAP	[26]
Fluorescein	0.33	23	n.a.	260	n.a.	FRAP	[26]
Na2-Fluorescein	0.376	25	Fluka	380	35	FRAP	[27]
Oregon Green 488 carboxylic acid	0.41230	23	Thermo Fisher	336	11	FCS	[22]
Rhodamine B	0.47901	23	Fluka	420	20	FCS	[22]
Rhodamine B	0.47901	22.5	Sigma-Aldrich	420	30	FCS	[28]
Rhodamine 6 G	0.47901	22.5	Molecular Probes	400	30	FCS	[28]
Rhodamine 6 G	0.47901	23	Thermo Fisher	400	20	FCS	[22]
Tetramethyl-Rhodamine methyl ester	0.50093	23	Thermo Fisher	412	18	FCS	[22]
Oregon Green 488 carboxylic acid succinimidyl ester	0.50938	23	Thermo Fisher	308	10	FCS	[22]
Rhodamine green succinimidyl ester	0.621	20	Molecular Probes	233	3	FCS	[29]
Alexa488 alkyne	0.774	32	Life Technologies	288	8	FCS	[30]
Fluorescent dextran	3	23	Thermo Fisher	161	22	FCS	[22]
Alexa488-dextran	3	32	Life Technologies	160	5	FCS	[30]
FITC-dextran	3	22	Pharmacia	98	6	FRAP	[31]
FITC-dextran	3	n.a.	Pharmacia	98	6	FRAP	[32]
FITC-dextran	4	25	Sigma-Aldrich	149	n.a.	FRAP	[33]
FITC-dextran	4	25	Sigma-Aldrich	135	10	FRAP	[23]
FITC-dextran	4	32	Sigma-Aldrich	135	6	FCS	[30]
FITC-dextran	4	20	Sigma-Aldrich	96	2.4	FCS	[34]
FITC-dextran	4	22	Sigma-Aldrich	89	n.a.	FRAP	[35]
FITC-dextran	4	19	Sigma-Aldrich	155	23	FRAP	[36]
FITC-dextran	9.4	20	Sigma-Aldrich	75	3	FRAP	[37]
Fluorescent dextran	10	23	Thermo Fisher	122	4	FCS	[22]
Rhodamine green dextran	10	20	Molecular Probes	115	4	FCS	[29]
Alexa488-dextran	10	32	Life Technologies	82	1.4	FCS	[30]
FITC-dextran	10	22	Sigma-Aldrich	76	n.a.	FRAP	[31]
FITC-dextran	10	20	Sigma-Aldrich	68	1	FCS	[34]
FITC-dextran	11	n.a.	Sigma-Aldrich	76	2.5	FRAP	[32]
FITC-dextran	11	22	Sigma-Aldrich	76	3	FRAP	[31]
FITC-dextran	12	25	Sigma-Aldrich	97	n.a.	FRAP	[33]
FITC-Insulin	12	25	Sigma-Aldrich	147	13	FRAP	[33]
FITC-dextran	17	22	Sigma-Aldrich	65	n.a.	FRAP	[31]
FITC-dextran	17.2	20	Sigma-Aldrich	64	2	FRAP	[37]
FITC-dextran	18	22	Sigma-Aldrich	65	7	FRAP	[31]
FITC-dextran	18	n.a.	Sigma-Aldrich	65	6.5	FRAP	[32]
FITC-dextran	20	22	Sigma-Aldrich	78	n.a.	FCS	[24]
FITC-dextran	20	22	Sigma-Aldrich	64	2	FRAP	[24]
FITC-dextran	20	29	Sigma-Aldrich	70	8	FRAP	[36]
FITC-dextran	20	22	Sigma-Aldrich	63	4	FRAP	[25]
FITC-dextran	21	25	Sigma-Aldrich	71	n.a.	FRAP	[33]
GFP	26.9	25	custom-made	87	n.a.	FCS	[38]
GFP	26.9	n.a.	custom-made	87	n.a.	FRAP	[39]
GFP	26.9	22	Clontech	82	n.a.	FCS	[24]

FITC-dextran	35.6	20	Sigma-Aldrich	44	5	FRAP	[37]
FITC-dextran	38	25	Sigma-Aldrich	62	n.a.	FRAP	[33]
Fluorescent dextran	40	23	Thermo Fisher	47	2	FCS	[22]
FITC-dextran	40	22	Sigma-Aldrich	45	n.a.	FCS	[40]
FITC-dextran	40	22	Sigma-Aldrich	45	n.a.	FCS	[24]
FITC-dextran	40	32	Sigma-Aldrich	45	1.1	FCS	[30]
FITC-dextran	40	22	Sigma-Aldrich	44	5	FRAP	[24]
FITC-dextran	40	22	Sigma-Aldrich	52	2	FRAP	[25]
FITC-dextran	41	22	Sigma-Aldrich	46	5	FRAP	[31]
FITC-dextran	41	n.a.	Sigma-Aldrich	46	4.6	FRAP	[32]
FITC-dextran	42	20	Sigma-Aldrich	39	0.4	FCS	[34]
FITC-dextran	51	25	Sigma-Aldrich	54	n.a.	FRAP	[33]
FITC-dextran	62	n.a.	Sigma-Aldrich	39	2.6	FRAP	[32]
FITC-dextran	62	22	Sigma-Aldrich	39	3	FRAP	[31]
FITC-BSA	67	25	n.a.	58	5	FRAP	[33]
FITC-dextran	70	22	Sigma-Aldrich	38	n.a.	FCS	[24]
FITC-dextran	70	22	Sigma-Aldrich	38	n.a.	FCS	[40]
Fluorescent dextran	70	23	Thermo Fisher	37	7	FCS	[22]
FITC-dextran	70	n.a.	Fluka	33	2.1	FCS	[41]
FITC-dextran	70	22	Sigma-Aldrich	30	2	FRAP	[24]
FITC-dextran	70	25	Thermo Fisher	30	3.1	FRAP	[27]
FITC-dextran	70	23	n.a.	23	n.a.	FRAP	[26]
FITC-dextran	70	22	Sigma-Aldrich	44	1	FRAP	[25]
FITC-dextran	71	25	Sigma-Aldrich	44	2	FRAP	[23]
FITC-dextran	71.2	20	Sigma-Aldrich	30	2	FRAP	[37]
FITC-dextran	77	20	Sigma-Aldrich	35	0.6	FCS	[34]
FITC-dextran	148	20	Sigma-Aldrich	25	3.1	FCS	[34]
FITC-dextran	148	20	Sigma-Aldrich	18	1	FRAP	[37]
FITC-dextran	150	22	Sigma-Aldrich	26	2	FRAP	[24]
FITC-dextran	150	22	Sigma-Aldrich	24	n.a.	FCS	[40]
FITC-dextran	150	22	Sigma-Aldrich	24	n.a.	FCS	[24]
FITC-dextran	150	20	Sigma-Aldrich	14	n.a.	FRAP	[42]
FITC-dextran	157	n.a.	Sigma-Aldrich	24	1.3	FRAP	[32]
FITC-dextran	157	22	Sigma-Aldrich	24	1	FRAP	[31]
FITC-dextran	167	25	Sigma-Aldrich	38	n.a.	FRAP	[33]
FITC-dextran	167	n.a.	Sigma-Aldrich	18.8	0.2	FRAP	[43]
FITC-dextran	260	25	Sigma-Aldrich	30	n.a.	FRAP	[33]
FITC-dextran	282	20	Sigma-Aldrich	16.6	0.8	FCS	[34]
FITC-dextran	464	20	Sigma-Aldrich	14	0.6	FCS	[34]
FITC-dextran	464	n.a.	Sigma-Aldrich	11	0.5	FRAP	[43]
FITC-dextran	500	22	Sigma-Aldrich	23	1	FRAP	[25]
FITC-dextran	580	25	Sigma-Aldrich	22	n.a.	FRAP	[33]
FITC-dextran	2000	25	Sigma-Aldrich	10	1	FRAP	[23]
Fluorescent dextran	2000	23	Thermo Fisher	6	1	FCS	[22]
FITC-dextran	2000	n.a.	Sigma-Aldrich	6.4	0.09	FRAP	[43]
FITC-dextran	2101	25	Sigma-Aldrich	14	n.a.	FRAP	[33]

Supplementary Table 8. Summary of tortuosity simulations.

Dimension	Geometry	Packing	Extracelluar volume fraction (EVF) (%)	Diffusion hindrance factor θ
2D	Circle	Regular	74	0.74
2D	Circle	Regular	59	0.61
2D	Circle	Random	56	0.57
2D	Circle	Random	36	0.49
2D	Circle	Ideal	25	0.44
3D	Cylinder	Regular	71	0.86
3D	Cylinder	Random	78	0.92
3D	Cylinder	Random	58	0.88
3D	Cylinder	Ideal	78	0.92
3D	Cylinder	Ideal	71	0.874
3D	Cylinder	Ideal	61	0.871
3D	Cylinder	Ideal	60	0.870
3D	Cylinder	Ideal	42	0.75
3D	Cuboid	Ideal	38	0.60

Supplementary Table 9. Diffusion coefficients determined by *in vitro* experiments and PyFRAP analysis in the presence of polyacrylamide beads. Mean diffusion values are given with standard error.

Dextran size (kDa)	Manufacturer	Condition	D ($\mu m^2/s$)	n
70	Thermo Fisher	Free	24.1 ± 0.4	13
70	Thermo Fisher	Beads	14.9 ± 0.5	17

Supplementary Table 10. Diffusion coefficients determined by *in vitro* and *in vivo* experiments and PyFRAP analysis with GFP and GFP fusion proteins. Mean diffusion values are given with standard error.

Molecule	**Manufacturer**	**Source**	**Condition**	**Context**	**D (µm^2/s) PyFRAP**	**n**
Recombinant GFP	Biovision	Protein	Free	*In vitro*	96.1 ± 2.2	23
Recombinant GFP	Biovision	Protein	Beads	*In vitro*	79.2 ± 4.1	18
Recombinant GFP	Biovision	Injected protein	Extracelluar matrix	*In vivo*	37.6 ± 3.7	15
Secreted GFP	In-house	Injected mRNA	Extracelluar matrix + production	*In vivo*	35.3 ± 4.8	17
Squint-GFP	In-house	Injected mRNA	Extracelluar matrix + production + binding	*In vivo*	1.7 ± 0.25	27

Supplementary Table 11. Parameters used for the simulation of FRAP experiments.

Variable	Definition	Default value
	Simulation	
D	Diffusion coefficient	$D = 50$ pixels^2/s
	Time stepping	
$t_{\mathrm{sim,start}}$	Simulation start time	0 s
$t_{\mathrm{sim,end}}$	Simulation end time	1680 s
n_{sim}	Number of time steps	4000
t_{scale}	Time-stepping scheme	Logarithmic
	Geometry	
r_{upper}	Upper radius of frustum	317.65 pixels
r_{lower}	Lower radius of frustum	224.25 pixels
h	Height of frustum	90.33 pixels
	Meshing	
v	Mesh element size	25 pixels^3
v_{BL}	Boundary layer element size	15 pixels^3
v_{slice}	Slice refinement element size	15 pixels^3
w_{BL}	Boundary layer thickness	30 pixels
	Solver	
ϵ	Solver tolerance	10^{-10}
N_{iter}	Solver iterations	1000

Supplementary Table 12. Fitting and model parameters, initial guesses, and bounded ranges. Note that we tried different initial guesses for the diffusion coefficient D, which prevented the minimisation algorithm from stopping at a local minimum. We then then took the fit that yielded the global minimum SSD.

Initial guesses		
Parameter	**Initial guess**	**Allowed range**
D (pixels^2/s)	1 - 200	0.01 - 400
k_1 (1/s)	0	0 - 100
k_2 ($[c]$/s)	0	0 - 100
E_{bleached}	1	0.1 - 3
E_{slice}	1	0.1 - 3
Fitting convergence		
Parameter	**Definition**	**Default value**
$N_{\max}$	Maximum number of function calls	1000
δ	Tolerance of termination	10^{-10}

Supplementary Table 13. Test data and settings to measure PyFRAP analysis speed.

	2D	**Frustum**	**Dome**
Geometry	2D circle	3D frustum	3D zebrafish dome
Number of images	301	301	301
Number of mesh cells	7000	20000	35000
Number of time steps	1000	3000	3000
Illumination correction	No	Yes	Yes
Median filter application	No	Yes	Yes

Supplementary Table 14. PyFRAP analysis speed.

Operating system	Version	Processor	Memory	2D test (s)	Frustum test (s)	Dome test (s)
Ubuntu	14.04 LTS	Intel Core i7-3520M 2.90 GHz	8 GB	97	378	489
Ubuntu	16.04 LTS	Intel Core i5-4210 2.60 GHz	8 GB	125	521	743
Ubuntu	16.04 LTS	Intel Xeon E3-1275 3.60 GHz	64 GB	73	347	437
Mac OS X	10.13.3	Intel Core i7-4790K 4.00 GHz	32 GB	79	282	386
Windows	8.1	Intel Core i7-5600U 2.60 Ghz	8 GB	91	373	567

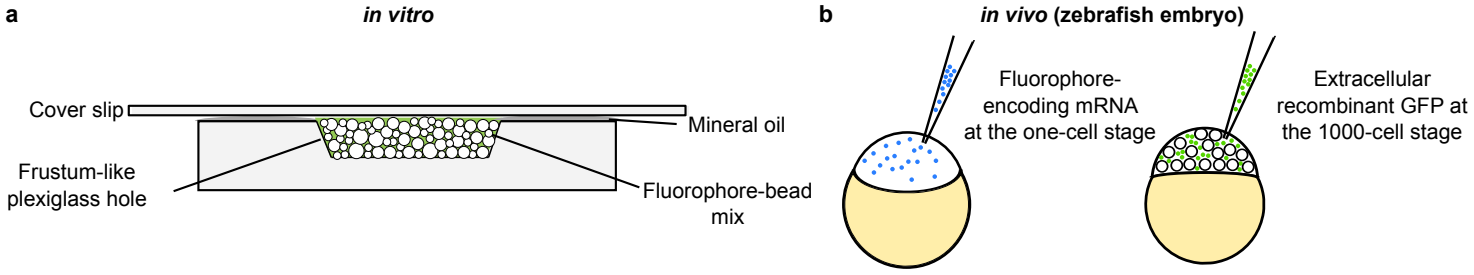

Supplementary Figure 1 | Sample preparation for *in vitro* and *in vivo* FRAP experiments. (a) *In vitro* experiments. Fluorophore solution was pipetted into a frustum-like plexiglass hole. The hole was then sealed with mineral oil and covered with a cover slip. The sample was flipped and placed under an inverted confocal microscope. **(b)** *In vivo* experiments in zebrafish embryos. mRNA encoding a fluorophore was injected into embryos at the one-cell stage, or recombinant GFP was injected into the extracellular space of embryos at the 1000-cell stage.

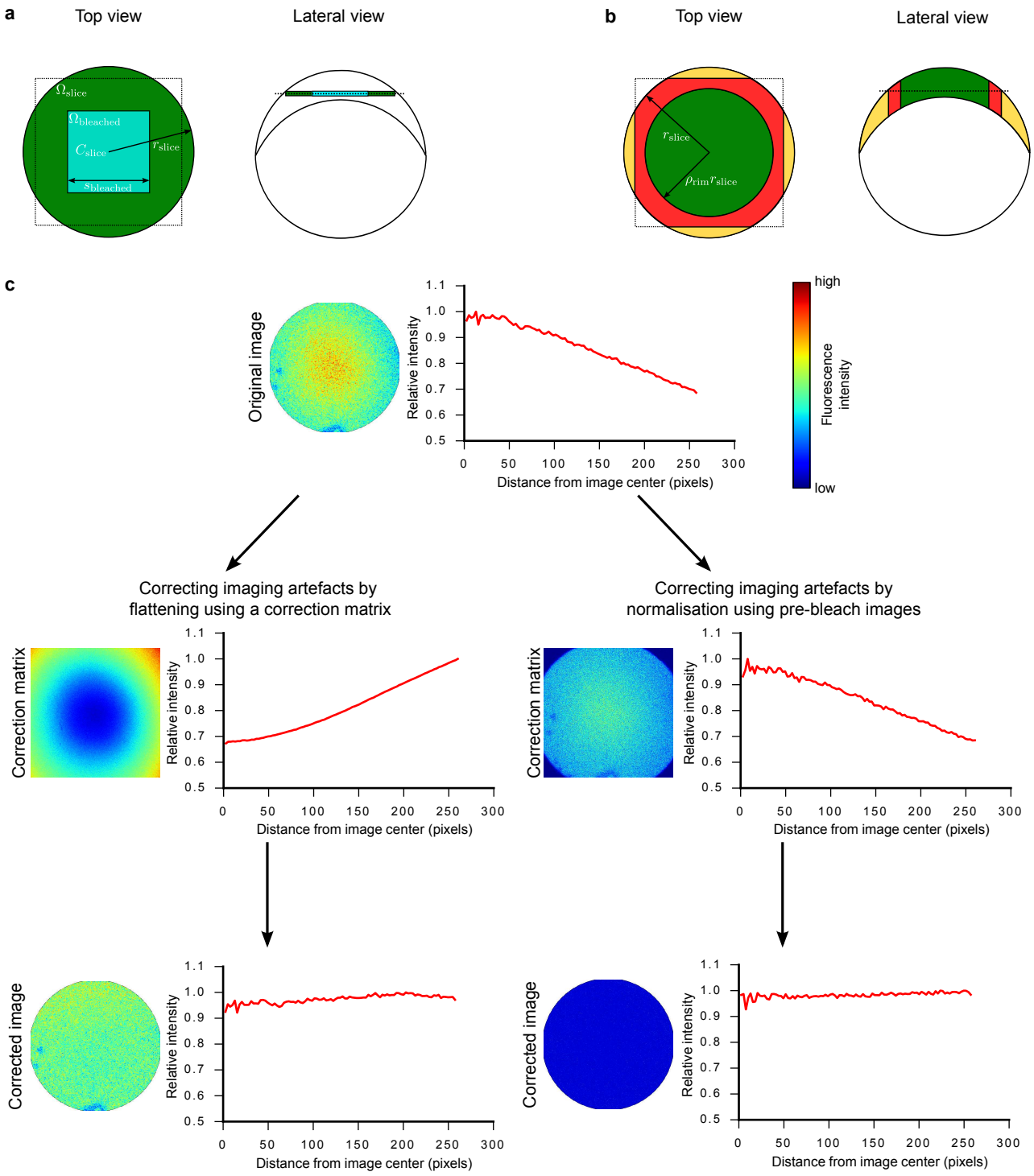

Supplementary Figure 2 | Image analysis in PyFRAP. (a) Basic regions of interest (ROIs) of FRAP analysis: The cyan square indicates the bleached region of the FRAP experiment inside the complete circular geometry within the imaging slice. The dashed lines indicate the location of the acquired image data. **(b)** Rim concentration calculation: Hypothetical data (orange) outside the acquired image (dashed line) is extrapolated through the average concentration in a slim rim of the visible fraction in the imaging slice (red). **(c)** Image manipulation techniques used to correct uneven illumination: Correction was either performed by multiplying the data with a correction matrix (flattening), or by dividing the data through an average pre-bleach image (normalisation). The original image shows a pre-bleach measurement of a uniformly distributed fluorophore. Deviations from the theoretical flat intensity profile are due to imaging artefacts.

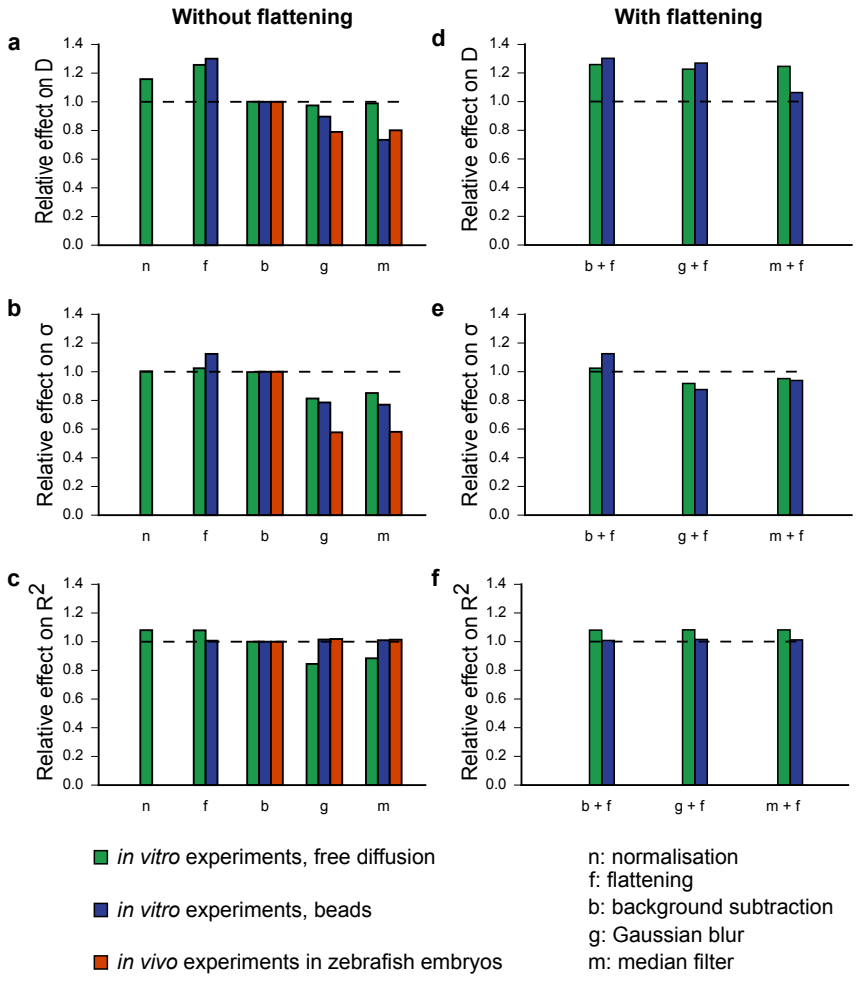

Supplementary Figure 3 | Analysis subset of image correction and smoothing techniques. Data sets were grouped by condition (*in vitro* experiments with free diffusion (green), *in vitro* experiments with beads (blue), and *in vivo* experiments in zebrafish embryos (orange)). Bar plots show the effect of each manipulation (n: normalisation, f: flattening, b: background subtraction, g: Gaussian blur, m: median filter) compared to analyses in which no manipulation was applied. Values above or below the dashed line indicate that the manipulation had an effect. **(a,b,c)** Effect on mean diffusion coefficient D, standard deviation σ, and R^2-value if only one of the five image manipulation techniques was applied, respectively. **(e,d,f)** Effect if flattening and one of the three remaining manipulation techniques was applied. *In vivo* experiments with zebrafish embryos were excluded for this analysis (see Supplementary Note 1 for details).

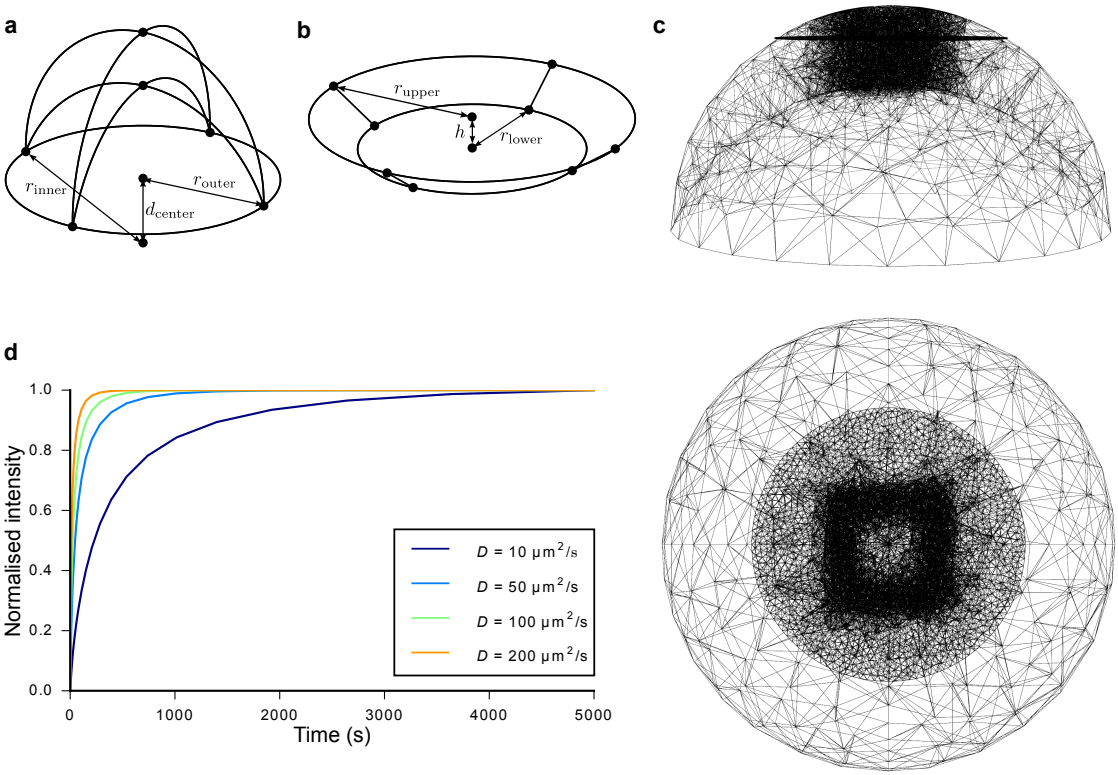

Supplementary Figure 4 | Simulation details for PyFRAP analysis. (a) The zebrafish dome geometry used to analyse *in vivo* experiments is described by the distance between the centers (d_{center}) and the radii (r_{inner}, r_{outer}) of two hemispheres. **(b)** The frustum geometry used to analyse *in vitro* experiments is described by the upper (r_{upper}) and lower (r_{lower}) radius and its height h. **(c)** Lateral and top views of tetrahedral meshes in the zebrafish dome geometry with a boundary layer mesh around the bleached area and a refined mesh in the imaging slice. **(d)** Scaling solution of a simulated FRAP recovery curve for different diffusion coefficients.

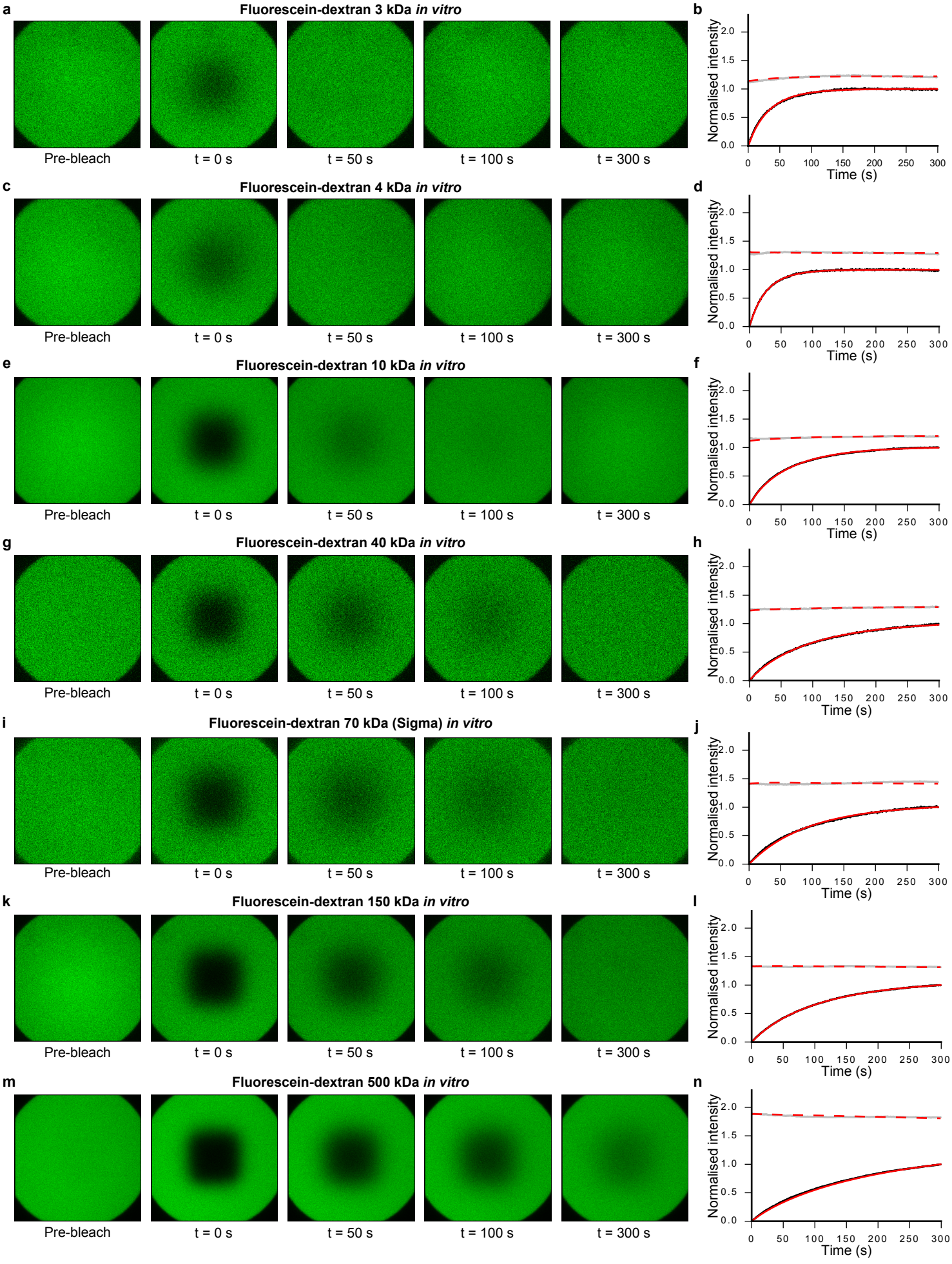

Supplementary Figure 5 | Examples of *in vitro* experiments and the resulting fits to measure free diffusion. (a,c,e,g,i,k,m) *In vitro* FRAP experiments with FITC-dextrans ranging from 3 kDa to 500 kDa. Maximum image intensities are the average pre-conversion intensities to facilitate comparison across data sets. **(b,d,f,h,j,l,n)** Black and grey dots represent data points of bleached and slice ROI, respectively. Red solid and dashed lines show the respective fits. Recovery curves were normalised between 0 (intensity in the bleached ROI at the first post-bleach time point) and 1 (intensity in the bleached ROI at the last post-bleach time point) to facilitate comparison across data sets.

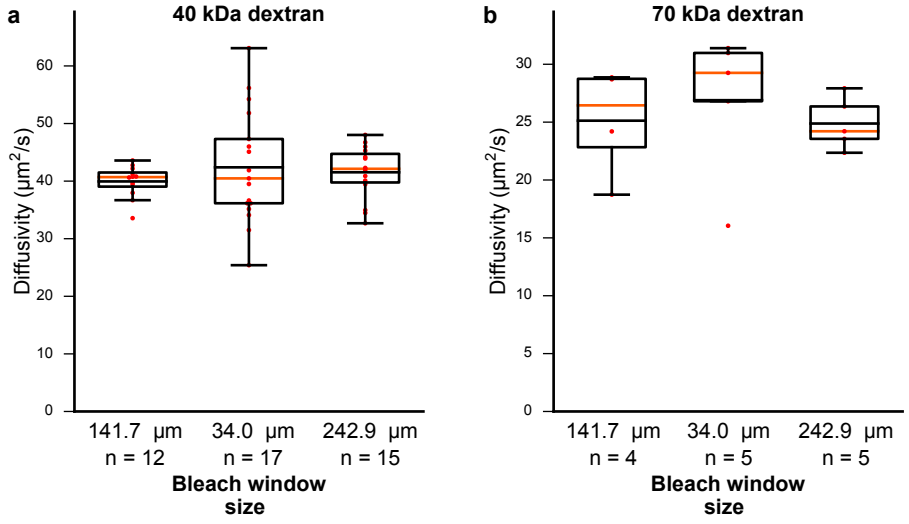

Supplementary Figure 6 | Different bleach window sizes do not affect diffusion coefficient estimates. (a) Results of control experiments with fluorescent dextran (40 kDa) for differently sized bleach windows. **(b)** Results of control experiments with fluorescent dextran (70 kDa) for differently sized bleach windows. Box plots in (a) and (b) show median (orange line), mean (black line), 25% quantiles (box), and all included data points (red markers). Whiskers extend to the smallest data point within the 1.5 interquartile range of the lower quartile, and to the largest data point within the 1.5 interquartile range of the upper quartile.

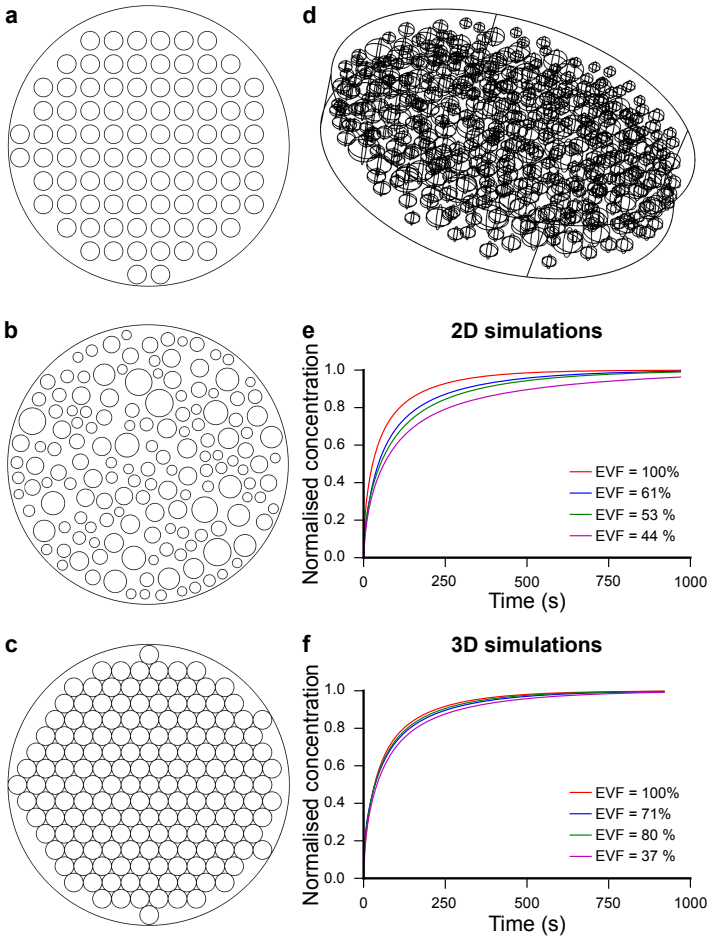

Supplementary Figure 7 | Simulations of tortuous environments in bead experiments. (a,b,c) Regularly (EVF = 59%), randomly (EVF = 56%), and ideally (EVF = 25%) placed beads in a two-dimensional circular domain. **(d)** Randomly (EVF = 78%) placed beads in a three-dimensional cylindrical domain. **(e,f)** Comparison between recovery curves in 2D and 3D bead simulations. Red lines indicate simulations without beads, blue lines indicate simulations with regularly placed beads, green lines indicate simulations with randomly placed beads, and magenta lines indicate simulations with ideally placed beads.

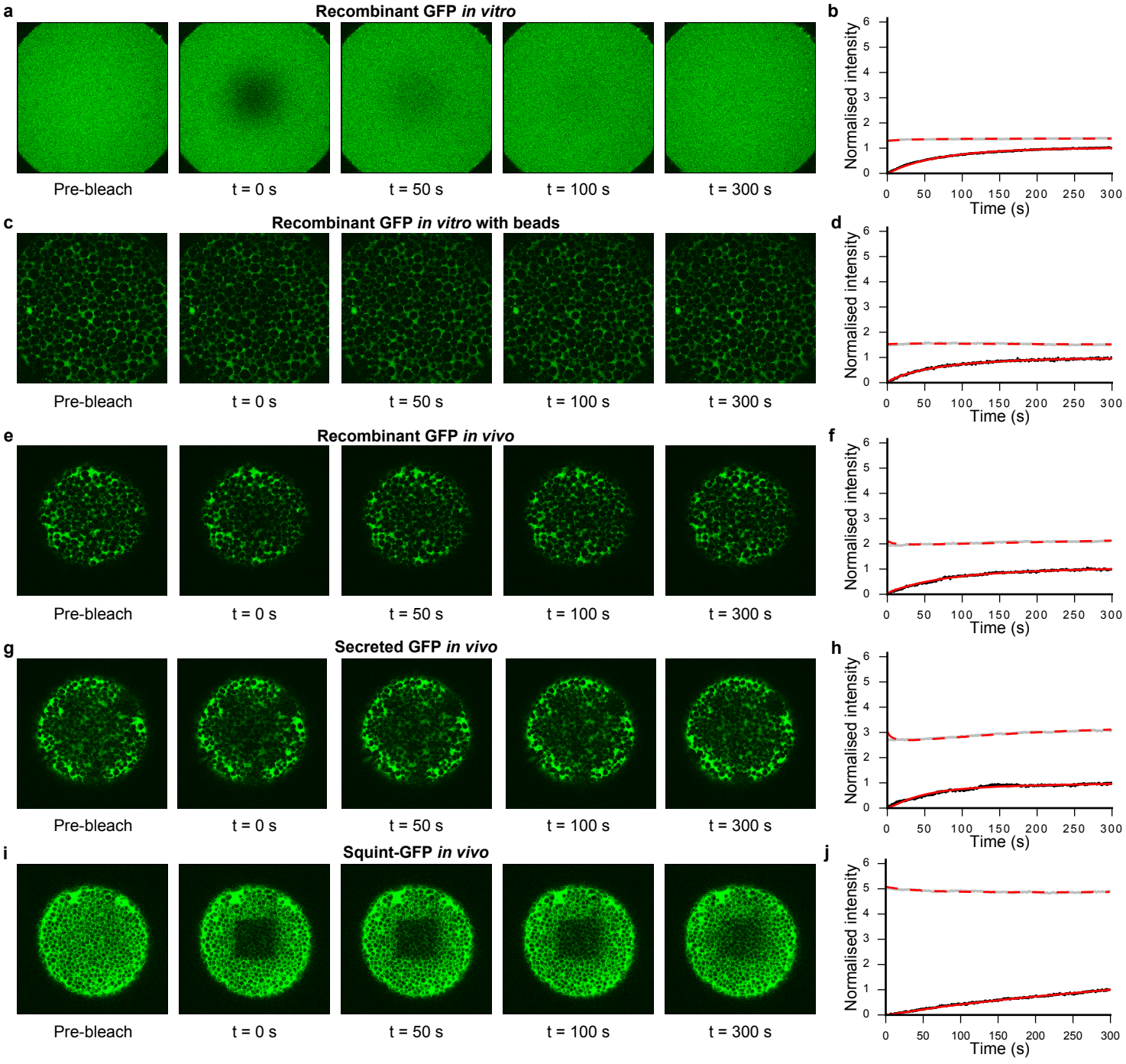

Supplementary Figure 8 | Examples of *in vitro* and *in vivo* experiments and the resulting fits. (a,b) *In vitro* FRAP experiment with recombinant GFP. **(c,d)** *In vitro* FRAP experiment with recombinant GFP mixed with polyacrylamide beads. **(e,f,g,h,i,j)** *In vivo* FRAP experiment in zebrafish embryos with recombinant GFP, secreted GFP, and Squint-GFP, respectively. **(b,d,f,h,j)** Black and grey dots represent data points of bleached and slice ROI, respectively. Red solid and dashed lines show the respective fits. Recovery curves were normalised between 0 (intensity in the bleached ROI at the first post-bleach time point) and 1 (intensity in the bleached ROI at the last post-bleach time point) to facilitate comparison across data sets.

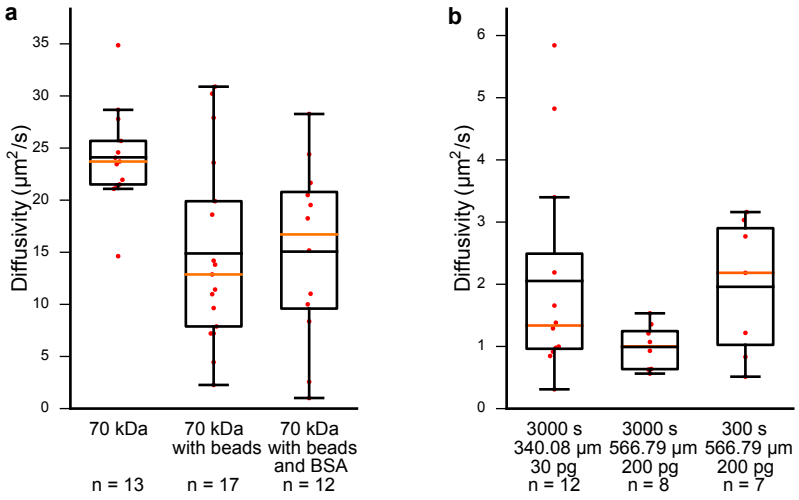

Supplementary Figure 9 | Results of control experiments for *in vitro* and *in vivo* FRAP experiments. (a) Results of control experiments with fluorescent dextran (70 kDa), and beads with or without BSA. BSA does not influence the diffusion of the fluorescent dextran. **(b)** Results of control experiments for different amounts (30 - 200 pg) of injected *Squint-GFP* mRNA, varying length of experiments (300 - 3000 s) and magnification (image size: 340.08 - 566.79 µm). Different imaging settings do not affect the measured diffusion coefficient of Squint-GFP. Box plots in (a) and (b) show median (orange line), mean (black line), 25% quantiles (box), and all included data points (red markers). Whiskers extend to the smallest data point within the 1.5 interquartile range of the lower quartile, and to the largest data point within the 1.5 interquartile range of the upper quartile.

Supplementary References

1. Rapsomaniki, M. A. *et al.* EasyFRAP: An interactive, easy-to-use tool for qualitative and quantitative analysis of FRAP data. *Bioinformatics* **28,** 1800–1801 (2012).
2. Miura, K. *FrapCalc* (accessed: 2016-12-12). `http://wiki.cmci.info/downloads/frap_analysis` (2016).
3. Schaff, J. C., Cowan, A. E., Loew, L. M. & Moraru, I. I. Virtual FRAP - an experiment-oriented simulation tool. *Biophysical Journal* **96,** 30a (2009).
4. Blumenthal, D., Goldstien, L., Edidin, M. & Gheber, L. A. Universal approach to FRAP analysis of arbitrary bleaching patterns. *Scientific Reports* **5,** 11655 (2015).
5. Müller, P. *et al.* Differential diffusivity of Nodal and Lefty underlies a reaction-diffusion patterning system. *Science* **336,** 721–724 (2012).
6. Müller, P., Rogers, K. W., Yu, S. R., Brand, M. & Schier, A. F. Morphogen transport. *Development* **140,** 1621–1638 (2013).
7. Pomreinke, A. P. *et al.* Dynamics of BMP signaling and distribution during zebrafish dorsal-ventral patterning. *Elife* **6,** e25861 (2017).
8. Sprague, B. L., Pego, R. L., Stavreva, D. A. & McNally, J. G. Analysis of binding reactions by Fluorescence Recovery After Photobleaching. *Biophysical Journal* **86,** 3473–3495 (2004).
9. Hrabe, J., Hrabetová, S. & Segeth, K. A model of effective diffusion and tortuosity in the extracellular space of the brain. *Biophysical Journal* **87,** 1606–1617 (2004).
10. Tao, L. & Nicholson, C. Maximum geometrical hindrance to diffusion in brain extracellular space surrounding uniformly spaced convex cells. *Journal of Theoretical Biology* **229,** 59–68 (2004).
11. Novak, I. L., Kraikivski, P. & Slepchenko, B. M. Diffusion in cytoplasm: Effects of excluded volume due to internal membranes and cytoskeletal structures. *Biophysical Journal* **97,** 758–767 (2009).
12. Donovan, P., Chehreghanianzabi, Y., Rathinam, M. & Zustiak, S. P. Homogenization theory for the prediction of obstructed solute diffusivity in macromolecular solutions. *PLoS ONE* **11,** e0146093 (2016).
13. Student. The probable error of a mean. *Biometrika* **6,** 1–25 (1908).
14. Welch, B. L. The generalisation of Student's problems when several different population variances are involved. *Biometrika* **34,** 28–35 (1947).
15. Wilcoxon, F. Individual comparisons by ranking methods. *Biometrics Bulletin* **1,** 80–83 (1945).
16. Mann, H. B. & Whitney, D. R. On a test of whether one of two random variables is stochastically larger than the other. *The Annals of Mathematical Statistics* **18,** 50–60 (1947).
17. Shapiro, S. S. & Wilk, M. B. An analysis of variance test for normality (complete samples). *Biometrika* **52,** 591–611 (1965).
18. Akaike, H. A new look at the statistical model identification. *IEEE Transactions on Automatic Control* **19,** 716–723 (1974).
19. Aaron, J. *FRAP* (accessed: 2016-12-12). `https://de.mathworks.com/matlabcentral/fileexchange/47327-frap-zip` (2016).
20. Kraft, L. J., Dowler, J. & Kenworthy, A. K. *Frap-Toolbox: Software for the analysis of Fluorescence Recovery After Photobleaching* (accessed: 2016-12-12). `http://www.fraptoolbox.com` (2014).

21. Ulrich, M. *et al.* Tropical-parameter estimation and simulation of reaction-diffusion models based on spatio-temporal microscopy images. *Bioinformatics* **22,** 2709–2710 (2006).

22. Zhang, Z., Nadezhina, E. & Wilkinson, K. J. Quantifying diffusion in a biofilm of Streptococcus mutans. *Antimicrobial Agents and Chemotherapy* **3,** 1075–1081 (2011).

23. Pluen, A., Netti, P. A., Jain, R. K. & Berk, D. A. Diffusion of macromolecules in agarose gels: Comparison of linear and globular configurations. *Biophysical Journal* **1,** 542–552 (1999).

24. Guiot, E. *et al.* Molecular dynamics of biological probes by Fluorescence Correlation Microscopy with two-photon excitation. *Journal of Fluorescence* **4,** 413–419 (2000).

25. Braga, J., Desterro, J. M. & Carmo-Fonseca, M. Intracellular macromolecular mobility measured by Fluorescence Recovery After Photobleaching with confocal laser scanning microscopes. *Molecular Biology of the Cell* **15,** 4749–4760 (2004).

26. Periasamy, N. & Verkman, A. Analysis of fluorophore diffusion by continuous distributions of diffusion doefficients: application to photobleaching measurements of multicomponent and anomalous diffusion. *Biophysical Journal* **1,** 557–567 (1998).

27. Schuster, E., Hermansson, A. M., Öhgren, C., Rudemo, M. & Lorén, N. Interactions and diffusion in fine-stranded β-lactoglobulin gels determined via FRAP and binding. *Biophysical Journal* **1,** 253–262 (2014).

28. Gendron, P. O., Avaltroni, F. & Wilkinson, K. J. Diffusion coefficients of several rhodamine derivatives as determined by pulsed field gradient-nuclear magnetic resonance and Fluorescence Correlation Spectroscopy. *Journal of Fluorescence* **6,** 1093–1101 (2008).

29. Visser, N. V., Hink, M. A., Hoek, A. V. & Visser, A. J. Comparison between Fluorescence Correlation Spectroscopy and time-resolved fluorescence anisotropy as illustrated with a fluorescent dextran conjugate. *Journal of Fluorescence* **3,** 251–255 (1999).

30. Kihara, T., Ito, J. & Miyake, J. Measurement of biomolecular diffusion in extracellular matrix condensed by fibroblasts using Fluorescence Correlation Spectroscopy. *PLoS ONE* **11** (2013).

31. Peters, R. Nucleo-cytoplasmic flux and intracellular mobility in single hepatocytes measured by fluorescence microphotolysis. *The EMBO Journal* **8,** 1831–6 (1984).

32. Lang, I., Scholz, M. & Peters, R. Molecular mobility and nucleocytoplasmic flux in hepatoma cells. *Journal of Cell Biology* **4,** 1183–1190 (1986).

33. Gribbon, P. & Hardingham, T. E. Macromolecular diffusion of biological polymers measured by confocal Fluorescence Recovery After Photobleaching. *Biophysical Journal* **2,** 1032–1039 (1998).

34. Gorisch, S. M. Histone acetylation increases chromatin accessibility. *Journal of Cell Science* **24,** 5825–5834 (2005).

35. Keminer, O. & Peters, R. Permeability of single nuclear pores. *Biophysical Journal* **1,** 217–228 (1999).

36. Floury, J., Madec, M. N., Waharte, F., Jeanson, S. & Lortal, S. First assessment of diffusion coefficients in model cheese by Fluorescence Recovery After Photobleaching (FRAP). *Food Chemistry* **2,** 551–556 (2012).

37. Arrio-Dupont, M., Cribier, S., Foucault, G., Devaux, P. & D'Albis, A. Diffusion of fluorescently labeled macromolecules in cultured muscle cells. *Biophysical Journal* **5,** 2327–2332 (1996).

38. Terry, B., Matthews, E. & Haseloff, J. Molecular characterization of recombinant green fluorescent protein by Fluorescence Correlation Microscopy. *Biochemical and Biophysical Research Communications* **1,** 21–27 (1995).

39. Swaminathan, R., Hoang, C. & Verkman, A. Photobleaching recovery and anisotropy decay of green fluorescent protein GFP-S65T in solution and cells: cytoplasmic viscosity probed by green fluorescent protein translational and rotational diffusion. *Biophysical Journal* **4,** 1900–1907 (1997).

40. Gulot, E. *et al.* Heterogeneity of diffusion inside microbial biofilms determined by Fluorescence Correlation Spectroscopy under two-photon excitation. *Photochemistry and Photobiology* **6,** 570–8 (2002).

41. Müller, K. P. *et al.* Multiscale analysis of dynamics and interactions of heterochromatin protein 1 by fluorescence fluctuation microscopy. *Biophysical Journal* **11,** 2876–2885 (2009).

42. Waharte, F., Steenkeste, K., Briandet, R. & Fontaine-Aupart, M. P. Diffusion measurements inside biofilms by image-based Fluorescence Recovery After Photobleaching (FRAP) analysis with a commercial confocal laser scanning microscope. *Applied and Environmental Microbiology* **17,** 5860–5869 (2010).

43. Braeckmans, K., Peeters, L., Sanders, N. N., De Smedt, S. C. & Demeester, J. Three-dimensional Fluorescence Recovery After Photobleaching with the confocal scanning laser microscope. *Biophysical Journal* **4,** 2240–2252 (2003).